



Therapeutic potential and physiological roles of Insulin-Degrading Enzyme illuminated by a DNA-templated macrocyclic inhibitor

Citation

Maianti, Juan Pablo. 2015. Therapeutic potential and physiological roles of Insulin-Degrading Enzyme illuminated by a DNA-templated macrocyclic inhibitor. Doctoral dissertation, Harvard University, Graduate School of Arts & Sciences.

Permanent link

<http://nrs.harvard.edu/urn-3:HUL.InstRepos:17467523>

Terms of Use

This article was downloaded from Harvard University's DASH repository, and is made available under the terms and conditions applicable to Other Posted Material, as set forth at <http://nrs.harvard.edu/urn-3:HUL.InstRepos:dash.current.terms-of-use#LAA>

Share Your Story

The Harvard community has made this article openly available. Please share how this access benefits you. [Submit a story](#).

[Accessibility](#)

***Therapeutic potential and physiological roles
of Insulin-Degrading Enzyme illuminated by
a DNA-templated macrocyclic inhibitor***

A dissertation presented

by

Juan Pablo Maianti

to

The Department of Chemistry and Chemical Biology

in partial fulfillment of the requirements

for the degree of

Doctor of Philosophy

in the subject of

Chemistry and Chemical Biology

Harvard University

Cambridge, Massachusetts

May 2015

© 2015 by Juan Pablo Maianti

All rights reserved.

Therapeutic potential and physiological roles of Insulin-Degrading Enzyme illuminated by a DNA-templated macrocyclic inhibitor

Abstract

Insulin-Degrading Enzyme (IDE) is a zinc-metalloprotease responsible for the clearance of insulin in peripheral tissues. Despite decades of speculation that inhibiting endogenous insulin degradation might treat Type-2 Diabetes, the functional relationship between IDE and glucose homeostasis remains unclear. IDE inhibitors that are active *in vivo* are therefore needed to elucidate IDE's physiological roles and to determine its potential to serve as a target for the treatment of diabetes.

In this thesis I describe the development of the first highly specific IDE *in vivo* probe, identified from a DNA-templated library of macrocycles, which enabled the first study of the physiological consequences of IDE inhibition. An X-ray structure of the macrocycle bound to IDE reveals that it engages a novel binding pocket away from the catalytic site, which explains its remarkable specificity and its suitability to study IDE *in vivo*. Treatment of lean and obese mice with this inhibitor revealed that IDE regulates multiple metabolic hormones, including glucagon and amylin, in addition to insulin. Under physiological conditions that mimic a meal, such as oral glucose administration, acute IDE

inhibition leads to substantial improvement in glucose tolerance, owing to the potentiation of endogenous insulin and amylin levels over glucagon signaling. These studies demonstrated the feasibility of modulating IDE activity as a therapeutic strategy to treat diabetes and expanded our understanding of the roles of IDE in glucose and hormone regulation.

Based on these studies we sought to develop substrate-selective inhibitors that block IDE's ability to degrade insulin but not its ability to degrade glucagon, which would represent a major step forward towards IDE-targeted therapeutics. The first-generation DNA-templated inhibitor was retailored into a fluorescent anisotropy tool for high-throughput screening of diverse small-molecule libraries. We discovered and characterized a family of IDE inhibitors with sub-micromolar potencies that inherited the remarkable specificity for IDE over other metalloproteases, and selectively obstruct IDE-mediated insulin degradation in a way that accommodates for glucagon cleavage.

In conclusion, these findings offer new insights into the biological roles of IDE and establish a novel strategy to selectively potentiate the physiological insulin response in order to improve blood sugar control in Type-2 Diabetes.

Dedicated to Nicole.

“Study enzymes under the most natural conditions of action, in the living cell itself. From the standpoint of preparative chemistry they may be looked upon as being of the utmost impurity. However, if one finds molecules that selectively interact with the enzymes, the rest of the cell interferes as little as does the glass wall of a test tube in which a chemical reaction is carried out.”

— Otto Warburg (1928), *Über die katalischen Wirkungen der lebendigen Substanz*, Springer-Verlag, Berlin (translated by Helmut Sies in *Trends in Biochemical Sciences*, 1980, 5, 182-185).

“But Natural Selection, as we shall hereafter see, is a power incessantly ready for action, and is immeasurably superior to man's feeble efforts, as the works of Nature are to those of Art.”

— Charles Darwin, *The Origin of Species*, Chapter 3.

Acknowledgements

I acknowledge the financial support from Fonds de la Recherche en Santé du Québec (FRSQ) for a three year PhD fellowship (#20318). I also acknowledge the support from the Alfred Bader Fellowship during the academic year 2010-2011, and the GSAS Merit Fellowship from the John Parker Bequest fund during the academic year 2014-2015.

First I would like to thank my advisor Prof. David Liu for his encouragement and investment in my scientific training, and above all for being an insightful and collegial mentor. Moreover, I had the huge benefit of working in close collaboration by Prof. Alan Saghatelian, who for all intents and purposes was my co-advisor during his tenure at Harvard. I thank you both for your boundless optimism, for granting me with broad intellectual independence, and for the responsibilities that you entrusted on me throughout the past five years.

I am very thankful to Prof. Nathanael Gray for taking part in my advising committee, for his continued encouragement, and his numerous insightful recommendations in small molecule development.

The research I described in this dissertation took our team in a number of particularly interdisciplinary directions, and undoubtedly, the bulk of this work would not have been achieved without the support of numerous talented student colleagues, our collaborators from other universities, and Harvard staff members.

I would like to thank Prof. Markus Seeliger and Zack Foda (Stony Brook University) for their excellent work in solving the IDE:6b co-crystal X-ray structure, which helped us understand the molecular basis of IDE inhibition. I

learnt a lot from Markus about protein structure when we mutated the inhibitor distal binding site to corroborate the placement of the 6b building blocks.

Dr. Maureen Charron (Albert Einstein College of Medicine) generously provided us with a large cohort of glucagon-receptor knockout mice. I thank her and Sally Du for welcoming me into her lab in New York on multiple occasions to carry out the experiments in collaboration with Sally. We are also indebted to Prof. Malcolm Leissring for providing the cohort of IDE knockout mice and controls that enabled us to corroborate the lack effects of 6bK in mice lacking the target.

I am very thankful to the contemporary colleagues of the DTS team for training and enriching exchange of ideas and protocols: Dr. Ralph Kleiner, Dr. Christoph Dumelin, Dr. Lynn McGregor, Dr. Jia Niu, Prof. Ryan Hilli, Dr. Rick McDonald, Dr. Dmitry Usanov, Alix Chan, Zhen Chen, Dennis Dobrovolsky, Dr. Phillip Lichtor, Dr. Yevgeny Brudno, Prof. David Gorin, Dr. Adam Kamlet, and Dr. Yu He. Ralph was an outstanding mentor during my early training.

Furthermore, I deeply thank all the contemporary Liu lab group members for their friendship and intellectual exchanges throughout these years: Ahmed Badran, Jeff Bessen, Dr. Jake Carlson, Dr. Grace Chen, Liwei Chen, Dr. James Cronican, Kevin Davis, Dr. Brent Dorr, Dr. John Guilinger, Chris Green, Johnny Hu, Bill Kim, Margie Li, Michael Packer, Dr. Vikram Pattanayak, Holly Rees, Tim Roth, Dr. David Thompson, as well as the postdoctoral researchers Prof. Bryan Dickinson, Dr. David Bryson, Dr. Brian Chaikind, Dr. Chihui An, Prof. Ed Curtis, Dr. Xue Gao, Dr. Nicole Gaudelli, Prof. Basil Hubbard, Dr. Alexis Komor, Dr. Jasmina Marjanovic, Prof. Aaron Leconte, Dr. Ning Sun, and Dr. John Zuris. I

underscore the helpful molecular biology contributions of Ahmed. Thanks are also due to Alekandar Markovic for keeping the lab running smoothly year after year.

The Saghatelian group was my lab away from lab, and I thank all the members including Dr. Amanda McFedries, Dr. Edwin Homan, and Dr. Anna Mari Lone for their help. Edwin and Anna Mari taught me the first glucose tolerance test procedures, and Amanda worked diligently with me throughout 2013-2014 to characterize the effects of acute IDE inhibition in mice.

I would like to thank Dr. Chuck Vanderburg for enabling the readout of multiplexed magnetic bead hormone panels at the Advanced Tissue Resource Center of the MassGeneral Institute for Neurodegenerative Disease.

I acknowledge the generous contributions of Dr. Bridget Wagner and Dr. Amedeo Vetere when I approached them with the wild idea of screening for new IDE inhibitors using fluorescence polarization. Thank you so much for welcoming me into the Broad Institute and enabling the small molecule screens.

More recently we begun working in closer collaboration with the Broad Institute to further develop the substrate-selective IDE inhibitor hits. I would like to thank Prof. Schreiber for his advice and generously making available a number of resources. I thank Dr. Marshall Morningstar for helping us establish a contractor to produce the azetidine core, as well as Dr. Sivaraman Dandapani and Dr. Mark Fitzgerald for providing me with the synthetic starting material to make the first batch of BRD-297. Thanks are due to Dr. Stephen Johnston for the microsomal stability characterization of 6bK and azetidine hits, and to Dr. Josh Bittker for printing the azetidine library plates.

All the *in vivo* work discussed in this thesis would not have been possible without the excellent support of the veterinary staff of the Biology Infrastructure Facility, in particular Dawn Hidenfelter, Jaime Moreno, Mimi Crowley, Dr. Mimi Lam, and Dr. Steven Niemi.

I would also like to acknowledge our most recent collaborators Prof. Peter Kang and Dr. Qingen Ke at the Beth Israel Deaconess Medical Center for welcoming me into their lab to explore the effects of IDE inhibition on blood pressure.

I am indebted to Prof. Matthew Shair for the opportunity of teaching Advanced Organic Synthetic Chemistry CHEM115 and I extend my thanks to all the class of CHEM115ers in Fall 2011.

Thanks are due to all the staff of the Chemistry and Chemical Biology Department for the excellent research facilities and support. In particular, I would like to thank Dr. Allen Alloise for his advice in multiple occasions, as well as Kathy Oakley for the warm welcome to the department.

Finally, I would like to thank my family and friends, near and far, for their support and constant encouragement.

This thesis is dedicated to my loving wife Dr. Nicole Darricarrère in acknowledgement of her unconditional support, kindhearted advice, and admirable dedication, throughout the past 10 years doing science together around the globe.

Thank you all most sincerely.

Table of Contents

Title page.....	i
Abstract	iii
Acknowledgments.....	vii
Table of Contents	xi
List of Sections.....	xii
List of Figures	xiv
List of Tables.....	xvii
Abbreviations	xviii

List of Sections

Chapter 1 – Introduction to Insulin-Degrading Enzyme and DNA-encoded platforms for small molecule discovery	1
1.1 - Introduction: small molecule discovery using DNA-encoded libraries	2
1.2 - The need for therapeutic validation of Insulin-Degrading Enzyme	11
1.3 - The search for the first physiologically active IDE inhibitor	22
1.4 - Outline of this thesis	25
1.5 - References.....	26
Chapter 2 – Identification of potent and highly specific IDE inhibitors from a DNA-templated library of macrocycles	41
2.1 – <i>In vitro</i> selection reveals a series of potent macrocyclic IDE inhibitors	42
2.2 – Complementary biochemical assays for IDE inhibition	44
2.3 – Structure-activity relationship of macrocyclic IDE inhibitors.....	48
2.4 – Metalloprotease selectivity of macrocyclic IDE inhibitors.....	52
2.5 – Biochemical studies and mode of inhibition of macrocycle 6b	53
2.6 – Structural basis of IDE inhibition and mutagenesis study to corroborate the novel distal binding site.....	57
2.7 – Methods.....	63
2.8 – References.....	87
Chapter 3 – Development of the first physiologically active IDE inhibitor	90
3.1 – Introduction (and spoiler alert)	91
3.2 – Biodistribution and pharmacokinetic properties of 6bK	93
3.3 – Augmentation of insulin hypoglycemic effects and abundance by IDE inhibition <i>in vivo</i>	97
3.4 – IDE inhibitor activity- and dose-response in glucose tolerance tests	99
3.5 – Features and limitations of 6bK as an <i>in vivo</i> probe.....	103
3.6 – Methods.....	106
3.7 – References.....	112
Chapter 4 – Discovery of the Anti-diabetic Activity of Insulin-Degrading Enzyme Inhibitors Mediated by Multiple Hormone Substrates.....	116

4.1 – Introduction: glucose tolerance tests and mice models of diabetes	117
4.2 – IDE inhibition improves blood glucose clearance following oral glucose administration	118
4.3 – IDE inhibition during an injected glucose challenge leads to impaired glucose tolerance	122
4.4 – IDE regulates multiple hormones <i>in vivo</i>	124
4.5 – IDE inhibition promotes glucagon signaling and gluconeogenesis.....	128
4.6 – IDE inhibition promotes amylin signaling and gastric emptying	132
4.7 – Knockout experiments corroborate the IDE on-target effects of 6bK ..	134
4.8 – Therapeutic implications of IDE inhibition.....	137
4.9 – Methods	142
4.10 – References.....	150
Chapter 5 – Discovery of substrate-selective IDE inhibitors that obstruct insulin degradation but allow IDE-mediated glucagon proteolysis	157
5.1 – Introduction: the need for new substrate-selective IDE inhibitors	158
5.2 – Optimization of an anisotropy assay using a fluorescent probe based on the first-generation DNA-templated macrocyclic inhibitor	159
5.3 – High-throughput screening of the Broad Institute libraries	163
5.4 – Discovery of substrate-selective inhibitors of IDE-mediated insulin degradation that allow glucagon proteolysis.....	174
5.5 – Metalloprotease specificity of IDE inhibitor hits.....	181
5.6 – Binding site mutagenesis and structural basis for substrate-selective IDE inhibition	183
5.7 – Perspective for the future of IDE-based therapeutics	190
5.8 – Methods.....	193
5.9 – References.....	205
Annex – Perl scripts used for deconvolution of <i>in vitro</i> selections.....	210

List of Figures

Figure 1.1 Scheme of an <i>in vitro</i> selection using a DNA-encoded library, followed by high-throughput sequencing decoding and deconvolution	3
Figure 1.2 Complementary methods to produce DNA-encoded libraries.....	4
Figure 1.3 Representative DNA-encoded libraries that resulted from DNA-recorded and DNA-routed methods, and compatible chemical reactions for DNA-encoded libraries	8
Figure 1.4 Ordered multistep DNA-templated translation of a mixture of DNA barcodes into a pilot 13,824 membered DNA-encoded library of macrocycles	9
Figure 1.5 Building blocks used in the 13,824 library of macrocycles.....	10
Figure 1.6 Unique structural and biochemical features of IDE	13
Figure 1.7 Classes of structurally distinct hormones cleaved by IDE <i>in vitro</i> assays	16
Figure 1.8 Insulin signaling cascade, showing the potential of IDE-mediated degradation to modulate insulin signaling on the insulin receptor	18
Figure 1.9 Phenotypic disconnect between cell-based observations of IDE inhibition <i>versus</i> studies using IDE ^{-/-} mice studies due to a metabolic compensatory phenotype	20
Figure 1.10 Anti-diabetic treatments classified based on their impact on insulin signaling..	22
Figure 1.11 Known inhibitors of IDE are weak or non-selective	24
Figure 2.1 Enrichment results from two independent <i>in vitro</i> selections against mouse N-His ₆ -IDE using the DNA-templated macrocycle library	42
Figure 2.2 Structures of IDE-binding macrocycles 1–6	44
Figure 2.3 Enrichment results from a third independent <i>in vitro</i> selection against human N-His ₆ -IDE ₍₄₉₋₁₀₁₉₎ using the DNA-templated macrocycle library	45
Figure 2.4 Cleavage of the fluorogenic substrate peptide Mca-RPPGFSAFK(Dnp)-OH by human and mouse IDE in the presence of inhibitors 6b and 6bK	46
Figure 2.5 Homogeneous time-resolved FRET (HTRF) assay for IDE-mediated insulin degradation in the presence of 6b analogs.....	46
Figure 2.6 LC-MS assay for ex vivo degradation of α -CGRP by endogenous IDE in mouse plasma in the presence of 6b	47
Figure 2.7 Solid supported synthesis routes to <i>cis</i> - and <i>trans</i> -alkene isomers of macrocycles based on a common intermediate.....	50
Figure 2.8 IDE inhibition potency of selection hits 1b to 6b and 30 structurally related analogs	51

Figure 2.9 Selectivity analysis of macrocycle 6bK reveals >1,000-fold selectivity for IDE.....	53
Figure 2.10 Saturation plot for 6b inhibition of IDE proteolysis of the fluorogenic peptide substrate	55
Figure 2.11 Dixon and Cornish-Bowden plots generated for 6b inhibition of IDE using the fluorogenic peptide substrate	56
Figure 2.12 Biochemical assays suggesting that 6b binds a site in IDE distinct from the conventional peptide substrate binding site known to bind substrate mimetic Ii1	57
Figure 2.13 Structural basis of IDE inhibition by macrocycle 6b	59
Figure 2.14 Activity assays for wild-type or mutant human IDE variants in the presence of 6bK	61
Figure 2.15 Small molecule-enzyme mutant complementation study to confirm the macrocycle binding site and placement of the building-blocks.....	62
Figure 2.14 Spectra for ¹ H- and ¹³ C-NMR of 6b , 6bK , and bisepi-6bK	82
Figure 2.15 Alignment for human and mouse IDE sequences.....	85
Figure 3.1 Fmoc-based solid-supported synthesis of 6bK followed by on-resin macrocyclization	94
Figure 3.2 Pharmacokinetic parameters of 6bK	96
Figure 3.3 Acute IDE inhibition affects the abundance and hypoglycemic action of insulin.....	98
Figure 3.4 Administration of 6bK to lean mice not followed by injection of a nutrient such as glucose.....	100
Figure 3.5 IDE inhibition by low-potency diastereomers of 6bK	100
Figure 3.6 Low-potency diastereomers of 6bK used to determine the effective dose range and confirm on-target IDE inhibition effects during IPGTTs in lean and DIO mice	102
Figure 3.7 Acute treatment with 6bK is well tolerated.....	104
Figure 4.1 Dependence of insulin and glucagon secretion on the route of glucose administration and the hyperinsulinemic phenotype of DIO <i>versus</i> lean mice	118
Figure 4.2 Physiological consequences of acute IDE inhibition by 6bK on oral glucose tolerance in lean and DIO mice.	120
Figure 4.3 Co-administration of IDE inhibitor 6bK and DPP4 inhibitor sitagliptin followed by an oral glucose challenge.....	121
Figure 4.4 Impact of the route of glucose administration on the phenotype of glucose tolerance in lean and DIO mice following treatment with IDE inhibitor 6bK	123

Figure 4.5 Acute IDE inhibition affects the abundance of multiple hormone substrates during an injected glucose challenge to DIO mice	126
Figure 4.6 Acute IDE inhibition potentiates multiple injected hormone substrates	127
Figure 4.7 The endogenous signaling activity of glucagon is required for impairment of injected glucose tolerance following acute IDE inhibition.....	130
Figure 4.8 Acute IDE inhibition modulates the endogenous signaling activity of glucagon during a pyruvate/gluconeogenesis challenge.....	131
Figure 4.9 Acute IDE inhibition modulates endogenous amylin signaling revealed by gastric emptying efficiency, an amylin-specific effect	133
Figure 4.10 Mice lacking IDE display no effects of 6bK treatment.....	136
Figure 4.11 Oral glucose tolerance of mice lacking IDE compared to WT lean mice	137
Figure 4.12 Summary of physiological consequences of acute IDE inhibition by 6bK on glucose tolerance in lean, DIO, and IDE ^{-/-} mice	139
Figure 4.13 Model for the expanded roles of IDE in glucose homeostasis and gastric emptying based on the results of this study	141
Figure 4.14 Western blot assay to confirm IDE ^{-/-} mice genotypes	149
Figure 5.1 Optimization of an anisotropy-based assay using the fluorescent probe FL-6b , based on the DNA-templated IDE inhibitor 6b	161
Figure 5.2 Determination of the assay Z-factor	161
Figure 5.3 Validation of on-target binding for the probe FL-6b using IDE variants	163
Figure 5.4 Validation of the anisotropy assay in high-throughput mode using 1,000 drug/bioactive compounds	164
Figure 5.5 High-throughput anisotropy probe-displacement assay screen using 10,000 compound informer set of the Broad Institute library collections	165
Figure 5.6 Structures of hits identified as putative distal-site IDE binders and IDE inhibitors	165
Figure 5.7 High-throughput screening of biaryl-substituted azetidine libraries	166
Figure 5.8 Structures of azetidine hits identified as putative distal-site IDE binders and IDE inhibitors	169
Figure 5.9 Surrogate proteolysis assay used to identify substrate-selective IDE inhibitors that allow IDE-mediated proteolysis of small peptide substrates.....	173
Figure 5.10 Optimization of homogeneous time-resolved FRET (HTRF) assays to report on IDE-mediated degradation of insulin and glucagon in the presence of inhibitors.....	175

Figure 5.11 Focused screen for substrate-selective inhibitory properties using the insulin and glucagon degradation endpoint HTRF assays.....	177
Figure 5.12 Concentration dependence profiles for substrate-selective IDE inhibitors	177
Figure 5.13 IDE-mediated cleavage of A β 40 and an amylin fluorogenic analog is partially allowed by insulin-selective IDE inhibitors	180
Figure 5.14 Analysis of metalloprotease specificity for substrate-selective IDE inhibitors...	181
Figure 5.15 Confirmation of the distal binding site for substrate-selective IDE inhibitors, and a docking model within human IDE	185
Figure 5.16 IDE-mediated degradation of glucagon is permitted by the ternary complexes of substrate-selective IDE inhibitors.....	186
Figure 5.17 Structural basis for substrate-selective IDE inhibition	187
Figure 5.18 Synthesis of BRD-297	198
Figure 5.19 Spectra for ¹ H-NMR of BRD-297	204

List of Tables

Table 1.1 Advantages and limitations of DNA-encoded libraries and <i>in vitro</i> selection for small molecule discovery	6
Table 1.2 Literature survey of putative IDE substrates identified by <i>in vitro</i> assays.....	17
Table 2.1 K_M^{app} and V_{max} parameters of IDE calculated by non-linear regression	55
Table 2.2 X-ray data collection and refinement statistics	75
Table 2.3 HPLC and high-resolution mass spectrometry analysis of IDE inhibitor analogs	79
Table 2.4 Site-directed mutagenesis primers	80
Table 2.5 Sequencing primers	80
Table 2.6 Site-directed IDE mutants used in the small molecule-enzyme mutant complementation studies.....	81
Table 3.1 Distinct properties of pharmaceutical drugs, drug leads, and <i>in vivo</i> probes, compared to 6bK	92
Table 3.2 Plasma binding, stability, and microsomal stability parameters for 6bK	94
Table 3.3 The features of 6bK satisfy the requirements for an <i>in vivo</i> probe.....	105
Table 4.1 RT-PCR primers for mouse liver gluconeogenesis markers	148
Table 5.1 Chemoinformatic properties of Broad Institute azetidine libraries.....	168
Table 5.2 Calculated drug-like properties of substrate-selective hits <i>versus</i> 6bK	169

Abbreviations

A	A β	Amyloid beta	
	ACE	Angiotensin Converting Enzyme	
	Akt	Protein kinase B (PKB)	
	Alloc	Allyloxycarbonyl protecting group	
	AMPK	AMP-activated protein kinase	
	ANP	Atrial natriuretic peptide	
	AP	Area Postrema of the brainstem	
	AR	Amylin receptor (calcitonin receptor plus RAMP1-3)	
	Ar	Aromatic	
	AUC	Area Under the Curve	
	B	bisepi	Epimer differing in the configuration of two chiral centers
BRENDA		BRAunschweig ENzyme DAtabase	
BRI		Biology Research Infrastructure facility at Harvard	
BSA		Bovine serum albumin	
C	C-peptide	C-terminal peptide from insulin maturation	
	C-term	Carboxy terminal	
	cDNA	Complementary DNA, synthesized from RNA template	
	CGRP	Calcitonin-Gene Related Peptide	
	cLog P	Calculated octanol-water partition coefficient	
	CYP450	Cytochrome P450 enzymes	
D	DIBAL	Diisobutylaluminium hydride	
	DIO	Diet-Induced Obese	
	DIPEA	<i>N,N</i> -Diisopropylethylamine	
	DMF	<i>N,N</i> -Dimethylformamide	
	DMSO	Dimethyl sulfoxide	
	DNA	Deoxyribonucleic acid	
	DNase	Enzyme that catalyzes the hydrolysis of deoxyribonucleic acids	
	Dnp	2,4-Dinitrophenyl quencher	
	DOS	Diversity-oriented synthesis	
	Dpa	<i>N</i> -3-(2,4-Dinitrophenyl)- <i>L</i> -2,3-diaminopropionyl	
	DPP	Dipeptidyl peptidase	
	DPP-IV	Dipeptidyl peptidase 4	
	DTS	DNA-templated synthesis	
	DTT	Dithiothreitol	
	E	[E]	Enzyme concentration
		EC	Enzyme code
EC50		Half maximal effective concentration	
ECE		Endothelin-converting enzyme 1	
EDC		1-Ethyl-3-(3-dimethylaminopropyl)carbodiimide	
EDTA		Ethylenediaminetetraacetic acid	
EGF-1		Epidermal growth factor	

	ELISA	Enzyme-linked immunosorbent assay
	epi	Epimer
	ESAC	Encoded self-assembling chemical (libraries)
	ETC	<i>Et cetera</i>
	ETH	Eidgenössische Technische Hochschule, Zürich, Switzerland
F	FAS	Faculty of Arts and Sciences
	FMOC	Fluorenylmethyloxycarbonyl protecting group
	FOXO1	Forkhead box protein O1 transcription factor
	FP	Fluorescence polarization
G	G6Pase	Glucose 6-phosphatase
	GCGR	G-coupled glucagon receptor
	GHRH	Growth-hormone-releasing hormone
	GIP	Glucose-dependent insulinotropic peptide
	GLP-1	Glucagon-like peptide 1
	GLUT4	Glucose transporter type 4
	GO	Gene ontology
	Grb2/SOS	Growth factor receptor-bound protein 2
	GS	Glycogen synthase
	GSK3	Glycogen synthase kinase 3
	GWAS	Genome-wide association study
H	HATU	1-[Bis(dimethylamino)methylene]-1H-1,2,3-triazolo[4,5-b]pyridinium 3-oxid hexafluorophosphate
	HEPES	4-(2-hydroxyethyl)-1-piperazineethanesulfonic acid
	HPLC	High precision liquid chromatography
	HTRF	Homogeneous Time Resolved Förster Resonance Energy Transfer
I	i.p.	Intraperitoneal
	IACUC	Institutional Animal Care and Use Committee
	IC ₅₀	Half maximal inhibitory concentration
	IC ₅₀ ^{app}	Apparent half maximal inhibitory concentration
	IDE	Insulin-Degrading Enzyme
	IDE-CF	Cysteine-free insulin-degrading enzyme
	IDMS	Isotope-dilution mass spectrometry
	IGF-1/2	Insulin-like growth factors 1 and 2
	Ii1	IDE inhibitor 1
	IKKb	Inhibitor of nuclear factor kappa-B kinase subunit beta
	I _{MAX}	Inhibition maximum
	INSL-3	Insulin-like 3
	IPGTT	Intraperitoneal glucose tolerance test
	IPTG	Isopropyl β-D-1-thiogalactopyranoside
	IR	Insulin receptor
	IRS1	Insulin receptor substrate 1
	ITT	Insulin tolerance test
J	JNK	c-Jun N-terminal kinases

K	K_M	Michaelis constant
	K_M^{app}	Apparent Michaelis constant
	KO	Knockout
L	LB	Lysogeny broth
	LC	Liquid chromatography
	LCMS	Liquid chromatography mass spectrometry
	LDS	Lithium dodecyl sulfate
	Log <i>P</i>	Octanol-water partition coefficient
M	MAPK	Mitogen-activated protein kinases
	Mca	7-Methoxycoumarin-4-acetyl fluorophore
	MeCN	Acetonitrile
	MMP-1	Matrix metalloproteinase-1
	mRNA	Messenger ribonucleic acid
	mTORC1	Mammalian target of rapamycin complex 1
N	N-term	Amino terminal
	NEP	Neprilysin
	NIH	National Institutes of Health
	NLN	Neurolysin
	NMM	<i>N</i> -Methylmorpholine
	NMP	<i>N</i> -Methylpyrrolidone
	NMR	Nuclear magnetic resonance spectroscopy
	NPH insulin	Neutral Protamine Hagedorn insulin
	Nu	Nucleophilic
	O	OD
OGTT		Oral glucose tolerance test
P	p	Probability
	p.o.	<i>Per os</i> (by mouth)
	PBS	Phosphate buffered saline
	PBST	Phosphate-Buffered Saline with Tween-20
	PCT	Patent Cooperation Treaty
	PDB	Protein Data Bank
	PDI	Protein disulfide-isomerase
	PDK1	Pyruvate dehydrogenase lipoamide kinase isozyme 1
	P_e	Apparent permeability
	PEG	Polyethylene glycol
	PEPCK	Phosphoenolpyruvate carboxykinase
	PEPCK	Phosphoenolpyruvate carboxykinase
	PGP	P-glycoprotein
	PI3K	Phosphoinositide 3-kinase
	PIP3	Phosphatidylinositol (3,4,5)-trisphosphate
	pIR	Phosphorylated insulin receptor
	PKB	Protein kinase B
PKC0	Protein kinase C	

	PMSF	Phenylmethylsulfonyl fluoride
	PPAR- γ	Peroxisome proliferator-activated receptor gamma
	PreP	Prolyl endopeptidase
	PtdIns(4,5)P ₂	Phosphatidylinositol (3,4)-bisphosphate
	PTEN	Phosphatidylinositol-3,4,5-trisphosphate 3-phosphatase
	PTP1B	Protein-tyrosine phosphatase 1B
	PTPL1	Protein tyrosine phosphatase non-receptor 13 (PTPN13)
	PTT	Pyruvate tolerance test
	PVDF	Polyvinylidene fluoride
Q	Q-TOF	Quadrupole time-of-flight
R	RCM	Ring-closing metathesis
	RMSD	Root-mean-square deviation
	RNA	Ribonucleic acid
	RNAi	Ribonucleic acid interference
	RT-PCR	Reverse-transcriptase polymerase chain reaction
	RTK	Receptor tyrosine kinase
S	[S]	Substrate concentration
	s.c.	Subcutaneous
	SAR	Structure-activity relationship
	SEM	Standard error of the mean
	SGLT-2	Sodium/glucose cotransporter 2
	SHIP2	Phosphatidylinositol-3,4,5-trisphosphate 5-phosphatase
	sNHS	Sulfo <i>N</i> -Hydroxysuccinimide
	SOS	Son of Sevenless, guanine nucleotide exchange factors
	Src	Proto-oncogene tyrosine-protein kinase c-Src
	SSAR	Stereochemical structure-activity relationship
T	TAPP1/2	Pleckstrin homology domain-containing family A1/2
	TBST	Tris-Buffered Saline with Tween 20
	TCEP	Tris(2-carboxyethyl)phosphine
	TFA	Trifluoroacetic acid
	TGF α	Tissue growth factor alpha
	THF	Tetrahydrofuran
	THOP	Thimet oligopeptidase
	Trt	Triphenylmethane protecting group
	TSC1/2	Tuberous sclerosis proteins 1 and 2 complex, hamartin and tuberin
U	U/kg	Units per kilogram
	USD	United States Dollar
	USER	Uracil-Specific Excision Reagent
	UV	Ultraviolet
	V _{max}	Maximum velocity at saturating substrate concentration
W	WT	Wild-type
X	XPhos-Pd G3	(2-Dicyclohexylphosphino-2',4',6'-triisopropyl-1,1'-biphenyl)[2-(2'-amino-1,1'-biphenyl)]palladium(II) methanesulfonate

Chapter 1

Introduction to Insulin-Degrading Enzyme and DNA-encoded platforms for small molecule discovery

Parts adapted from: Maianti *et al*, *Nature* **511**, 94–98 (2014).

1.1 – Introduction: small molecule discovery using DNA-encoded libraries

The discovery of small molecules capable of selectively modulating the activity of biological targets is a major focus of research endeavors in academic and pharmaceutical laboratories worldwide. Because this form of biological intervention has traditionally provided the most widely applicable route towards therapeutics, our society invests heavily on bioactive small molecule research and development, totaling over USD ~100 billion per year globally^{1,2}. Furthermore, there is a continuous push to complement the limitations of small molecules with emerging therapeutic approaches based on biologic macromolecules (hormones, vaccines, antibodies, nucleic acids, genome editing enzymes, protein delivery, *etc.*)^{3,4} and cell-based treatments (transplantation, encapsulation, induced-pluripotent stem cells, *etc.*)⁵. Small molecule probe compounds that are active *in vivo* have also proven valuable to study biological processes that are inaccessible using other techniques, such as the validation of putative therapeutic targets through proof-of-concept experiments⁶⁻⁸. Biological interrogation with small molecules is especially powerful in combination with genome-wide association studies⁹, animal models of disease¹⁰, genetic modification tools¹¹, modern analytical techniques^{12,13} and high-throughput sequencing¹⁴⁻¹⁶.

DNA-encoded libraries are an emerging technology that is being increasingly implemented to meet the continuous demand to discover novel small molecules¹⁷. Over the course of the last decade, these technologies have gained recognition as useful discovery platforms complementary to conventional high-throughput

screening^{18,19}, as well as fragment-based screening^{20,21}, transition state-based design²², unbiased phenotypic screening^{23,24}, and natural product prospecting²⁵⁻²⁸.

The inherent features of DNA as a high-density information polymer, which can be replicated and sequenced, make it an excellent medium for molecular barcoding of synthetic molecules¹⁷. The theoretical diversity of a 20-mer oligonucleotide can be used to encode billions of synthetic molecules (4^{20}), yet the decoding and deconvolution of this mixture does not scale linearly with library size¹⁷. The sub-femtomol sensitivity of PCR amplification enables the routine evaluation of minute quantities of DNA-barcodes, coupled with inexpensive and high-coverage DNA sequencing methods that provide the statistical power to detect even modest changes

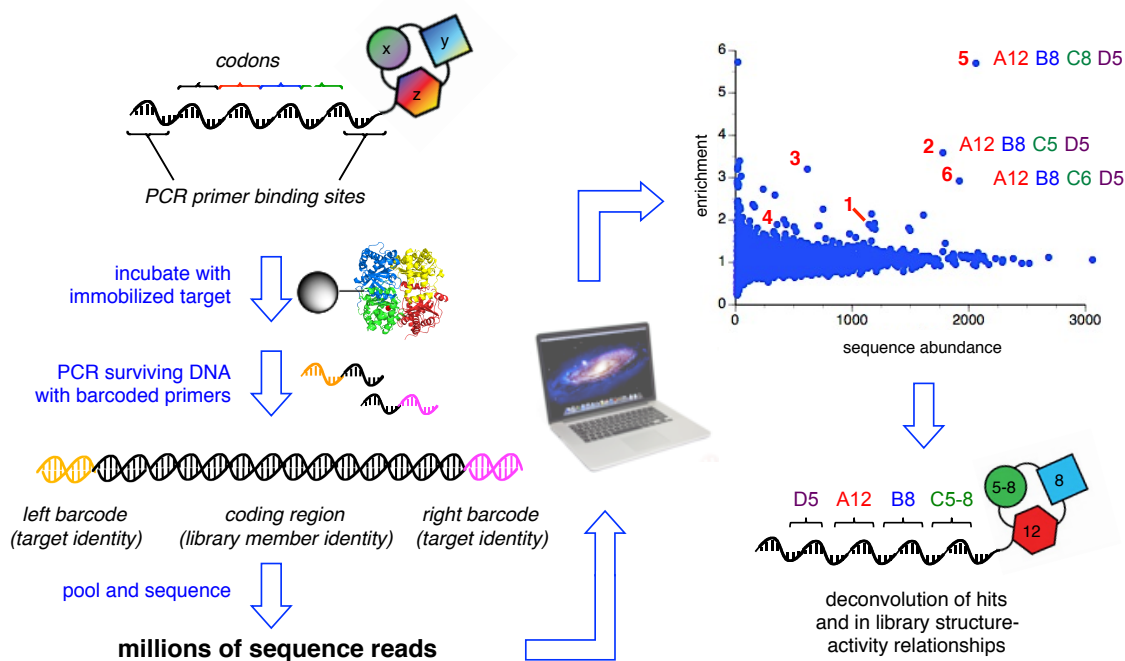


Figure 1.1 | Scheme of an *in vitro* selection using a DNA-encoded library, followed by high-throughput sequencing decoding and deconvolution.

in the relative composition of a DNA-encoded library^{17,29}. Therefore, large collections of small molecules covalently tagged with DNA barcodes are amenable to selection-based methods (**Figure 1.1**), in which all the library members are exposed at the same time to a target of interest. This “one-pot” experiment is subsequently manipulated, washed, or separated, in order to enrich the library members that interact with the target, over the vast majority of irrelevant molecules. This enrichment causes a telling shift in the library composition that is detected by high-throughput sequencing pre- and post-selection (**Figure 1.1**)^{17,30,31}.

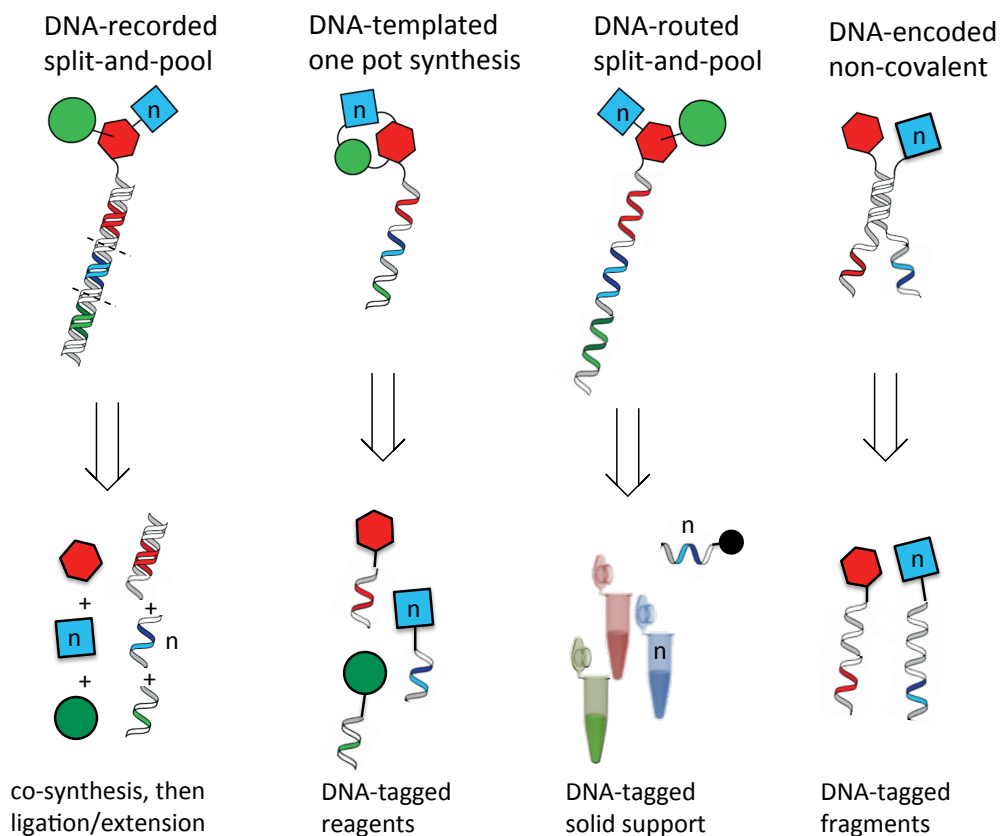


Figure 1.2 | Complementary methods to produce DNA-encoded libraries¹⁷.

In practice, many dozen targets of interest are evaluated in parallel selection experiments, then each PCR amplification step is carried out with indexing primers that track the target identity, and allow pooling for high-throughput DNA sequencing *en masse* (**Figure 1.1**)³². Only a minute fraction of a DNA-encoded library is exposed to the target (<1 pmol), and the eluate can be recycled multiple times. Hence, *in vitro* selection is a simple but powerful and efficient technology to discover small molecules, complementary to traditional assay-based screening (**Table 1.1**)^{18,19}. The use of DNA-encoded libraries is not limited to affinity-based enrichment with immobilized targets³⁰, since other forms of selective pressure can be the basis of selection^{33,34}, including proximity-based PCR priming (reaction- or interaction-dependent)^{31,35}, and potentially even gel-extraction of large circularized DNA could serve as the basis of *in vitro* selection³⁶. The hits identified from high-throughput screening are resynthesized in scale, and subjected to a “counter-screen” or activity-based assay, which is not subject to the limitations of scale-up and optimization necessary for high-throughput screening^{18,19}.

The predecessors of DNA-encoded libraries were biological materials that inherently link a phenotype to a genotype. For example, technologies such as RNA/DNA aptamers³⁷, phage-display³⁸, and mRNA-display^{39,40}, share this quality and are amenable to *in vitro* selection methodologies. However, Nature does not provide equivalent machinery for the translation of DNA into synthetic molecules⁴¹⁻⁴⁶ nor sequence-defined synthetic polymers^{47,48}. The first theoretical framework to

Table 1.1 | Advantages and limitations of DNA-encoded libraries and *in vitro*

selection for small molecule discovery.

<i>In vitro</i> selection, DNA-encoded libraries	Target-based high-throughput screening
<1 pmol library aliquots stored at -80 °C, which can be recycled multiple times	plate collection requires upkeep and chemical resynthesis
<i>en masse</i> one-pot binding interrogation, only hits validated by activity-based assays	discrete interrogation of each library member in activity-based assays
routine off-the-shelf activity-based assays can be used to counter-screen hits	extensively optimized activity-based assays are required (Z-factor > 0.5)
requires low-tech equipment (pipettes, magnets, etc.) and access to inexpensive high-throughput DNA-sequencing facility	requires automated screening infrastructure, specialized instruments for reading each assay, and compound management system
library size can be increased with a complementary DNA barcode set	plate collection requires upkeep and resynthesis
synthesis is technically more challenging but effort does not scale linearly with library size	combinatorial or diversity-oriented synthesis required for each library member
library of sizes $>10^6$ – 10^7 have been routinely evaluated with targets of interest, libraries as large as 10^8 have been reported	individual screening campaigns of 10^5 – 10^6 compounds from collections comprising $<10^7$ compounds
multiple replicates and variations in selection conditions can be evaluated (washing stringency, ligand elution, additives, etc.)	usually limited in resources to run one or two replicates, using one assay condition
repertoire of building block coupling reactions is limited to DNA- and water compatible reactions (needs improvement)	extensive repertoire of combinatorial building block coupling reactions
limited chemotypes in each library, building blocks and appendages provide diversity	small collections with multiple chemotypes effectively explore ‘chemical space’
incomplete building block coupling may difficult barcode interpretation, only the Liu macrocycle library has a built-in purification	the purity and identity of the hit compounds is corroborated afterwards

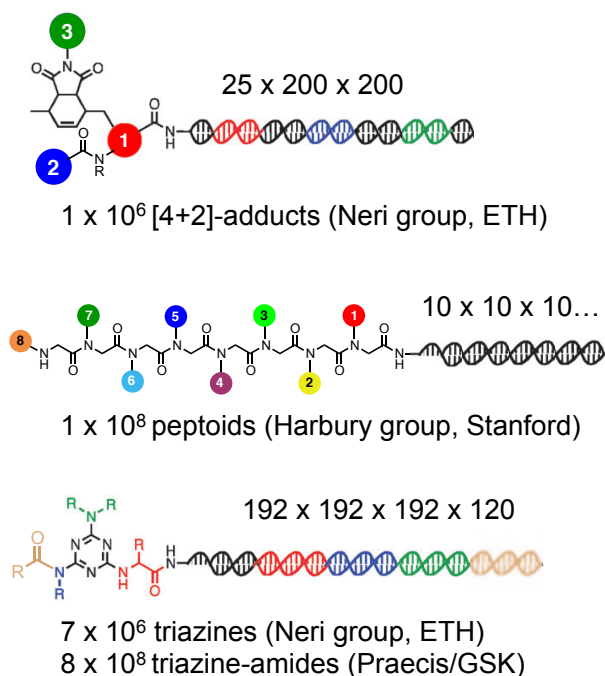
encode synthetic peptides using DNA was first provided by Brenner and Lerner⁴⁹.

They proposed the “recording” of a sequence of split-and-pool synthetic steps by

applying consequent steps of DNA synthesis. While visionary, this strategy posed significant restrictions and technical challenges^{50,51}. Therefore, multiple groups have developed novel and improved strategies for the production of DNA-encoded libraries, which offer complementary solutions for bringing together combinatorial chemistry or “split-and-pool” chemical synthesis and DNA barcodes (**Figure 1.2**)¹⁷.

The three conceptually distinct strategies that emerged over the past decade are *i*) “DNA-templated synthesis”, developed by the Liu group^{41-46,52,53}, *ii*) “DNA-recording” of chemical steps using several methods that improve on the original technique^{51,54-57}; and more recently *iii*) “DNA-routing” of reagents into spatial segregation for split-and-pool chemical synthesis⁵⁸⁻⁶¹ (**Figure 1.2**). In addition, the approach known as encoded self-assembling combinatorial (ESAC) libraries⁶², is a variation on the use of base-pairing to display synthetic fragments in close proximity, under the assumption that they may bind a target as one entity (**Figure 1.2**).

The general approach to “DNA-recording” requires iterative extension steps of the oligonucleotide barcode catalyzed by a DNA polymerase or DNA ligase enzyme to record each chemical reaction¹⁷. Hence, the growing barcode records the history of the reagents as they are subjected to split-and-pool chemical synthesis. Similarly, “DNA-routing” involves using solid supports tagged with DNA sequences that use base-pairing hybridization to enforce the spatial segregation of complementary DNA-barcoded materials into reaction vessels⁵⁸, which is essentially a DNA-directed



Representative reactions compatible with DNA-encoded libraries:

- amide/ester coupling
- Diels-Alder [4+2]
- Huisgen “click” [3+2]
- Nu-Ar substitution
- 1,4-addition
- Wittig olefination
- imine/hydrazone condensations
- reductive amination
- S- or N-alkylation
- mild acid/base treatment
- periodate diol cleavage
- thiol redox

Figure 1.3 | (A) Representative DNA-encoded libraries that resulted from DNA-recorded^{56,57} and DNA-routed⁵⁸⁻⁶¹ methods. (B) Chemical reactions that have been carried out in the context of DNA-encoded libraries or that are predicted to be compatible⁴⁶.

splitting method for split-and-pool synthesis⁶⁰. These technical advances have enabled the production of libraries comprised of 10⁶ to 10⁸ compounds suitable for *in vitro* selection experiments (**Figure 1.3**)^{57,61}. Each of these libraries shows ingenuity in solving to some degree the limitations discussed in **Table 1.1**, including the repertoire of compatible chemistry, and the diversity of chemotypes and appendages, to promote an effective exploration of the ligands ‘chemical space’ beyond relying on the massive size of the DNA-encoded library (**Figure 1.3**)^{57,61}.

David Liu and co-workers discovered that nucleic acid hybridization is a versatile and generally effective method to promote bond-forming reactions by

increasing the effective molarity of chemical reactants tagged with DNA⁴¹⁻⁴⁵. The DNA templates and DNA-reagents share a codon-anticodon relationship reminiscent of ribosomal protein synthesis. The design of a “codeset” of mutually orthogonal codons enabled ordered-multistep⁶³ DNA-guided translation of libraries of templates with multiple reagents in a single solution with high sequence fidelity. Gartner, Tse, and Liu described the first DNA-templated small molecule library by sequentially applying three amide condensation steps and one Wittig macrocyclization⁴⁵ (**Figure 1.4**), a technology commercialized by Ensemble Therapeutics¹⁷.

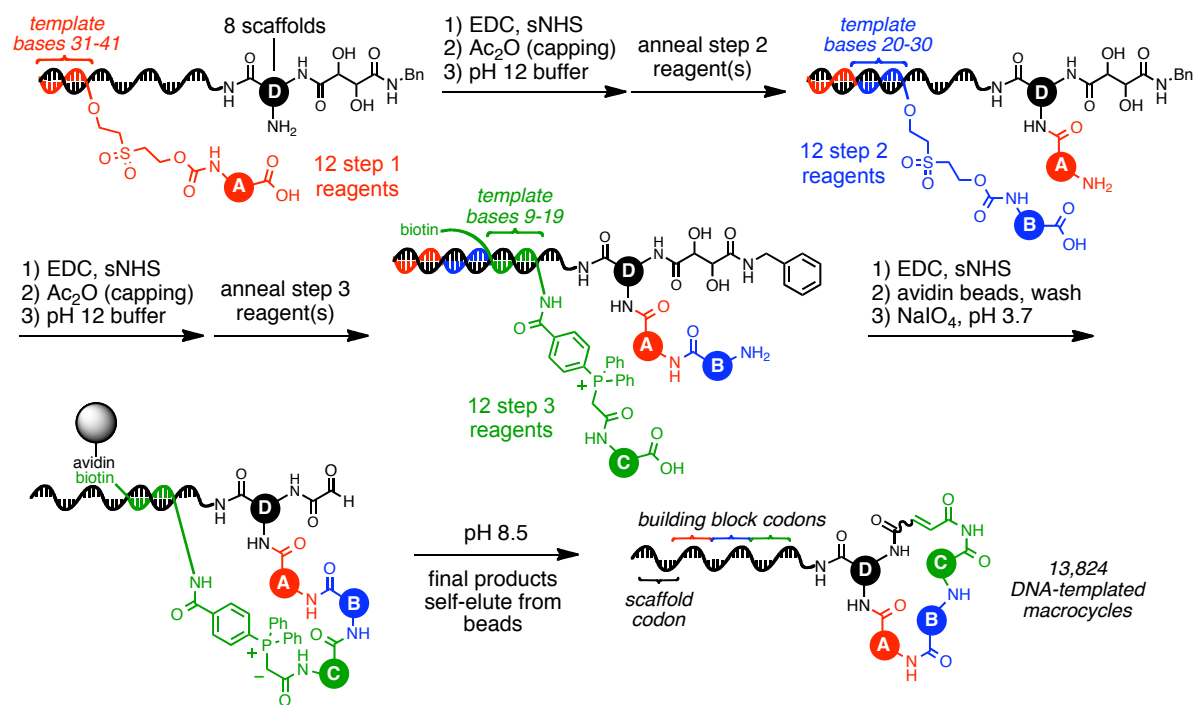


Figure 1.4 | Ordered multistep DNA-templated translation of a mixture of DNA barcodes into a pilot 13,824 membered DNA-encoded library of macrocycles. Adapted from ref. 63.

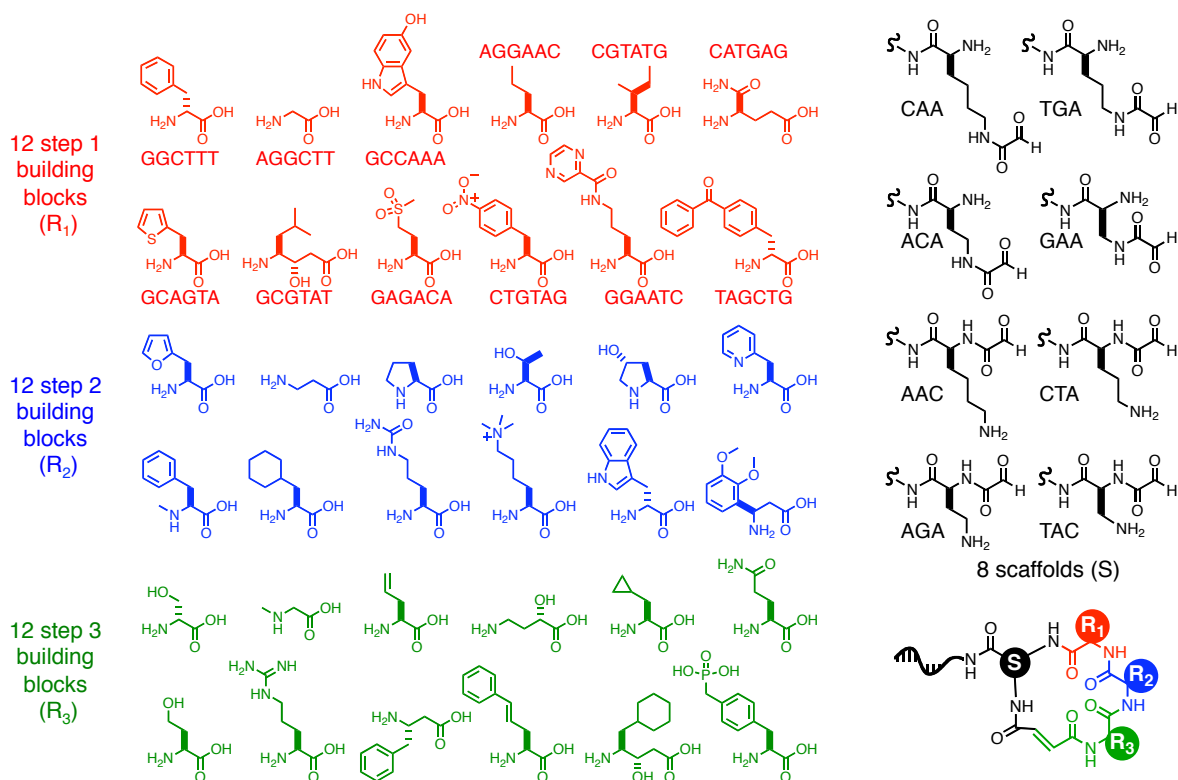


Figure 1.5 | Building blocks used in the 13,824 library of macrocycles, adapted from ref. 63.

Subsequent advances in DNA-templated synthesis enabled the production of a 13,824-membered macrocycle library comprising non-proteinogenic amino acid building blocks (**Figure 1.5**)⁶³ suitable for *in vitro* selection and small molecule discovery³², which was used in this dissertation (Chapter 2)⁶⁴. The promising results from this prototype library have prompted the Liu group to expand the codeset of DNA templates to produce a 256,000-membered library of macrocycles⁶³.

Whereas the DNA-encoded library efforts shown in **Figure 1.3** have focused on maximizing library size^{57,61}, the pilot size 13,824-membered DTS macrocycle library⁶³ has proven very competitive in the number of hit reported and target

versatility^{32,64}. These medium-sized peptidic macrocycles occupy an intermediate chemical space between small molecule and small proteins⁶⁵⁻⁶⁷ (e.g. peptidic hormones, toxins, venoms, and stapled peptides), and may result in lower per-atom ligand efficiency than in traditional small molecules. Furthermore, macrocycles are generally thought as privileged structures due to their biophysical and pharmacological properties discussed in detail in Chapter 3 (Section 3.1)⁶⁵⁻⁶⁷.

Demonstrating the generality of the concept of DNA-templated synthesis (DTS) the Liu lab has applied it to the synthesis of DNA-encoded libraries⁶³, a system for discovery of bond-forming reactions³⁴, and a system for enzyme-free translation of sequence-defined synthetic polymers⁴⁸. Furthermore, over the course of just a few years *in vitro* selections using the DNA-templated macrocycle library has led to the identification of potent and selective *Src* kinase inhibitors developed by Ralph Kleiner^{17,32}, and the IDE inhibitors described in this work.

1.2 – The need for therapeutic validation of Insulin-Degrading Enzyme

The controversial term “undruggable” has surfaced as a descriptor for targets displaying biophysical properties that repeatedly frustrate small molecule development and/or screening efforts^{68,69}, however, with continued effort many targets once considered “undruggable” have been conquered^{70,71}. An important amount of resources in academia and industry are devoted to identifying small molecules for these targets, because they have been strongly implicated in disease mechanisms based on evidence from multiple complementary techniques and proof-

of-principle experiments^{69,71} (e.g. knock-out, knock-down, mutagenesis, overexpression, bump-hole, targeted degradation, *etc.*)⁷². Meanwhile, another class of untapped targets have proven intractable for proof-of-concept validation, or attempts to evaluate their physiological roles in disease mechanisms have led to obscure or unexplainable *in vivo* phenotypic observations, which further discouraged researchers from developing bioactive small molecule probes^{6,73}. Insulin-degrading enzyme (IDE) is a long-standing member of this class of “neglected” putative therapeutic targets^{11,71,74}.

The discovery of insulin and its use to treat diabetes was a turning point in the history of medicine, for which Frederick Banting and John Macleod were awarded the Nobel Prize in 1923⁷⁵. Long before we understood the structure of insulin⁷⁶ or molecular details of hormone signaling, researchers reasoned that insulin should be subject to endogenous inactivation⁷⁷, and that blocking this process could mimic the supplementation of insulin. Advances in methods for the detection and measurement of insulin⁷⁸, enabled the search for the degradation pathway⁷⁹. In a seminal 1949 publication, the English physician I. Arthur Mirsky⁸⁰ reported the biochemical fractionation of rat and cattle livers to identify the first enzyme capable of degradation of radiolabeled insulin⁸¹. Mirsky gave this activity the name *insulinase*, and over the decades it has been referred to as *neutral thiol peptidase*, *insulysin*, and more recently as Insulin-Degrading Enzyme, or IDE (EC 3.4.24.56, GO:0004231)⁸².

We currently have a sophisticated level of understanding of the structural and biochemical features of IDE (**Figure 1.6**). IDE is a 110 KDa globular zinc-dependent

metalloprotease of an evolutionary distinct origin, evidenced by an inverted set of zinc-binding residues (HxxEH motif)⁸³, which is an example of convergent evolution relative to the HExxH motif of other metalloprotease classes. Orthologs of IDE have been found throughout the tree of life, including bacteria and fungi⁸⁴, and it is highly conserved in mammals (>95% amino acid identity between human and mouse

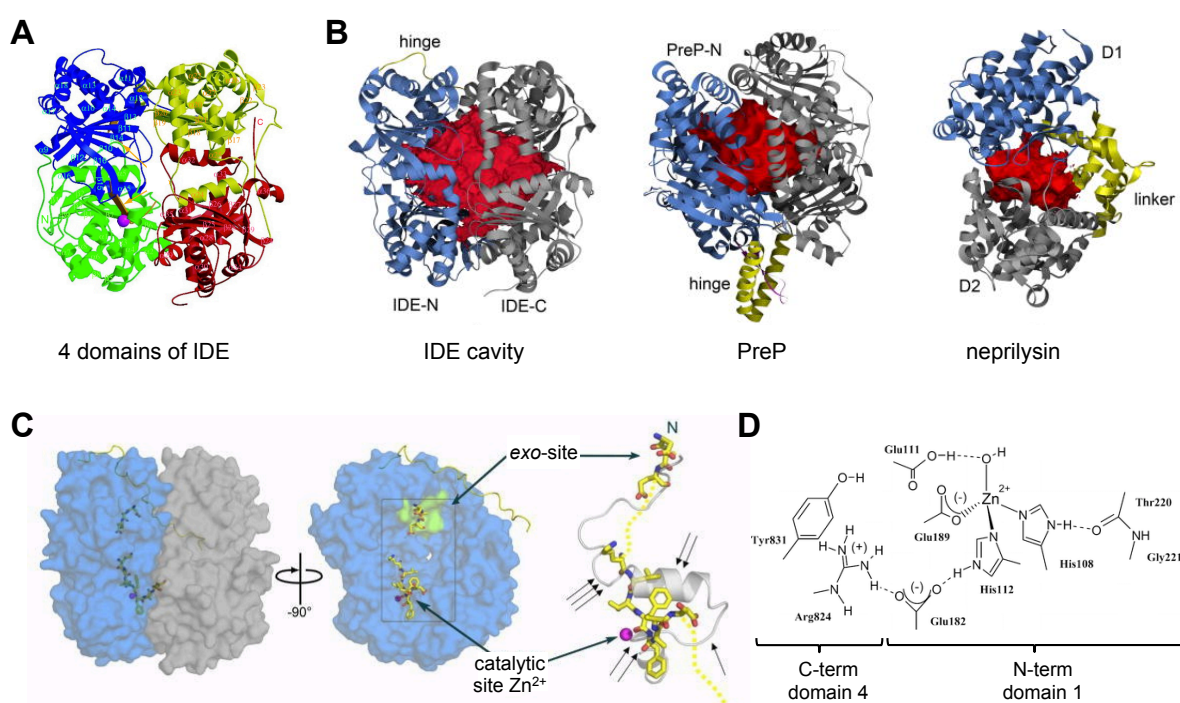


Figure 1.6 | Unique structural and biochemical features of IDE. **(A)** Organization of IDE domains (domains 1, 2, 3, and 4 are colored green, blue, yellow, and red, respectively). **(B)** Comparison of the internal chambers (red volumes) of IDE, preprolyl peptidase PreP and neprilysin. Other colors highlight the hinges regions (yellow) connecting the N-terminal (blue) and C-terminal (grey) halves. **(C)** Location of the catalytic site and *exo*-site on the N-terminal half of IDE. **(D)** Network of hydrogen-bonds between the distal domains 1 and 4 that activate the deprotonation of water by Zn²⁺ when IDE is in the closed state. Adapted from reference 86.

orthologs, Chapter 2). The main isoform of human IDE₍₄₂₋₁₀₁₉₎ makes a cooperative homodimer⁸⁵, and each monomer is comprised of four structurally homologous $\alpha\beta$ roll domains that together define a massive internal chamber (**Figure 1.6**)⁸⁶. Only domain 1 has a zinc-dependent catalytic site, and the other domains appear to be ancient remnants of gene duplication events that led to the evolution of the cavity (<25% sequence similarity).

The IDE chamber has an approximately triangular prism shape⁸⁶ (base dimensions 35×34×30 Å and a height of 36 Å) with a total cavity volume of ~13,000 Å³ (**Figure 1.6A**). This cavity perfectly encapsulates the entire insulin hormone (51 residues) and is the largest chamber defined by a single polypeptide encoded in our genome, over twice the volume of the prolyl endopeptidase (PreP) or neprilysin (NEP) active sites (**Figure 1.6B**). An extended loop “hinge” of 28 residues connects domains 2 and 3 to allow the N- and C-terminal halves to open (**Figure 1.6B**)^{86,87}. However, the catalytic site of domain 1 is only activated in the closed state, owing to hydrogen-bond contributions from domain 4 (**Figure 1.6D**)⁸⁶.

Unlike most proteases, the peptide substrates cleaved by IDE lack a consensus sequence. Instead, the biophysical features of IDE dictate whether a substrate can interact and become entrapped in the chamber^{86,88}. These features are: *i*) overall size and shape (<51 residues); *ii*) positive charge repulsion at the substrate C-terminus, *iii*) binding of hydrophobic patches along the catalytic cleft; and *iv*) the ability of the substrate to make cross- β -sheet interactions with an exposed region of the IDE chamber known as the *exo*-site (**Figure 1.6C**)⁸⁶⁻⁸⁸. Notably, this is a characteristic of

amyloidogenic peptides that are effectively degraded by IDE (A β , amylin, and insulin)⁸⁹ suggesting this aggregating behavior may have evolved to promote their degradation.

The biochemical properties of IDE chamber and the unique substrate recognition mechanism⁸⁶⁻⁹⁰ has posed a significant challenge to understanding the repertoire of *in vivo* substrates beyond insulin⁸². In fact, IDE was identified before most hormones had been discovered, and over the past three decades multiple research groups have found that IDE is capable of cleaving a wide range of peptide substrates *in vitro* (**Figure 1.7A**) for which experimental validation *in vivo* (or *ex vivo*) has not previously been possible. The kinetic parameters for most putative substrates were measured by approximate methods (**Table 1.2**). Nevertheless, it is possible to recognize two broad classes: those substrates of high affinity for the IDE chamber (low K_M , e.g. insulin and homologs, A β peptides, CGRP group, ANP, *etc.*)⁸⁶⁻⁹⁰, and substrates that interact with low affinity but that are rapidly cleaved ($K_M > 1 \mu\text{M}$, e.g. glucagon, bradykinin, somatostatin, *etc.*)⁹¹. Despite decades of research, these putative substrates have only been shown to be cleaved *in vitro* by purified IDE (**Table 1.2**).

Table 1.2 | Literature survey of putative IDE substrates identified by *in vitro* assays.

IDE substrates <i>in vitro</i> (reference)	Alternative degrading enzymes (Brenda db)	k_{cat} (min^{-1})	K_M (μM)	k_{cat}/K_M	IC_{50} (μM)	X-ray struct.	IDE substrate <i>in vivo</i> (ref.)
insulin ^{81,82}	lysosomal proteases, disulfide reductase	1.52	<0.03	50	-	2WBY 2WC0	KO study ^{93,94}
A β (40, 42) ^{95,96}	NEP, cathepsin D	52	1.23	43	-	2G47 2WK3	KO study ^{90,93,97}
calcitonin-gene related peptide ⁹⁸	ECE, PREP	-	-	-	-	-	KO study ⁹⁸
glucagon ^{99,100}	NEP, nardilysin, DPP-IV, cathepsins B and C	38.5	3.46	11	weak	2G49	this thesis
amylin ¹⁰¹	-	n/a	0.3*	n/a	0.16	3HGZ 2G48	this thesis
TGF- α ¹⁰²	-	-	0.15*	-	0.08	3E50	-
IGF-1 ^{90,103}	DPP-IV	-	weak	-	-	-	-
IGF-2 ^{90,103}	-	-	0.1*	-	0.06	3E4Z	-
somatostatin-14 ¹⁰⁴	nardilysin, dactylisin, aminopeptidase B, THOP, neurotensin-degrading enzyme	22.8	7.5	3.0	-	-	-
bradykinin ¹⁰⁵	ACE, aminopeptidase P, carboxypeptidase N, NEP, DPP-II, DPP-IV,	-	4.2	-	-	3CWW	-
kallidin ¹⁰⁵	ACE, aminopeptidase P, carboxypeptidase N	-	7.3	-	-	-	-
atrial NP (ANP) ^{106,107}	NEP	-	0.06	-	-	3N57	-
B-type NP (BNP) ¹⁰⁷	NEP, fibroblast activation protein- α	-	weak	-	>1	3N56	-
relaxin ¹⁰⁸	-	-	0.11*	-	0.054	-	-
relaxin-3 ¹⁰⁸	-	-	0.36*	-	0.182	-	-
insulin-like peptide 3 ¹⁰⁹	-	0.15	0.055	2.7	-	-	-
β -endorphin (1-31) ¹⁰⁵	NEP	21	13	1.6	-	-	-
growth hormone releasing factor (1-29) ¹⁰⁵	DPP-IV, NEP	23.4	11.9	2.0	-	-	-
pancreastatin (1-49) ¹⁰⁵	-	10.6	41.7	0.25	-	-	-
dynorphin B (1-13) ¹⁰⁵	NEP	15.1	18.3	0.8	-	-	-
A (1-17) ¹⁰⁵	NEP	18.4	37.4	0.5	-	-	-
B (1-9) ¹⁰⁵	NEP	10.3	26.8	0.4	-	-	-
A (1-13) ¹⁰⁵	NEP	3.74	40.6	0.09	-	-	-
A (1-10) ¹⁰⁵	NEP	3.74	39.4	0.09	-	-	-
A (1-8) ¹⁰⁵	NEP	0.66	63.5	0.01	-	-	-
A (1-9) ¹⁰⁵	NEP	0.33	60.5	0.01	-	-	-

(*) K_M estimated based on IC_{50} for inhibition of insulin degradation. Abbreviations: A β = amyloid beta; TGF-alpha = transforming growth factor-alpha; IGF = insulin-like growth factor; NP = natriuretic peptide; GRF = gastrin release factor; NEP = neprilysin; PREP = prolyl endopeptidase; ECE = endothelin converting enzyme; THOP = thimet oligopeptidase; ACE = angiotensin-converting enzyme; DPP = dipeptidylpeptidase. Known non-substrates of IDE include glucagon-like peptide 1 (GLP-1), glucose-dependent insulinotropic peptide (GIP), epithelial growth factor 1 (EGF-1), pro-insulin, and C-peptide.

possible. Only two substrates, beyond insulin, had been functionally linked to IDE activity *in vivo* (**Figure 1.7A**) based on the elevated levels measured in knockout IDE^{-/-} mice, A β was reported by Selkoe and coworkers⁹³, and CGRP was reported the Saghatelian group⁹⁸. Recently, human genome-wide association studies (GWAS) have identified predisposing and protective variants of the IDE locus linked to Type-2 Diabetes¹¹⁰⁻¹¹⁴ and Alzheimer's disease¹¹⁴⁻¹¹⁸. These studies suggest an evolutionarily conserved functional connection between IDE and glucose regulation

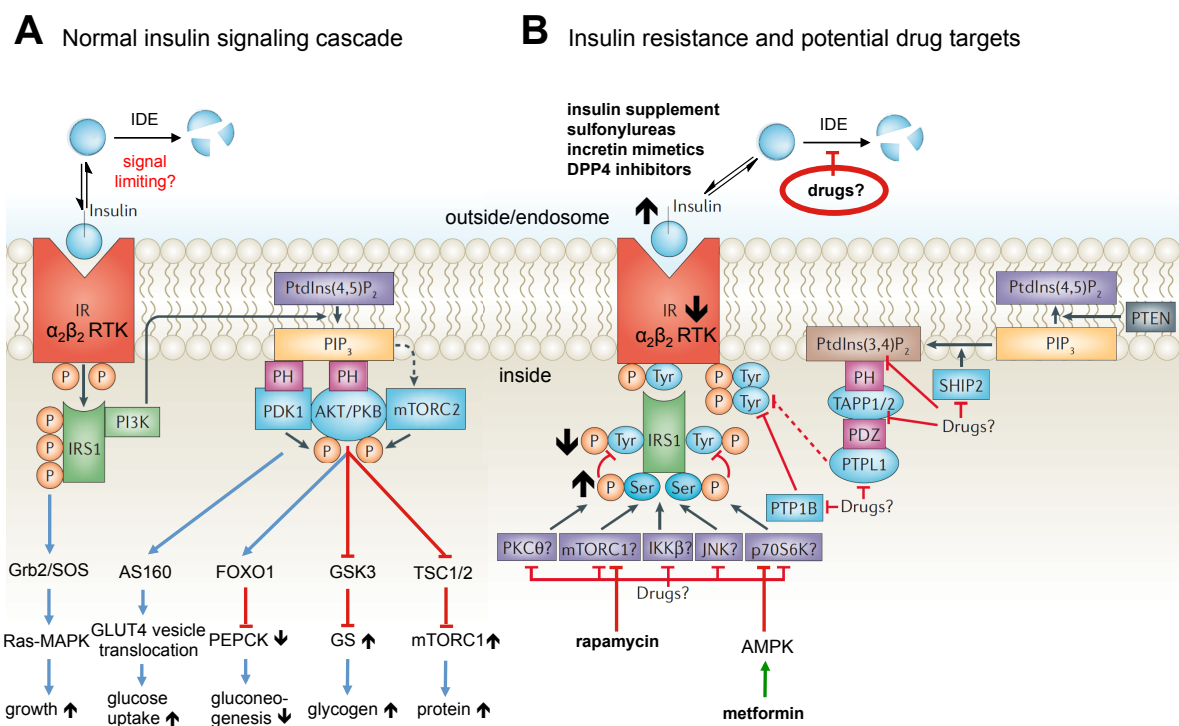


Figure 1.8 | (A) Insulin signaling cascade, showing the potential of IDE-mediated degradation to modulate insulin signaling on the insulin receptor (IR). (B) Effects of insulin resistance on the insulin signaling cascade: IR gene down-regulation (\downarrow), reduced tyrosine kinase activity (\downarrow), increased IR-inhibitory serine phosphorylation (\uparrow), and physiological compensation by elevated insulin levels (\uparrow). The role of approved anti-diabetic treatments are shown, and hypothetical untapped drug targets are highlighted, including IDE. Adapted from ref. 110.

in humans, and also corroborate that IDE activity is one of the enzymatic mechanisms that contribute to A β clearance in the brain⁹³.

The biochemical characterization of IDE-mediated insulin degradation *ex vivo* and *in vivo* was carried out by Duckworth, Hamel, Bennett, and others over the decades 1980–2000⁸². These studies support a role for IDE as the primary enzymatic mechanism for insulin clearance in the body, complemented by minor contribution from redundant non-specific pathways including protein-disulfide isomerase (PDI), and lysosomal acidic proteases (e.g. cathepsin D)⁸². The insulin cleavage pattern of IDE *in vitro* matched the cellular and endosomal degradation products, suggesting that IDE is the rate limiting step of the pathway of insulin degradation (**Figure 1.8**)⁸².

Although IDE is expressed ubiquitously in all cells, the liver and kidneys are the most important sites of insulin degradation⁸². Insulin is secreted by the pancreas into portal circulation, and up to half may be removed by first-pass transit through the liver by receptor-mediated internalization¹¹⁹. This process provides the first opportunity for IDE-mediated degradation. Subsequently, the kidney is responsible for removal of approximately 50% of insulin from systemic circulation, followed by the bulk of muscle tissue that accounts the remaining insulin clearance¹²⁰. Although relatively little insulin is ultimately excreted in urine, the processes of endocytosis, pinocytosis, and transcytosis exposes insulin to IDE, as well as the lysosomal

by inhibiting IDE-mediated degradation in the liver, kidneys, and insulin-responsive tissues (**Figure 1.8**)^{81,82,123}.

In cell culture, IDE overexpression leads to increased insulin degradation¹²⁴, and blocking IDE using a zinc-chelating inhibitor leads to elevated IR phosphorylation and downstream signaling¹²¹ (**Figure 1.9**). These studies strongly suggest that endosomal IDE-mediated degradation modulates insulin signaling activity at the cellular level¹²⁵ (**Figure 1.8**). Based on the known biochemistry of IDE, inhibition of this enzyme is expected to elevate insulin levels and augment the response to glucose^{81,82}. To validate this hypothesis using a surrogate genetic model, the Selkoe group produced mice lacking a functional IDE gene (IDE^{-/-} mice). The IDE^{-/-} mice were shown to have elevated insulin levels, but counterintuitively these animals exhibited impaired, rather than improved, glucose tolerance^{93,94}. Physiological studies with IDE^{-/-} mice concluded that chronic elevation of insulin in these animals may result in a compensatory lowering of insulin receptor expression levels, which leads to impaired glucose clearance following a glucose load^{93,94}. Hence, the insulin resistance phenotype may also explain the elevated insulin (hyperinsulinemia, **Figure 1.8**). This model raises the possibility that in the absence of such compensatory effects, *acute* inhibition of IDE may lead to improved physiological glucose tolerance by enhancing glucose uptake at multiple insulin-responsive tissues^{82,123}. These observations highlight the need for a selective small-molecule IDE inhibitor to characterize the biological functions and therapeutic relevance of this enzyme *in*

*vivo*⁶, uncoupled from confounding physiological adaptations that arise in IDE knock-out mice^{93,94}.

1.3 – The search for the first physiologically active IDE inhibitor

Research into the biosynthesis, secretion, and signaling of insulin has led to the development of multiple treatments for diabetes (**Figure 1.10**). In contrast, there is no therapeutic strategy that deals with the stabilization of endogenous insulin elicited in response to blood sugar. The dynamic interplay between the production and proteolytic degradation of peptide hormones is a key mechanism underlying the regulation of human metabolism. Inhibition of the peptidases and proteases that degrade these hormones can elevate their effective concentrations and augment signaling. The resulting insights can lead to the development of novel therapeutics¹²⁶, for example dipeptidyl peptidase 4 (DPP4) inhibitors are anti-diabetic

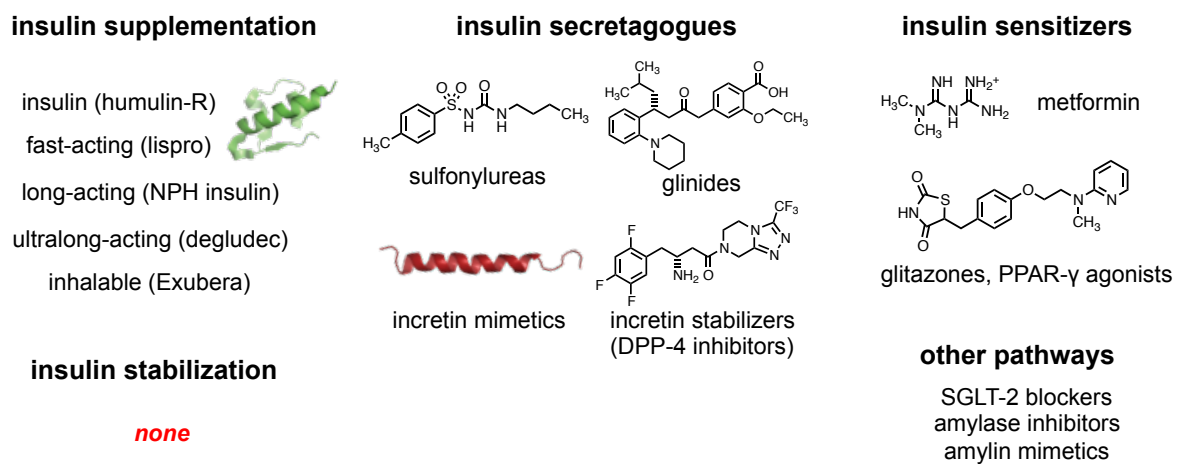


Figure 1.10 | Anti-diabetic treatments classified based on their impact on insulin signaling.

drugs that increase the concentration of the insulin-stimulating hormone glucagon-like peptide 1 (GLP-1), resulting in elevated insulin concentrations and lower blood glucose levels¹²⁷. Despite 60 years of speculation that inhibiting the degradation of insulin could treat diabetes, the relationship between IDE and glucose homeostasis remains unclear due to the lack of IDE inhibitors that are active *in vivo*^{81,82}. Indeed, the blockbuster DPP4 inhibitor drugs provide a template for the development of IDE-based treatments, in particular because DPP4 also cleaves a complex repertoire of substrates *in vitro*^{128,129}. This is also the case for the peptidases angiotensin-converting enzyme¹³⁰ (ACE) and neprilysin^{131,132} (NEP) that are targets of anti-hypertensive drugs.

In contrast to genetic approaches, small molecules can probe a target's therapeutic potential in a manner uncoupled from compensatory developmental mechanisms, with dose and temporal control.^{133,134} A selective and physiologically active small-molecule IDE inhibitor would therefore enable the validation of IDE as a potential anti-diabetes target and provide a starting point for the development of a new class of diabetes therapeutics (**Figure 1.8**). There is ample precedent for metalloprotease inhibitors that target the catalytic site¹³⁵. However, a central challenge is specific inhibition of one homolog over >185 metalloproteases encoded in the human and mouse genomes¹³⁶. Three classes of weak or non-specific IDE inhibitors have been previously identified *ad hoc* and by high-throughput screening (**Figure 1.11A-C**)¹²¹. These comprised multiple metal-binding chemotypes^{121,137,138},

thiol reactive analogs^{121,139}, and the depsipeptide antibiotic bacitracin that acts as a weak competitive inhibitor⁸². More recently, the research groups of Professors

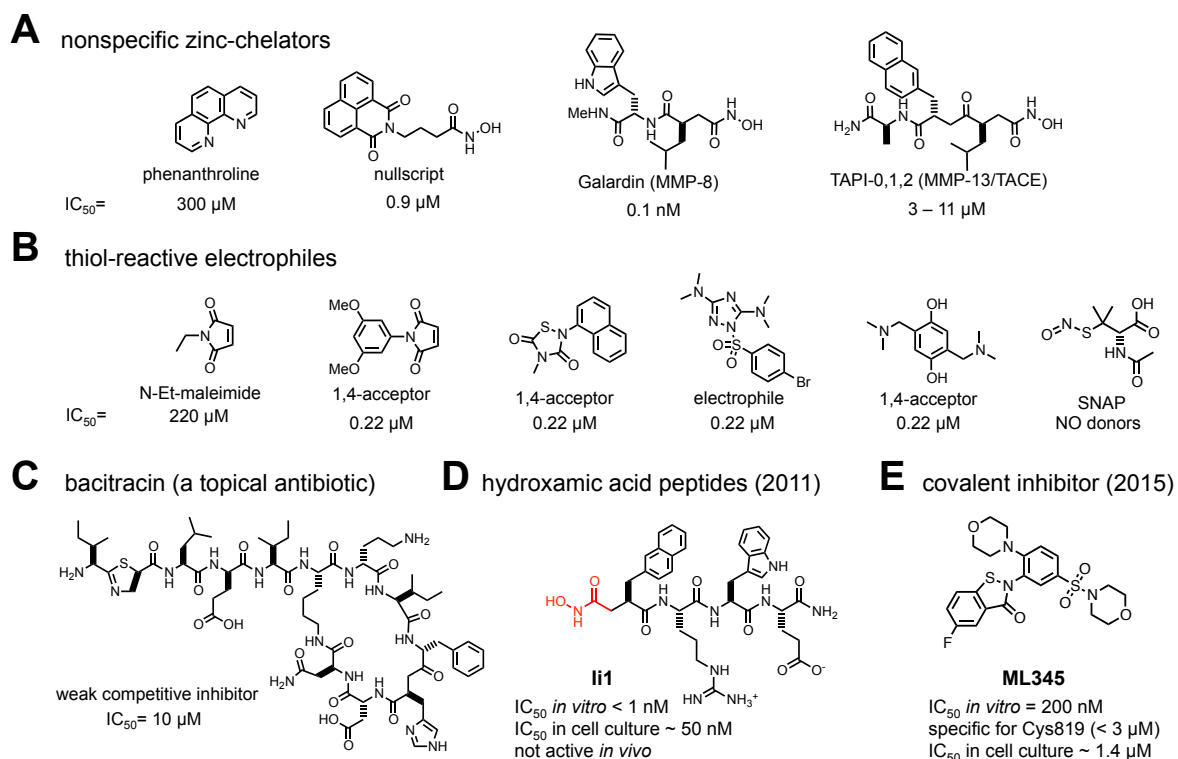


Figure 1.11 | Known inhibitors of IDE are weak or non-selective. (A) Multiple metal-binding chemotypes that inhibit IDE identified *ad hoc* and by high-throughput screening^{121,137,138}. **(B)** Non-specific thiol reactive analogs identified by high-throughput screening^{121,139}. **(C)** Structure of the major component of the depsipeptide antibiotic bacitracin that acts as a weak competitive inhibitor of IDE⁸². **(D)** Zinc-chelating IDE inhibitor **Ii1** comprising a hydroxamic acid (red) connected to a linear peptide¹²¹. **(E)** Recently reported thiol-reactive benzoisothiazolidone covalent IDE inhibitor **ML345** identified from a high-throughput screening effort¹³⁹ (see the analog in entry 3 of panel B).

Leissring and Selkoe reported the design of zinc-chelating inhibitors of IDE comprising a hydroxamic acid connected to a linear peptide or retro-inverso peptide scaffold (**Figure 1.11D**)^{121,137}. The inhibitor **Ii1** was reportedly unstable *in vivo*^{94,139}, and displays modest specificity for IDE (Chapter 2), given that such compounds derive potency from the zinc-chelating hydroxamic acid group, which has the potential to interact strongly with other metalloproteases and metal-binding proteins¹⁴⁰. More recently, a thiol-reactive covalent inhibitor **ML345** was identified from a high-throughput screening effort¹³⁹ (**Figure 1.11E**, this is a benzoisothiazolidone analog of entry 3 in panel **B**). This compound is modestly selective for IDE Cys819 over other thiols, however, the specificity profile was only tentatively determined <2 μ M, and *in vivo* activity was not reported¹³⁹.

IDE inhibitors that are active *in vivo* are therefore needed to elucidate IDE's physiological roles and to determine its potential to serve as a target for the treatment of diabetes. The Liu and Saghatelian labs therefore initiated a multidisciplinary collaboration integrating synthetic chemistry, chemical biology, structural biology, and animal physiology to discover and characterize small molecules that inhibit IDE.

1.4 – Outline of this thesis

In this thesis I describe the development of a new small-molecule IDE inhibitor identified from a DNA-templated library (Chapter 2) that is potent and inhibits IDE with high specificity through a novel binding pocket outside the catalytic site. We demonstrated this IDE inhibitor is active *in vivo* and validated it as a probe tool

(Chapter 3), which was the key to perform the first therapeutic validation experiments of acute IDE inhibition in mice (Chapter 4). Following up on the observations of the physiological consequences of inhibiting IDE on multiple hormone substrates modulated *in vivo*, we developed a second new class of substrate-selective IDE inhibitors that obstruct insulin degradation by IDE, but accommodate for IDE-mediated cleavage of other substrates, especially glucagon (Chapter 5).

The findings reported in this thesis offer new insights into the physiological roles of IDE, indicate specific strategies for modulating metabolic hormone physiology through IDE inhibition in combination with synergistic drugs, and provide an unprecedented approach to selectively inhibit IDE-mediated degradation of insulin over other substrates, rather than merely blocking the enzyme. More broadly, this work heralds the development of IDE-based therapeutics for the treatment of high blood sugar by selectively potentiating insulin, and favorably shifting the insulin-glucagon ratio, which has broad implications for glucoregulation in multiple stages of Type-2 Diabetes.

1.5 – References

- 1 Moses, H., 3rd *et al.* The anatomy of medical research: US and international comparisons. *JAMA* **313**, 174-189, (2015).
- 2 Herper, M. How Much Does Pharmaceutical Innovation Cost? A Look At 100 Companies. (2013).
<<http://www.forbes.com/sites/matthewherper/2013/08/11/the-cost-of-inventing-a-new-drug-98-companies-ranked/%3E>.

- 3 Pennisi, E. The CRISPR craze. *Science* **341**, 833-836, (2013).
- 4 Zuris, J. A. *et al.* Cationic lipid-mediated delivery of proteins enables efficient protein-based genome editing in vitro and in vivo. *Nat Biotechnol* **33**, 73-80, (2015).
- 5 Fischbach, M. A., Bluestone, J. A. & Lim, W. A. Cell-based therapeutics: the next pillar of medicine. *Science translational medicine* **5**, 179ps177, (2013).
- 6 Workman, P. & Collins, I. Probing the probes: fitness factors for small molecule tools. *Chem Biol* **17**, 561-577, (2010).
- 7 Bucci, M., Goodman, C. & Sheppard, T. L. A decade of chemical biology. *Nat Chem Biol* **6**, 847-854, (2010).
- 8 Kritzer, J. A. Grand challenge commentary: Beyond discovery: probes that see, grab and poke. *Nat Chem Biol* **6**, 868-870, (2010).
- 9 Doria, A., Patti, M. E. & Kahn, C. R. The emerging genetic architecture of type 2 diabetes. *Cell Metab* **8**, 186-200, (2008).
- 10 Zambrowicz, B. P. & Sands, A. T. Knockouts model the 100 best-selling drugs--will they model the next 100? *Nat Rev Drug Discov* **2**, 38-51, (2003).
- 11 Knight, Z. A. & Shokat, K. M. Chemical genetics: where genetics and pharmacology meet. *Cell* **128**, 425-430, (2007).
- 12 Cravatt, B. F., Wright, A. T. & Kozarich, J. W. Activity-based protein profiling: from enzyme chemistry to proteomic chemistry. *Annual review of biochemistry* **77**, 383-414, (2008).
- 13 Vinayavekhin, N., Homan, E. A. & Saghatelian, A. Exploring disease through metabolomics. *ACS chemical biology* **5**, 91-103, (2010).
- 14 An integrated encyclopedia of DNA elements in the human genome. *Nature* **489**, 57-74, (2012).

- 15 Pattanayak, V. *et al.* High-throughput profiling of off-target DNA cleavage reveals RNA-programmed Cas9 nuclease specificity. *Nat Biotechnol* **31**, 839-843, (2013).
- 16 Nguyen, U. T. *et al.* Accelerated chromatin biochemistry using DNA-barcoded nucleosome libraries. *Nat Methods* **11**, 834-840, (2014).
- 17 Kleiner, R. E., Dumelin, C. E. & Liu, D. R. Small-molecule discovery from DNA-encoded chemical libraries. *Chem Soc Rev*, in press, (2011).
- 18 Sundberg, S. A. High-throughput and ultra-high-throughput screening: solution- and cell-based approaches. *Current opinion in biotechnology* **11**, 47-53, (2000).
- 19 Mayr, L. M. & Bojanic, D. Novel trends in high-throughput screening. *Curr Opin Pharmacol* **9**, 580-588, (2009).
- 20 Blundell, T. L., Jhoti, H. & Abell, C. High-throughput crystallography for lead discovery in drug design. *Nat Rev Drug Discov* **1**, 45-54, (2002).
- 21 Murray, C. W. & Rees, D. C. The rise of fragment-based drug discovery. *Nat Chem* **1**, 187-192, (2009).
- 22 Schramm, V. L. Enzymatic transition states and transition state analogues. *Current opinion in structural biology* **15**, 604-613, (2005).
- 23 Zon, L. I. & Peterson, R. T. In vivo drug discovery in the zebrafish. *Nat Rev Drug Discov* **4**, 35-44, (2005).
- 24 Schenone, M., Dancik, V., Wagner, B. K. & Clemons, P. A. Target identification and mechanism of action in chemical biology and drug discovery. *Nat Chem Biol* **9**, 232-240, (2013).
- 25 Li, J. W. & Vederas, J. C. Drug discovery and natural products: end of an era or an endless frontier? *Science* **325**, 161-165, (2009).

- 26 Ganesan, A. The impact of natural products upon modern drug discovery. *Curr Opin Chem Biol* **12**, 306-317, (2008).
- 27 Newman, D. J. & Cragg, G. M. Natural products as sources of new drugs over the 30 years from 1981 to 2010. *Journal of natural products* **75**, 311-335, (2012).
- 28 Velasquez, J. E. & van der Donk, W. A. Genome mining for ribosomally synthesized natural products. *Curr Opin Chem Biol* **15**, 11-21, (2011).
- 29 Mannocci, L. *et al.* High-throughput sequencing allows the identification of binding molecules isolated from DNA-encoded chemical libraries. *Proc Natl Acad Sci U S A* **105**, 17670-17675, (2008).
- 30 Doyon, J. B., Snyder, T. M. & Liu, D. R. Highly sensitive in vitro selections for DNA-linked synthetic small molecules with protein binding affinity and specificity. *J Am Chem Soc* **125**, 12372-12373, (2003).
- 31 McGregor, L. M., Gorin, D. J., Dumelin, C. E. & Liu, D. R. Interaction-dependent PCR: identification of ligand-target pairs from libraries of ligands and libraries of targets in a single solution-phase experiment. *J Am Chem Soc* **132**, 15522-15524, (2010).
- 32 Kleiner, R. E., Dumelin, C. E., Tiu, G. C., Sakurai, K. & Liu, D. R. In vitro selection of a DNA-templated small-molecule library reveals a class of macrocyclic kinase inhibitors. *J Am Chem Soc* **132**, 11779-11791, (2010).
- 33 Chan, A. I., McGregor, L. M. & Liu, D. R. Novel selection methods for DNA-encoded chemical libraries. *Curr Opin Chem Biol* **26C**, 55-61, (2015).
- 34 Kanan, M. W., Rozenman, M. M., Sakurai, K., Snyder, T. M. & Liu, D. R. Reaction discovery enabled by DNA-templated synthesis and in vitro selection. *Nature* **431**, 545-549, (2004).
- 35 Gorin, D. J., Kamlet, A. S. & Liu, D. R. Reactivity-dependent PCR: direct, solution-phase in vitro selection for bond formation. *J Am Chem Soc* **131**, 9189-9191, (2009).

- 36 Koussa, M. A., Halvorsen, K., Ward, A. & Wong, W. P. DNA nanoswitches: a quantitative platform for gel-based biomolecular interaction analysis. *Nat Methods* **12**, 123-126, (2015).
- 37 Wilson, D. S. & Szostak, J. W. In vitro selection of functional nucleic acids. *Annual review of biochemistry* **68**, 611-647, (1999).
- 38 Smith, G. P. & Petrenko, V. A. Phage Display. *Chem Rev* **97**, 391-410, (1997).
- 39 Roberts, R. W. & Szostak, J. W. RNA-peptide fusions for the in vitro selection of peptides and proteins. *Proc Natl Acad Sci U S A* **94**, 12297-12302, (1997).
- 40 Hanes, J. & Pluckthun, A. In vitro selection and evolution of functional proteins by using ribosome display. *Proc Natl Acad Sci U S A* **94**, 4937-4942, (1997).
- 41 Li, X., Gartner, Z. J., Tse, B. N. & Liu, D. R. Translation of DNA into synthetic N-acyloxazolidines. *J Am Chem Soc* **126**, 5090-5092, (2004).
- 42 Gartner, Z. J., Kanan, M. W. & Liu, D. R. Multistep small-molecule synthesis programmed by DNA templates. *J Am Chem Soc* **124**, 10304-10306, (2002).
- 43 Gartner, Z. J., Kanan, M. W. & Liu, D. R. Expanding the reaction scope of DNA-templated synthesis. *Angew Chem Int Ed Engl* **41**, 1796-1800, (2002).
- 44 Gartner, Z. J. & Liu, D. R. The generality of DNA-templated synthesis as a basis for evolving non-natural small molecules. *J. Am. Chem. Soc.* **123**, 6961-6963, (2001).
- 45 Gartner, Z. J. *et al.* DNA-templated organic synthesis and selection of a library of macrocycles. *Science* **305**, 1601-1605, (2004).
- 46 Li, X. & Liu, D. R. DNA-templated organic synthesis: nature's strategy for controlling chemical reactivity applied to synthetic molecules. *Angew Chem Int Ed Engl* **43**, 4848-4870, (2004).

- 47 Brudno, Y., Birnbaum, M. E., Kleiner, R. E. & Liu, D. R. An in vitro translation, selection and amplification system for peptide nucleic acids. *Nat Chem Biol* **6**, 148-155, (2010).
- 48 Niu, J., Hili, R. & Liu, D. R. Enzyme-free translation of DNA into sequence-defined synthetic polymers structurally unrelated to nucleic acids. *Nat Chem* **5**, 282-292, (2013).
- 49 Brenner, S. & Lerner, R. A. Encoded combinatorial chemistry. *Proc Natl Acad Sci U S A* **89**, 5381-5383, (1992).
- 50 Nielsen, J., Brenner, S. & Janda, K. D. Synthetic methods for the implementation of encoded combinatorial chemistry. *J. Am. Chem. Soc* **115**, 9812-9813, (1993).
- 51 Needels, M. C. *et al.* Generation and screening of an oligonucleotide-encoded synthetic peptide library. *Proc Natl Acad Sci U S A* **90**, 10700-10704, (1993).
- 52 Hansen, M. H. *et al.* A yoctoliter-scale DNA reactor for small-molecule evolution. *J Am Chem Soc* **131**, 1322-1327, (2009).
- 53 He, Y. & Liu, D. R. Autonomous multistep organic synthesis in a single isothermal solution mediated by a DNA walker. *Nat Nanotechnol* **5**, 778-782, (2010).
- 54 Buller, F. *et al.* Design and synthesis of a novel DNA-encoded chemical library using Diels-Alder cycloadditions. *Bioorg Med Chem Lett* **18**, 5926-5931, (2008).
- 55 Dumelin, C. E., Scheuermann, J., Melkko, S. & Neri, D. Selection of streptavidin binders from a DNA-encoded chemical library. *Bioconjugate chemistry* **17**, 366-370, (2006).
- 56 Buller, F. *et al.* Selection of Carbonic Anhydrase IX Inhibitors from One Million DNA-Encoded Compounds. *ACS chemical biology* **6**, 336-344, (2011).

- 57 Clark, M. A. *et al.* Design, synthesis and selection of DNA-encoded small-molecule libraries. *Nat Chem Biol* **5**, 647-654, (2009).
- 58 Halpin, D. R. & Harbury, P. B. DNA display I. Sequence-encoded routing of DNA populations. *PLoS biology* **2**, E173, (2004).
- 59 Halpin, D. R. & Harbury, P. B. DNA display II. Genetic manipulation of combinatorial chemistry libraries for small-molecule evolution. *PLoS biology* **2**, E174, (2004).
- 60 Halpin, D. R., Lee, J. A., Wrenn, S. J. & Harbury, P. B. DNA display III. Solid-phase organic synthesis on unprotected DNA. *PLoS biology* **2**, E175, (2004).
- 61 Wrenn, S. J., Weisinger, R. M., Halpin, D. R. & Harbury, P. B. Synthetic ligands discovered by in vitro selection. *J Am Chem Soc* **129**, 13137-13143, (2007).
- 62 Melkko, S., Scheuermann, J., Dumelin, C. E. & Neri, D. Encoded self-assembling chemical libraries. *Nat Biotechnol* **22**, 568-574, (2004).
- 63 Tse, B. N., Snyder, T. M., Shen, Y. & Liu, D. R. Translation of DNA into a library of 13,000 synthetic small-molecule macrocycles suitable for in vitro selection. *J Am Chem Soc* **130**, 15611-15626, (2008).
- 64 Maianti, J. P. *et al.* Anti-diabetic activity of insulin-degrading enzyme inhibitors mediated by multiple hormones. *Nature* **511**, 94-98, (2014).
- 65 Cherney, R. J. *et al.* Macrocyclic amino carboxylates as selective MMP-8 inhibitors. *J Med Chem* **41**, 1749-1751, (1998).
- 66 Driggers, E. M., Hale, S. P., Lee, J. & Terrett, N. K. The exploration of macrocycles for drug discovery--an underexploited structural class. *Nat Rev Drug Discov* **7**, 608-624, (2008).

- 67 Wessjohann, L. A., Ruijter, E., Garcia-Rivera, D. & Brandt, W. What can a chemist learn from nature's macrocycles?--a brief, conceptual view. *Mol Divers* **9**, 171-186, (2005).
- 68 Drews, J. Genomic sciences and the medicine of tomorrow. *Nat Biotechnol* **14**, 1516-1518, (1996).
- 69 Hopkins, A. L. & Groom, C. R. The druggable genome. *Nat Rev Drug Discov* **1**, 727-730, (2002).
- 70 Ostrem, J. M., Peters, U., Sos, M. L., Wells, J. A. & Shokat, K. M. K-Ras(G12C) inhibitors allosterically control GTP affinity and effector interactions. *Nature* **503**, 548-551, (2013).
- 71 Overington, J. P., Al-Lazikani, B. & Hopkins, A. L. How many drug targets are there? *Nat Rev Drug Discov* **5**, 993-996, (2006).
- 72 Lindsay, M. A. Target discovery. *Nat Rev Drug Discov* **2**, 831-838, (2003).
- 73 Bunnage, M. E., Chekler, E. L. & Jones, L. H. Target validation using chemical probes. *Nat Chem Biol* **9**, 195-199, (2013).
- 74 Leissring, M. A. & Selkoe, D. J. Structural biology: enzyme target to latch on to. *Nature* **443**, 761-762, (2006).
- 75 "The Nobel Prize in Physiology or Medicine 1923". Nobelprize.org. Nobel Media AB 2014.
<http://www.nobelprize.org/nobel_prizes/medicine/laureates/1923/%3E.
- 76 "Frederick Sanger - Nobel Lecture: The Chemistry of Insulin". Nobelprize.org. Nobel Media AB 2014.
<http://www.nobelprize.org/nobel_prizes/chemistry/laureates/1958/sanger-lecture.html%3E.
- 77 Tomizawa, H. H., Nutley, M. L., Narahara, H. T. & Williams, R. H. The mode of inactivation of insulin by rat liver extracts. *J Biol Chem* **214**, 285-294, (1955).

- 78 Yalow, R. S. & Berson, S. A. Assay of plasma insulin in human subjects by immunological methods. *Nature* **184 (Suppl 21)**, 1648-1649, (1959).
- 79 "Rosalyn Yalow - Nobel Lecture: Radioimmunoassay: A Probe for Fine Structure of Biological Systems". Nobelprize.org. Nobel Media AB 2014. <http://www.nobelprize.org/nobel_prizes/medicine/laureates/1977/yalow-lecture.html%3E.
- 80 Danowski, T. S. & Hofmann, K. I. Arthur Mirsky. 1907-1974. *Diabetes* **24**, 776-778, (1975).
- 81 Mirsky, I. A. & Broh-Kahn, R. H. The inactivation of insulin by tissue extracts; the distribution and properties of insulin inactivating extracts. *Arch Biochem* **20**, 1-9, (1949).
- 82 Duckworth, W. C., Bennett, R. G. & Hamel, F. G. Insulin degradation: progress and potential. *Endocr Rev* **19**, 608-624, (1998).
- 83 Becker, A. B. & Roth, R. A. An unusual active site identified in a family of zinc metalloendopeptidases. *Proc Natl Acad Sci U S A* **89**, 3835-3839, (1992).
- 84 Affholter, J. A., Fried, V. A. & Roth, R. A. Human insulin-degrading enzyme shares structural and functional homologies with E. coli protease III. *Science* **242**, 1415-1418, (1988).
- 85 Song, E. S., Rodgers, D. W. & Hersh, L. B. A monomeric variant of insulin degrading enzyme (IDE) loses its regulatory properties. *PLoS One* **5**, e9719, (2010).
- 86 Shen, Y., Joachimiak, A., Rosner, M. R. & Tang, W. J. Structures of human insulin-degrading enzyme reveal a new substrate recognition mechanism. *Nature* **443**, 870-874, (2006).
- 87 McCord, L. A. *et al.* Conformational states and recognition of amyloidogenic peptides of human insulin-degrading enzyme. *Proc Natl Acad Sci U S A* **110**, 13827-13832, (2013).

- 88 Manolopoulou, M., Guo, Q., Malito, E., Schilling, A. B. & Tang, W. J. Molecular basis of catalytic chamber-assisted unfolding and cleavage of human insulin by human insulin-degrading enzyme. *J Biol Chem* **284**, 14177-14188, (2009).
- 89 Guo, Q., Manolopoulou, M., Bian, Y., Schilling, A. B. & Tang, W. J. Molecular basis for the recognition and cleavages of IGF-II, TGF-alpha, and amylin by human insulin-degrading enzyme. *J Mol Biol* **395**, 430-443, (2010).
- 90 Malito, E., Hulse, R. E. & Tang, W. J. Amyloid beta-degrading cryptidases: insulin degrading enzyme, presequence peptidase, and neprilysin. *Cellular and molecular life sciences : CMLS* **65**, 2574-2585, (2008).
- 91 Malito, E. *et al.* Molecular bases for the recognition of short peptide substrates and cysteine-directed modifications of human insulin-degrading enzyme. *Biochemistry* **47**, 12822-12834, (2008).
- 92 Sies, H. From enzymology in vitro to physiological chemistry in vivo. *Trends in Biochemical Sciences* **5**, 182-185, (1980).
- 93 Farris, W. *et al.* Insulin-degrading enzyme regulates the levels of insulin, amyloid beta-protein, and the beta-amyloid precursor protein intracellular domain in vivo. *Proc Natl Acad Sci U S A* **100**, 4162-4167, (2003).
- 94 Abdul-Hay, S. O. *et al.* Deletion of insulin-degrading enzyme elicits antipodal, age-dependent effects on glucose and insulin tolerance. *PLoS One* **6**, e20818, (2011).
- 95 Kurochkin, I. V. & Goto, S. Alzheimer's beta-amyloid peptide specifically interacts with and is degraded by insulin degrading enzyme. *FEBS letters* **345**, 33-37, (1994).
- 96 Qiu, W. Q. *et al.* Insulin-degrading enzyme regulates extracellular levels of amyloid beta-protein by degradation. *J Biol Chem* **273**, 32730-32738, (1998).

- 97 Miller, B. C. *et al.* Amyloid-beta peptide levels in brain are inversely correlated with insulin activity levels in vivo. *Proc Natl Acad Sci U S A* **100**, 6221-6226, (2003).
- 98 Kim, Y. G., Lone, A. M., Nolte, W. M. & Saghatelian, A. Peptidomics approach to elucidate the proteolytic regulation of bioactive peptides. *Proc Natl Acad Sci U S A* **109**, 8523-8527, (2012).
- 99 Duckworth, W. C. & Kitabchi, A. E. Insulin and glucagon degradation by the same enzyme. *Diabetes* **23**, 536-543, (1974).
- 100 Shroyer, L. A. & Varandani, P. T. Purification and characterization of a rat liver cytosol neutral thiol peptidase that degrades glucagon, insulin, and isolated insulin A and B chains. *Archives of biochemistry and biophysics* **236**, 205-219, (1985).
- 101 Bennett, R. G., Duckworth, W. C. & Hamel, F. G. Degradation of amylin by insulin-degrading enzyme. *J Biol Chem* **275**, 36621-36625, (2000).
- 102 Hamel, F. G., Gehm, B. D., Rosner, M. R. & Duckworth, W. C. Identification of the cleavage sites of transforming growth factor alpha by insulin-degrading enzymes. *Biochimica et biophysica acta* **1338**, 207-214, (1997).
- 103 Misbin, R. I., Almira, E. C., Duckworth, W. C. & Mehl, T. D. Inhibition of insulin degradation by insulin-like growth factors. *Endocrinology* **113**, 1525-1527, (1983).
- 104 Ciaccio, C. *et al.* Somatostatin: a novel substrate and a modulator of insulin-degrading enzyme activity. *J Mol Biol* **385**, 1556-1567, (2009).
- 105 Safavi, A., Miller, B. C., Cottam, L. & Hersh, L. B. Identification of gamma-endorphin-generating enzyme as insulin-degrading enzyme. *Biochemistry* **35**, 14318-14325, (1996).
- 106 Muller, D., Baumeister, H., Buck, F. & Richter, D. Atrial natriuretic peptide (ANP) is a high-affinity substrate for rat insulin-degrading enzyme. *European journal of biochemistry / FEBS* **202**, 285-292, (1991).

- 107 Muller, D., Schulze, C., Baumeister, H., Buck, F. & Richter, D. Rat insulin-degrading enzyme: cleavage pattern of the natriuretic peptide hormones ANP, BNP, and CNP revealed by HPLC and mass spectrometry. *Biochemistry* **31**, 11138-11143, (1992).
- 108 Bennett, R. G., Heimann, D. G. & Hamel, F. G. Degradation of relaxin family peptides by insulin-degrading enzyme. *Annals of the New York Academy of Sciences* **1160**, 38-41, (2009).
- 109 Zhang, W. J., Luo, X. & Guo, Z. Y. In vitro degradation of insulin-like peptide 3 by insulin-degrading enzyme. *The protein journal* **29**, 93-98, (2010).
- 110 Karamohamed, S. *et al.* Polymorphisms in the insulin-degrading enzyme gene are associated with type 2 diabetes in men from the NHLBI Framingham Heart Study. *Diabetes* **52**, 1562-1567, (2003).
- 111 Gu, H. F. *et al.* Quantitative trait loci near the insulin-degrading enzyme (IDE) gene contribute to variation in plasma insulin levels. *Diabetes* **53**, 2137-2142, (2004).
- 112 Sladek, R. *et al.* A genome-wide association study identifies novel risk loci for type 2 diabetes. *Nature* **445**, 881-885, (2007).
- 113 Zeggini, E. *et al.* Replication of genome-wide association signals in UK samples reveals risk loci for type 2 diabetes. *Science* **316**, 1336-1341, (2007).
- 114 Bartl, J. *et al.* Disorder-specific effects of polymorphisms at opposing ends of the Insulin Degrading Enzyme gene. *BMC medical genetics* **12**, 151, (2011).
- 115 Carrasquillo, M. M. *et al.* Concordant association of insulin degrading enzyme gene (IDE) variants with IDE mRNA, Abeta, and Alzheimer's disease. *PLoS One* **5**, e8764, (2010).
- 116 Mueller, J. C. *et al.* Weak independent association signals between IDE polymorphisms, Alzheimer's disease and cognitive measures. *Neurobiology of aging* **28**, 727-734, (2007).

- 117 Nowotny, P. *et al.* Association studies between risk for late-onset Alzheimer's disease and variants in insulin degrading enzyme. *American journal of medical genetics. Part B, Neuropsychiatric genetics : the official publication of the International Society of Psychiatric Genetics* **136B**, 62-68, (2005).
- 118 Blomqvist, M. E. *et al.* Sequence variants of IDE are associated with the extent of beta-amyloid deposition in the Alzheimer's disease brain. *Neurobiology of aging* **26**, 795-802, (2005).
- 119 Duckworth, W. C., Hamel, F. G. & Peavy, D. E. Hepatic metabolism of insulin. *The American journal of medicine* **85**, 71-76, (1988).
- 120 Rabkin, R., Ryan, M. P. & Duckworth, W. C. The renal metabolism of insulin. *Diabetologia* **27**, 351-357, (1984).
- 121 Leissring, M. A. *et al.* Designed inhibitors of insulin-degrading enzyme regulate the catabolism and activity of insulin. *PLoS One* **5**, e10504, (2010).
- 122 Duckworth, W. C. Insulin degradation: mechanisms, products, and significance. *Endocr Rev* **9**, 319-345, (1988).
- 123 Kitamura, T., Kahn, C. R. & Accili, D. Insulin receptor knockout mice. *Annual review of physiology* **65**, 313-332, (2003).
- 124 Kuo, W. L., Gehm, B. D. & Rosner, M. R. Regulation of insulin degradation: expression of an evolutionarily conserved insulin-degrading enzyme increases degradation via an intracellular pathway. *Mol Endocrinol* **5**, 1467-1476, (1991).
- 125 Cohen, P. The twentieth century struggle to decipher insulin signalling. *Nat Rev Mol Cell Biol* **7**, 867-873, (2006).
- 126 Drag, M. & Salvesen, G. S. Emerging principles in protease-based drug discovery. *Nat Rev Drug Discov* **9**, 690-701, (2010).
- 127 Drucker, D. J. The biology of incretin hormones. *Cell Metab* **3**, 153-165, (2006).

- 128 Mentlein, R., Gallwitz, B. & Schmidt, W. E. Dipeptidyl-peptidase IV hydrolyses gastric inhibitory polypeptide, glucagon-like peptide-1(7-36)amide, peptide histidine methionine and is responsible for their degradation in human serum. *European journal of biochemistry / FEBS* **214**, 829-835, (1993).
- 129 Tagore, D. M. *et al.* Peptidase substrates via global peptide profiling. *Nat Chem Biol* **5**, 23-25, (2009).
- 130 Zaman, M. A., Oparil, S. & Calhoun, D. A. Drugs targeting the renin-angiotensin-aldosterone system. *Nat Rev Drug Discov* **1**, 621-636, (2002).
- 131 Erdos, E. G. & Skidgel, R. A. Neutral endopeptidase 24.11 (enkephalinase) and related regulators of peptide hormones. *Faseb J* **3**, 145-151, (1989).
- 132 Mangiafico, S., Costello-Boerrigter, L. C., Andersen, I. A., Cataliotti, A. & Burnett, J. C., Jr. Neutral endopeptidase inhibition and the natriuretic peptide system: an evolving strategy in cardiovascular therapeutics. *European heart journal* **34**, 886-893c, (2013).
- 133 Specht, K. M. & Shokat, K. M. The emerging power of chemical genetics. *Curr Opin Cell Biol* **14**, 155-159, (2002).
- 134 Jaeschke, A. & Davis, R. J. Chemical genetic analysis of signal transduction pathways. *Expert Opin Ther Targets* **10**, 485-488, (2006).
- 135 Turk, B. Targeting proteases: successes, failures and future prospects. *Nat Rev Drug Discov* **5**, 785-799, (2006).
- 136 Puente, X. S., Sanchez, L. M., Overall, C. M. & Lopez-Otin, C. Human and mouse proteases: a comparative genomic approach. *Nature reviews. Genetics* **4**, 544-558, (2003).
- 137 Abdul-Hay, S. O. *et al.* Optimization of peptide hydroxamate inhibitors of insulin-degrading enzyme reveals marked substrate-selectivity. *J Med Chem* **56**, 2246-2255, (2013).

- 138 Charton, J. *et al.* Imidazole-derived 2-[N-carbamoylmethyl-alkylamino]acetic acids, substrate-dependent modulators of insulin-degrading enzyme in amyloid-beta hydrolysis. *European journal of medicinal chemistry* **79**, 184-193, (2014).
- 139 Bannister, T. D. *et al.* ML345, A Small-Molecule Inhibitor of the Insulin-Degrading Enzyme (IDE). *Probe Reports from the NIH Molecular Libraries Program* (2010). <<http://www.ncbi.nlm.nih.gov/pubmed/23833801%3E>.
- 140 Saghatelian, A., Jessani, N., Joseph, A., Humphrey, M. & Cravatt, B. F. Activity-based probes for the proteomic profiling of metalloproteases. *Proc Natl Acad Sci U S A* **101**, 10000-10005, (2004).

Chapter 2

Identification of potent and highly specific IDE inhibitors from a DNA-templated library of macrocycles

Adapted from: Maianti *et al*, *Nature* **511**, 94–98 (2014).

Contributions: I synthesized analogs, performed the specificity studies, and determined the mode of inhibition of the inhibitors described in this chapter. Dr. Ralph E. Kleiner performed the *in vitro* selection and validated the hits. Zachariah H. Foda solved the X-ray structure of IDE-**6b**. Help from other colleagues is acknowledged in the text.

2.1 – *In vitro* selection reveals a series of potent macrocyclic IDE inhibitors

To discover small-molecule binders of IDE, the Liu and Saghatelian labs undertook a collaboration to perform *in vitro* selections on the previously described DNA-templated library of 13,824 synthetic macrocycles^{1,2} for the ability to bind immobilized mouse IDE (**Figure 2.1**). The protein N-His₆-mIDE₍₄₉₋₁₀₁₉₎ for this experiment was provided by Whitney Nolte in Alan Saghatelian's group.

This library of 13,824 DNA-templated macrocycles^{1,2} had previously yielded highly selective *Src* kinase inhibitors.^{3,4} The unbiased design features and structural diversity of the macrocycle library suggested it may also contain ligands for other classes of proteins. The two independent IDE selection experiments performed by Ralph Kleiner resulted in the identification of six putative IDE-binding macrocycles that share common structural features (**Figure 2.2**).

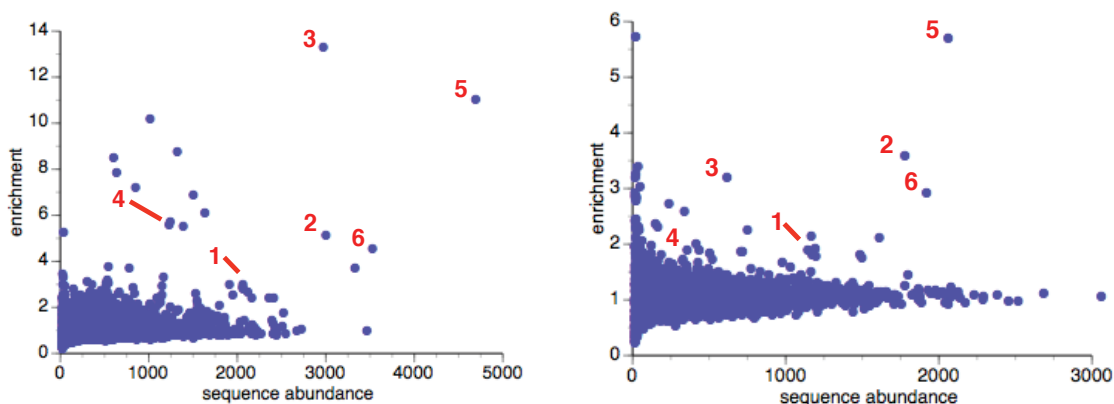


Figure 2.1 | Enrichment results from two independent *in vitro* selections against mouse N-His₆-IDE using the DNA-templated macrocycle library¹⁸. The numbers highlight compounds enriched at least 2-fold in both selections.

These six macrocycles were synthesized without their oligonucleotide templates and without the 5-atom macrocycle-DNA linker using a combination of solid- and solution-phase synthesis as either of two possible *cis*- or *trans*-alkene stereoisomers^{2,3}. Biochemical assays revealed that four of the six *trans*-macrocycles assayed were *bona fide* inhibitors of IDE with $IC_{50} \leq 1.5 \mu\text{M}$ (**Figure 2.2**) using the commercially available fluorogenic peptide Mca-RPPGFSAFK(Dnp)-OH (R&D).

I corroborated these results by performing an *in vitro* selection against human IDE using the same DNA-templated library, which revealed enrichment of the barcodes for hits **1**, **2**, **5**, and **6** previously identified as binders of mouse IDE, as well as structurally related macrocycles, which is to be expected given that mouse and human share IDE 95% amino acid identity (see Methods, **Figure 2.15**). The results of the second *in vitro* selection using human IDE (**Figure 2.3**) are consistent with the low to sub-micromolar IC_{50} values of the *trans*-isomers **1b**, **2b**, **5b** and **6b**, however, human IDE did not produce enrichment of the structures **3** or **4**, consistent with the relatively modest inhibitory activity of these macrocycles of either *cis*- or *trans*-alkene configuration against the human ortholog of IDE. The most active inhibitor among the library members enriched in all three selections, the 20-membered macrocycle **6b**, potently inhibits human IDE ($IC_{50} = 60 \text{ nM}$).

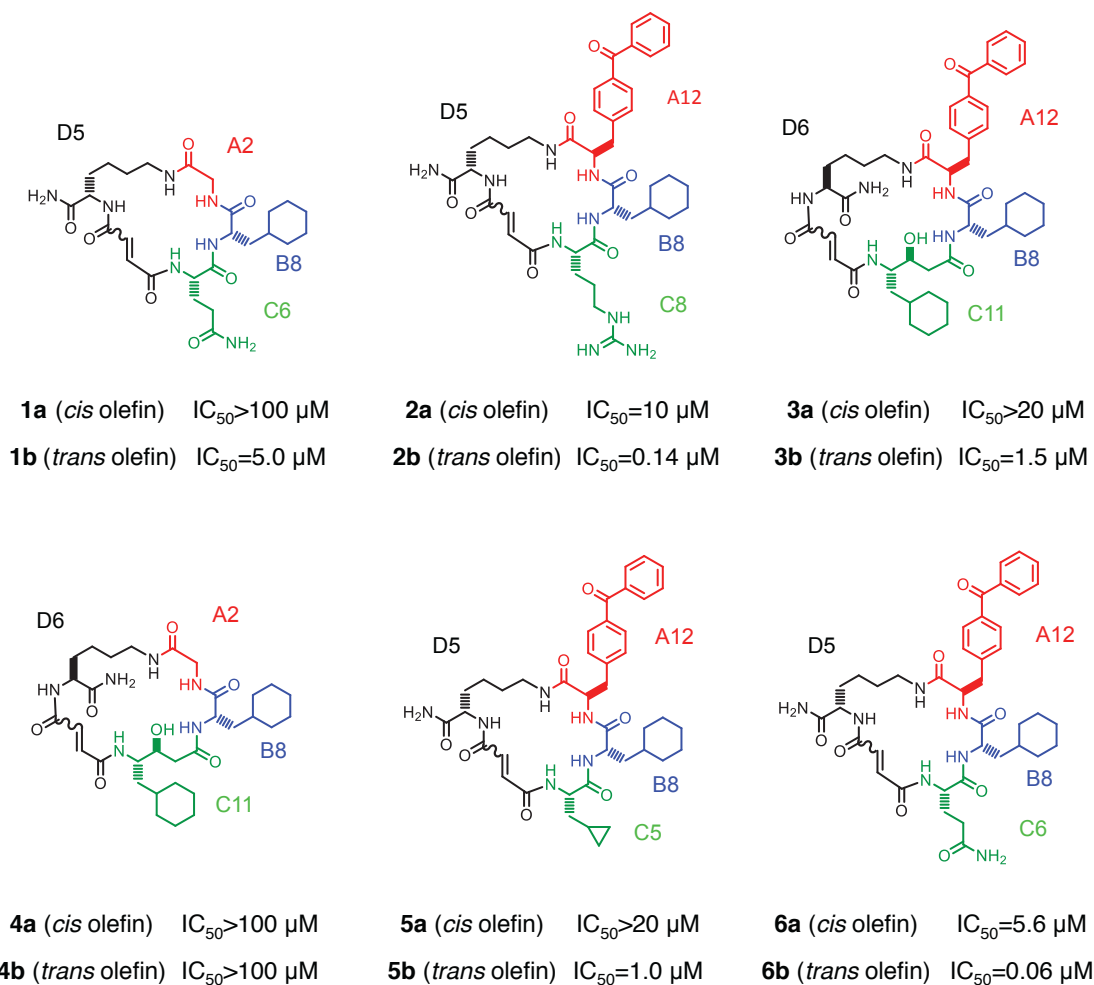


Figure 2.2 | Structures of IDE-binding macrocycles **1–6** decoded from DNA library barcodes corresponding to building blocks A, B, C and D (see Chapter 1, **Figure 1.5**). The *cis*- and *trans*-alkene isomers are labeled ‘*a*’ and ‘*b*’, respectively.

2.2 – Complementary biochemical assays for IDE inhibition

The inhibitory activity of **6b** to on IDE proteolytic activity was confirmed by four complementary *in vitro* assays, which reveal the cleavage of multiple substrates and use different sources of IDE. The most useful method for routine IC_{50} determination and comparison among **6b** analogs is the known fluorogenic peptide assay, using the decapeptide Mca-RPPGFSAFK(Dnp)-OH. This is a weak affinity

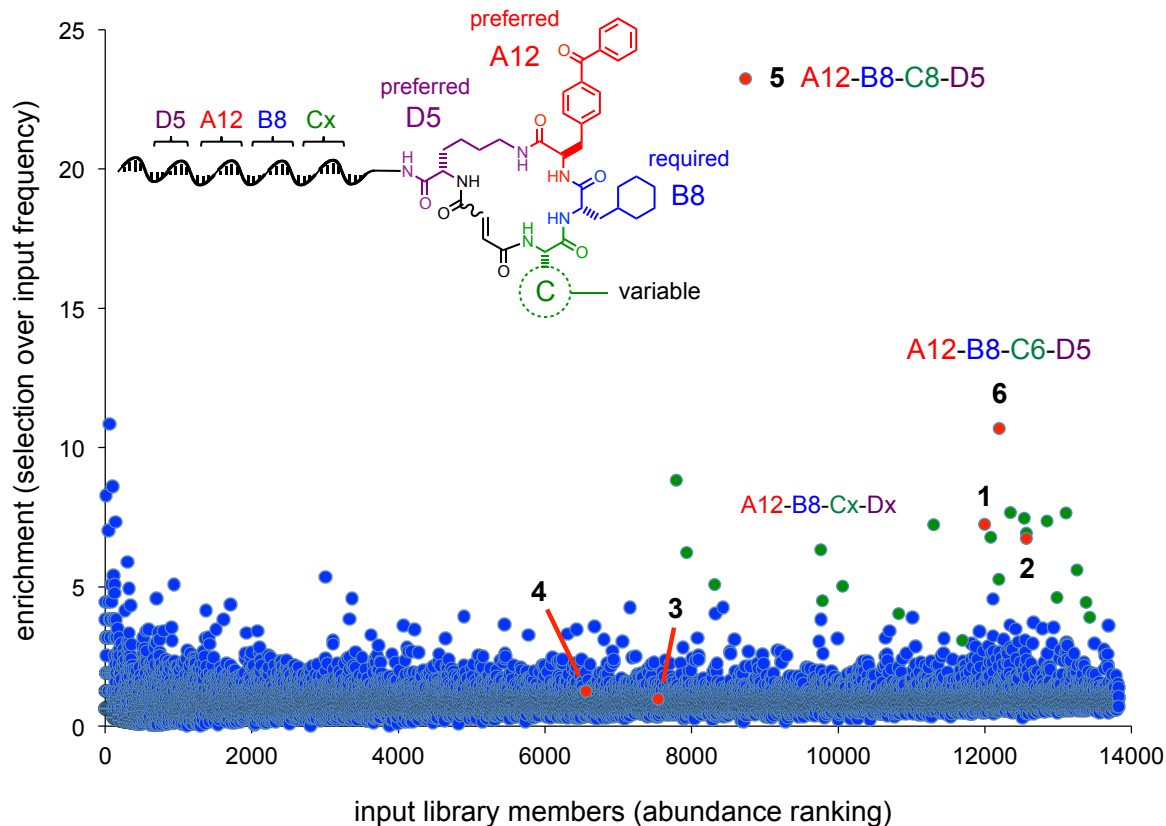


Figure 2.3 | Enrichment results from a third independent *in vitro* selection against human *N*-His₆-IDE₍₄₉₋₁₀₁₉₎ using the DNA-templated macrocycle library¹⁸. The labeled red points represent the barcodes for the structures **1** – **6** observed in previous selections, and the green points highlight barcodes related to the sequences A12-B8-Cx-Dx or Ax-B8-C6-Dx.

substrate for IDE ($K_M \sim 5 \mu\text{M}$) derived from the sequence of Bradykinin (RPPGFSPFR), which is also a low affinity *in vitro* substrate of IDE (Chapter 1, **Table 1.2**) and multiple other enzymes (ECE-1, ACE, Neprilysin, and Cathepsins). The fluorogenic peptide assay revealed the IC₅₀ potency of **6b** was comparable for the His₆-tagged main isoforms of mouse and human IDE₍₄₉₋₁₀₁₉₎ (**Figure 2.4**), using protein expressed from *E. coli* in house, or purchased from R&D produced in insect cells (*Spodoptera frugiperda* Sf 21).

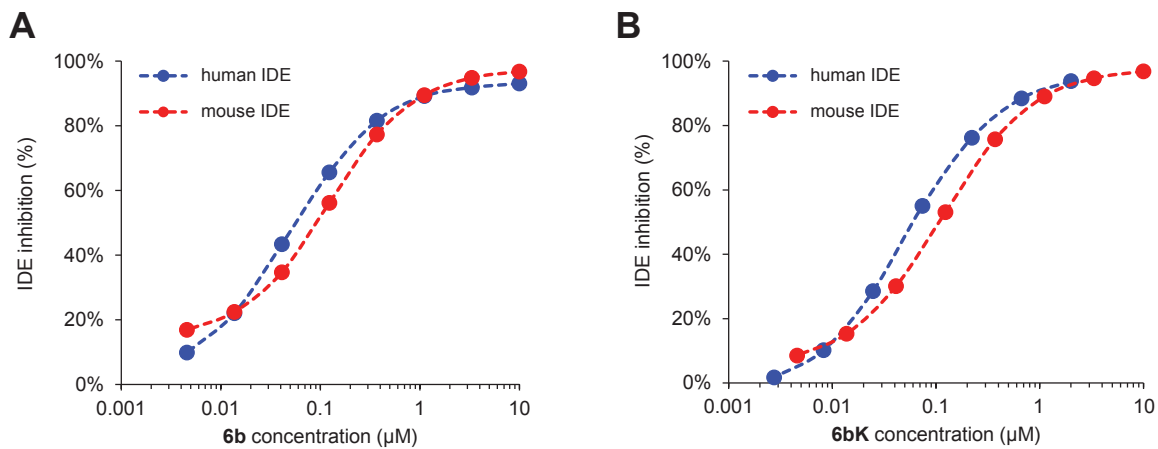


Figure 2.4 | Cleavage of the fluorogenic substrate peptide Mca-RPPGFSAFK(Dnp)-OH by human and mouse IDE in the presence of inhibitors (A) **6b** and (B) **6bK** (C = Lys).

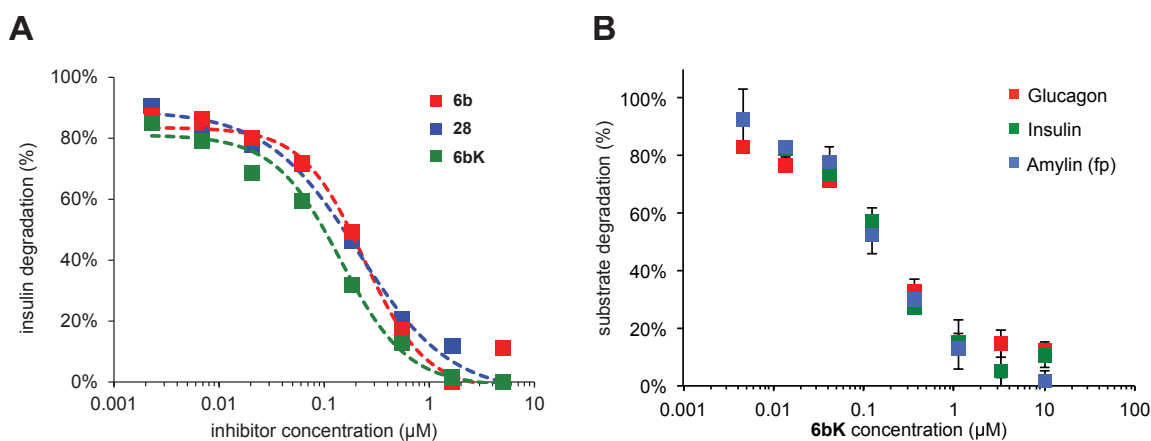


Figure 2.5 | (A) Homogeneous time-resolved FRET (HTRF) assay for IDE-mediated insulin degradation in the presence of **6b** analogs. (B) Assays comparing the EC_{50} of **6bK** inhibition of IDE cleavage of insulin, glucagon, and a fluorogenic amylin analog (see Chapter 5).

To confirm inhibition of IDE cleavage activity on relevant metabolic hormone substrates, I optimized dual-antibody Homogeneous Time-Resolved FRET (HTRF) assays against insulin and glucagon. This endpoint assays reveal the extent of IDE-

mediated cleavage following a short incubation and quenching with excess **Ii1** to stop the reaction (**Figure 2.5**). I investigated **6b** and the analog **6bK**, which has the glutamine residue substituted by lysine. The inhibitors **6b** and **6bK** achieved complete inhibition of IDE cleavage of insulin at concentrations above 10 μM with $\text{EC}_{50} = 0.1 \mu\text{M}$, which is consistent with the data derived using the fluorogenic decapeptide. Furthermore, **6bK** inhibited IDE-mediated degradation of glucagon and amylin, with similar EC_{50} as insulin, suggesting that the macrocycles obstruct IDE in

Dr. Yun-Gon Kim in Alan Saghatelian's group corroborated that **6b** inhibits the cleavage of calcitonin-gene related peptide ($\alpha\text{-CGRP}_{1-37}$) added to diluted mouse plasma harboring endogenous IDE, detected by LC-MS assay⁵ (**Figure 2.6**).

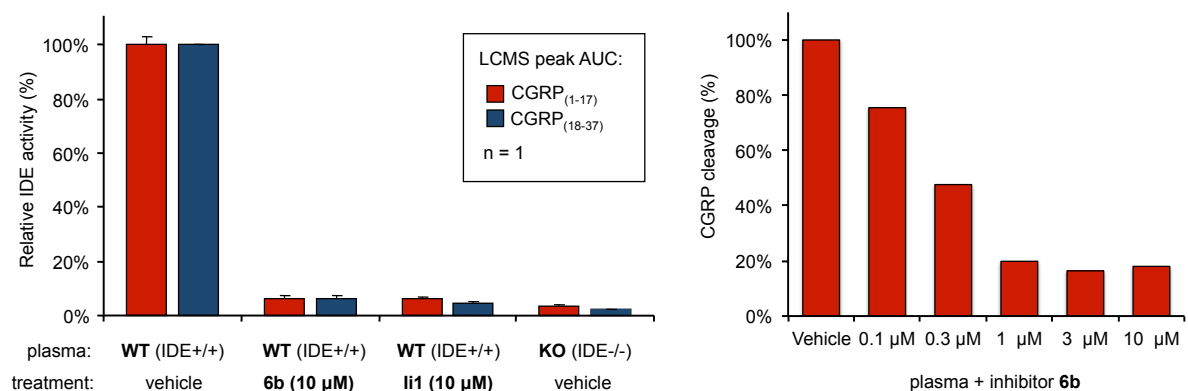


Figure 2.6 | LC-MS assay for *ex vivo* degradation of $\alpha\text{-CGRP}$ (10 μM) by endogenous IDE in mouse plasma in the presence of **6b**. Plasma from IDE^{-/-} knockout mice and WT plasma treated with inhibitor **Ii1** were used as controls.

2.3 – Structure-activity relationship of macrocyclic IDE inhibitors

We devised general synthetic routes towards *cis*- and *trans*-alkene macrocycles using on-resin amide macrocyclization (**Figure 2.7**). For convenience we replaced the Wittig reaction that produces unreliable yields of *cis*- and *trans*-isomers, which are often difficult to purify^{3,4}. We synthesized and biochemically assayed 30 analogs of **6b** in which each building block was systematically varied to elucidate structure-activity relationships of these inhibitors (**Figure 2.8**). Consistently with the results of *in vitro* selection using human IDE (**Figure 2.3**) these studies revealed the structural requirements required for potent IDE inhibition by this new class of molecules, including a *trans*-fused 20-membered macrocycle, the stereochemistry of the macrocycle substituents, and the size, shape, and hydrophobicity of the A and B building blocks (**Figure 2.8**).

The IDE chamber harbors eight exposed cysteine residues, therefore non-selective covalent mode of inhibition has been observed in multiple small molecule development efforts (Chapter 1, **Figure 1.11**). Using two **6b** analogs, I was able to rule out a covalent-adduct inhibitory mechanism through either Michael addition or a Schiff base by synthesizing the analogs **6c** (reduced linker, $IC_{50} = 570$ nM) and **7** (lacking the ketone, $IC_{50} = 60$ nM). The fact that IDE is subject to inhibition by non-specific covalent modifiers as well as zinc chelation has hindered the identification of selective IDE inhibitors using high-throughput screening assays for over a decade. Recently, the first covalent IDE inhibitor **ML345** (*in vitro* $IC_{50} \sim 200$ nM) was

published by the NIH Molecular Libraries Program, but *in vivo* data has not been reported to date.

In contrast to the strict requirements at positions A and B of the **6b** structure, different building blocks were tolerated at position C (**Figure 2.7**). Based on these results, we identified the inhibitor **6bK** ($IC_{50} = 50$ nM) as an ideal candidate for *in vivo* studies because it exhibits enhanced water solubility relative to **6b**, and can be readily synthesized on gram scale (Chapter 3, **Figure 3.1**)⁶.

The original point of attachment of **6b** to the oligonucleotide DNA template and 5-atom linker tolerated appendages such as a biotin handle (**30**, $IC_{50} = 80$ nM) or fluorescein (**31**, $IC_{50} = 100$ nM). I demonstrated the benzophenone groups of the tagged inhibitors **30** and **31** can generate adducts by exposure to UV light (360 nm, 1 min) specifically with IDE, but not BSA, and this interaction was outcompeted by 10 μ M **6b**. This UV-induced tagging method may prove useful as a tool to characterize IDE in cell culture.

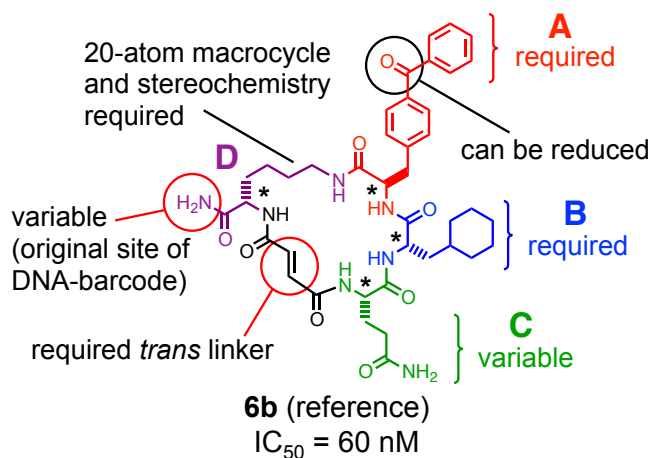
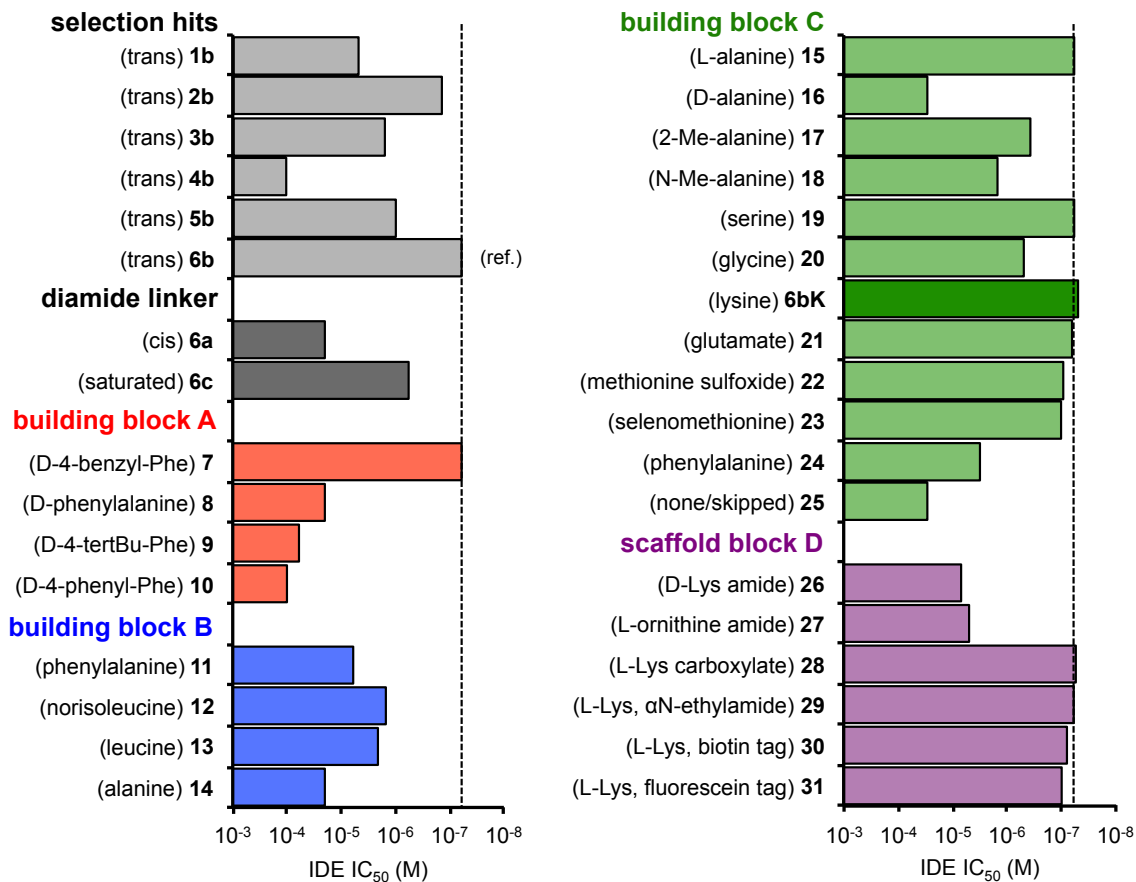


Figure 2.8 | IDE inhibition potency of selection hits **1b** to **6b** and 30 structurally related analogs in which the linker, scaffold, and three building blocks were systematically varied.

2.4 – Metalloprotease selectivity of macrocyclic IDE inhibitors

Selectivity is a crucial feature of effective probes to elucidate physiological functions⁶. In particular, the active sites of metalloproteases share multiple features and are not easily discriminated by competitive inhibitors. It is arguably a simple approach to inhibit IDE by chelation of the catalytic site zinc atom, however, there is an inherent concern in achieving selectivity for IDE over the >185 metalloproteases encoded in the human genome, as well as the other zinc-binding proteins *in vivo* (e.g. the insulin hexamers that are stabilized by a zinc atom).

For comparison in specificity studies, I synthesized the hydroxamic acid inhibitor **Ii1** using the reported procedures⁷, and purified it by HPLC. Next, I characterized the protease inhibition selectivity of **6bK**; this inhibitor exhibited $\geq 1,000$ -fold specificity *in vitro* for inhibition of IDE over all other metalloproteases tested: thimet oligopeptidase (THOP), neurolysin (NLN), neprilysin (NEP), matrix metalloprotease 1 (MMP-1), and angiotensin converting-enzyme (ACE) (**Figure 2.9**). In contrast, the substrate mimetic hydroxamic acid inhibitor **Ii1**⁷ was not as selective and it potently inhibited IDE ($IC_{50} = 0.6$ nM), THOP ($IC_{50} = 6$ nM), and NLN ($IC_{50} = 185$ nM) (**Figure 2.9**). More recently, a smaller variant of **Ii1** called **14a**,⁸ comprising the hydroxamic acid and the first two residues, was reported to have similar potency and selectivity profile as **Ii1**. Therefore, the **6bK** inhibitor is vastly superior in IDE specificity to the literature standards.

The remarkable selectivity of **6bK**, in contrast with the known promiscuity of some active site-directed metalloprotease inhibitors⁹, led us to speculate that the macrocycle engages a binding site distinct from the enzyme's catalytic site.

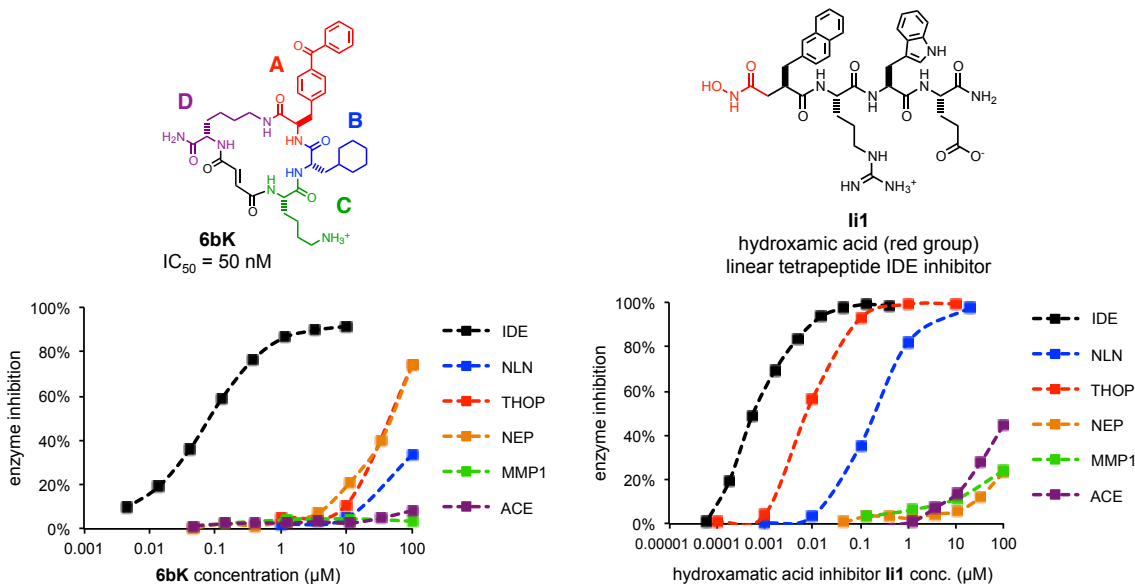


Figure 2.9 | Selectivity analysis of macrocycle **6bK** reveals > 1,000-fold selectivity for IDE (■, IC_{50} = 50 nM) over all other metalloproteases tested. Inhibitor **II1**⁷ inhibits IDE (■ IDE, IC_{50} = 0.6 nM), and also thimet oligopeptidase (■ THOP, IC_{50} = 6 nM) and neurolysin (■ NLN, IC_{50} = 185 nM), but not neprilysin (■ NEP), matrix metalloprotease 1 (■ MMP1), or angiotensin converting-enzyme (■ ACE).

2.5 – Biochemical studies and mode of inhibition of macrocycle 6b

In solution IDE exists predominantly as a homodimer, in equilibrium with monomer and tetramer species¹⁰. Cooperativity and structural cross-talk due to the dimeric nature of IDE deviate its biochemical parameters from the Michaelis–Menten model, in particular for proteolysis of small substrates¹¹ (**Figure 2.10**). For such

cases, the mode of inhibition of IDE inhibitors should not be interpreted using the linearization methods of Lineweaver–Burk (double-reciprocal plots) or Eadie–Hofstee because the lines are curved in these diagrams. The substrate saturation plots for IDE display changes in both K_M^{app} and V_{max} with increasing **6b** due to the dimer cooperativity, and the lines are of sigmoidal shape with a Hill coefficient $n = 2.1$ to 1.7 (**Table 2.1**), a level of homodimer cooperativity that is consistent with literature reports^{10,12}. The extrapolation of the plot of K_M^{app}/V_{max} versus **6b** concentration suggests a competitive $K_i = 55$ nM (**Figure 2.10**), a parameter that approximately predicts the $IC_{50} = 85$ nM for **6b** using 2.5 μ M fluorogenic substrate (observed $IC_{50} = 60$ nM, **Figure 2.1**).

Next, I studied the mode of inhibition of **6b** using Dixon and Cornish-Bowden plots, which combined provide a simple graphical method for determining inhibition constants and mode of inhibition for competitive, mixed, uncompetitive, and non-competitive inhibitors¹³. The plot profiles that arise from increasing substrate concentration are predictive of a competitive mode of inhibition for **6b** (**Figure 2.11**)¹³. The intersecting lines extrapolate to $K_i = 35$ nM, a parameter that accurately predicts the $IC_{50} = 57$ nM for **6b** at 2.5 μ M fluorogenic substrate (observed $IC_{50} = 60$ nM, **Figure 2.1**).

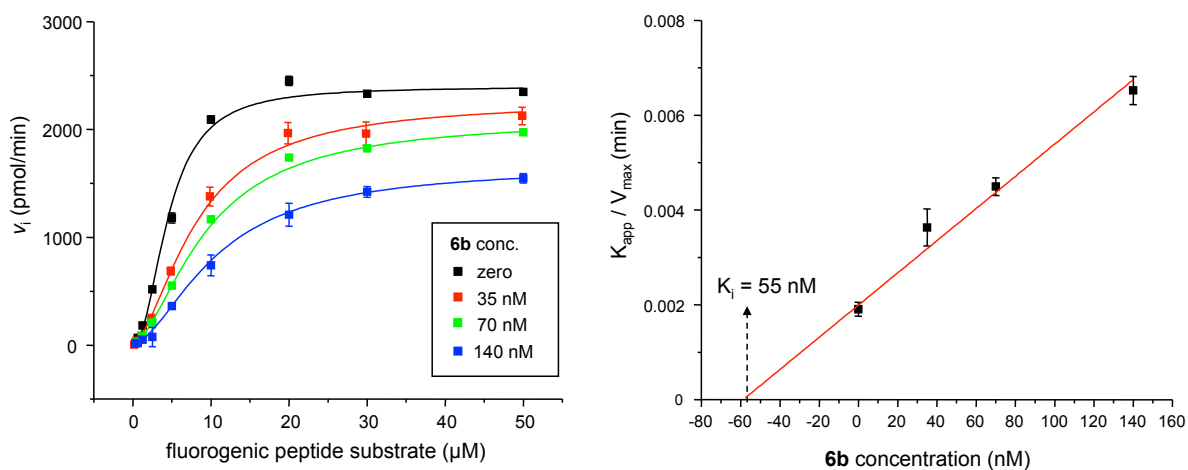


Figure 2.10 | Saturation plot for **6b** inhibition of IDE proteolysis of the fluorogenic peptide substrate. In this biochemical assay both K_M^{app} and V_{max} change with increasing **6b** due to the known dimer cooperativity in IDE (Hill coefficient $n = 2.1$ to 1.7)¹². The K_M^{app} and V_{max} values obtained from non-linear fitting (Table 2.1) predict $K_i = 55$ nM for **6b** by extrapolation.

Table 2.1 | K_M^{app} and V_{max} parameters of IDE calculated by non-linear regression.

Value \pm SE	DMSO alone	35 nM 6b	70 nM 6b	140 nM 6b
V_{max} (pmol.min ⁻¹)	2396 \pm 46	2262 \pm 87	2092 \pm 27	1651 \pm 24
K_M^{app} (μM)	4.6 \pm 0.3	8.2 \pm 0.6	9.4 \pm 0.3	10.8 \pm 0.3
Hill coef. n	2.1 \pm 0.2	1.7 \pm 0.1	1.7 \pm 0.1	1.7 \pm 0.1

These preliminary biochemical studies suggested that **6b** blocks substrate binding competitively. To investigate if **6b** interacts within the large IDE cavity I used Yonetani–Theorell double inhibitor plots that reveal if two ligands bind mutually exclusively within the enzyme, or if their binding sites are not overlapping¹⁴. The antibiotic bacitracin, which displays weak affinity for the IDE

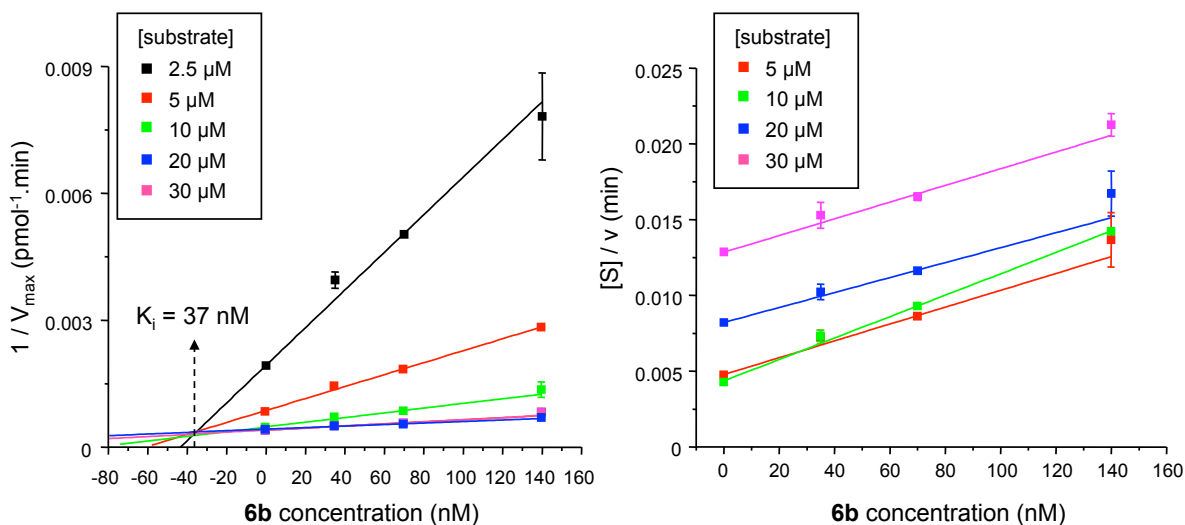


Figure 2.11 | Dixon and Cornish-Bowden plots generated for **6b** inhibition of IDE using the fluorogenic peptide substrate. This specific combination of plot profiles that arises from increasing substrate concentration is predictive of a competitive mode of inhibition for **6b**. The intersecting lines extrapolate to $K_i = 37$ nM for **6b**.

cavity ($IC_{50} = 10$ μ M) displayed mutually exclusive activity in the presence **6b** (**Figure 2.12**). However, the Yonetani–Theorell double inhibitor kinetic assay revealed synergistic, rather than competitive, inhibition by macrocycle **6b** and the substrate mimetic **Ii1** (**Figure 2.12**). The X-ray co-crystal structure of **Ii1** within IDE shows the inhibitor interacting with the zinc atom in the catalytic domain as well as the groove where the substrate backbone is held for proteolysis⁷. Therefore, the biochemical data strongly suggests that **6b** inhibits IDE competitively within the cavity from a site that is distal to the catalytic domain, which explains the remarkable level of selectivity for IDE *versus* other metalloproteases (**Figure 2.8**).

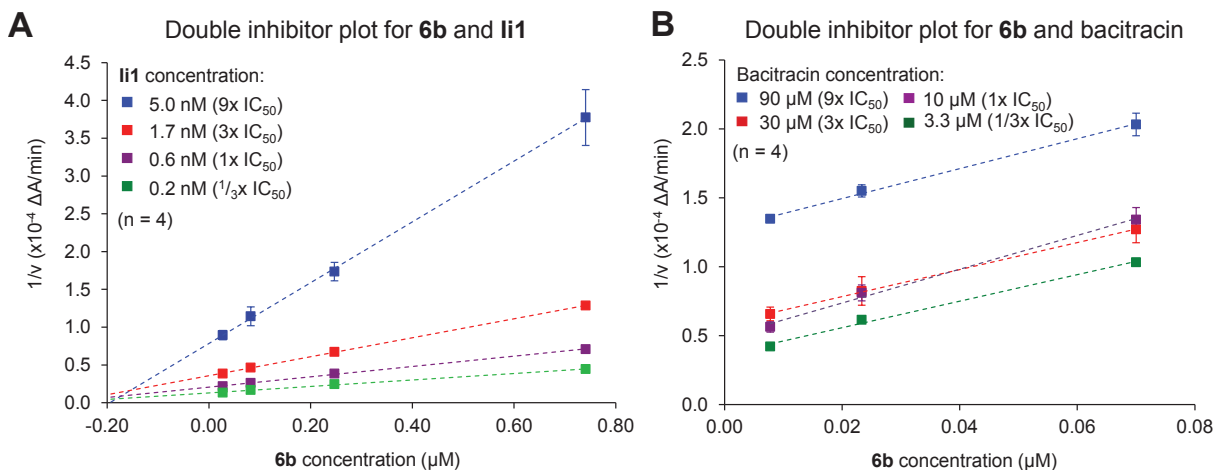


Figure 2.12 | Biochemical assays suggesting that **6b** binds a site in IDE distinct from the conventional peptide substrate binding site known to bind substrate mimetic **Ii1**. Yonetani–Theorell double inhibitor plots of IDE activity in the presence of (a) **6b** and **Ii1**, or (b) **6b** and bacitracin. Crossing lines indicate synergistic and independent binding of inhibitors, while parallel lines indicate competition for binding to the enzyme¹⁴.

2.6 – Structural basis of IDE inhibition and mutagenesis study to corroborate the novel distal binding site

In collaboration with Prof. Markus Seeliger and Zachariah Foda (Stony Brook University) we determined the X-ray crystal structure of catalytically inactive cysteine-free human IDE-E111Q¹⁵ bound to **6b** at 2.7 Å resolution (**Figure 2.13**, see **Table 2.2** for refinement statistics). The enzyme adopted a closed conformation and its structure is essentially identical to that of apo-IDE (PDB 3QZ2, RMSD = 0.257 Å). Macrocycle **6b** occupies a binding pocket at the interface of IDE domains 1 and 2 (**Figure 2.13A**), and is positioned more than 11 Å away from the zinc ion in the catalytic site (**Figure 2.13B-C**). This distal binding site is a unique structural feature

of IDE compared to related metalloproteases¹⁶, and does not overlap with the binding site of the substrate-mimetic inhibitor **II1**⁷. The structure suggests that by engaging this distal site, the macrocycle competes with substrate binding and abrogates key interactions that are necessary to unfold peptide substrates for cleavage¹⁷⁻¹⁹ (**Figure 2.13D**).

Because a section of the macrocycle was unresolved in the electronic density map, as observed with other ligands co-crystallized within the IDE cavity,²⁰ I sought to test the relevance of our structural model of the macrocycle:IDE complex (**Figure 2.13**) to macrocycle:IDE binding in solution. I identified IDE mutations predicted by the structural model to impede **6b** binding (**Figure 2.13B**), prepared the corresponding mutant IDE proteins, and measured their abilities to be inhibited by **6b** and **6bK**. In addition, I also synthesized **6b** analogs designed to complement these

Figure 2.13 | Structural basis of IDE inhibition by macrocycle 6b. (A) X-ray co-crystal structure of IDE bound to macrocyclic inhibitor **6b** (2.7 Å resolution, pdb: 4LTE). IDE domains 1, 2, 3, and 4 are colored green, blue, yellow, and red, respectively. Macrocycle **6b** is represented as a ball-and-stick model, and the catalytic zinc atom is represented as an orange sphere. (B) Relative position of macrocycle **6b** bound 11 Å from the catalytic zinc atom. The glutamine residue and four atoms of the macrocycle were unresolved (spanning a distance of 6.9 Å corresponding to four unresolved bonds). (C) Electron density map (composite omit map contoured at 1σ) and model of IDE-bound macrocycle **6b** interacting with a 10 Å-deep hydrophobic pocket. The *p*-benzoyl-phenylalanine is shown in red, the cyclohexylalanine in blue, the fumarate linker in grey, and the *D*-lysine backbone in purple. (D) Superposition of the **6b** model (surface rendering) on the IDE:insulin co-crystal structure (pdb: 2WBY)¹⁹.

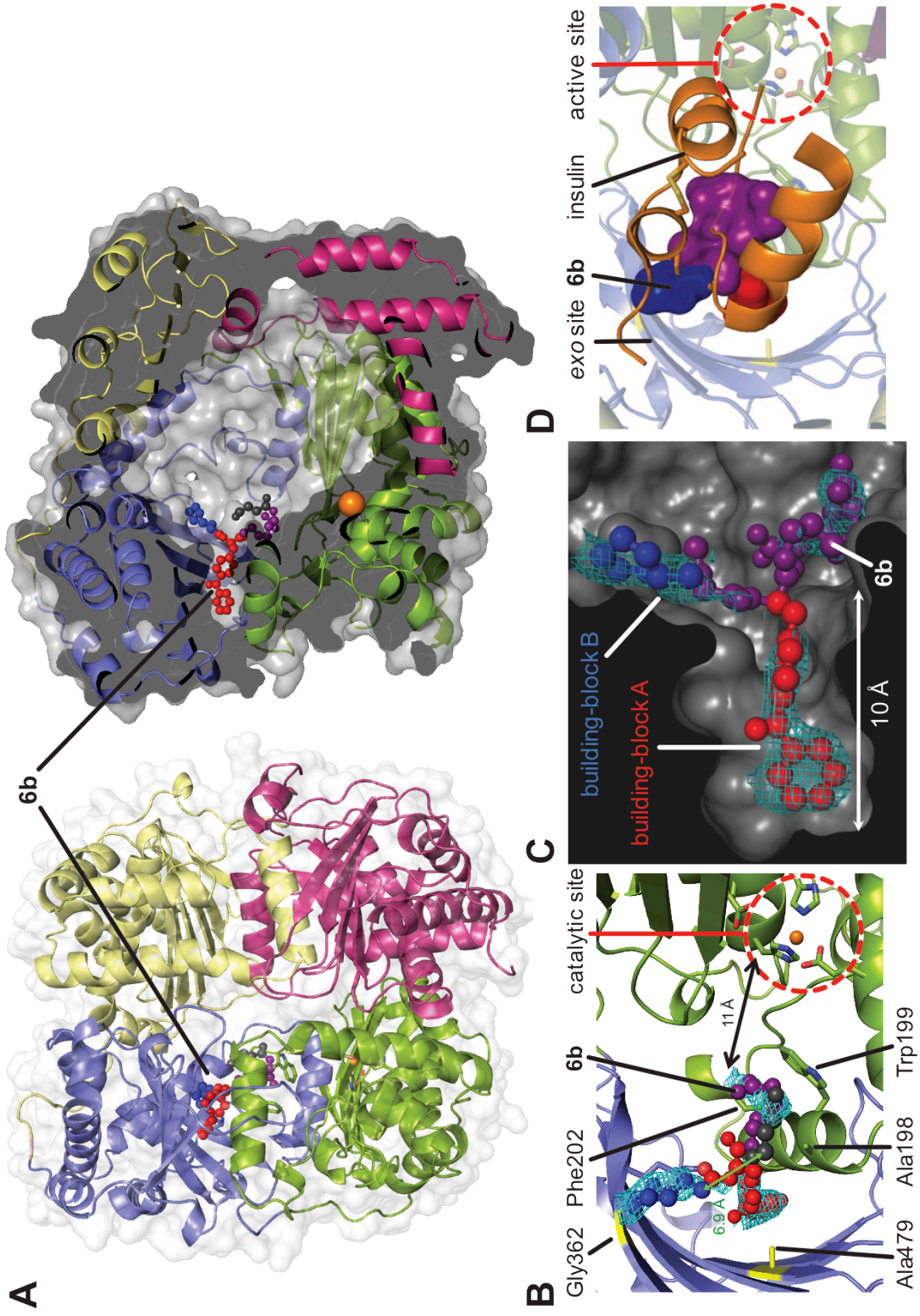


Figure 2.13 | Structural basis of IDE inhibition by macrocycle 6b (full caption in the previous page)

mutations and rescue inhibitor potency (**Figure 2.14**). Building block A (*p*-benzoyl-phenylalanine in **6b**) occupies a 10 Å-deep pocket in the crystal structure (**Figure 2.13C**), defined by residues Leu201, Gly205, Tyr302, Thr316, and Ala479. As predicted by the structural model, mutation of Ala479 to leucine decreased the potency of inhibitors **6b** and **6bK** more than 600-fold, consistent with a significant steric clash in the binding site between Leu479 and the distal benzoyl group in building block A (**Figure 2.15**). Replacement of the *p*-benzoyl-phenylalanine building block with the smaller *tert*-butyl-phenylalanine, macrocycle **9**, inhibited Ala479Leu-IDE with equal potency as wild-type IDE, consistent with the ability of the smaller macrocycle **9** to accommodate the added bulk of the leucine side chain (**Figure 2.15**). Likewise, building block B (cyclohexylalanine in **6b**) makes contacts in the structure with the peptide backbone and residues Ile374, Val360, Gly361, and Gly362 located on the lateral β-strand 13 of IDE domain 2. These residues are thought to assist in unfolding of large peptide substrates by promoting cross-β-sheet interactions¹⁷⁻¹⁹. Mutation of Gly362 to glutamine decreased the inhibition potencies of **6b** and **6bK** at least 50-fold compared to wild-type IDE (**Figure 2.15**). A modified macrocycle (**13**) in which the cyclohexylalanine building block was replaced with a smaller leucine residue inhibited Gly362Gln-IDE and wild-type IDE comparably, consistent with a model in which the smaller B building block complemented the larger size of the glutamine side chain (**Figure 2.15**).

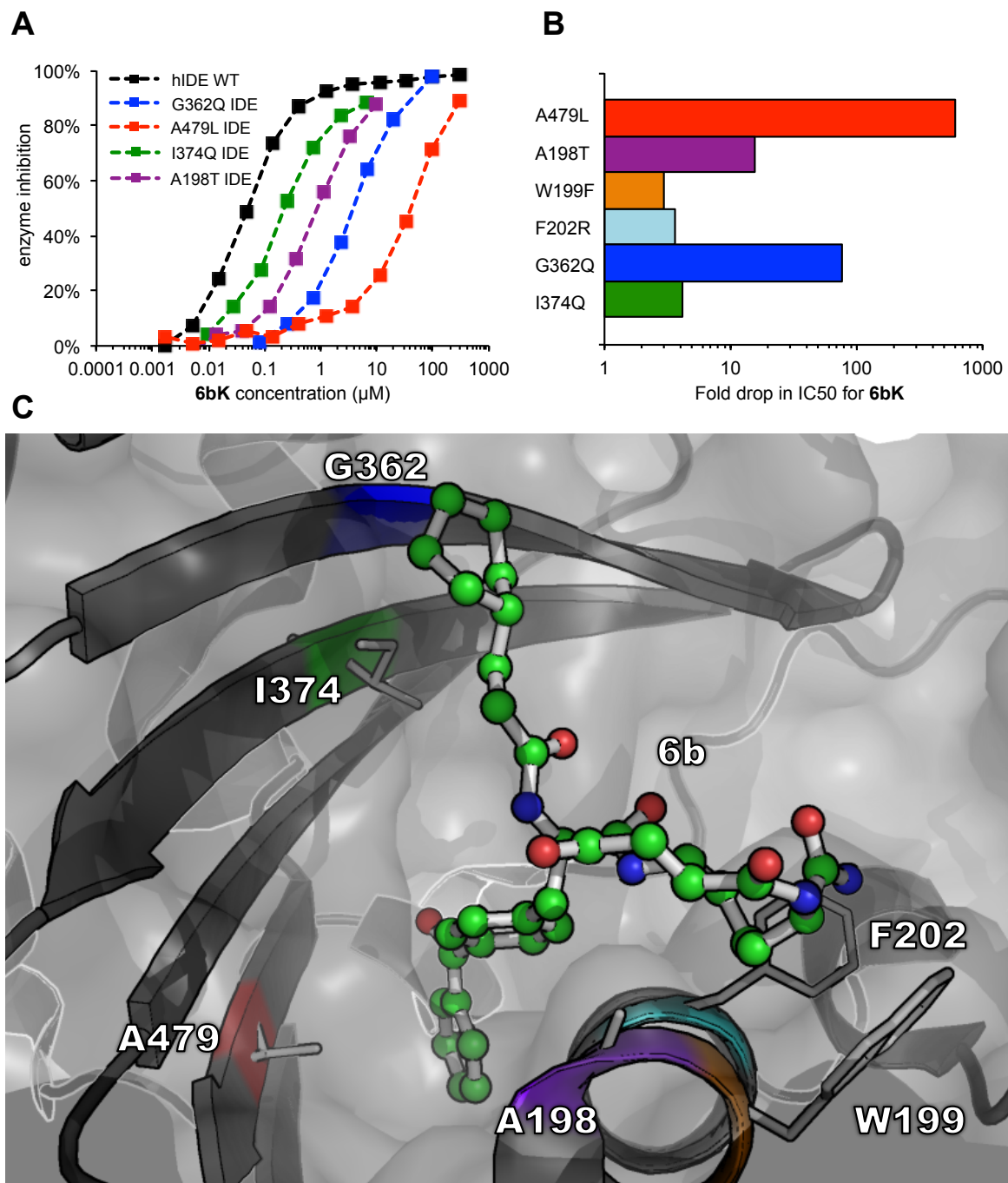


Figure 2.14 | Activity assays for wild-type or mutant human IDE variants in the presence of 6bK. (A) Mutagenesis of residues Ala479Leu (■) and Gly362Gln (■) hindered the inhibition potency of 6bK by > 600- and > 50-fold, respectively, compared to that of wild-type human IDE (■). (B) The mutations Ala198Tyr (■), Ile374Gln (■), Phe202Arg (■), and Trp199Phe (■) modestly impact the potency of 6bK by 3 to 11-fold. (C) View of the binding site of macrocycle 6b, with the mutated residues color-coded.

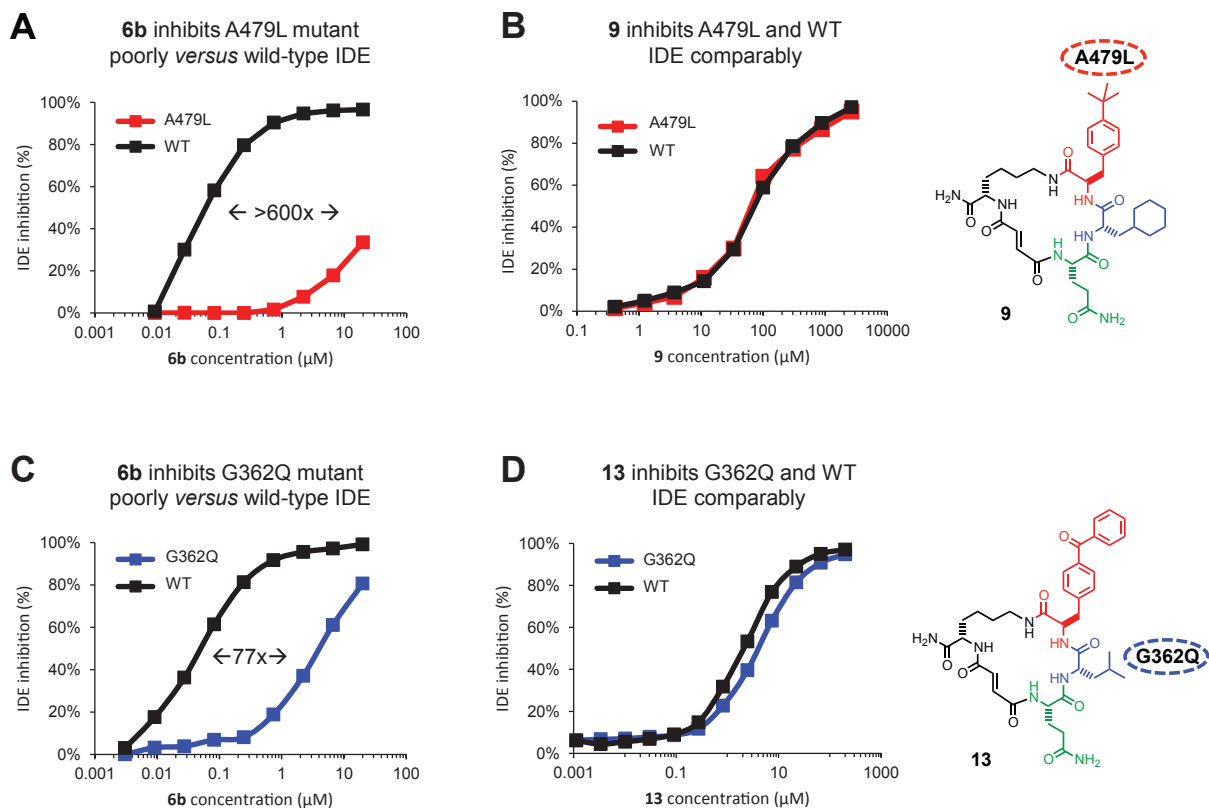


Figure 2.15 | Small molecule-enzyme mutant complementation study to confirm the macrocycle binding site and placement of the benzophenone and cyclohexyl building-block groups. (A) IDE mutant A479L is inhibited by **6b** >600-fold less potently compared to wild-type IDE. (B) Analog **9**, in which the *p*-benzoyl ring is substituted for a smaller *tert*-butyl group, inhibits A479L IDE and WT IDE comparably. (C) Similarly, IDE mutant G362Q is inhibited 77-fold less potently by **6b** compared with WT IDE. (D) Analog **13**, in which the L-cyclohexyl alanine side chain was substituted with a smaller L-leucine side chain, inhibits G362Q IDE and WT IDE comparably. The full list of IDE mutants investigated is shown in Table 2.6 (Methods section).

Taken together, these structural and biochemical studies provide strong evidence for the proposed distal binding site of **6b** and demonstrate the ability of the DNA-templated macrocycle library to provide inhibitors that achieve unusual selectivity by targeting residues beyond the catalytic site. IDE is the only homolog of the M16 clade of metalloproteases, which is evolutionarily distinct from other zinc-dependent metalloprotease members and characterized by an inverted zinc-binding motif¹⁶⁻¹⁹. This distinct phylogenetic origin, together with the unusual binding mode of these macrocyclic inhibitors to IDE, may contribute to the unusual specificity of **6bK** among proteases tested and this encouraged us to explore the properties of **6bK** *in vivo* (Chapters 3–4).

2.7 – Methods

***In vitro* selection of a DNA-templated library with immobilized mouse IDE.** The *in vitro* selection used here was adapted from previously described protocols^{1,3} using a DNA-templated library of 13,824 macrocycles². Recombinant N-His₆-tagged mouse IDE₄₂₋₁₀₁₉ (isoform containing the amino acids 42-1019 of the IDE sequence) was purified using immobilized cobalt magnetic beads (Dynabeads® His-Tag Isolation & Pulldown, Invitrogen®) according to the manufacturer's instructions. This purified IDE was confirmed to be catalytically active using the peptide substrate assay described below. IDE protein (~20 µg) was loaded onto the solid support by

incubating the protein with beads (30 μ L) at 25 $^{\circ}$ C for 30 min in 300 μ L of pH 8.0 buffer containing 50 mM phosphate, 300 mM NaCl and 0.01 % Tween-20 (PBST buffer), and washed twice with the same buffer. Two individually prepared protein-bead suspensions were incubated for 30 min with 5 pmol of the DNA-templated macrocycle library at RT, in pH 7.4 buffer containing 50 mM Tris-HCl, 150 mM NaCl, 0.05 % Tween-20 (TBST buffer) supplemented with 0.01 % BSA and 3 mg/mL yeast RNA (Ambion[®]). The beads were washed three times with 200 μ L TBST buffer. The enriched library fraction was eluted by treatment with 200 mM imidazole in PBST buffer (50 μ L) for 5 min.

The eluate solution was isolated and purified by buffer exchange using Sephadex spin-columns (Centrisep, Princeton Separation), according to the manufacturer's instructions. PCR amplification of the enriched pool of library barcodes was performed as previously reported³, using primers that append adaptors for Illumina sequencing and a 7-base identifier. The long adaptor primer was 5'-AATGATACGGCGACCACCGAGATCTACACTCTTTCCCT ACACGACGCTCTTCCGATCTXXXXXXXXCCCTGTACAC and the short adaptor primer was 5'-CAAGCAGAAGACGGCATAACGAGCTCTTCCGATC TGAGTGGGATG (the 7-base identifier was **XXXXXXXX**). The PCR amplicons were purified by polyacrylamide gel electrophoresis, extracted, and quantified using qPCR and Picogreen assays (Invitrogen).

High-throughput DNA sequencing was performed on an Illumina Genome Analyzer instrument at the Harvard FAS Center for Systems Biology, Cambridge,

MA, to yield an average of ~3.8 million sequence reads for each selection, untreated bead control and pre-selection library. Deconvolution of library barcodes and enrichment calculations were performed with custom software as described previously³. Variations in library member abundance as a result of binding to immobilized IDE was revealed by calculating fold-enrichment over the pre-selection library for the two independent selection experiments.

Protease assays with fluorogenic peptide substrates. The proteases IDE₄₂₋₁₀₁₉, recombinant human IDE₄₂₋₁₀₁₉ (R&D Systems), neprilysin (R&D), and angiotensin-converting enzyme (R&D) were assayed using the fluorophore/quencher-tagged peptide substrate Mca-RPPGFSAFK(Dnp)-OH (R&D) according to the manufacturer's instructions and recommended buffers. For IDE the recommended buffer is 50 mM Tris pH 7.5, 1 M NaCl. The enzyme mixtures (48 μ L) were transferred to a 96-well plate and combined with 2 μ L of inhibitor in DMSO solutions, in 3-fold dilution series. The mixtures were allowed to equilibrate for 10 min and the enzymatic reaction was started by addition of substrate peptide in assay buffer (50 μ L), mixed, and monitored on a fluorescence plate reader (excitation at 320 nm, emission at 405 nm). Similarly, thimet oligopeptidase (R&D) and neurolysin (R&D) were assayed using substrate Mca-PLGPK(Dnp)-OH (R&D) according to the manufacturer's instructions and recommended buffers. Matrix metalloproteinase-1 (R&D) was activated and assayed according to the manufacturer's instructions with substrate Mca-KPLGL-Dpa-AR-NH₂ (R&D). All

assay data points were obtained in duplicate. Data for the Yonetani–Theorell double inhibition plot was generated using 1 μL of each inhibitor (**6b**, and **Ii1** or bacitracin) under otherwise identical conditions as above, at concentrations corresponding to $\frac{1}{3}\text{x}$, 1x, 3x and 9x of respective IC_{50} values against hIDE (R&D).^{14,21}

IDE degradation assays for insulin (HTRF). A solution of 0.8 $\mu\text{g}/\text{mL}$ IDE (R&D) in pH 7.5 buffer containing 20 mM HEPES, 135 mM NaCl (24 μL) was transferred to a PCR strip, and combined with 1 μL of each inhibitor (10 mM in DMSO, or as a 3-fold dilution series). A solution of insulin in “Assay Diluent” (25 μL) was added to a final concentration of 20 ng/mL, and incubated at 30 °C for 15 min. This procedure was optimized to result in $\sim 75\%$ degradation of insulin. The reaction was terminated by 1:1 dilution into “Assay Diluent” containing inhibitor **Ii1** at 200 nM (or **6bk**, 10 μM) and chilled on ice. The remaining insulin in the sample was quantified using 10 μL of the quenched enzymatic reaction using the sensitive-range protocol Homogeneous Time-Resolved FRET Insulin assay (CisBio® 62INSPEB) in 20 μL total volume according to the manufacturer’s instructions (384 well-plate Greiner 784904 non-binding). Fluorescence was measured using a Tecan M1000Pro plate reader (excitation = 320 nm, emission = 665 and 620 nm, lag time = 60 μs) according the assay manufacturer’s recommendations. A blank well and a standard curve are required (non-linear).

IDE degradation assays for glucagon (HTRF). A solution of 0.05 µg/mL IDE (R&D) in 1x assay “Diluent #5” (24 µL) was transferred to a PCR strip, and combined with 1 µL of each inhibitor (10 mM in DMSO, or as a 3-fold dilution series). A solution of glucagon in the same buffer (25 µL) was added to a final concentration of 4 ng/mL, and incubated at RT for 10 min. This procedure was optimized to result in ~75 % degradation of glucagon. The reaction was terminated by 1 µL **Ii1** in 1x assay “Diluent #5” containing inhibitor **Ii1** at 5 µM (or **6bk**, 0.5 mM) and chilled on ice. The remaining glucagon in the sample was quantified using 10 µL of the quenched enzymatic reaction using the sensitive-range protocol Homogeneous Time-Resolved FRET Glucagon assay (CisBio® 62GLCPEF) in 20 µL total volume according to the manufacturer’s instructions (384 well-plate Greiner 784904 non-binding). Fluorescence was measured using a Tecan M1000Pro plate reader (excitation = 340 nm, emission = 665 and 620 nm, lag time = 60 µs) according to the assay manufacturer’s recommendations. A blank well and a standard curve are required (linear).

IDE degradation assay for calcitonin-gene related peptide (CGRP).

Degradation of CGRP by endogenous IDE in mouse plasma was analyzed by LC-MS for the formation of CGRP₁₋₁₇ and CGRP₁₈₋₃₇ as previously reported⁵. The substrate was added to a final concentration of 10 µM, and **6b** was added to a final concentration of 0.1 to 10 µM.

General procedure for synthesis of macrocycle inhibitors. Rink amide resin (NovaPEG Novabiochem®, ~0.49 mmol/g, typically at a scale of 0.1 to 2 mmol) was swollen with ~10 volumes of anhydrous DMF for 1 h in a peptide synthesis vessel with mixing provided by dry nitrogen bubbling. In a separate flask, *N*^α-allyloxycarbonyl-*N*^ε-2-Fmoc-L-lysine (5 equiv.) and 2-(1*H*-7-azabenzotriazol-1-yl)-1,1,3,3-tetramethyl uronium hexafluorophosphate (HATU, 4.75 equiv.) were dissolved in anhydrous DMF (~10 vol.), then treated with *N,N'*-diisopropylethylamine (DIPEA, 10 equiv.) for 5 min at RT. The solution was combined with the pre-swollen Rink amide resin and mixed with nitrogen bubbling overnight. The vessel was eluted and the resin was washed three times with *N*-methyl-2-pyrrolidone (NMP, ~10 vol.). Following each coupling step, Fmoc deprotection was effected with 20 % piperidine in NMP (~20 vol.) for 20 min, repeated three times, followed by washing three times with NMP (~10 vol.) and twice with anhydrous DMF (~10 vol.). The general procedure for amide coupling of building blocks A, B and C was treatment of the resin with solutions of HATU-activated *N*^α-Fmoc amino acids (5 equiv.) for 3-5 hours in anhydrous DMF, mixing with dry nitrogen bubbling. The general procedure for HATU-activation was treating a solution of *N*^α-Fmoc amino acid (5 equiv.) and HATU (4.75 equiv.) in anhydrous DMF (10 vol.) with DIPEA (10 equiv.) for 5 min at RT.

Following the final Fmoc deprotection procedure, the α -amine of building block C was coupled with allyl fumarate monoester (10 equiv.) using activation conditions as previously described with HATU (9.5 equiv.) and DIPEA (20 equiv.) in

anhydrous DMF (~10 vol.). Allyl fumarate coupling was accomplished by overnight mixing with dry nitrogen bubbling, followed by washing five times with NMP (~10 vol.) and three times with CHCl₃ (~10 vol.). Simultaneous allyl ester and *N*-allyloxycarbonyl group cleavage in solid support was effected with three consecutive treatments with a solution of tetrakis(triphenylphosphine)palladium(0) (0.5 equiv.) dissolved in degassed CHCl₃ containing acetic acid and *N*-methylmorpholine (40:2:1 ratio, ~20 vol.), mixing by nitrogen bubbling for 30 min. The resin was then washed twice subsequently with ~20 vol. of 5 % DIPEA in DMF, then twice with a 5 % solution of sodium diethyldithiocarbamate trihydrate in DMF (~20 vol.), twice with 5 % solution of hydroxybenzotriazole monohydrate in DMF, and finally washed with 50 % CH₂Cl₂ in DMF and re-equilibrated with anhydrous DMF (~10 vol.).

Treating the resin with pentafluorophenyl diphenylphosphinate (5 equiv.) and DIPEA (10 equiv.) in anhydrous DMF (~10 vol.) mixing by nitrogen bubbling overnight produced the macrocyclized products. The resin was washed with NMP (~20 vol.) and CH₂Cl₂ (~20 vol.) and dried by vacuum. The macrocyclized product was cleaved from the resin by two 15 min treatments of the macrocycle-bound resin with 95 % TFA containing 2.5 % water and 2.5 % triisopropylsilane (~20 vol.), followed by two TFA washes (~5 vol.). The TFA solution was dried to a residue under rotatory evaporation, and the peptide was precipitated by the addition of dry Et₂O. The ether was decanted and the remaining solid was dried and dissolved in a minimum volume of 3:1 DMF-water prior to purification by liquid chromatography. HPLC purification was performed on a C18 21.2x250 mm column (5 μm particle,

100 Å pore size, Kromasil®), using a gradient of 30 % to 80 % MeCN/water over 30 min, and solvents containing 0.1 % TFA. Fractions containing the desired macrocyclic peptide were combined and freeze-dried to produce a white powder. Typical yields were 5-15 % based on resin loading. Purity was determined by HPLC (Zorbax SB-C18 2.1x150 mm column, 5 µm particle) with UV detection at 230 nm, using a gradient of 30 % to 80 % MeCN/water over 30 min, and solvents containing 0.1 % TFA. The formula of final products was confirmed by accurate mass measurements using an Agilent 1100 LC-MSD SL instrument (**Table 2.3**).

Spectra for inhibitor 6b

¹H NMR (600 MHz, DMSO-*d*₆) δ 8.50 (d, *J* = 7.8 Hz, 1H), 8.42–8.36 (m, 1H), 8.07 (d, *J* = 9.0 Hz, 1H), 7.74 (d, *J* = 7.3 Hz, 1H), 7.71–7.65 (m, 3H), 7.59–7.54 (m, 4H), 7.38 (s, 1H), 7.31–7.28 (m, *J* = 8.1 Hz, 2H), 7.15 (d, *J* = 8.6 Hz, 1H), 6.97 (s, 1H), 6.85 (d, *J* = 15.8 Hz, 1H), 6.81 (s, 1H), 6.68 (d, *J* = 15.8 Hz, 1H), 4.56 (td, *J* = 9.3, 4.3 Hz, 1H), 4.21–4.14 (m, *J* = 6.9 Hz, 2H), 3.97 (ddd, *J* = 10.2, 7.5, 2.9 Hz, 1H), 3.03–2.93 (m, 3H), 2.70 (dd, *J* = 13.4, 10.2 Hz, 1H), 2.19 (td, *J* = 15.0, 7.6 Hz, 1H), 2.13 (td, *J* = 15.4, 7.9 Hz, 1H), 1.92–1.86 (m, 2H), 1.82–1.68 (m, 2H), 1.63–1.55 (m, 3H), 1.55–1.48 (m, *J* = 9.0 Hz, 3H), 1.42–1.26 (m, 4H), 1.26–1.22 (m, 1H), 1.15–1.00 (m, 5H), 0.83 (dd, *J* = 21.5, 9.6 Hz, 1H), 0.71 (dd, *J* = 24.8, 13.9 Hz, 1H).

¹³C NMR (100 MHz, DMSO-*d*₆) δ 195.44, 173.33 (2C), 171.35 (3C), 165.19, 164.16, 142.35, 137.28, 135.03, 132.96, 132.50 (2C), 132.03, 129.65 (2C), 129.53 (2C),

129.47, 128.53 (2C), 55.54, 53.51, 53.43, 49.95, 40.43, 38.98, 36.40, 33.63, 33.24, 31.47, 31.33, 29.15, 29.02, 27.02, 25.99, 25.78, 25.51, 21.92.

High resolution mass, calculated $[M+H]^+ = 758.3872$, found 758.3878, $\Delta = 0.791$ ppm.

Spectra for inhibitor 6bK (trifluoroacetate salt)

^1H NMR (600 MHz, DMSO- d_6) δ 8.49–8.44 (m, 2H), 8.04 (d, $J = 8.8$ Hz, 1H), 7.72 (d, $J = 7.1$ Hz, 1H), 7.71–7.67 (m, $J = 3.1$ Hz, 2H), 7.67–7.59 (m, 3H), 7.59–7.52 (m, 4H), 7.38 (s, 1H), 7.29 (d, $J = 8.2$ Hz, 2H), 7.15 (d, $J = 8.6$ Hz, 1H), 6.96 (s, $J = 2.1$ Hz, 1H), 6.75 (dd, $J = 81.5, 15.8$ Hz, 2H), 4.58 (td, $J = 9.2, 4.2$ Hz, 1H), 4.23 (dd, $J = 15.6, 7.8$ Hz, 1H), 4.19 (ddd, $J = 10.4, 8.4, 3.8$ Hz, 1H), 3.98 (ddd, $J = 11.1, 7.0, 3.0$ Hz, 1H), 3.25 (ddd, $J = 21.3, 13.6, 7.2$ Hz, 1H), 2.99 (dt, $J = 12.6, 7.9$ Hz, 1H), 2.95 (ddd, $J = 13.3, 10.5, 5.2$ Hz, 1H), 2.76 (tt, $J = 12.7, 6.5$ Hz, 2H), 2.70 (dd, $J = 13.3, 10.0$ Hz, 1H), 1.81–1.74 (m, 1H), 1.73–1.65 (m, 3H), 1.63–1.48 (m, 8H), 1.45–1.38 (m, 3H), 1.37–1.20 (m, 4H), 1.18–1.11 (m, 1H), 1.11–0.96 (m, 4H), 0.89–0.79 (m, 1H), 0.73 (qd, $J = 12.6, 3.6$ Hz, 1H).

^{13}C NMR (100 MHz, DMSO- d_6) δ 195.57, 173.64, 171.60, 171.53, 171.45, 165.36, 164.42, 158.89 (TFA, q, $J = 34.0$ Hz), 142.40, 137.40, 135.16, 133.02, 132.58 (2C), 132.14, 129.75 (2C), 129.65 (2C), 129.58, 128.60 (2C), 116.50 (TFA, q, $J = 294.8$ Hz), 55.37, 53.68, 53.56, 50.12, 38.79, 36.46, 33.84, 33.32, 31.33, 30.94, 29.23, 29.10, 26.60, 26.07, 26.00, 25.75, 22.61, 22.03.

High resolution mass, calculated $[M+H]^+ = 758.4236$, found 758.4233, $\Delta = -0.396$ ppm.

Spectra for bisepi-6bK (trifluoroacetate salt)

^1H NMR (600 MHz, DMSO- d_6) δ 8.45 (d, $J = 6.5$ Hz, 1H), 8.38 (d, $J = 8.9$ Hz, 1H), 7.73–7.65 (m, 5H), 7.65–7.59 (m, $J = 8.2$ Hz, 5H), 7.57 (dd, $J = 14.5, 6.7$ Hz, 3H), 7.39 (s, 1H), 7.30 (d, $J = 8.2$ Hz, 2H), 7.01 (s, 1H), 6.90 (s, 2H), 4.32 (ddd, $J = 14.6, 10.0, 4.0$ Hz, 2H), 4.21 (dd, $J = 13.3, 6.3$ Hz, 1H), 3.99 (dt, $J = 8.3, 6.4$ Hz, 1H), 3.11 (dd, $J = 13.8, 5.9$ Hz, 1H), 3.08–3.00 (m, 2H), 2.82 (dd, $J = 12.7, 5.7$ Hz, 1H), 2.79–2.72 (m, 2H), 1.83–1.76 (m, $J = 7.2$ Hz, 1H), 1.73 (d, $J = 11.3$ Hz, 1H), 1.68–1.60 (m, $J = 9.4$ Hz, 4H), 1.55 (qd, $J = 14.1, 7.5$ Hz, 6H), 1.46–1.33 (m, 3H), 1.33–1.20 (m, 4H), 1.10 (d, $J = 9.2$ Hz, 3H), 1.02 (dd, $J = 23.9, 11.8$ Hz, 1H), 0.91 (dd, $J = 21.9, 10.1$ Hz, 1H), 0.79 (dd, $J = 22.0, 10.7$ Hz, 1H).

^{13}C NMR (100 MHz, DMSO- d_6) δ 195.62, 173.82, 171.54, 171.04, 169.78, 165.09, 163.98, 158.66 (TFA, q, $J = 32.4$ Hz), 143.28, 137.35, 135.06, 133.37, 132.59 (2C), 132.07, 129.59 (4C), 129.46, 128.57 (2C), 116.80 (TFA, q, $J = 296.4$ Hz), 55.27, 54.51, 52.52, 50.23, 38.73, 38.61, 36.48, 33.79, 33.45, 31.46, 30.84, 30.45, 28.19, 26.62, 26.09, 25.77, 23.07, 22.63.

High resolution mass, calculated $[M+H]^+ = 758.4236$, found 758.4232, $\Delta = -0.527$ ppm.

Expression and purification of recombinant cysteine-free hIDE (IDE-CF). We expressed cysteine-free catalytically-inactive, human IDE (IDE-CF) in pPROEX vector¹⁷. IDE-CF contains the following substitutions: C110L, E111Q, C171S, C178A, C257V, C414L, C573N, C590S, C789S, C812A, C819A, C904S, C966N, and C974A. IDE was expressed and purified as previously described¹⁷. Briefly, IDE-CF was transformed into *E. coli* BL21-CodonPlus (DE3)-RIL, grown at 37 °C to a cell density of 0.6 O.D. and induced with IPTG at 16 °C for 19 hours. Cells were lysed and the lysate was subjected to Ni-affinity (GE LifeScience) and anion exchange chromatography (GE LifeScience). The protein was further purified by size exclusion chromatography (Superdex S200 column) three successive times, first without inhibitor then two times after addition of 2-fold molar excess of **6b**.

IDE-CF•6b co-crystallization. Eluent from size exclusion chromatography was concentrated to 20 mg/ml in 20 mM Tris, pH 8.0, 50 mM NaCl, 0.1 mM PMSF and 2-fold molar excess of **6b** was added to form the protein-inhibitor complex. The complex was mixed with equal volumes of reservoir solution containing 0.1 M HEPES (pH 7.5), 20 % (w/v) PEGMME-5000, 12 % tacsimate and 10 % dioxane. Crystals appeared after 3-5 days at 25 °C and were then equilibrated in cryoprotective buffer containing well solution and 30 % glycerol. IDE-CF•**6b** complex crystals belong to the space group $P6_5$, with unit-cell dimensions $a = b = 262 \text{ \AA}$ and $c = 90 \text{ \AA}$, and contain two molecules of IDE per asymmetric unit (see Appendix for refinement statistics).

X-Ray Diffraction. X-ray diffraction data were collected at the National Synchrotron Light Source at Brookhaven National Laboratories beamline X29 at 100K and 1.075 Å.

IDE-CF•6b structure determination. Data were processed in space group $P6_5$ using autoProc²². The structure was phased by molecular replacement using the structure for human IDE E111Q (residues 45-1011, with residues 965-977 missing) in complex with inhibitor compound 41367 (PDB: 2YPU) as a search model in Phaser²³. The model of the structure was built in Coot²⁴ and refined in PHENIX²⁵, using NCS (torsion-angle) and TLS (9 groups per chain). In the Ramachandran plot, 100 % of the residues appear in the allowed regions, 97.2 % of the residues appear in the favored regions, and 0 % of the residues appear in the outlier regions (see Appendix for refinement statistics). The structural model of IDE and inhibitor was refined using non-crystallographic symmetry restraints due to the high degree of structural similarity between the two chains of the protein the asymmetric unit. The root-mean-square deviation between the two chains is 0.5 Å for the protein chains, and 0.9 Å for the ligand atoms, indicating high structural similarity between the two chains. Structure coordinates are deposited in the Protein Data Bank (accession number **4TLE**).

Table 2.2 | X-ray data collection and refinement statistics.

Data collection	hIDE-CF•6b
Space group	P6 ₅
Cell dimensions	
<i>a</i> , <i>b</i> , <i>c</i> (Å)	261.97,261.97,90.8
α , β , γ (°)	90,90,120
Resolution (Å)	130.99- 2.70
<i>R</i> _{merge}	0.135 (0.683)
<i>I</i> / σI	14.85 (2.1)
Completeness (%)	100 (99.9)
Redundancy	7.4
Refinement	
Resolution (Å)	2.705
No. reflections	97302
<i>R</i> _{work} / <i>R</i> _{free}	0.1563/0.2009
No. atoms	
Protein	15531
Ligand/ion	160
Water	563
<i>B</i> -factors	
Protein	Chain A: 29.23 Chain B: 30.51
Ligand/ion	Chain A: 64.42 Chain B: 63.53
Water	31.67
R.m.s. deviations	
Bond lengths (Å)	0.012
Bond angles (°)	1.36
PDB accession code	4LTE

Site-directed mutagenesis, expression, and purification of human IDE. The reported N-His₆-tagged human IDE₄₂₋₁₀₁₉ construct was introduced in the expression plasmid pTrcHis-A (Invitrogen) using primers for uracil-specific excision reactions (USER) by *Taq* (NEB) and *Pfu* polymerases (PfuTurbo CX®, Agilent). The IDE gene was amplified with the primers 5'-ATCATCATATGAATAATCCAGCCA-*dU*-CAAGAGAATAGG and 5'-ATGCTAGCCATACCTCAGA *G-dU*-TTGCAGCCATGAAG (underlined sequences represent overhangs, and italics highlight the PCR priming sequence). Similarly, the pTrcHis-A vector was amplified for USER cloning with the primers 5'-ATGGCTGGATTATTCATATGATGA-*dU*-GATGATGATGAGAACCC and 5'-ACTCTGAGGTATGGCTAGCA-*dU*-GACTGGTG. Mutant IDE constructs were generated by amplifying the full vector construct with USER cloning primers introducing a mutant overhang (**Table 2.4**).

All PCR products were purified on microcentrifuge membrane columns (MinElute®, Qiagen) and quantified by UV absorbance (NanoDrop). Each fragment (0.2 pmol) was combined in a 10 µL reaction mixture containing 20 units *DpnI* (NEB), 0.75 units of USER mix (Endonuclease VIII and Uracil-DNA Glycosylase, NEB), 20 mM Tris-acetate, 50 mM potassium acetate, 10 mM magnesium acetate, 1 mM dithiothreitol at pH 7.9 (1x NEBuffer 4). The reactions were incubated at 37 °C for 45 min, followed by heating to 80 °C and slow cooling to 30 °C (0.2 °C/s). The hybridized constructs were directly used for heat-shock transformation of chemically competent NEB turbo *E. coli* cells according to

the manufacturer's instructions. Transformants were selected on carbenicillin LB agar, and isolated colonies were cultured overnight in 2 mL LB.

The plasmid was extracted using a microcentrifuge membrane column kit (Miniprep®, Qiagen), and the sequence of genes and vector junctions were confirmed by Sanger sequencing (**Table 2.5**). The plasmid constructs were transformed by heat-shock into chemically-competent expression strain Rosetta 2 (DE3) pLysS *E. coli* cells (EMD Millipore), and selected on carbenicillin/chloramphenicol LB agar. Cells transformed with IDE pTrcHis A constructs were cultured overnight at 37 °C in 2 XYT media (31 g in 1L) containing 100 µg/mL ampicillin and 34 µg/mL chloramphenicol. Expression of His6-tagged IDE proteins was induced when the culture measured OD600 ~0.6 by addition of isopropyl-β-D-1-thiogalactopyranoside (IPTG) to 1 mM final concentration, incubated overnight at 37 °C, followed by centrifugation 10,000 g for 30 min at 4 °C.

Recombinant His6-tagged proteins were purified by Ni(II)-affinity chromatography (IMAC sepharose beads, GE Healthcare®) according to the manufacturer's instructions. The cell pellets were resuspended in pH 8.0 buffer containing 50 mM phosphate, 300 mM NaCl, 10 mM imidazole, 1 % Triton X-100 and 1 mM tris(2-carboxyethyl)phosphine hydrochloride (TCEP), and were lysed by probe sonication for 4 min at <4 °C, followed by clearing of cell debris by centrifugation at 10,000 g for 25 min at 4 °C. The supernatant was incubated with Ni(II)-doped IMAC resin (2 mL) for 3 h at 4 °C. The resin was washed twice with the cell resuspension/lysis buffer, and three times with pH 8.0 buffer containing 50

mM phosphate, 300 mM NaCl, 50 mM imidazole and 1 mM TCEP. Elution was performed in 2 mL aliquots by raising the imidazole concentration to 250 mM and subsequently to 500 mM in the previous buffer. The fractions were combined and the buffer was exchanged to the recommended IDE buffer (R&D) using spin columns with 100 KDa molecular weight cut off membranes (Millipore). Protein yields were typically ~10 µg/L, and >90 % purity based on gel electrophoresis analysis (Coomassie stained). IDE-specific protease activity was >95 % as assessed by inhibition of degradation of peptide substrate Mca-RPPGFSAFK(Dnp)-OH (R&D) by 20 µM **6bK**, compared with pre-quantitated commercially available human IDE (R&D). The complete list of IDE mutations assayed is shown in **Table 2.6**.

Table 2.3 | HPLC and high-resolution mass spectrometry analysis of IDE inhibitor analogs.

Compound	Purity (%)	Formula	[M+H] ⁺ expected	[M+H] ⁺ found	Ion count	Δ (ppm)
1a	87.5	C ₂₆ H ₄₁ N ₇ O ₇	564.3140	564.3135	17505	-0.886
1b	66.4	C ₂₆ H ₄₁ N ₇ O ₇	564.3140	564.3141	237080	0.177
2a	84.1	C ₄₁ H ₅₅ N ₉ O ₇	786.4297	786.4290	523007	-0.890
2b	95.3	C ₄₁ H ₅₅ N ₉ O ₇	786.4297	786.4272	627894	-3.179
3a	84.3	C ₄₆ H ₆₂ N ₆ O ₈	827.4702	827.4703	111258	0.121
3b	89.9	C ₄₆ H ₆₂ N ₆ O ₈	827.4702	827.4703	26066	0.121
4a	93.7	C ₃₂ H ₅₂ N ₆ O ₇	633.3970	633.3975	1344574	0.789
4b	79.7	C ₃₂ H ₅₂ N ₆ O ₇	633.3970	633.3967	591800	-0.474
5a	97.1	C ₄₁ H ₅₂ N ₆ O ₇	741.3970	741.3987	517852	2.293
5b	75.4	C ₄₁ H ₅₂ N ₆ O ₇	741.3970	741.3967	208124	-0.405
6a	98.3	C ₄₀ H ₅₁ N ₇ O ₈	758.3872	758.3886	875721	1.846
6b	98.9	C ₄₀ H ₅₁ N ₇ O ₈	758.3872	758.3878	14154	0.791
7	89.6	C ₄₀ H ₅₃ N ₇ O ₇	744.4079	744.4079	21411	-0.040
8	94.9	C ₃₃ H ₄₇ N ₇ O ₇	654.3610	654.3606	413032	-0.611
9	80.1	C ₃₇ H ₅₅ N ₇ O ₇	710.4236	710.4239	180420	0.422
10	76.9	C ₃₉ H ₅₁ N ₇ O ₇	730.3923	730.3917	644559	-0.821
11	92.6	C ₄₀ H ₄₅ N ₇ O ₈	752.3402	752.3399	77585	-0.399
12	96.0	C ₃₇ H ₄₇ N ₇ O ₈	718.3559	718.3550	145796	-1.253
13	95.7	C ₃₇ H ₄₇ N ₇ O ₉	718.3559	718.3569	24610	1.392
14	58.2	C ₃₄ H ₄₁ N ₇ O ₈	676.3089	676.3082	400965	-1.035
15	77.5	C ₃₈ H ₄₈ N ₆ O ₇	701.3657	701.3671	124002	1.996
16	67.3	C ₃₈ H ₄₈ N ₆ O ₇	701.3657	701.3683	19335	3.707
17	83.2	C ₃₉ H ₅₀ N ₆ O ₇	715.3814	715.3808	298036	-0.839
18	92.3	C ₃₉ H ₅₀ N ₆ O ₇	715.3814	715.3832	701250	2.516
19	37.4	C ₃₈ H ₄₈ N ₆ O ₈	717.3606	717.3586	128261	-2.788
20	74.5	C ₃₇ H ₄₆ N ₆ O ₇	687.3501	687.3503	135532	0.291
21	95.6	C ₄₀ H ₅₀ N ₆ O ₉	759.3712	759.3726	13461	1.844
22	97.9	C ₄₀ H ₅₂ N ₆ O ₈ S	777.3640	777.3634	121542	-0.772
23	88.5	C ₄₀ H ₅₂ N ₆ O ₇ Se	807.3144	807.3139	1497	-0.619
24	52.4	C ₄₄ H ₅₂ N ₆ O ₇	777.3970	777.3981	15952	1.415
25	63.5	C ₃₅ H ₄₃ N ₅ O ₆	630.3286	630.3282	136628	-0.635
26	74.4	C ₄₀ H ₅₁ N ₇ O ₈	758.3872	758.3876	119065	0.527
27	90.9	C ₃₉ H ₄₉ N ₇ O ₈	744.3715	744.3708	210827	-0.940
29	75.3	C ₄₂ H ₅₅ N ₇ O ₈	786.4185	786.4178	234651	-0.890
28	94.3	C ₄₀ H ₅₀ N ₆ O ₉	759.3712	759.3705	89863	-0.922
30	97.5	C ₅₄ H ₇₅ N ₉ O ₁₁ S	1058.5380	1058.5402	23247	2.078
31	81.6	C ₆₅ H ₇₁ N ₇ O ₁₅	1190.5081	1190.5063	442	-1.512
6bK	96.6	C ₄₁ H ₅₅ N ₇ O ₇	758.4236	758.4233	501430	-0.396
heavy-6bK	96.4	C ₃₅ ¹³ C ₆ H ₅₅ N ₅ ¹⁵ N ₂ O ₇	766.4378	766.4388	227096	1.305
bisepi-6bK	96.7	C ₄₁ H ₅₅ N ₇ O ₇	758.4236	758.4232	133009	-0.527
epiA-6bK	96.6	C ₄₁ H ₅₅ N ₇ O ₇	758.4236	758.4258	1320288	2.901
epiB-6bK	94.9	C ₄₁ H ₅₅ N ₇ O ₇	758.4236	758.4235	216951	-0.132
epiC-6bK	93.9	C ₄₁ H ₅₅ N ₇ O ₇	758.4236	758.4235	177995	-0.132
li1	94.8	C ₃₇ H ₄₅ N ₆ O ₈	744.3464	744.3474	662	1.343

Table 2.4 | Site-directed mutagenesis primers.

Mutation	Primers (forward, reverse)
A198Q	ACATGAGAAGAATGTGATGAATGA-dU-CAGTGGAGAC ATCATTCATCACATTCTTCTCATG-dU-TCTG
A198T	AGACTCTTTCAATTGGAAAAAGC-dU-ACAGGG AGCTTTTCCAATTGAAAGAGTC-dU-CCAGGTATCATTTCATCACATTCTTCTCATGTTC
A198C	AGACTCTTTCAATTGGAAAAAGC-dU-ACAGGG AGCTTTTCCAATTGAAAGAGTC-dU-CCAGCAATCATTTCATCACATTCTTCTCATGTTC
A198Y	ACATGAGAAGAATGTGATGAATGA-dU-TACTGGAGAC ATCATTCATCACATTCTTCTCATG-dU-TCTG
W199L	ACATGAGAAGAATGTGATGAATGA-dU-GCCTTAAGACTC ATCATTCATCACATTCTTCTCATG-dU-TCTG
W199F	AGACTCTTTCAATTGGAAAAAGC-dU-ACAGGG AGCTTTTCCAATTGAAAGAGTC-dU-GAAGGCATCATTTCATCACATTCTTCTC
W199Y	AGACTCTTTCAATTGGAAAAAGC-dU-ACAGGG AGCTTTTCCAATTGAAAGAGTC-dU-ATAGGCATCATTTCATCACATTCTTCTC
F202L	ACATGAGAAGAATGTGATGAATGA-dU-GCCTGGAGACTCTTGCAATTG ATCATTCATCACATTCTTCTCATG-dU-TCTG
F202R	AGACTCTTTCAATTGGAAAAAGC-dU-ACAGGG ATGAAATGATGCCGGAGAC-dU-CCGTCAATTGGAAAAAGCTACAGGG
I310R	ACCCATTAAAGATCGTAGGAATC-dU-CTATGTGACATTTCCCATAC AGATTCCCTACGATCTTTAATGGG-dU-ACTATTTGTAAAGTTGTTTAAAG
Y314F	ACCCATTAAAGATATAGGAATCTC-dU-TCGTGACATTTCCCATACCTGACCTTC AGAGATTCCCTAATATCTTTAATGGG-dU-ACTATTTG
V360Q	AAAGGGCTGGGTTAATACTCT-dU-CAGGGTGGGCAG AAGAGTATTAACCCAGCCCTT-dU-GACTTAAG
V360R	AAAGGGCTGGGTTAATACTCT-dU-AGGGGTGGGCAGAAGGAAGGAGC AAGAGTATTAACCCAGCCCTT-dU-GACTTAAG
G361Q	AAAGGGCTGGGTTAATACTCT-dU-GTTCAGGGGCAGAAGGAAGGAGCCC AAGAGTATTAACCCAGCCCTT-dU-GACTTAAG
G362Q	AAAGGGCTGGGTTAATACTCT-dU-GTTGGTCAGCAGAAGGAAGGAGCCCCGAG AAGAGTATTAACCCAGCCCTT-dU-GACTTAAG
K364A	AAGGAGCCCGAGGTTTA-dU-GTTTTTTATC ATAAAACCTCGGGCTCCT-dU-CCGCCTGCCACCAACAAGAGTATT
I374Q	ATGTTTTTTCAGATTAATGTGGACT-dU-GACCGAGGAAGG AAGTCCACATTAATCTGAAAAACA-dU-AAAACCTCGGGCTCCTTC
A479L	ATGTCCGGGTTCTGATAGTTTCTAAA-dU-CTTTTGAAGGAAAACTG ATTTAGAACTATCAGAACCCGGACA-dU-TTCTGGTCTGAG

Table 2.5 | Sequencing primers.

Sequencing primers	
Seq_Fw1	GATTAACCTTATTATTAAAAATTAAGAGG
Seq_Re1	CAACATGTAATAATCCTTCTCGGTC
Seq_Fw2	GCATGAAGGTCCCTGGAAGTCTG
Seq_Re2	AGGAAGGGTTACATCATCCAGAGC
Seq_Fw3	CCATGTACTACCTCCGCTTGC
Seq_Re3	GCAGATCTCGAGCTCGGATC
Seq_Fw4	GCTTATGTGGACCCCTTGCACTG

Table 2.6 | Site-directed IDE mutants used in the small molecule-enzyme mutant complementation studies.

Protein	Batch	Relative activity	Ii1 IC ₅₀ shift *	6b IC ₅₀ shift	13 IC ₅₀ shift	9 IC ₅₀ shift	Prediction
hIDE WT	1	1.0	1.0	1.0	1.0	1.0	
hIDE WT	2	1.0	1.0	1.0	1.0	-	
hIDE WT	3	1.0	1.0	1.0	1.0	-	
A198Q	1	1.4	1.0	2.3	-	-	
A198T	2	1.5	1.0	16	13.6	-	scaffold interaction
A198Y	2	2.3	1.1	0.5	-	-	
W199F	2	1.3	1.8	3.0	3.2	-	modest interaction
W199Y	2	0.3	1.4	1.8	-	-	
F202L	1	0.7	1.7	1.7	2.3	-	
F202R	2	0.9	1.1	3.7	4.1	-	modest interaction
I310R	2	3.0	1.9	0.8	0.7	-	
Y314F	2	3.5	1.0	1.2	-	-	
V360Q	1	2.6	0.9	1.5	-	-	
V360R	3	0.4	0.9	1.4	-	-	
G361Q	3	0.7	0.9	0.8	-	-	
G362Q	3	1.2	0.6	77	1.8	-	cyclohexyl ring interaction
K364A	2	4.3	1.0	26	10.0	-	scaffold interaction
I374Q	1	1.2	1.0	4.2	-	-	cyclohexyl ring interaction
A479L	1	0.5	0.9	>600	-	1.0	<i>p</i> -benzoyl interaction

* NB: **Ii1** is not known to interact with any of these residues. Significant changes in IC₅₀ for **Ii1** were presumed to indicate misfolding or other non-inhibitor-specific protein structure changes. For example, W199L IDE displayed an IC₅₀ shift of 21-fold for **Ii1**, 13-fold for **6b**, and 17-fold for analog **13**. The data for mutation I374Q has been corrected after the publication, the original data was relevant to I375Q-IDE due to incorrect primer design.

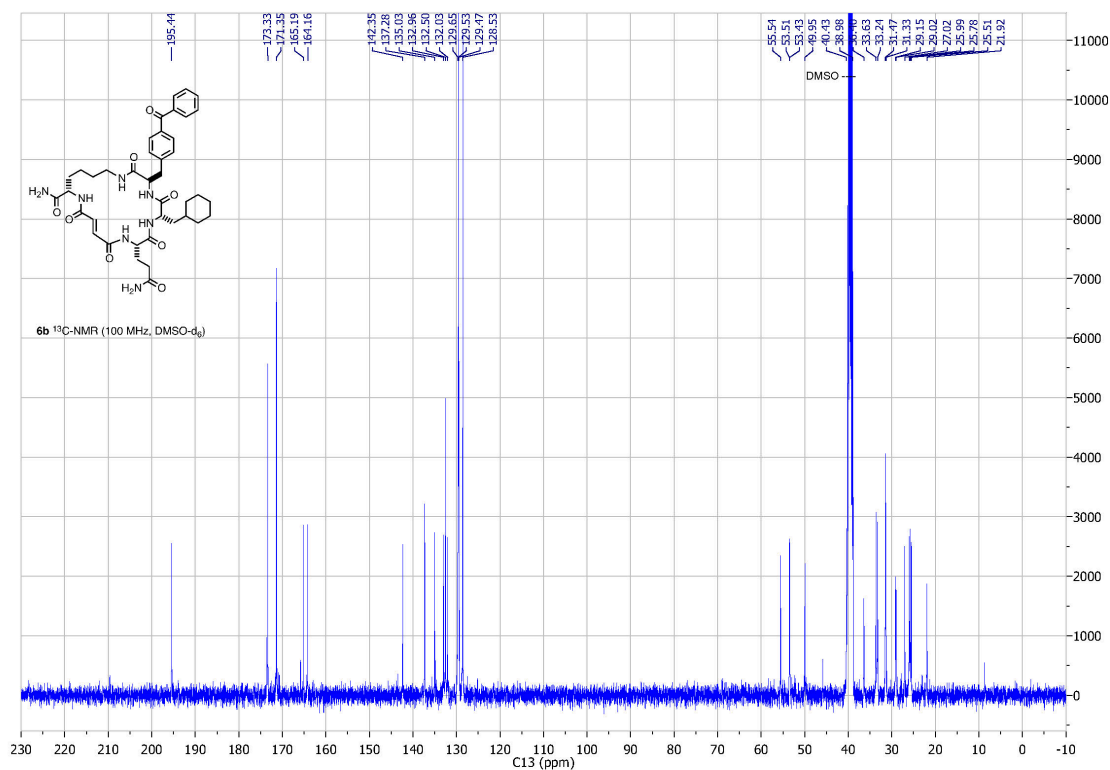
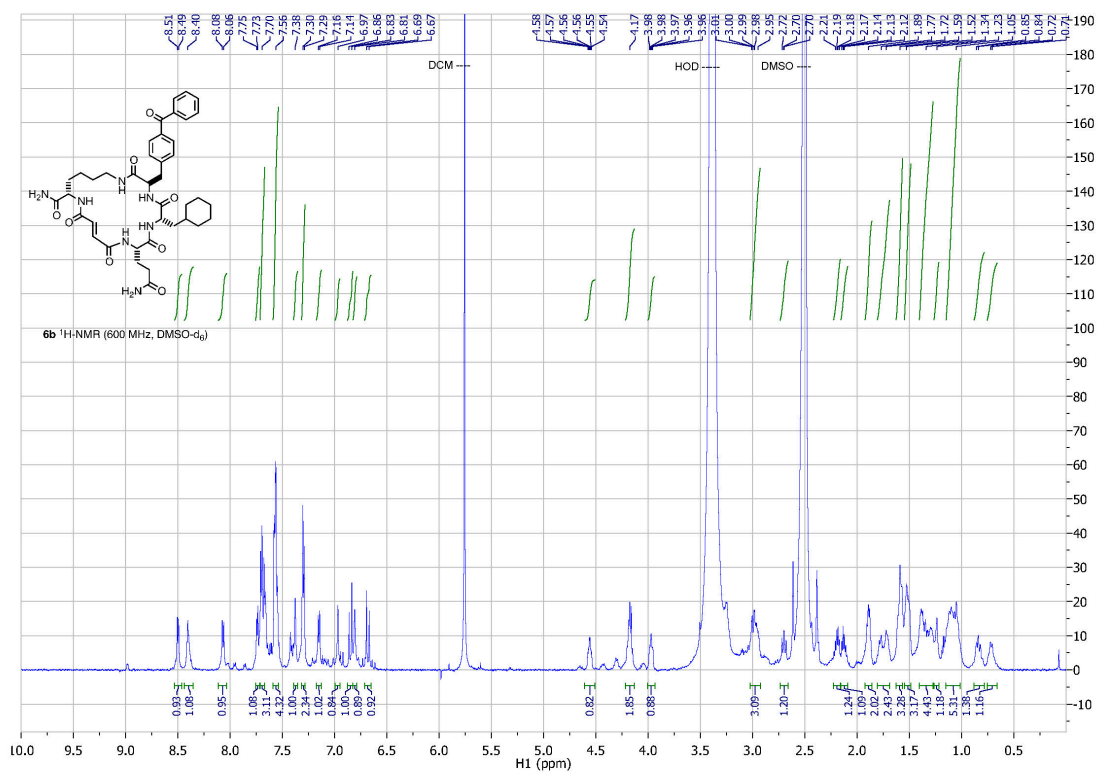


Figure 2.14 | Spectra for ¹H- and ¹³C-NMR of **6b**, **6bK**, and **bisepi-6bK**.


```

MRYRLAWLLHPALPSTFRSVLGARLPPPERLCGFQKKTYSKMNNPAIKRIGNHITKSPED 60 human IDE
MRNGLVWLLHPALPGTLRSILGARPPPAKLLCGFPKQTYSTMSNP AIQRIEDQIVKSPED 60 mouse IDE
** * .***** .:***:**** **.: **** *:***.*.*****:*** ::* .*****
KREYRGLELANGIKVLLISDPTTDKSSAALDVHIGSLSDPPNIAGLSHFCEHMLFLGTKK 120 human IDE
KREYRGLELANGIKVLLISDPTTDKSSAALDVHIGSLSDPPNIPGLSHFCEHMLFLGTKK 120 mouse IDE
*****.*****
YPKENEYSQFLSEHAGSSNAFTSGEHTNYYFDVSHHELEGALDRFAQFFLCPLFDESCKD 180 human IDE
YPKENEYSQFLSEHAGSSNAFTSGEHTNYYFDVSHHELEGALDRFAQFFLCPLFDASCKD 180 mouse IDE
***** ****
REVNAVDSEHEKNVMNDARWRLFQLEKATGNPKHPFSKFGTGNKYTLETRPNQEGIDVQR 240 human IDE
REVNAVDSEHEKNVMNDARWRLFQLEKATGNPKHPFSKFGTGNKYTLETRPNQEGIDVREE 240 mouse IDE
*****:*****
LLKFHSAYSSNLMAVCVGLGRESLDDLTLNVVKLFSEVENKNVPLPEFPEHPFQEEHLKQ 300 human IDE
LLKFHSTYYSSNLMAICVGLGRESLDDLTLNVVKLFSEVENKNVPLPEFPEHPFQEEHLRQ 300 mouse IDE
*****:*****:*****:*****
LYKIVPIKDIRNLYVTFFPIPDLQKYKSNPGHYLGHGHEGPGSLLSELKSKGWVNTLV 360 human IDE
LYKIVPIKDIRNLYVTFFPIPDLQYYKSNPGHYLGHGHEGPGSLLSELKSKGWVNTLV 360 mouse IDE
*****
GGQKEGARGFMFFIINVDLTEEGLLHVEDIILHMFQYIQKLR AEGPQEWVVFQECKDLNAV 420 human IDE
GGQKEGARGFMFFIINVDLTEEGLLHVEDIILHMFQYIQKLR AEGPQEWVVFQECKDLNAV 420 mouse IDE
*****
AFRFKDKERPRGYTSKIAGILHYYPLEEVLTAEYLL EEFRDPDIEMVLDKLRPENVRVAI 480 human IDE
AFRFKDKERPRGYTSKIAGKLYHYPPLNGVLTAEYLL EEFRDPDIDMVLDKLRPENVRVAI 480 mouse IDE
*****:*****
VSKSFEGKTDRETEWYGTQYKQEAIPDEVIKQWQADNLNGKFKLPTKNEFIPTNFEILPL 540 human IDE
VSKSFEGKTDRETEWYGTQYKQEAIPEDI IQWQADNLNGKFKLPTKNEFIPTNFEILSL 540 mouse IDE
*****:*****:*.*****
EKEATPYPALIKDTAMSKLWFKQDDKFFLPKACLNF EFFSPFAYVDPLHCNMAYLYLELL 600 human IDE
EKEATPYPALIKDTAMSKLWFKQDDKFFLPKACLNF EFFSPFAYVDPLHCNMAYLYLELL 600 mouse IDE
**.:*****
KDSLNEYAYAAELAGLSYDLQNTIYGYLSVKGYNDKQPI LLKKIIEKMATFEIDEKRFE 660 human IDE
KDSLNEYAYAAELAGLSYDLQNTIYGYLSVKGYNDKQPI LLKKITEKMATFEIDKKRFE 660 mouse IDE
*****:****
I I KEAYMRS LNNFRAEQPHQHAMY YLRLLMTEVAWTKDELKEALDDVTL PRLKAFIPQLL 720 human IDE
I I KEAYMRS LNNFRAEQPHQHAMY YLRLLMTEVAWTKDELKEALDDVTL PRLKAFIPQLL 720 mouse IDE
*****
SRLHIEALLHGNI TKQAALGIMQMVEDTLIEHAHTK PL LPSQLVRYREVQLPDRGWVYQ 780 human IDE
SRLHIEALLHGNI TKQAALGIMQMVEDTLIEHAHTK PL LPSQLVRYREVQLPDRGWVYQ 780 mouse IDE
*****
QRNEVHNNCGIEIYYQTD MQSTSENMFLELFCQI ISEPCFNTLRTKEQLGYIVFSGPRRA 840 human IDE
QRNEVHNNCGIEIYYQTD MQSTSENMFLELFCQI ISEPCFNTLRTKEQLGYIVFSGPRRA 840 mouse IDE
*****
NGIQGLRFIIQSEKPPHYLESRVEAFLITMEKSI EDMT EEFQKH I QALAIRRLDKPKKL 900 human IDE
NGIQGLRFIIQSEKPPHYLESRVEAFLITMEKAI EDMT EEFQKH I QALAIRRLDKPKKL 900 mouse IDE
*****
SAECAKYWGEI ISQQYNFDRDNTEVA YLKT LTKEDI IKFYKEMLAVDAPRRHKVSVHVLA 960 human IDE
SAECAKYWGEI ISQQYNFDRDNTEVA YLKT LTKDDI IRFYQEMLAVDAPRRHKVSVHVLA 960 mouse IDE
*****:**** *****:***:*.*****
REMDSCPVGGEFPCQNDINLSQAPALPQPEVIQNMTE FKRGLPLFPLVKPHINFMAAKL 1019 human IDE
REMDSCPVGGEFPCQNDINLSQAPALPQPEVIQNMTE FKRGLPLFPLVKPHINFMAAKL 1019 mouse IDE
*****.*****:*.*****:*****

```

Figure 2.15 | Alignment for human and mouse IDE sequences (95% identity), only 10/45 variations are predicted to have any impact on local structure. Aligned using CLUSTAL 2.1.

2.8 – References

- 1 Gartner, Z. J. *et al.* DNA-templated organic synthesis and selection of a library of macrocycles. *Science* **305**, 1601-1605, (2004).
- 2 Tse, B. N., Snyder, T. M., Shen, Y. & Liu, D. R. Translation of DNA into a library of 13,000 synthetic small-molecule macrocycles suitable for in vitro selection. *J Am Chem Soc* **130**, 15611-15626, (2008).
- 3 Kleiner, R. E., Dumelin, C. E., Tiu, G. C., Sakurai, K. & Liu, D. R. In vitro selection of a DNA-templated small-molecule library reveals a class of macrocyclic kinase inhibitors. *J Am Chem Soc* **132**, 11779-11791, (2010).
- 4 Georghiou, G., Kleiner, R. E., Pulkoski-Gross, M., Liu, D. R. & Seeliger, M. A. Development and structure-based mechanism of highly specific macrocyclic Src kinase inhibitors from a DNA-template library. *submitted*, (2011).
- 5 Kim, Y. G., Lone, A. M., Nolte, W. M. & Saghatelian, A. Peptidomics approach to elucidate the proteolytic regulation of bioactive peptides. *Proc Natl Acad Sci U S A* **109**, 8523-8527, (2012).
- 6 Workman, P. & Collins, I. Probing the probes: fitness factors for small molecule tools. *Chem Biol* **17**, 561-577, (2010).
- 7 Leissring, M. A. *et al.* Designed inhibitors of insulin-degrading enzyme regulate the catabolism and activity of insulin. *PLoS One* **5**, e10504, (2010).
- 8 Abdul-Hay, S. O. *et al.* Optimization of peptide hydroxamate inhibitors of insulin-degrading enzyme reveals marked substrate-selectivity. *J Med Chem* **56**, 2246-2255, (2013).
- 9 Saghatelian, A., Jessani, N., Joseph, A., Humphrey, M. & Cravatt, B. F. Activity-based probes for the proteomic profiling of metalloproteases. *Proc Natl Acad Sci U S A* **101**, 10000-10005, (2004).

- 10 Song, E. S., Rodgers, D. W. & Hersh, L. B. A monomeric variant of insulin degrading enzyme (IDE) loses its regulatory properties. *PLoS One* **5**, e9719, (2010).
- 11 Song, E. S., Rodgers, D. W. & Hersh, L. B. Mixed dimers of insulin-degrading enzyme reveal a cis activation mechanism. *J Biol Chem* **286**, 13852-13858, (2011).
- 12 Song, E. S., Cady, C., Fried, M. G. & Hersh, L. B. Proteolytic fragments of insulysin (IDE) retain substrate binding but lose allosteric regulation. *Biochemistry* **45**, 15085-15091, (2006).
- 13 Cornish-Bowden, A. A simple graphical method for determining the inhibition constants of mixed, uncompetitive and non-competitive inhibitors. *Biochem J* **137**, 143-144, (1974).
- 14 Schenker, P. & Baici, A. Simultaneous interaction of enzymes with two modifiers: reappraisal of kinetic models and new paradigms. *J Theor Biol* **261**, 318-329, (2009).
- 15 Malito, E. *et al.* Molecular Bases for the Recognition of Short Peptide Substrates and Cysteine-Directed Modifications of Human Insulin-Degrading Enzyme†. *Biochemistry* **47**, 12822-12834, (2008).
- 16 Malito, E., Hulse, R. E. & Tang, W. J. Amyloid beta-degrading cryptidases: insulin degrading enzyme, presequence peptidase, and neprilysin. *Cellular and molecular life sciences : CMLS* **65**, 2574-2585, (2008).
- 17 Shen, Y., Joachimiak, A., Rosner, M. R. & Tang, W. J. Structures of human insulin-degrading enzyme reveal a new substrate recognition mechanism. *Nature* **443**, 870-874, (2006).
- 18 Guo, Q., Manolopoulou, M., Bian, Y., Schilling, A. B. & Tang, W. J. Molecular basis for the recognition and cleavages of IGF-II, TGF-alpha, and amylin by human insulin-degrading enzyme. *J Mol Biol* **395**, 430-443, (2010).

- 19 Manolopoulou, M., Guo, Q., Malito, E., Schilling, A. B. & Tang, W. J. Molecular basis of catalytic chamber-assisted unfolding and cleavage of human insulin by human insulin-degrading enzyme. *J Biol Chem* **284**, 14177-14188, (2009).
- 20 Loge, C. *et al.* Novel 9-oxo-thiazolo[5,4-f]quinazoline-2-carbonitrile derivatives as dual cyclin-dependent kinase 1 (CDK1)/glycogen synthase kinase-3 (GSK-3) inhibitors: synthesis, biological evaluation and molecular modeling studies. *European journal of medicinal chemistry* **43**, 1469-1477, (2008).
- 21 Parker, M. G. & Weitzman, P. D. The regulation of *Acinetobacter* sp. alpha-oxoglutarate dehydrogenase complex. *Biochem J* **130**, 39P, (1972).
- 22 Vonrhein, C. *et al.* Data processing and analysis with the autoPROC toolbox. *Acta crystallographica. Section D, Biological crystallography* **67**, 293-302, (2011).
- 23 McCoy, A. J. *et al.* Phaser crystallographic software. *Journal of applied crystallography* **40**, 658-674, (2007).
- 24 Emsley, P. & Cowtan, K. Coot: model-building tools for molecular graphics. *Acta crystallographica. Section D, Biological crystallography* **60**, 2126-2132, (2004).
- 25 Adams, P. D. *et al.* PHENIX: a comprehensive Python-based system for macromolecular structure solution. *Acta Crystallographica Section D* **66**, 213-221, (2010).

Chapter 3

Development of the first physiologically active IDE inhibitor

Adapted from: Maianti *et al*, *Nature* **511**, 94–98 (2014).

Contributions: I designed and performed the experiments and pharmacokinetic measurements described in this chapter. Edwin A. Homan and Amanda K. McFedries assisted with *in vivo* experiments. Help from other colleagues is acknowledged in the text.

3.1 – Introduction (and spoiler alert)

This chapter aims to synthesize all the experimental evidence to evaluate the viability of **6bK** as a highly specific and physiologically active IDE inhibitor probe. In practice, the process of selecting and validating an *in vivo* probe candidate, among multiple analogs available, typically relies on the results of dose-response trials and phenotypic observations that are used to “build a case” for subsequent follow up studies with the molecule. For this reason, this chapter does not recount a linear timeline of experiments of increasing complexity, and specific observations such as glucose tolerance phenotypes are not concurrently rationalized in the text from a mechanistic point of view until the next chapter. The physiological functions of IDE are discussed in detail in Chapter 4.

In this study I followed the guidelines reviewed by Workman and Collins¹ to validate the suitability of an *in vivo* probe. *In vivo* probes must satisfy a number of biochemical and biophysical features, which significantly overlap but that are distinct from the properties of pharmaceutical drugs and drug-lead molecules (**Table 3.1**).¹

Table 3.1 | Distinct properties of pharmaceutical drugs, drug leads, and *in vivo* probes, compared to **6bK**. Adapted from reference 1.

Property	Pharmaceutical drugs	Drug leads	<i>In vivo</i> probes	6bK features
Aqueous solubility	>10–100 µg/ml	>10–100 µg/ml	>0.05 µg/ml in low % DMSO aqueous solutions	~0.5 mM / ~400 µg/mL in 1% DMSO
Membrane permeability	10× permeability of mannitol in CaCo-2 assay desirable; minimal PGP-mediated efflux	$P_e > 10^{-6} \text{ ms}^{-1}$ (in vitro assay); minimal PGP-mediated efflux	Permeability essential; minimal PGP-mediated efflux in cell lines of interest	Not applicable, IDE is an extracellular target
Chemically reactive groups	None present unless a well characterized and selective mechanistic requirement	None present unless a well characterized and selective mechanistic requirement	None present unless a well characterized and selective mechanistic requirement	See Figure 2.3
Molecular weight (Da)	<500–550	<350–450	Likely to be <450	758 Da
Lipophilicity (LogP)	<5	<4	Likely to be <5	<1 predicted
H-bond donors	= <5	<4–5	Likely to be <3	8
H-bond acceptors	= <10	<8–9	Likely to be <11	7
Rotatable bonds	= <10	<8	Likely to be <10	10
Potency (IC_{50} or K_i)	10^{-8} – 10^{-9} M	10^{-6} – 10^{-8} M	10^{-7} – 10^{-9} M	5×10^{-8} M
Ligand efficiency	NA	>0.3 kcal mol ⁻¹ atom ⁻¹ heavy	NA	NA
Target selectivity	Well-defined selectivity; polypharmacology acceptable	Well-defined selectivity; >10-fold over related targets; minimal activity on common off-targets	Well-defined selectivity; >10–100-fold against closely related targets; polypharmacology undesirable	>1000-fold selective for IDE, distal binding site not present in other metalloprotease enzymes
Pharmacokinetics	Well-defined therapeutic window and <i>in vivo</i> pharmacokinetics	Stable in microsomes; no CYP450 inhibition	Good pharmacokinetics not essential for <i>in vitro</i> and cellular use, but required for <i>in vivo</i> animal work	Determined in Chapter 3

3.2 – Biodistribution and pharmacokinetic properties of **6bK**

Theoretical studies predict that macrocyclic ligands are privileged structures for interacting with protein pockets and surfaces in complex biological mixtures.²⁻⁴ The degrees of freedom of rotatable bonds are decreased by covalently tying up a molecule in a medium-size macrocycle. In contrast to a linear molecule or peptidic scaffold of comparable structure, fewer low-energy conformations are accessible in solution or by interacting with proteins. The consequences of added rigidity include:

- i)* lower entropic cost for on-target binding interaction through an accessible low-energy conformation, which has a generally favorable impact on K_i values;
- ii)* higher selectivity, due to increased entropic cost of binding off-target sites when the accessible conformations cannot accommodate steric clashes with the protein;
- iii)* improved stability in the presence of proteases due to occlusion of labile bonds from nucleophile attack and/or carbonyl activation (as well as the effect of point *ii*).

To study the stability, physicochemical, and pharmacokinetic properties of **6bK** it was first necessary to produce milligram to gram quantities. I used the synthetic route shown in **Figure 3.1** to produce over 2 grams of **6bK** trifluoroacetate salt in 10–15% yield based on resin loading, relying on a single HPLC purification step.

In collaboration with Dr. Stephen Johnston at the Broad Institute we determined that **6bK** displayed significant stability during incubations with plasma and liver microsome preparations (74 % and 78 % remaining after 1 h, respectively), suggesting that this compound may be sufficiently stable *in vivo* to inhibit IDE activity (**Table 3.2**). Plasma protein binding assays indicated that ~6 % of **6bK**

remains unbound (**Table 3.2**) and potentially available to engage its target at sites of insulin degradation, extracellularly or in early endosome compartments of target tissues^{5,6}.

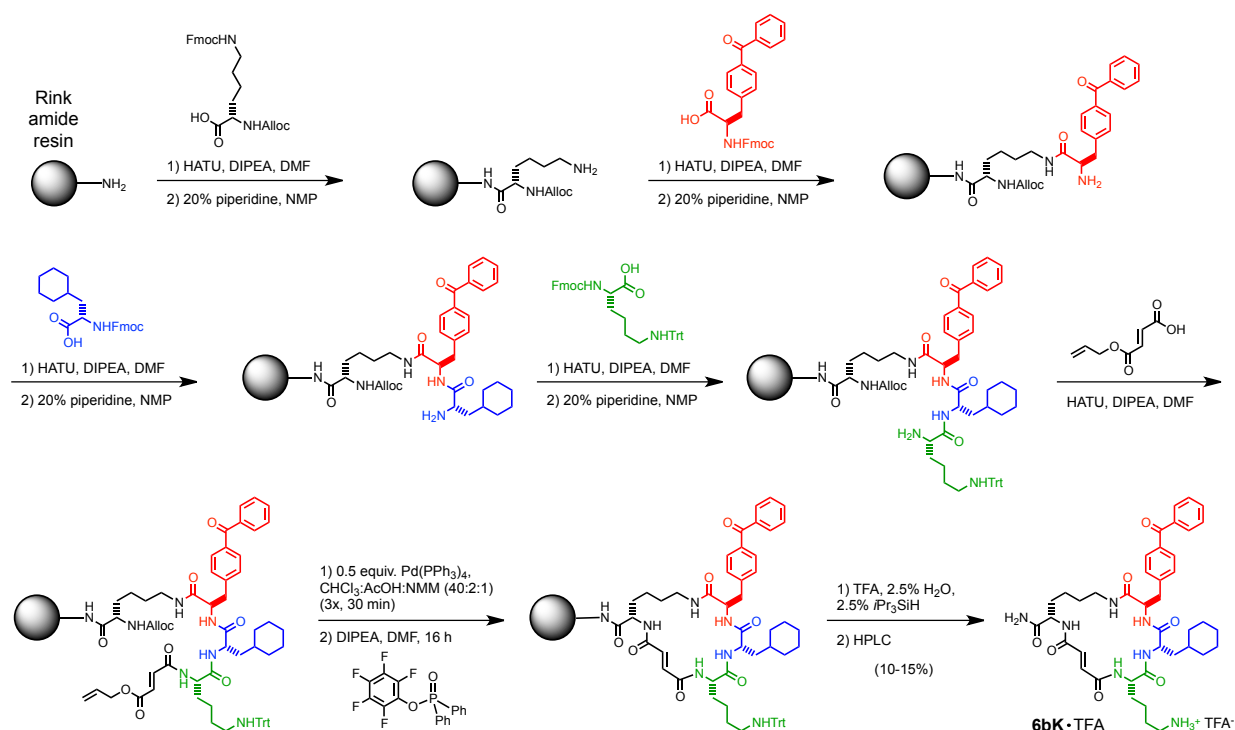


Figure 3.1 | Fmoc-based solid-supported synthesis of **6bK** followed by on-resin macrocyclization. This synthetic route is amenable to gram-scale production of **6bK** using a single purification step.

Table 3.2 | Plasma binding, plasma stability, and microsomal stability parameters for **6bK**. Data are averages of replicate results, Dr. Stephen Johnston (Broad Institute).

Sample	Plasma binding	Plasma Stability (1 h)	Microsomal stability (1 h)
mouse	94 %	74 %	78 %
human	86 %	83 %	80 %

To measure plasma half-life *in vivo*, we treated mice by intraperitoneal (i.p.) injection of 80 mg/kg **6bK** using a formulation of sterile saline and Captisol® (CyDex), a β -cyclodextrin-based agent used to improve solubilization and delivery⁷. The aqueous solubility of **6bK** is augmented more than 20-fold by formulation with Captisol®, simplifying the preparation of injection volumes such as 10 mL/kg (i.e. 250 μ L for a 25 g mouse) and providing reliable bioavailability through different preparations of **6bK**.

I observed that plasma and tissue concentrations of **6bK** could not be determined directly owing to non-specific losses during sample preparation (see Methods). Therefore, I used isotope-dilution mass spectrometry (IDMS) to account for these losses by spiking a ¹³C- and ¹⁵N-labeled **6bK** analog (**Figure 3.2**). In mice treated with **6bK**, the plasma levels of inhibitor were detectable within 5 min post-injection, reached peak concentration (> 100 μ M) at 60 min, and were maintained at a detectable level for at least 4 h (**Figure 3.2A**).

I observed prompt biodistribution of **6bK** into liver, kidney, and pancreatic tissues (**Figure 3.2B**). In contrast, **6bK** was undetectable in the brain of mice (within the limits of the LCMS assay and injection of 10-fold concentrated sample). This suggested the favorable feature of this macrocycle for proof-of-concept studies since it may not inhibit IDE within brain tissues, where IDE activity is needed for the clearance of β -amyloid peptides⁸. Indeed, brain tissue levels of A β (40) and A β (42) peptides in mice injected with **6bK** were unchanged 2 h-post injection compared to vehicle-treated controls (**Figure 3.2D**). While longitudinal studies may be needed,

this data is consistent with the inability of **6bK** to inhibit IDE in the brain during short-term administration.

Collectively, these measurements indicate that 80 mg/kg **6bK** treatment (2 mg/mouse) transiently achieves >100 to 1,000-fold IC_{50} levels of inhibitor in circulation and in liver and kidney, the main insulin-degrading organs, which suggest the viability of using **6bK** to inhibit IDE *in vivo*.

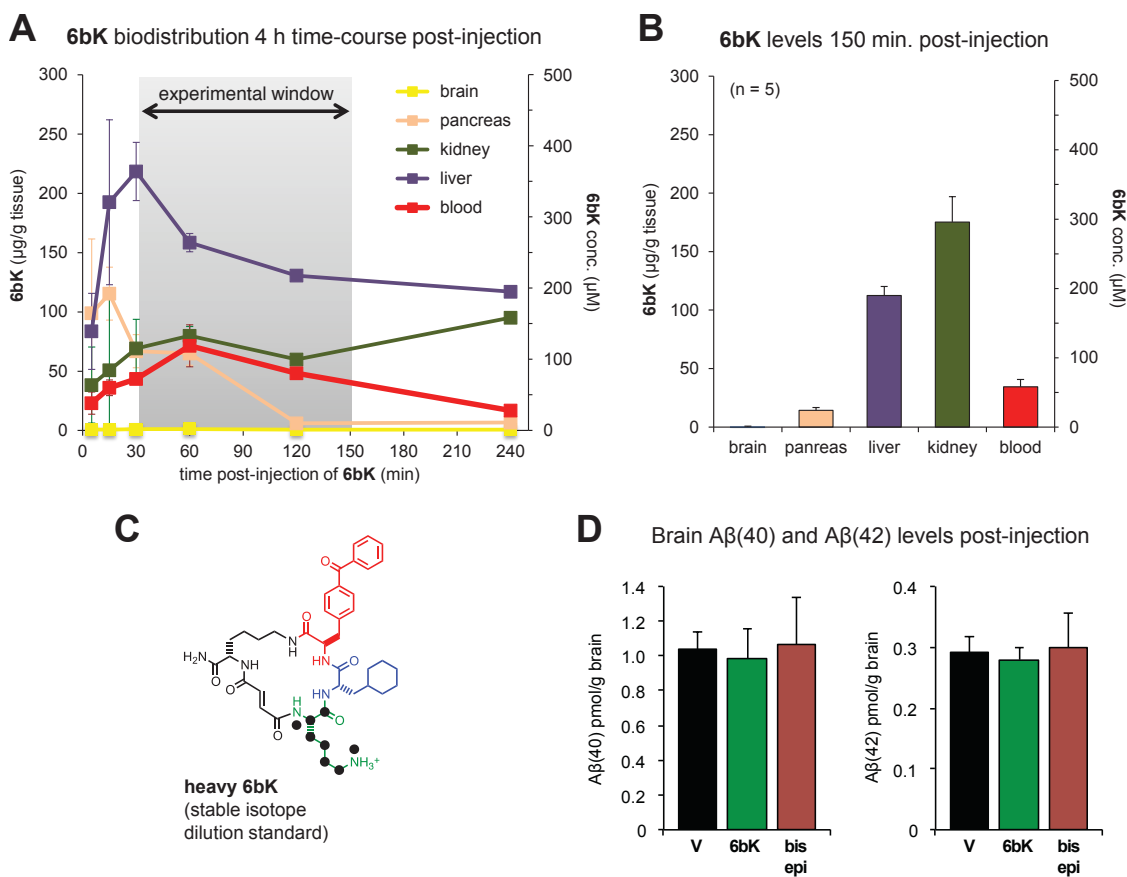


Figure 3.2 | Pharmacokinetic parameters of 6bK. (A) Concentration of **6bK** in mice tissues and plasma collected over 4 hours (n = 1-2). (B) Average biodistribution of **6bK** in five lean mice at 150 min post-injection of **6bK** 80 mg/kg i.p. at the endpoint of a IPGTT experiment. **6bK** was not detectable in the brain even using 10-fold concentrated samples

(**Figure 3.2 cont.**) for LC-MS injection compared to other tissues. (C) Heavy **6bK** was synthesized with ^{15}N , ^{13}C -lysine for stable-isotope dilution LC-MS quantitation. (D) Treatment of C57BL/6J lean mice with **6bK** (■, 80 mg/kg, n = 6) does not change brain levels of A β (40) or A β (42) peptides in the brain 2 h post injection compared to treatment with vehicle alone (■, n = 5) or inactive diastereomer **bisepi-6bK** (■, 80 mg/kg, n = 6). All data points and error bars represent mean \pm SEM.

3.3 – Augmentation of insulin hypoglycemic effects and abundance by IDE inhibition *in vivo*

Our experiments determined the circulation time of **6bK** is within the timescale for standard physiological experiments with live animals.^{9,10} In particular we identified reliable exposure to **6bK** in >100 IC₅₀ levels during the period 30–150 min post-injection (**Figure 3.2A**). To evaluate the ability of **6bK** to inhibit IDE activity *in vivo* we subjected non-fasted mice to insulin tolerance tests (ITT)¹⁰ following a single injection with **6bK** (80 mg/kg) formulated in Captisol®⁷. The insulin injections were carried out 30 min post-injection, corresponding to the time before the highest **6bK** concentration in plasma (approximately 100 μM , ~1000-fold the IC₅₀ for mouse IDE). Following a subcutaneous insulin injection, mice treated with **6bK** experienced lower hypoglycemia and higher insulin levels compared to vehicle controls ($p < 0.01$, **Figure 3.3A**). At a later time, we repeated this ITT experiment using a quarter dose of insulin injection to elicit a less pronounced hypoglycemic effect and we observed identical results (**Figure 3.3B**). In 1955, Arthur Mirsky used a similar ITT assay to suggest the feasibility of insulin stabilization by injecting rats

and mice with preparations of an undefined endogenous IDE inhibitor crudely fractionated from bovine livers (presumably a competitive substrate; **Table 1.2**)^{11,12}. With our current understanding of the biochemistry and physiological roles of IDE it would be worthwhile to identify this putative “endogenous” inhibitor in the future.

Our experiments with **6bK** provide the first evidence that a well-defined, selective, and physiologically stable pharmacological IDE inhibitor can augment the abundance and activity of insulin *in vivo* (**Figure 3.3**).

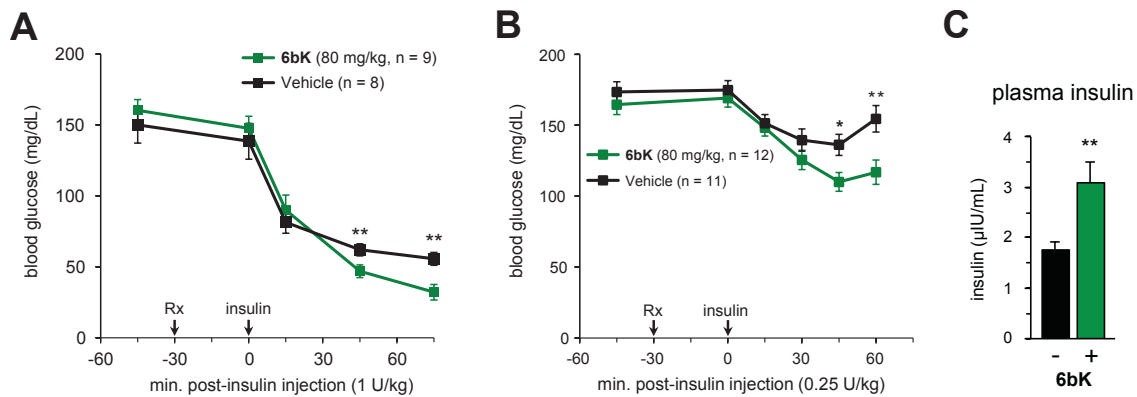


Figure 3.3 | Acute IDE inhibition affects the abundance and hypoglycemic action of insulin. (A and B) Blood glucose responses and abundance of injected insulin (Humulin-R) in lean mice 30 min after treatment with **6bK** (■, 80 mg/kg) or vehicle alone (■). (A) Insulin i.p. (1 U/kg) after 5-hour fast. (B) Insulin s.c. (0.25 U/kg) after 5-hour fast. (C) Trunk blood was collected at the last time point of this experiment for plasma hormone measurements. All data points and error bars represent mean ± SEM. Significance tests were performed using two-tail Student’s t-test, and significance levels shown are $p < 0.05$ (*) or $p < 0.01$ (**) versus the vehicle-only control group.

3.4 – IDE inhibitor activity- and dose-response in glucose tolerance tests

Experiments that rely on the administration of substrate exogenously are subject to some of the caveats of *in vitro* cleavage assays (Chapter 1, Section 1.2). The supra-physiological concentrations (>10-100-fold basal levels) can overwhelm endogenous degradation pathways, producing measurements that are not relevant to the physiological function of the hormone. Moreover, the phenotype of a hormonal treatment can depend on overall dose, rate and/or route of administration¹³⁻¹⁸.

To explore the effect of acute IDE inhibition on endogenously elicited hormone signaling under physiologically relevant conditions we first turned to glucose challenges, which are standard for animal experimentation^{9,19-22}, and for diagnosis of insulin resistance in human patients²³⁻²⁶. It is worth noting that mice treated with **6bK** (80 mg/kg) but not given a glucose challenge do not display significant changes in baseline glucose or basal hormone levels compared to vehicle controls (**Figure 3.4**), suggesting this approach cannot be used to study IDE physiology on basal hormone levels. Compensatory pancreatic hormone feedback and/or redundant degradation pathways potentially overshadow any impact of IDE inhibition on basal levels of insulin, glucagon, or amylin²⁷⁻²⁹.

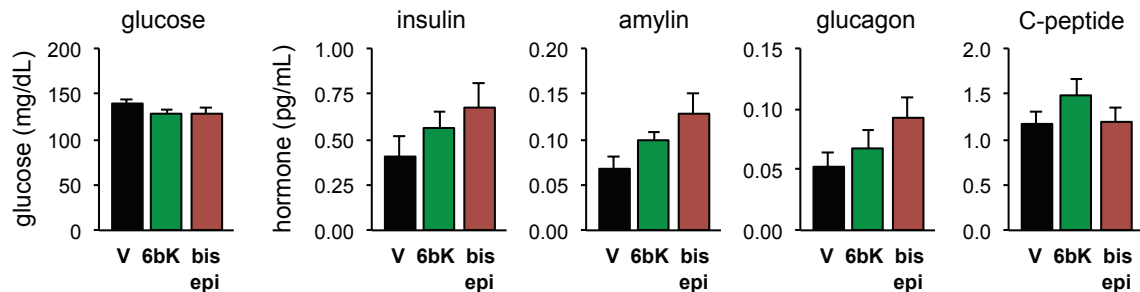


Figure 3.4 | Administration of **6bK** (■, 80 mg/kg) to lean mice not followed by injection of a nutrient such as glucose (or pyruvate; see Figure 4.8) did not significantly alter basal blood glucose or basal hormone levels compared to **bisepi-6bK** (■) or vehicle controls (■) 30 min post-injection. C-peptide is an inactive marker of β -cell secretion of insulin and amylin used as a control. All data points and error bars represent mean \pm SEM.

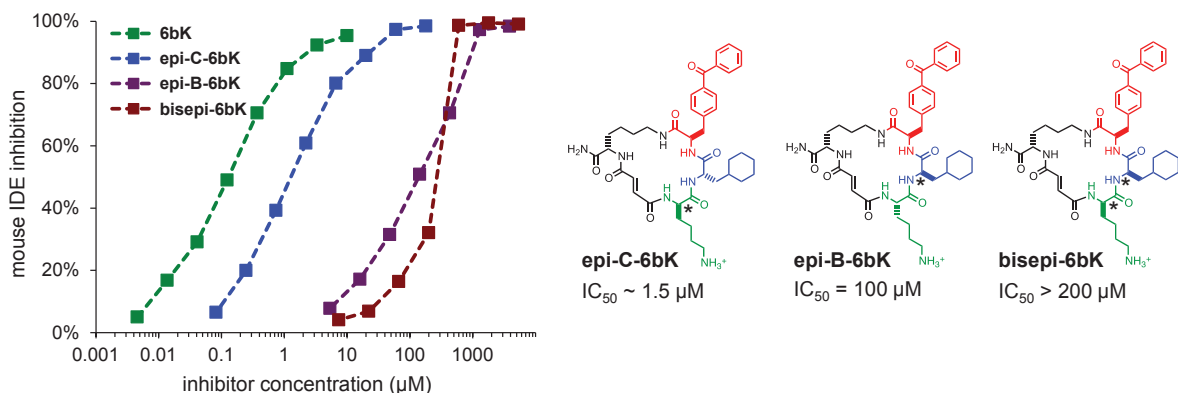


Figure 3.5 | **Low-potency diastereomers of 6bK.** Inhibition of mouse IDE activity by low potency diastereomers of **6bK**. The stereocenters altered in each compound relative to those of **6bK** are labeled with a star.

In order to corroborate that our phenotypic observations during glucose tolerance tests were due to on-target IDE inhibition I synthesized epimers of **6bK** of diminished inhibitory potency to use as *in vivo* controls (**Figure 3.5**). For most *in*

in vivo studies we favored the analog with two stereochemical changes on building block B and C, called **bisepi-6bK**, which is thus identical to **6bK** in chemical composition and bond connectivity, but is essentially inactive as an IDE inhibitor ($IC_{50} > 200 \mu M$, **Figure 3.5**). This control is also superior in lacking any potential contamination with **6bK** arising from enantiomeric impurities in commercial Fmoc-amino acids, or from α -carbon racemization during amide coupling (**Figure 3.1**).

Testing **6bK** at several doses, in parallel with the low-activity controls (**Figure 3.6**), led us to establish that the effective dose of **6bK** is approximately 2 mg/mouse *i.p.*, representing 80 mg/kg for lean C57BL/6J mice (25 g), and 60 mg/kg for diet-induced obese (DIO) mice (35-45 g). In particular, we performed numerous dose-response relationship experiments during *i.p.* glucose tolerance tests (IPGTT) studies using lean and DIO mice. We observed the phenotypic changes in glucose profiles were dependent on **6bK** dose, and no effects were observed in cohorts treated with vehicle alone or inactive **bisepi-6bK**, indicating that the both glucose tolerance effects correlate with IDE activity (**Figure 3.6**, and see **Figure 4.2** for optimal dose). We observed that doses below 1.5 mg/mouse **6bK** led to variable glucose profiles towards the end of the experiments, whereas doses above 4 mg/mouse were not well tolerated, producing lethargy.

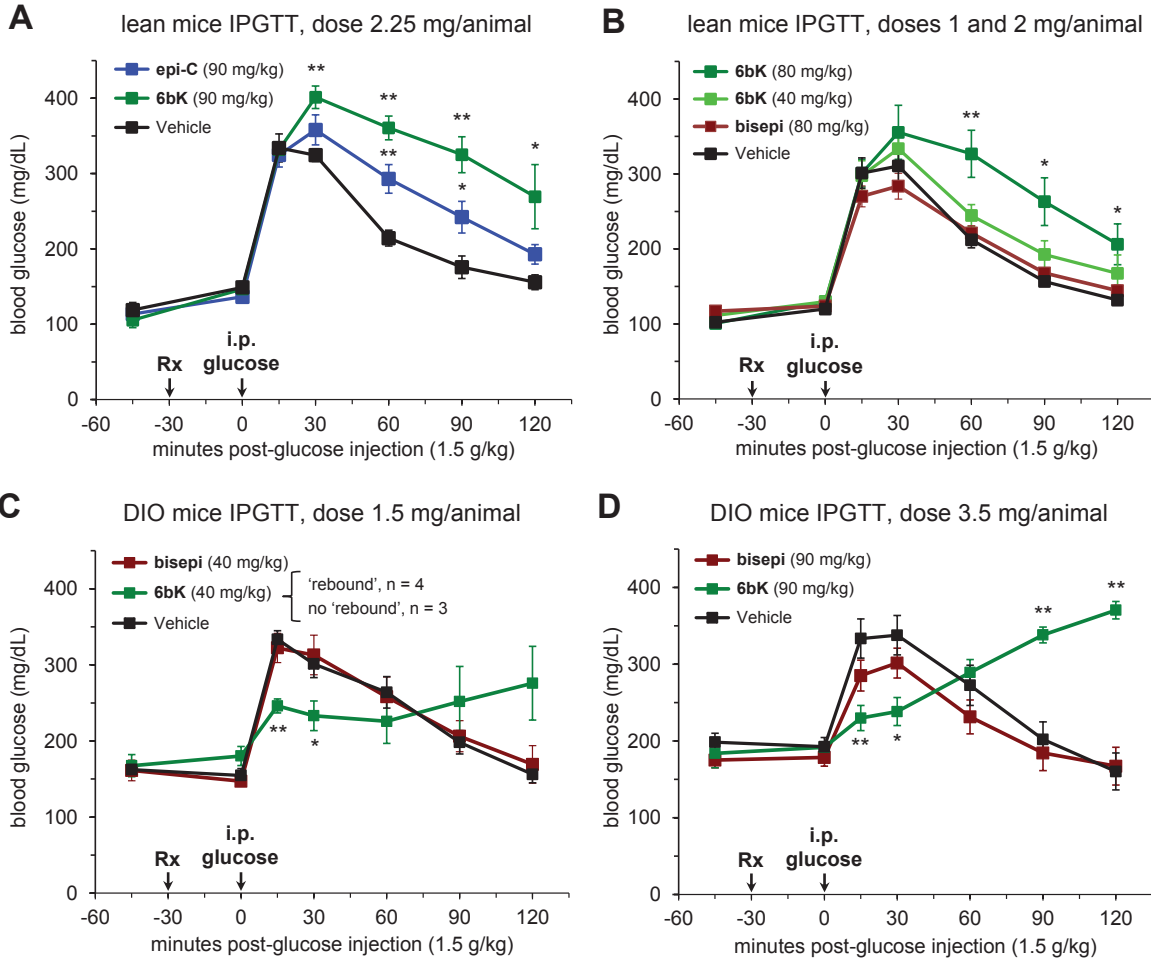


Figure 3.6 | Low-potency diastereomers of 6bK used to determine the effective dose range and confirm on-target IDE inhibition effects during IPGTTs in lean and DIO mice. (A to E) In dose optimization experiments the effects of **6bK** (■, 90 to 40 mg/kg) were compared with equal doses of either weakly active stereoisomer **epi-C-6bK** (■) or inactive stereoisomer **bisepi-6bK** (■) and vehicle controls (■) in IPGTTs using lean and obese mice. DIO mice treated with low doses of **6bK** (■, 40 mg/kg) responded to IPGTT in either of two ways: improved glucose tolerance throughout the experiment (n = 3) or a hyperglycemic rebound as described in the main text (n = 4), suggesting this dose is too low to achieve a consistent effect (note the large error bars). DIO mice treated with high doses of **6bK** (■, 3.5 mg/animal, 90 mg/kg) respond similarly to Figure 4.4 (2 mg/animal, 60 mg/kg), but the weak activity observed for **bisepi-6bK** ($IC_{50} > 100 \mu M$) using a matching dose (■, 90 mg/kg) compared to vehicle alone (■) suggests that 60 mg/kg (2 mg/animal) is an

(**Figure 3.6 cont.**) appropriate dose for DIO mice experiments. All data points and error bars represent mean \pm SEM. Statistics were performed using a two-tail Student's t-test, and significance levels shown in the figures are * $p < 0.05$ versus vehicle control group; ** $p < 0.01$ versus vehicle control group.

3.5 – Features and limitations of **6bK** as an *in vivo* probe

In conclusion, we determined the dose of **6bK** inhibitor that produces reliable effects on insulin hypoglycemic action as well as glucose tolerance, which is also well tolerated, did not produce adverse reactions, and did not induce body weight loss or detectable behavioral abnormalities (**Figure 3.7A–B**). We showed that **6bK** treatment transiently achieves >100 to 1,000-fold IC_{50} levels of inhibitor in the peripheral organs responsible for insulin degradation, which suggests the viability of **6bK** as a potential *in vivo* IDE inhibitor probe to study the physiological roles of this enzyme. The features of **6bK** are summarized in **Table 3.3**¹.

The **6bK** validation presented in this work is limited to short terminal experiments using a single dose of the experimental agent, which is in accordance with the standing committee on the Use of Animals in Research and Teaching at Harvard University (see Methods section). The optimal dose of **6bK** was determined for mice of the C57BL/6J genetic background (Jackson Laboratories). Deviations from the procedures described herein may require revalidation of the IDE on-target effects using the appropriate injection controls, dose-response analysis, as well as IDE^{-/-} knockout mice (described in Chapter 4). Similarly, we have not determined if

non-specific off-target effects may appear in repeated once-daily dosing or using chronic administration paradigms due to accumulation of **6bK** or other metabolites.

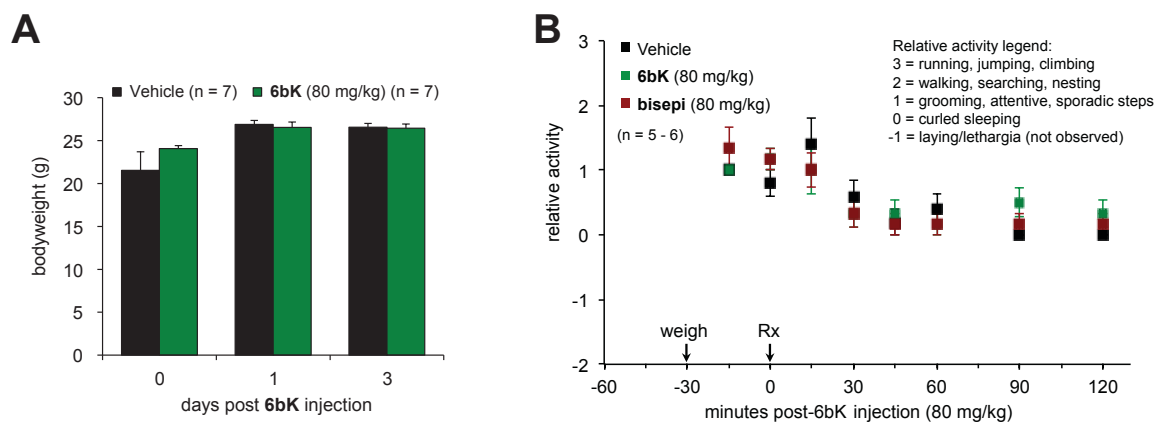


Figure 3.7 | Acute treatment with 6bK is well tolerated. (A) Body weight measurements for C57BL/6J mice treated with **6bK** (■, 80 mg/kg i.p.) or vehicle alone (■). (B) Behavioral scoring observations during a typical experiment. Mice treated with **6bK** (■, 80 mg/kg) are active, display normal posture, normal grooming, and response to stimulation, compared to vehicle controls (■). All data points and error bars represent mean \pm SEM.

Table 3.3 | The features of **6bK** satisfy the requirements for an *in vivo* probe¹.

Adapted from reference 1.

Chemistry		6bK
Structure	Discrete chemical species, characterized spectroscopically; Defined structure with reproducible preparative method	✓ Fig. 3.1
Stability	Defined purity and stability in test media; Free from non-specific chemical reactivity	✓ Table 3.2
Solubility	Sufficiently soluble in aqueous media; e.g. >100 μM; No aggregation effects in biochemical assays	✓ Fig. 2.4-6
Permeability	Proven passive membrane permeability, or define active transport mechanisms	n/a, target is extracellular
Potency		
Biochemical	Typically <100 nM in an <i>in vitro</i> biochemical assay; Sufficient to confidently associate with cellular activity	✓ Fig. 2.4-5
Cellular	Typically <1-10 μM in a mechanistic cell-based assay; Sufficient to confidently address hypotheses in cells; Concentration-dependent effect on the biological target	✓ Fig. 2.6
Analogs	Closely related structures identified with similar activity; Correlation of biochemical target activity and activity in cells; Correlation of biomarkers of target modulation with biochemical and cellular potency	✓ Fig. 2.8 Fig. 3.5 Fig. 3.6
In vivo	Pharmacokinetic properties sufficient to achieve levels in target tissue relevant to cellular potency	✓ Fig. 3.2-3
Selectivity		
Profile	Defined selectivity for related targets or known targets of chemotype; Typically >10-100 fold in biochemical assay; typically >50 kinases profiled for kinase inhibitors; broader pharmacology profiling desirable	✓ >1000-fold Fig. 2.9
Inactive analog	Analog with no biochemical target activity shows no activity in cells	✓ Fig. 3.6
Other chemotypes	Probes from a different chemical class with similar activity	✓ e.g. Ii1
Chemo-informatics	Awareness of other activities associated with the chemical class	✓ Fig. 3.2-3
Context		
Genetic methods	RNAi and/or mutants of target available for complimentary experiments	✓ IDE ^{-/-} mice
Target	Cellular context of the target and potential linked activities considered	✓ Fig. 3.3-6
Application	Fitness of the probe to test the specific biological hypothesis considered	✓ Section 3.3-4
Availability	Origin, identity and properties fully disclosed; Available for use without restrictions; Accessible in quantities (15-20 mg) for follow-up studies	✓ Fig. 3.1 >2 g made

3.6 – Methods

Dosing and formulation of macrocycle inhibitors for *in vivo* studies.

The doses of **6bK** used in this study were chosen based on literature precedent for small molecules and drugs of similar potencies^{2,30-35}. Procedures using experimental compounds were in accordance with the standing committee on the Use of Animals in Research and Teaching at Harvard University, the guidelines and rules established by the Faculty of Arts and Sciences' Institutional Animal Care and Use Committee (IACUC), and the National Institutes of Health Guidelines for the Humane Treatment of Laboratory Animals.

Purified macrocycle inhibitors were dissolved in DMSO-*d*₆ (~200 to 250 mg/mL stock solutions). A sample aliquot (5 μL) of the macrocycle solution was diluted with 445 μL DMSO-*d*₆, then combined with 50 μL of freshly prepared solution of 20 mM CH₂Cl₂ in DMSO-*d*₆ in for ¹H-NMR acquisition (600 MHz, relaxation time = 2 sec). The inhibitor concentration was calculated using the integral of the CH₂Cl₂ singlet (δ 5.76 ppm, 2H)³⁶, which appears in an uncluttered region of these spectra^{37,38}. For injectable formulations (10 mL/kg i.p. injection volume), the macrocycle inhibitor solution in DMSO-*d*₆ (200 – 250 mg/mL, based on free-base molecular weight) was combined with 1:20 w/w Captisol® powder (CyDex)⁷. The resulting slurry was supplemented with DMSO-*d*₆ to make up to 5 % of the final formulation volume, mixed thoroughly and dissolved with sterile saline solution (0.9 % NaCl). Vehicle controls were identically formulated with 5 % DMSO-*d*₆ and equal amount of Captisol®. The formulated solutions of inhibitor

were clear with no visible particles, and were stored overnight at 4 °C prior to injection.

Stable isotope dilution LC-MS, pharmacokinetics, and tissue distribution

measurements. Heavy-labeled macrocycle inhibitor (**heavy-6bK**) was synthesized as described above, substituting “building block C” with *N*^α-Fmoc-*N*^ε-Boc-lysine ¹³C₆ ¹⁵N₂ (98 atom %, Sigma-Aldrich). The product was 8 mass-units heavier than **6bK**, otherwise with identical properties and IC₅₀. Plasma samples (15 μL) from **6bK**-treated mice and vehicle controls were combined with 5 μL of **heavy-6bK** in PBS (final concentration of 10 μM), and incubated for 30 min on ice. Plasma proteins were precipitated with 180 μL cold 1 % TFA in MeCN, sonicated 2 min, and centrifuged 13,000 g for 1 min. The supernatant was diluted 100- and 1000-fold for liquid chromatography-mass spectrometry (LC-MS) analysis. Tissue samples (~100 mg) from **6bK**-treated mice and vehicle controls were weighed and disrupted in Dounce homogenizers with PBS buffer (0.5 mL/100 mg sample), supplemented with 5 μM **heavy-6bK** and protease inhibitor cocktail (1 tablet/50 mL PBS, Roche diagnostics). The lysate was incubated on ice for 30 min, sonicated 5 min and centrifuged at 13,000 g for 5 min. The bulk of supernatant proteins were precipitated by denaturation at 95 °C for 5 min, removed by centrifugation. A 50 μL aliquot of the supernatant was treated with 450 μL cold 1 % TFA in MeCN, cleared by centrifugation and diluted 100-fold for LC-MS analysis as described above for plasma samples. A standard curve of **6bK** and **heavy-6bK** (1 μM each and 3-fold

serial dilutions) were used for LC-MS quantitation using a Waters Q-TOF premier instrument.

In vivo studies, general information. Wild-type C57BL/6J and diet-induced obese (DIO) C57BL/6J age-matched male adult mice were purchased from Jackson Laboratories. The age range was 13 to 15 weeks for lean mice, and 24 to 26 weeks for DIO mice. All animals were individually housed on a 14-h light, 10-h dark schedule at the Biology Research Infrastructure (BRI), Harvard University. Cage enrichment included cotton bedding and a red plastic hut. Water and food were available *ad libitum*, consisting respectively of normal chow (Prolab® RHM 3000) or high-fat diet (60 kcal % fat, D12492, Research Diets Inc.). Adult IDE knock-out mice (IDE^{-/-}) fully back-crossed to the C67BL/6J line were obtained from Mayo Clinic (Florida), and housed in the Biology Research Infrastructure (BRI), Harvard University, for 8 weeks prior to experiments as described above, and experiments were conducted on age-matched mice cohorts ranging 17 to 21 weeks old. All animal care and experimental procedures were in accordance with the standing committee on the Use of Animals in Research and Teaching at Harvard University, the guidelines and rules established by the Faculty of Arts and Sciences' Institutional Animal Care and Use Committee (IACUC), and the National Institutes of Health Guidelines for the Humane Treatment of Laboratory Animals. Power analysis to determine animal cohort numbers was based on preliminary results and literature precedent, usually requiring between 5 and 8 animals per group. Animals were only

excluded from the cohorts in cases when we identified occasional DIO mice with an outlier diabetic phenotype (e.g. >200 mg/dL fasting blood glucose). Age- and weight-matched mice were randomized to each treatment group.

Glucose tolerance tests GTT and blood glucose measurements. Prior to a glucose challenge, the animals were fasted for 14 h (8 pm to 10 am, during the dark cycle) while individually housed in a clean cage with inedible wood-chip as a floor substrate, cotton bedding and a red plastic hut. Inhibitor, vehicle or control compounds were administered by a single intraperitoneal (i.p.) injection 30 min prior to the glucose challenge. Dextrose was formulated in sterile saline (3 g in 10 mL total), and the dose was adjusted by fasted body weight. For IPGTTs, 1.5 g/kg dextrose was administered by i.p. injection at a dose of 5 mL/kg. Blood glucose was measured using AccuCheck® meters (Aviva) from blood droplets obtained from a small nick at the tip of the tail, at timepoints -45, 0, 15, 30, 45, 60, 90 and 120 min with reference to the time of glucose injection. The area of the blood glucose response profile curve corresponding to each animal was calculated by the trapezoid method⁹, using as reference each individual baseline blood glucose measurement prior to glucose administration ($t = 0$) or the lowest point of the curve. The sum of the trapezoidal areas between the 0, 15, 30, 45, 60, 90 and 120 minute time points corresponding to each animal were summed to obtain the area under the curve (AUC). The relative area values are expressed as a percentage relative to the average AUC of the vehicle cohort, which is defined as 100 %. Values are reported as mean \pm

S.E.M. Statistics were performed using a two-tail Student's t-test, and significance levels shown in the figures are * $p < 0.05$ versus vehicle control group or ** $p < 0.01$ versus vehicle control group unless otherwise stated.

Insulin Tolerance Test (ITT). For hormone challenges animals were fasted individually housed as described above. For ITT the fasting period was 6 h (7 am to 1 pm). Inhibitor or vehicle alone was injected i.p. as previously described, 30 min prior to the hormone challenge. Insulin (Humulin-R®, Eli Lilly) was injected subcutaneously (s.c.) 0.25 U/kg or intraperitoneally i.p. 1 U/kg formulated in sterile saline (5 mL/kg). Blood glucose was measured at timepoints -45, 0, 15, 30, 45, 60 and 75 min with reference to the time of hormone injection, by microsampling from a tail nick as described above. Values are reported as mean \pm S.E.M. Statistics were performed using a two-tail Student's t-test, and significance levels shown in the figures are * $p < 0.05$ versus vehicle control group or ** $p < 0.01$ versus vehicle control group.

Blood collection and plasma hormone measurements. Blood was collected in EDTA-coated tubes (BD Microtainer®) from trunk bleeding (~500 μ L) after CO₂-euthanasia for all hormone assays. The plasma was immediately separated from red blood cells by centrifugation 10 min at 1800 g, aliquoted, frozen over dry ice and stored at -80 °C. Insulin, glucagon, amylin and pro-insulin C-peptide fragment were quantified from 10 μ L plasma samples using magnetic-bead Multiplexed Mouse

Metabolic Hormone panel (Milliplex, EMD Millipore) according to the manufacturer's instructions, using a Luminex FlexMap 3D instrument. Plasma containing high levels of human insulin (Humulin-R) were quantified using 25 μ L samples with Insulin Ultrasensitive ELISA (ALPCO). Values are reported as mean \pm S.E.M. Statistics were performed using a two-tail Student's t-test, and significance levels shown in the figures are * $p < 0.05$ versus vehicle control group or ** $p < 0.01$ versus vehicle control group.

Amyloid peptide measurements. Lean C57BL/6J mice were treated with **6bK** (80 mg/kg), vehicle alone, or **bisepi-6bK** (80 mg/kg). Two hours post-injection, hemibrains were promptly dissected after CO₂-euthanasia and stored at -80 °C until extraction. A hemibrain (~150 mg wet weight) was homogenized in a Dounce homogenizer in 0.2% diethylamine and 50 mM NaCl (900 μ L). The homogenate was centrifuged at 20,000 \times g for 1 h at 4°C to remove insoluble material. A fraction of supernatant (100 μ L) was neutralized with 1:10 volume of Tris HCl, pH 6.8. The sample was diluted 1:4 in assay buffer, and analyzed for A β (40) and A β (42) levels using the respective A β ELISA assays (Invitrogen) following the manufacturer's protocols.

3.7 – References

- 1 Workman, P. & Collins, I. Probing the probes: fitness factors for small molecule tools. *Chem Biol* **17**, 561-577, (2010).
- 2 Cherney, R. J. *et al.* Macrocyclic amino carboxylates as selective MMP-8 inhibitors. *J Med Chem* **41**, 1749-1751, (1998).
- 3 Driggers, E. M., Hale, S. P., Lee, J. & Terrett, N. K. The exploration of macrocycles for drug discovery--an underexploited structural class. *Nat Rev Drug Discov* **7**, 608-624, (2008).
- 4 Wessjohann, L. A., Ruijter, E., Garcia-Rivera, D. & Brandt, W. What can a chemist learn from nature's macrocycles?--a brief, conceptual view. *Mol Divers* **9**, 171-186, (2005).
- 5 Duckworth, W. C., Bennett, R. G. & Hamel, F. G. Insulin degradation: progress and potential. *Endocr Rev* **19**, 608-624, (1998).
- 6 Leissring, M. A. *et al.* Designed inhibitors of insulin-degrading enzyme regulate the catabolism and activity of insulin. *PLoS One* **5**, e10504, (2010).
- 7 Stella, V. J. & He, Q. Cyclodextrins. *Toxicologic pathology* **36**, 30-42, (2008).
- 8 Farris, W. *et al.* Insulin-degrading enzyme regulates the levels of insulin, amyloid beta-protein, and the beta-amyloid precursor protein intracellular domain in vivo. *Proc Natl Acad Sci U S A* **100**, 4162-4167, (2003).
- 9 Andrikopoulos, S., Blair, A. R., Deluca, N., Fam, B. C. & Proietto, J. Evaluating the glucose tolerance test in mice. *American journal of physiology. Endocrinology and metabolism* **295**, E1323-1332, (2008).
- 10 Rana, K. *et al.* Increased adiposity in DNA binding-dependent androgen receptor knockout male mice associated with decreased voluntary activity and not insulin resistance. *American journal of physiology. Endocrinology and metabolism* **301**, E767-778, (2011).

- 11 Yamato, M. *et al.* High-fat diet-induced obesity and insulin resistance were ameliorated via enhanced fecal bile acid excretion in tumor necrosis factor-alpha receptor knockout mice. *Molecular and cellular biochemistry* **359**, 161-167, (2012).
- 12 Mirsky, I. A., Perisutti, G. & Diengott, D. Effect of insulinase-inhibitor on destruction of insulin by intact mouse. *Proc Soc Exp Biol Med* **88**, 76-78, (1955).
- 13 Molina, J. M., Cooper, G. J., Leighton, B. & Olefsky, J. M. Induction of insulin resistance in vivo by amylin and calcitonin gene-related peptide. *Diabetes* **39**, 260-265, (1990).
- 14 Kolterman, O. G., Gottlieb, A., Moyses, C. & Colburn, W. Reduction of postprandial hyperglycemia in subjects with IDDM by intravenous infusion of AC137, a human amylin analogue. *Diabetes Care* **18**, 1179-1182, (1995).
- 15 Young, A. Effects on plasma glucose and lactate. *Adv Pharmacol* **52**, 193-208, (2005).
- 16 Young, A. Inhibition of glucagon secretion. *Adv Pharmacol* **52**, 151-171, (2005).
- 17 Young, A. A., Cooper, G. J., Carlo, P., Rink, T. J. & Wang, M. W. Response to intravenous injections of amylin and glucagon in fasted, fed, and hypoglycemic rats. *The American journal of physiology* **264**, E943-950, (1993).
- 18 Young, A. A., Rink, T. J. & Wang, M. W. Dose response characteristics for the hyperglycemic, hyperlactemic, hypotensive and hypocalcemic actions of amylin and calcitonin gene-related peptide-I (CGRP alpha) in the fasted, anaesthetized rat. *Life sciences* **52**, 1717-1726, (1993).
- 19 Ahren, B., Holst, J. J., Martensson, H. & Balkan, B. Improved glucose tolerance and insulin secretion by inhibition of dipeptidyl peptidase IV in mice. *European journal of pharmacology* **404**, 239-245, (2000).

- 20 Surwit, R. S., Kuhn, C. M., Cochrane, C., McCubbin, J. A. & Feinglos, M. N. Diet-induced type II diabetes in C57BL/6J mice. *Diabetes* **37**, 1163-1167, (1988).
- 21 Winzell, M. S. & Ahren, B. The high-fat diet-fed mouse: a model for studying mechanisms and treatment of impaired glucose tolerance and type 2 diabetes. *Diabetes* **53 Suppl 3**, S215-219, (2004).
- 22 Ahren, B., Winzell, M. S. & Pacini, G. The augmenting effect on insulin secretion by oral versus intravenous glucose is exaggerated by high-fat diet in mice. *The Journal of endocrinology* **197**, 181-187, (2008).
- 23 Mazzola, N. Review of current and emerging therapies in type 2 diabetes mellitus. *The American journal of managed care* **18**, S17-26, (2012).
- 24 Mooradian, A. D. & Thurman, J. E. Drug therapy of postprandial hyperglycaemia. *Drugs* **57**, 19-29, (1999).
- 25 Nielsen, L. L. Incretin mimetics and DPP-IV inhibitors for the treatment of type 2 diabetes. *Drug Discov Today* **10**, 703-710, (2005).
- 26 Bock, G. *et al.* Pathogenesis of pre-diabetes: mechanisms of fasting and postprandial hyperglycemia in people with impaired fasting glucose and/or impaired glucose tolerance. *Diabetes* **55**, 3536-3549, (2006).
- 27 Cherrington, A. D. *et al.* The role of insulin and glucagon in the regulation of basal glucose production in the postabsorptive dog. *The Journal of clinical investigation* **58**, 1407-1418, (1976).
- 28 Rizza, R. A. Pathogenesis of fasting and postprandial hyperglycemia in type 2 diabetes: implications for therapy. *Diabetes* **59**, 2697-2707, (2010).
- 29 Unger, R. H. & Cherrington, A. D. Glucagonocentric restructuring of diabetes: a pathophysiologic and therapeutic makeover. *The Journal of clinical investigation* **122**, 4-12, (2012).

- 30 Acosta, D. *et al.* First measurements of inclusive W and Z cross sections from run II of the fermilab tevatron collider. *Physical review letters* **94**, 091803, (2005).
- 31 Kim, H. J., Vosseler, C. A., Weber, P. C. & Erl, W. Docosaheanoic acid induces apoptosis in proliferating human endothelial cells. *Journal of cellular physiology* **204**, 881-888, (2005).
- 32 Abazov, V. M. *et al.* Search for supersymmetry with gauge-mediated breaking in diphoton events at D0. *Physical review letters* **94**, 041801, (2005).
- 33 Messerli, F. H. & Grossman, E. Diabetes, hypertension, and cardiovascular disease: an update. *Hypertension* **38**, E11, (2001).
- 34 Leissring, M. A. & Turner, A. J. Regulation of distinct pools of amyloid beta-protein by multiple cellular proteases. *Alzheimer's research & therapy* **5**, 37, (2013).
- 35 Lankas, G. R. *et al.* Dipeptidyl peptidase IV inhibition for the treatment of type 2 diabetes: potential importance of selectivity over dipeptidyl peptidases 8 and 9. *Diabetes* **54**, 2988-2994, (2005).
- 36 Gottlieb, H. E., Kotlyar, V. & Nudelman, A. NMR Chemical Shifts of Common Laboratory Solvents as Trace Impurities. *The Journal of organic chemistry* **62**, 7512-7515, (1997).
- 37 Kleiner, R. E., Dumelin, C. E., Tiu, G. C., Sakurai, K. & Liu, D. R. In vitro selection of a DNA-templated small-molecule library reveals a class of macrocyclic kinase inhibitors. *J Am Chem Soc* **132**, 11779-11791, (2010).
- 38 Georghiou, G., Kleiner, R. E., Pulkoski-Gross, M., Liu, D. R. & Seeliger, M. A. Development and structure-based mechanism of highly specific macrocyclic Src kinase inhibitors from a DNA-template library. *submitted*, (2011).

Chapter 4

Discovery of the Anti-diabetic Activity of Insulin-Degrading Enzyme Inhibitors Mediated by Multiple Hormone Substrates

Adapted from: Maianti *et al*, *Nature* **511**, 94–98 (2014).

Contributions: I designed and performed the experiments and hormone measurements described in this chapter. Amanda K. McFedries assisted with the *in vivo* experiments. Xiu Quan Du assisted with the KO mice experiments at Maureen Charron's group (Albert Einstein College of Medicine, NY).

4.1 – Introduction: glucose tolerance tests and mice models of diabetes

To determine the physiological consequences of acute IDE inhibition *in vivo*, we evaluated the glucose tolerance of mice treated with **6bK**. This model was chosen due to: *i*) the short treatment duration^{1,2}; *ii*) the extensive mechanistic validation and understanding provided by decades of research³⁻⁶; and *iii*) its direct relevance to human disease management and diagnosis⁷⁻⁹. We used two standard methods of glucose delivery, either oral gavage or i.p. injection,¹ and two different mouse models, lean or diet-induced obese (DIO) mice^{3,4}. These four conditions were chosen to survey the role of IDE activity under a broad range of endogenous insulin levels and insulin sensitivity^{1,4}. Oral glucose administration, for example, results in greater insulin secretion compared to injected glucose delivery (**Figure 4.1**). Passage of glucose through the gut causes the release of GLP-1, which strongly augments glucose-dependent insulin secretion^{4,10}. This phenomenon is referred to as the ‘incretin effect’ and is magnified in DIO mice⁴. In addition, DIO mice display hyperinsulinemia and insulin resistance compared to lean mice, enabling us to test the consequences of IDE inhibition in a model that resembles early type-2 diabetes in humans³.

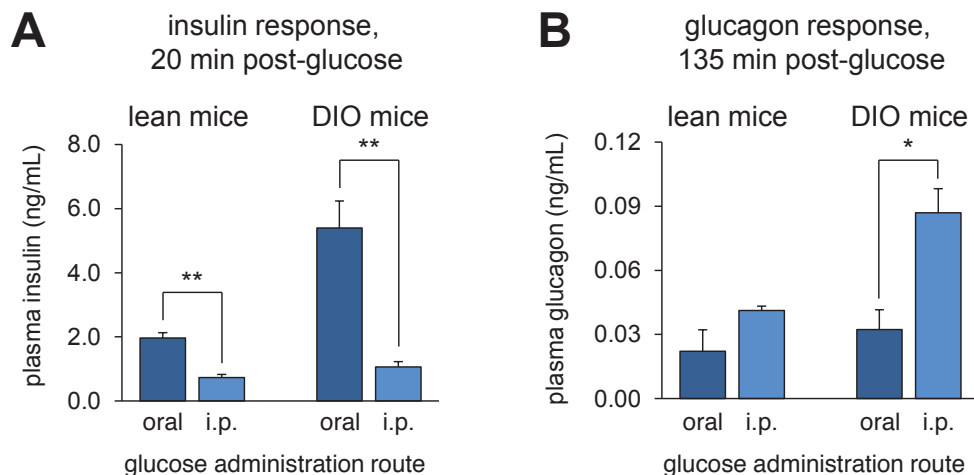


Figure 4.1 | Dependence of insulin and glucagon secretion on the route of glucose administration (oral or i.p.) and the hyperinsulinemic phenotype of DIO versus lean mice. (A) The early insulin response to glucose in lean and DIO mice is higher during OGTT than IPGTT. (B) Suppression of glucagon secretion post-glucose administration is less effective after IPGTT and in DIO mice. All data points and error bars represent mean \pm SEM. Significance tests were performed using two-tail Student's t-test, and significance levels shown are $p < 0.05$ (*) or $p < 0.01$ (**) versus the vehicle-only control group.

4.2 – IDE inhibition improves blood glucose clearance following oral glucose administration

In all glucose tolerance experiments we included two control groups: vehicle alone, and the inactive isomer¹¹ **bisepi-6bK**, which is identical to **6bK** in chemical composition and bond connectivity, but has virtually no IDE inhibition activity ($IC_{50} > 200 \mu M$, **Figures 3.6–3.7**). In all glucose tolerance studies I used a standardized formulation of compound dissolved in sterile saline plus Captisol®¹², and I injected an effective dose of **6bK** (or inactive control) of 2 mg/mouse i.p., representing 80

mg/kg for lean C57BL/6J mice (25 g), and 60 mg/kg for diet-induced obese (DIO) mice (35-45 g), unless otherwise stated (Chapter 3, Section 3.4).

In one set of experiments we examined the effect of **6bK** on blood glucose levels during an oral glucose tolerance test (OGTT). Lean or DIO mice were fasted overnight for these experiments, and then treated with a single dose of **6bK**, vehicle alone, or a matching dose of inactive **bisepi-6bK**. After 30 minutes, glucose was administered by oral gavage, and glycemia was measured from a droplet of blood obtained from a tail nick throughout a period of 2 hours. This timeframe corresponds approximately to peak concentration of **6bK** in peripheral circulation, which is sustained reliably above 100-fold (and up to 1,000-fold) the IC₅₀ levels of **6bK** in blood, as well as the liver and the kidneys, the main sites of insulin degradation^{13,14} (**Figure 3.2A**).

Importantly, we observed that both lean and DIO mice treated with **6bK** displayed significantly improved oral glucose tolerance compared to vehicle or inactive **bisepi-6bK** control groups (**Figure 4.2**). The two control groups exhibited similar blood glucose profiles, indicating that the observed effects of **6bK** on glucose tolerance are lost when the stereochemistry of **6bK** is altered in a way that abolishes IDE inhibition (see Section 4.7 for IDE^{-/-} knockout controls, **Figure 4.10**).

The literature suggests that effects of similar magnitude on oral glucose tolerance in mice have been observed using several approved human anti-diabetic therapeutics^{8,15,16}. We showed that the glucose tolerance improvement provided by the anti-diabetes DPP4 inhibitor drug sitagliptin (administered at a higher-than-

standard murine dosing¹⁷) was comparable to the effect of **6bK** dosed to littermate DIO mice (**Figure 4.3**). Moreover, co-administration of sitagliptin and **6bK** (low dose, 40 mg/kg) resulted in effectively lower blood glucose levels than with either inhibitor alone (**Figure 4.3B**). The additive effects of these inhibitors suggests that DPP4 and IDE regulate distinct nodes along the insulin signaling pathway, and furthermore that co-administration of IDE inhibitors with drugs targeting the incretin pathway could provide promising therapeutic strategies (Section 4.8).

Collectively, these observations support a model in which IDE regulates glucose-induced insulin signaling, and therefore glucose tolerance, and demonstrate that acute IDE inhibition improves post-prandial glucose control in lean and DIO mice (**Figures 4.2–4.3**). Together, these results represent the first time that IDE inhibition has been shown to improve blood glucose clearance through the activity of endogenous insulin in a living animal^{13,14,18-20}.

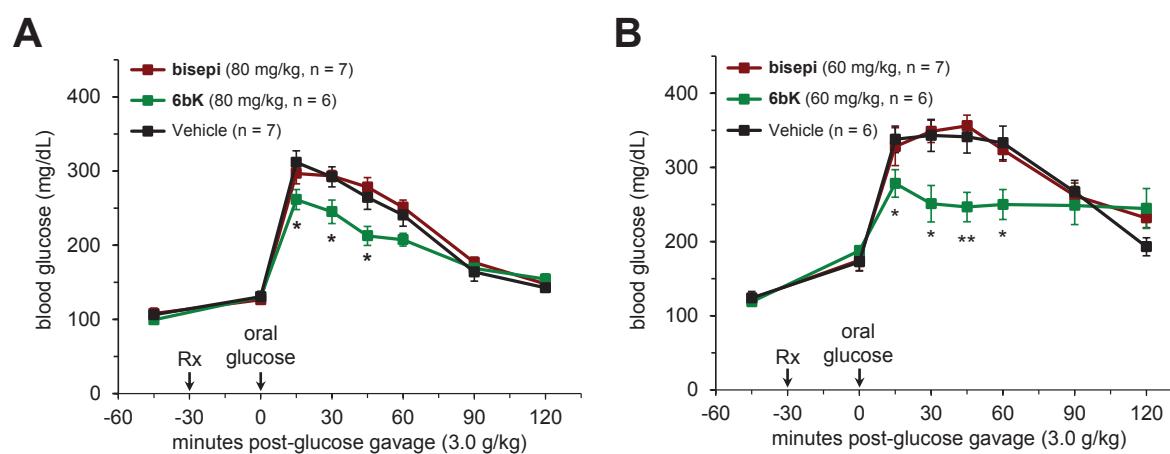


Figure 4.2 | Physiological consequences of acute IDE inhibition by 6bK on oral glucose tolerance in lean and DIO mice. (A) Male C57BL/6J lean (25 g) mice were treated with a single i.p. injection of IDE inhibitor **6bK** (■, 80 mg/kg), inactive control **bisepi-6bK** (■, 80

(**Figure 4.2 cont.**) mg/kg), or vehicle alone (■) 30 min prior to glucose gavage (3.0 g/kg). (**B**) DIO mice (35-45 g) were treated with **6bK** (■, 60 mg/kg), and inactive control **bisepi-6bK** (■, 60 mg/kg) or vehicle alone (■) 30 min prior to glucose gavage (3.0 g/kg). All data points and error bars represent mean ± SEM. Significance tests were performed using two-tail Student's t-test, and significance levels shown are $p < 0.05$ (*) or $p < 0.01$ (**) versus the vehicle-only control group.

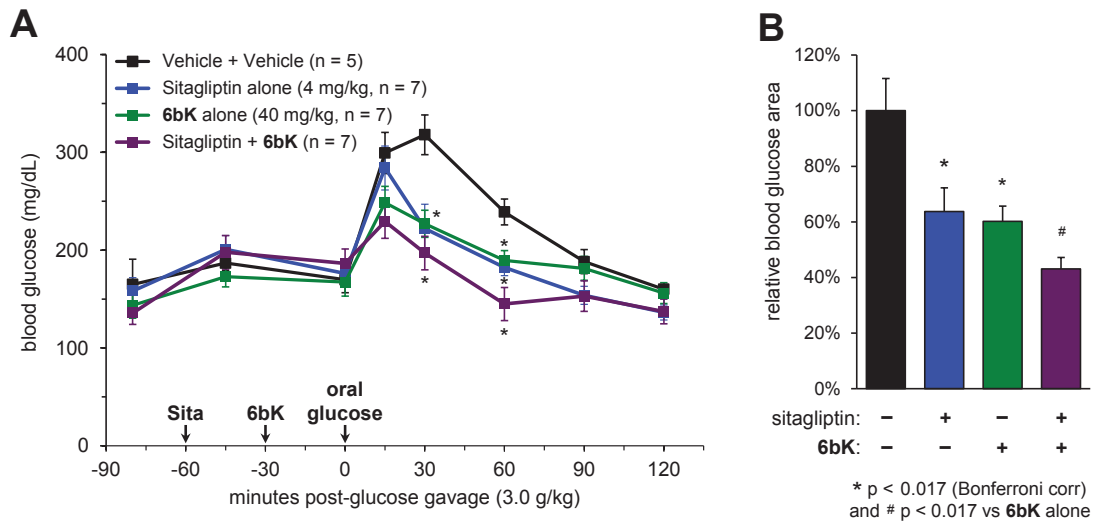


Figure 4.3 | Co-administration of IDE inhibitor 6bK and DPP4 inhibitor sitagliptin followed by an oral glucose challenge. (**A**) DIO mice were first treated with either oral gavage of sitagliptin (■/■ 4 mg/kg, 5 mL/kg in sterile saline) or saline alone. After 30 min, the mice were treated either with a low dose of **6bK** (■/■ 40 mg/kg) or vehicle alone (■), and after an additional 30 min all mice were given a bolus of glucose by gavage (3.0 g/kg, 10 mL/kg). Mice treated with the combination of sitagliptin and **6bK** displayed glucose levels lower than baseline ($t = 0$) after 60 min. (**B**) Blood glucose profile areas of sitagliptin and **6bK** were similarly reduced by 60-64% compared to vehicle alone, and further 15% lower when sitagliptin and **6bK** were co-administered together. All data points and error bars represent mean ± SEM. Statistics were performed using a one-tail Student's t-test. Significance levels shown in the figures are: * $p < 0.017$ (Bonferroni correction) versus vehicle control group, # $p < 0.017$ versus the **6bK** cohort. See the Methods section for a description of the AUC calculation.

4.3 – IDE inhibition during an injected glucose challenge leads to impaired glucose tolerance

Prior work using IDE^{-/-} mice characterized the effect of i.p. glucose injections, therefore we repeated the above experiments with **6bK** followed by i.p. injected glucose tolerance tests (IPGTTs) to provide a more direct comparison with the knockout animal experiments^{6,20}. In contrast to the observed improvement in oral glucose tolerance upon **6bK** treatment (**Figure 4.2A**), IDE inhibition with **6bK** followed by a glucose injection (1.5 g/kg i.p.) resulted in *impaired* glucose tolerance after 2 h in both lean and obese mice compared to vehicle alone or **bisepi-6bK**-treated controls (**Figure 4.4A**). These changes in the glucose response profiles of lean mice treated with **6bK** compared to vehicle controls resemble the reported differences between IDE^{-/-} and IDE^{+/+} mice during similar IPGTTs^{6,20} (Chapter 1). Moreover, DIO mice treated with **6bK** followed by glucose injection displayed a biphasic response: glucose levels are lower over the initial 30 minutes of the IPGTT, followed by a hyperglycemic “rebound” starting 1 h after glucose injection (**Figure 4.4B**). Both the suppression of peak glucose levels and the magnitude of the hyperglycemic rebound were dependent on **6bK** dose, and neither effect was observed in cohorts treated with vehicle alone or inactive **bisepi-6bK**, indicating that the impaired glucose tolerance during an IPGTT correlates with IDE activity (**Figure 4.4B** and **Figure 3.6**).

Collectively, the results of the OGTTs and IPGTTs indicate that the route of glucose administration impacts the physiological response of **6bK**-treated animals in

ways that cannot be explained by a simple model in which IDE's physiological role is only to degrade insulin. Instead, these results strongly suggest a role for IDE in regulating other glucose-regulating peptide hormones *in vivo*. These results prompted us to investigate other putative substrates of IDE identified using *in vitro* cleavage assays (Section 4.4), and to treat IDE^{-/-} knockout mice lacking the target of **6bK** to show that glucose tolerance changes upon **6bK** treatment are mediated by IDE under both OGTT and IPGTT conditions (see Section 4.7, **Figure 4.10**).

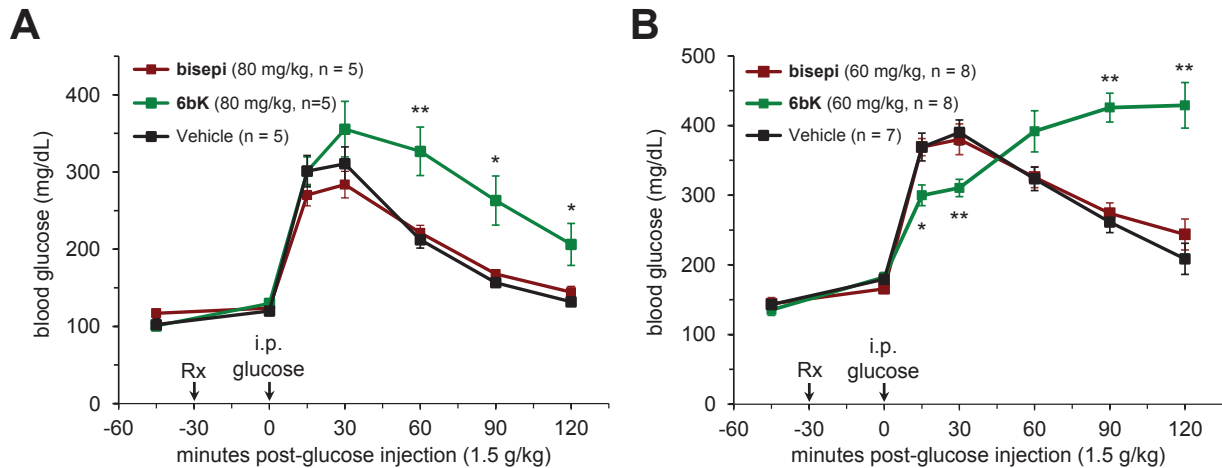


Figure 4.4 | Impact of the route of glucose administration on the phenotype of glucose tolerance in lean and DIO mice following treatment with IDE inhibitor 6bK. Glucose tolerance phenotypes after i.p. injection of glucose (1.5 g/kg) in, respectively, lean (**A**) and DIO (**B**) male mice treated with **6bK** (■), inactive **bisepi-6bK** (■), or vehicle alone (■). All data points and error bars represent mean ± SEM. Significance tests were performed using two-tail Student's t-test, and significance levels shown are $p < 0.05$ (*) or $p < 0.01$ (**) versus the vehicle-only control group.

4.4 – IDE regulates multiple hormones *in vivo*

The biochemical properties of IDE and its substrate recognition mechanism²¹⁻²³ enable this enzyme to cleave a wide range of peptide substrates *in vitro* (Chapter 1, **Figure 1.7**) for which experimental validation *in vivo* has not previously been possible. Two glucose-regulating hormones, beyond insulin, that are potential candidates for physiological regulation by IDE during a glucose challenge are glucagon and amylin. Despite decades of research, only purified IDE has been previously shown to cleave these two peptides *in vitro*²⁴⁻²⁶, but neither hormone is known to be regulated by IDE activity *in vivo* or *ex vivo*. Compared to insulin, glucagon is a modest *in vitro* IDE substrate ($K_M = 3.5 \mu\text{M}$ for glucagon versus $K_M < 30 \text{ nM}$ for insulin)²⁴, although IDE is capable of degrading glucagon at a comparable rate if present in sufficiently high concentrations ($k_{\text{cat}} = 38 \text{ min}^{-1}$ for glucagon)²⁵. Amylin is also a substrate for IDE *in vitro* ($K_M \approx 0.3 \mu\text{M}$)²⁶. Other proteases suggested to degrade glucagon include nardilysin, cathepsins B and D, in cells and *in vitro*^{27,28}, and neprilysin, which was shown to play a role in renal clearance of glucagon²⁹. However, none of these enzymes are known to regulate endogenous processing of these hormones, modulate blood glucose levels, or correlate with metabolic disease susceptibility. To our knowledge, no proteases have been previously shown to degrade amylin *in vivo*²⁶.

To begin to probe the possibility that glucagon or amylin are regulated *in vivo* by IDE, I measured the plasma levels of these hormones at 20 and 130 minutes post-glucose injection in DIO mice treated with **6bK** or vehicle alone during an IPGTT

(**Figure 4.5**). Plasma collected 20 minutes post-glucose injection showed elevated insulin and amylin levels, but unchanged glucagon levels, for the **6bK**-treated cohort relative to the control group (**Figure 4.5A**). During the hyperglycemic rebound 130 min post-injection, glucagon levels for the **6bK** group were strongly elevated above 200 pg/mL, compared with 90 pg/mL glucagon in control mice (**Figure 4.5A**). Consistent with these elevated glucagon levels, expression of a gluconeogenesis transcriptional marker, G6Pase (glucose-6-phosphatase mRNA)^{30,31}, was elevated in the livers of **6bK**-treated mice compared to control mice (**Figure 4.5B**).

Because hormone abundance measurements can be difficult to interpret during fluctuations in blood glucose that in turn affect pancreatic hormone secretion, we performed additional studies to confirm the relationship between IDE activity and glucagon and amylin levels *in vivo*. To more directly establish the effect of IDE inhibition on the clearance of insulin, amylin, and glucagon *in vivo*, I injected each of these three hormones into lean mice 30 min after treatment with **6bK** or vehicle alone (**Figure 4.6**). The **6bK**-treated cohorts exhibited significantly stronger blood glucose responses to each of these hormones compared to vehicle controls; mice treated with **6bK** experienced hypoglycemia during insulin tolerance tests (**Figure 4.6A**) and hyperglycemia following challenges with either amylin (**Figure 4.6B**) or glucagon (**Figure 4.6C**) relative to control animals. Similar to glucagon, acute administration of a high dose (50–100-fold above physiological levels) of amylin to rodents is known to result in a transient increase in blood glucose levels through gluconeogenesis and activation of lactic acid flux from muscle tissue to the liver (the

Cori cycle)³². Moreover, I determined that in each case the plasma level of the hormone injected remained elevated at the end of the procedure in **6bK**-treated mice relative to control animals, demonstrating a role for IDE in regulating the abundance of these hormones (**Figure 4.6A-C insets**).

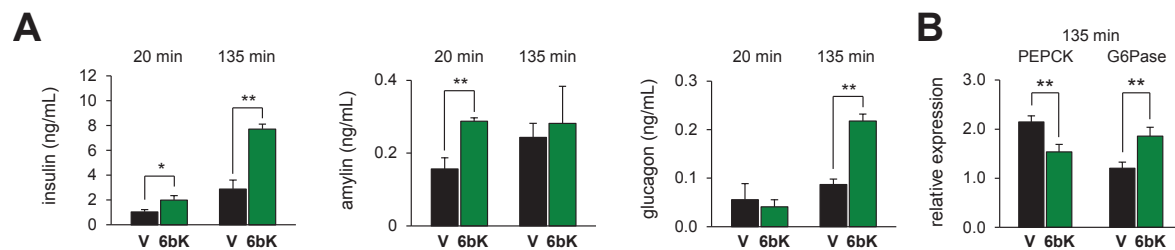


Figure 4.5 | Acute IDE inhibition affects the abundance of multiple hormone substrates during an injected glucose challenge to DIO mice. (A) Plasma hormone measurements at 20 and 135 minutes post-IPGTT (**Figure 4.4B**) for DIO mice treated with 6bK (■) or vehicle alone (■). (B) RT-PCR analysis of DIO liver samples collected at 135 min post-IPGTT reveals 50 % higher glucose-6-phosphatase (G6Pase) and 30 % lower phosphoenolpyruvate carboxykinase (PEPCK) transcript levels for the **6bK**-treated cohort (■) versus vehicle-only (V) controls (■). All data points and error bars represent mean \pm SEM. Significance tests were performed using two-tail Student's t-test, and significance levels shown are $p < 0.05$ (*) or $p < 0.01$ (**) versus the vehicle-only control group.

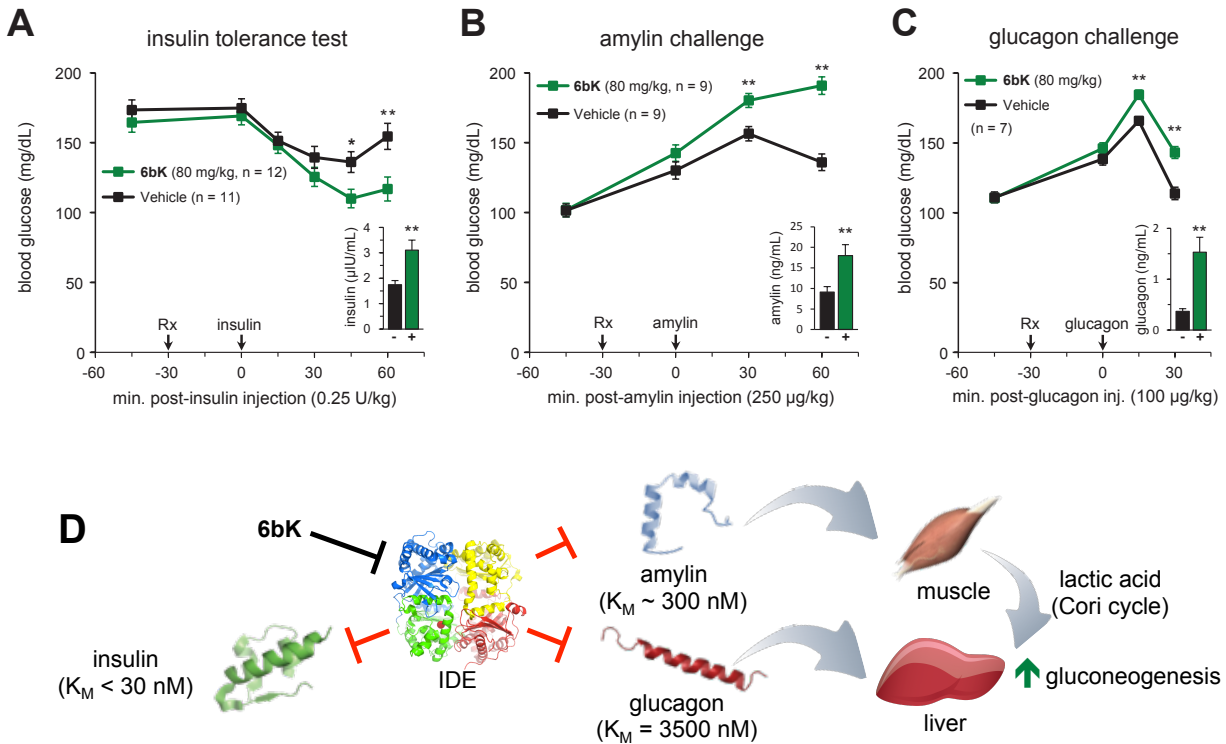


Figure 4.6 | Acute IDE inhibition potentiates multiple injected hormone substrates.

Blood glucose responses and abundance of injected hormones in lean mice 30 min after treatment with **6bK** (■, 80 mg/kg) or vehicle alone (■). (A) Insulin s.c. (0.25 U/kg) after 5-hour fast. (B), Amylin s.c. (250 μg/kg) after overnight fast. (C) Glucagon s.c. (100 μg/kg) after overnight fast. Trunk blood was collected at the last time points for plasma hormone measurements (insets). All data points and error bars represent mean ± SEM. Significance tests were performed using two-tail Student’s t-test, and significance levels shown are $p < 0.05$ (*) or $p < 0.01$ (**) versus the vehicle-only control group. (D) Model showing the connection between the injected hormones in panels A–C and the corresponding changes in blood glucose levels, which are augmented by inhibition of IDE-mediated hormone degradation *in vivo*.

4.5 – IDE inhibition promotes glucagon signaling and gluconeogenesis

Taken together, our results strongly suggest that IDE activity regulates the stability and physiological activities of glucagon and amylin, in addition to insulin. Higher glucagon levels upon **6bK** treatment provide a possible explanation for impaired glucose tolerance observed during an IPGTT. Substrates are processed by IDE at rates dependent on their relative concentrations, and we observed two- to four-fold higher insulin levels during OGTT than IPGTT, consistent with the incretin effect^{1,4,10}. During an OGTT, IDE inhibition therefore results primarily in an increase in insulin signaling and lower blood glucose levels. In contrast, during an IPGTT the incretin pathway is circumvented, insulin secretion levels are lower^{1,4} and glucagon secretion is not suppressed by GLP-1¹⁰. Hence, in the context of IPGTT, the loss of IDE-mediated glucagon degradation by **6bK** inhibition results in elevation of glucagon and gluconeogenesis (**Figures 4.4 and 4.5**). The biphasic IPGTT profile that results using DIO mice is also consistent with this model (**Figure 4.4B**). DIO mice have higher insulin levels^{3,4}, and the early improvement in glucose tolerance is explained by IDE inhibition primarily potentiating insulin during this period, but this effect is short-lived as glucagon levels rise. This transient improvement is absent in lean mice, in which insulin is secreted to lower concentrations during IPGTTs, compared to either OGTT or a DIO mouse (**Figure 4.1**). This model predicts that abrogating glucagon signaling should reverse the elevation of blood glucose by **6bK** treatment during an IPGTT, while not substantially affecting the signaling pathways through which **6bK** treatment lowers blood glucose during an OGTT.

To test these hypotheses, we collaborated with Dr. Maureen Charron (Albert Einstein College of Medicine) to repeat the glucose tolerance experiments using $GCGR^{-/-}$ mice that lack the G-protein coupled glucagon receptor (**Figure 4.7**)³³⁻³⁶. As expected, mice lacking glucagon signaling exhibited a further improvement in oral glucose tolerance upon **6bK** treatment relative to vehicle controls that was similar to the oral glucose tolerance improvement observed in wild-type mice (**Figure 4.7A** versus **Figure 4.2A**). This result is consistent with a model in which insulin and amylin signaling in these mice is intact and regulated by IDE, albeit a rapid clearance of blood glucose is observed for both these cohorts due to the insulin sensitivity that characterizes $GCGR^{-/-}$ mice³³⁻³⁶. In contrast, glucose tolerance in $GCGR^{-/-}$ mice following IPGTT was not impaired by **6bK** treatment, consistent with a model in which glucagon signaling is responsible for driving the impaired glucose tolerance of wild-type lean and DIO mice upon **6bK** treatment during an IPGTT (compare **Figure 4.7B** and **Figure 4.4A**). This observation supports a model in which IDE regulates glucagon signaling during IPGTTs. Under these conditions and using a dose of dextrose i.p. 1.5 g/kg, there was no further lowering of blood glucose in **6bK**-treated $GCGR^{-/-}$ mice, possibly because IPGTT elicits modest insulin secretion, and amylin-induced gastric emptying effects cannot play a role³⁷. Taken together, our results suggest that IDE inhibition promotes endogenous glucagon signaling that can impair glucose tolerance during an IPGTT in wild-type mice.

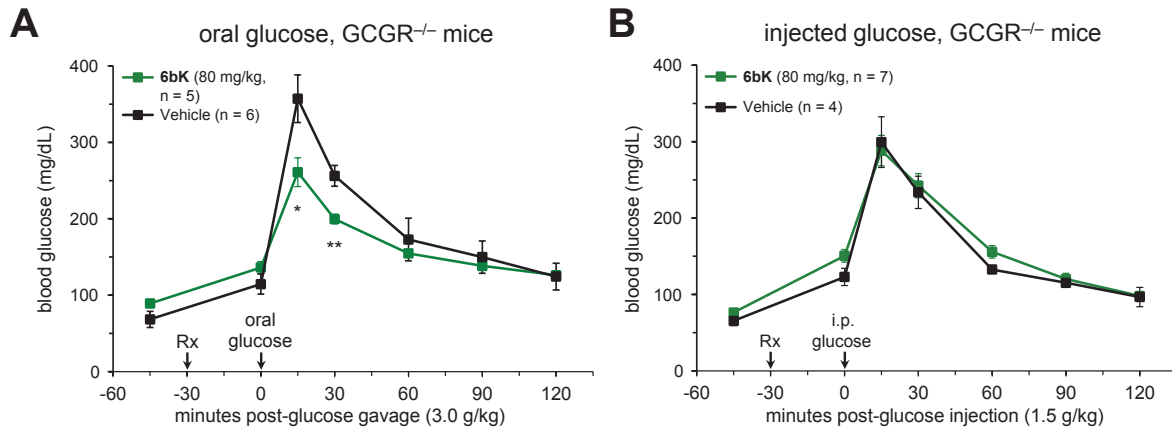


Figure 4.7 | The endogenous signaling activity of glucagon is required for impairment of injected glucose tolerance following acute IDE inhibition. G-protein-coupled glucagon receptor knockout mice (GCGR^{-/-}, C57BL/6J background) treated with IDE inhibitor **6bK** (■, 80 mg/kg) display altered glucose tolerance relative to vehicle-treated mice (■) if challenged with oral glucose (A) but not i.p. injected glucose (B). All data points and error bars represent mean ± SEM. Significance tests were performed using two-tail Student's t-test, and significance levels shown are $p < 0.05$ (*) or $p < 0.01$ (**) versus the vehicle-only control group.

To investigate the effect of IDE inhibition on endogenously secreted glucagon using a complementary method, I subjected mice treated with **6bK**, vehicle, or inactive **bisepi-6bK** to a pyruvate tolerance test (PTT). This challenge evaluates the ability of the liver, under the influence of glucagon, to use pyruvate as a gluconeogenic substrate³⁸ (Figure 4.8). I measured a panel of hormones and liver mRNA markers after the procedure and observed the **6bK**-treated cohort displayed significantly elevated plasma glucagon and increased expression of liver gluconeogenic markers compared to both control groups (50% higher PEPCK, phosphoenolpyruvate carboxykinase, and 40% higher G6Pase, glucose-6-

phosphatase)^{30,31}. However, the **6bK** cohort also experienced significantly lower blood glucose during the PTT, suggesting that IDE inhibition produced a concomitant stimulation of systemic glucose clearance that outweighed the gluconeogenic output of the liver. These results collectively suggest that under conditions that favor gluconeogenesis IDE inhibition can augment endogenous glucagon signaling accounting for impaired, rather than improved, glucose tolerance during IPGTT.

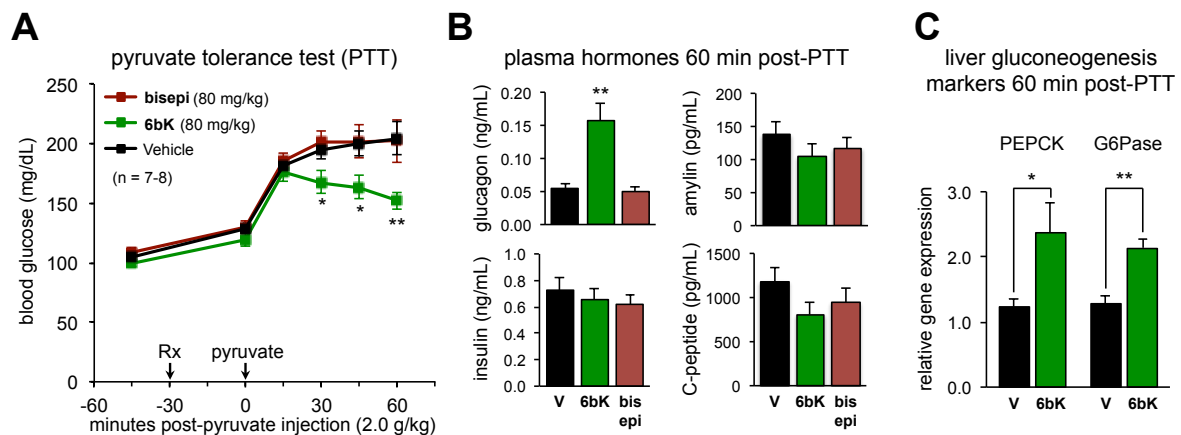


Figure 4.8 | Acute IDE inhibition modulates the endogenous signaling activity of glucagon during a pyruvate/gluconeogenesis challenge. (A) Wild-type mice fasted overnight were injected i.p. with pyruvate (2.0 g/kg) 30 min after treatment with **6bK** (■), inactive analog **bisepi-6bK** (■), or vehicle alone (■). (B) Plasma hormone measurements 60 min post-PTT reveal elevated glucagon but similar insulin levels for the **6bK**-treated cohort (■) relative to **bisepi-6bK** (■), or vehicle (■) controls. (C) RT-PCR analysis of liver samples 60-min post-PTT revealed elevated gluconeogenesis transcriptional markers for the **6bK**-treated group (■) relative to vehicle controls (■). All data points and error bars represent mean \pm SEM. Significance tests were performed using two-tail Student's t-test, and significance levels shown are $p < 0.05$ (*) or $p < 0.01$ (**) versus the vehicle-only control group.

4.6 – IDE inhibition promotes amylin signaling and gastric emptying

Amylin is co-secreted with insulin, making up 5% of the secretory granules of β -cells. Amylin is involved in glycemic control by inhibiting gastric emptying through the vagal route⁹, promoting satiety during meals^{37,39}, and antagonizing glucagon signaling⁴⁰. Unlike the effect of a non-physiologically high dose, amylin's endogenous functions supports the concept that increased amylin levels are beneficial for blood glucose control during meals. Indeed, a synthetic analog of amylin, pramlintide (Symlin) is an injectable drug used clinically to manage post-prandial hyperglycemia (**Figure 4.9D**)^{8,16}.

However, the blood glucose effects of amylin during an oral glucose tolerance experiment would be overshadowed by the rapid absorption of glucose through the walls of the stomach/duodenum, as well as the dominant hypoglycemic action of insulin on blood sugar. Therefore, to study the effect of IDE inhibition on endogenous amylin signaling I optimized a gastric retention assay⁴¹, which is an amylin-specific process triggered by receptors in the Area Postrema (AP) of the brainstem^{9,37}. Using phenol red to label a glucose solution (see Methods) we measured the gastric emptying efficiency of mice pre-treated with **6bK**, inactive control **bisepi-6bK**, or vehicle alone (**Figure 4.9**). Mice treated with **6bK** exhibited 2-fold slower gastric emptying of the labeled glucose solution measured at 30 minutes post-gavage compared to vehicle and **bisepi-6bK**-treated controls (**Figure 4.9**). Moreover, I demonstrated that co-administration of the specific amylin receptor antagonist **AC187**³⁷ blocked the effects of **6bK** on gastric emptying. Collectively,

these data reveal that IDE inhibition can slow post-prandial gastric emptying and demonstrate a role for IDE in modulating amylin signaling *in vivo* at physiologically relevant substrate levels. These results also suggest that IDE inhibition may mimic the effect of amylin supplementation with pramlintide/Symmlin during meals and its beneficial effects on post-prandial glucose control^{8,10}. However, in a therapeutic context pramlintide/Symmlin must be co-injected twice daily with insulin, and our findings raise the possibility that IDE-targeting drugs could replace these injections by raising endogenous amylin and insulin levels during meals.

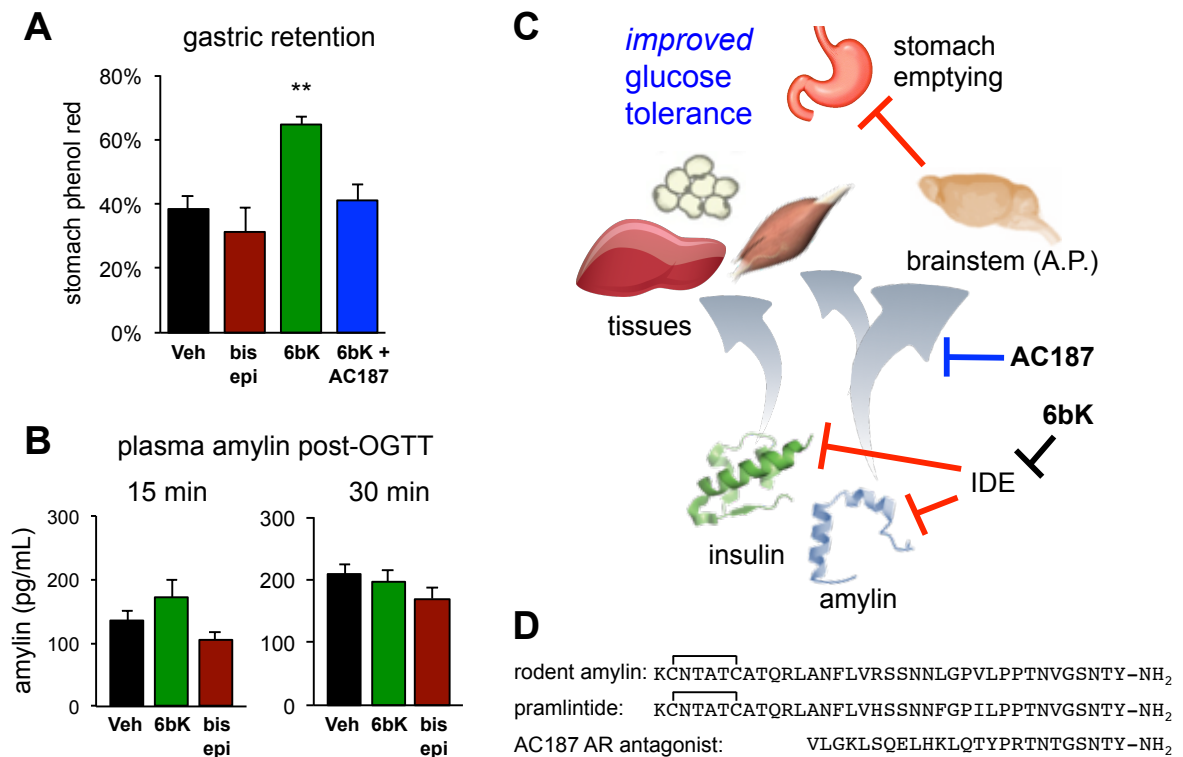


Figure 4.9 | Acute IDE inhibition modulates endogenous amylin signaling revealed by gastric emptying efficiency, an amylin-specific effect. (A) Wild-type mice fasted overnight were given an oral glucose bolus, supplemented with 0.1 mg/mL phenol red,

(Figure 4.9 cont.) 30 min after treatment with **6bK** alone (■), **6bK** co-administered with the specific amylin receptor antagonist **AC187** (■, 3 mg/kg i.p.), vehicle alone (■), or inactive **bisepi-6bK** (■). The stomachs were dissected at 30 min post-glucose gavage. (B) Plasma hormone measurements 15 and 30 min post-OGTT reveal modestly elevated amylin levels for the **6bK**-treated cohort (■, n.s.) relative to **bisepi-6bK** (■), or vehicle (■) controls. (C) Model representing the mechanisms through which amylin is involved in glycemic control by antagonizing glucagon signaling⁴⁰, and by inhibiting gastric emptying through the vagal route acting on the Area Postrema of the brainstem⁹, which also promotes satiety during meals⁴². (D) Amino acid sequences of rodent amylin, pramlintide (Symlin), and **AC187**, a structurally related amylin receptor (AR) antagonist peptide. All data points and error bars represent mean ± SEM. Significance tests were performed using two-tail Student's t-test, and significance levels shown are $p < 0.05$ (*) or $p < 0.01$ (**) versus the vehicle-only control group.

4.7 – Knockout experiments corroborate the IDE on-target effects of **6bK**

To further test if the observed effects of **6bK** are specific to its interaction with IDE, we repeated the GTT experiments using IDE^{-/-} knockout mice^{6,20}. Mice lacking IDE were unaffected by **6bK** treatment (Figure 4.10), and exhibited blood glucose responses and profile areas (AUC) indistinguishable to that of the vehicle-treated cohort in both OGTT and IPGTT experiments (Figure 4.12). These results show that the blood glucose profile improvement during OGTT and impairment during IPGTT of **6bK**-treated wild-type mice are mediated by IDE (Figures 4.2–4.4) and support our observations from dose-response experiments and **bisepi-6bK** inactive control injections (Chapter 3, Section 3.4).

It has been previously proposed that IDE^{-/-} knockout mice undergo pronounced compensatory changes in metabolic regulation, as evidenced by changes

in insulin resistance and down regulation of insulin receptors^{6,20}. However, our results suggest that glucagon is an IDE substrate that has not been accounted for in this model leading to impaired glucose tolerance. The prediction is that if compensation is indeed occurring in mice chronically lacking IDE, then adult IDE^{-/-} mice should display *impaired* tolerance both to oral and injected glucose because they have lower insulin-receptor levels. Therefore, we performed an OGTT using IDE^{-/-} mice and compared it to age-matched wild-type IDE^{+/+} mice (**Figure 4.11**). Unlike **6bK**-treated animals, which show improved glucose tolerance during an oral GTT, IDE^{-/-} mice have impaired oral glucose tolerance when compared to similarly treated IDE^{+/+} mice (**Figure 4.11A**), thus corroborating that chronic deletion of IDE leads to a dysregulation of the insulin axis that is not predictive of the outcome of IDE inhibition^{6,20}. This data supports the compensatory model described by Abdul-Hay *et al.* in 2011 relying on IPGTT experiments (**Figure 4.11B**), while also demonstrating the value of small-molecule probes to validate therapeutic targets that are masked by compensation following gene deletion. Moreover, these results further support that compensation is occurring with IDE^{-/-} mice and that, in these absence of these compensatory changes, inhibition of IDE can result in improved glucose tolerance through potentiation of insulin signaling.

Many of the concerns about long-term effects of IDE inhibition can be potentially inferred from studies using IDE knockout mice^{6,20,43}. Mice lacking IDE activity are viable, fertile, do not display conspicuous phenotypic defects, and have normal body weight, as well as normal organ sizes and morphologies. While

additional studies are needed to progress these discoveries towards human therapeutics, these attributes of IDE^{-/-} KO mice are encouraging for the potential pharmaceutical inhibition of IDE⁴⁴. Nevertheless, it is possible that chronic inhibition of IDE is not necessarily desirable; instead, our findings suggest that transient pre-meal IDE inhibition may be a promising approach to help manage post-prandial hyperglycemia. For a competitive inhibitor that obstructs binding of all substrates to the IDE chamber (with the exception of substrate-selective IDE inhibitors developed in Chapter 5) a short lasting pre-meal therapeutic strategy would generate less concern about side effects, given that IDE's role in degrading glucagon may modulate basal blood glucose levels between meals.

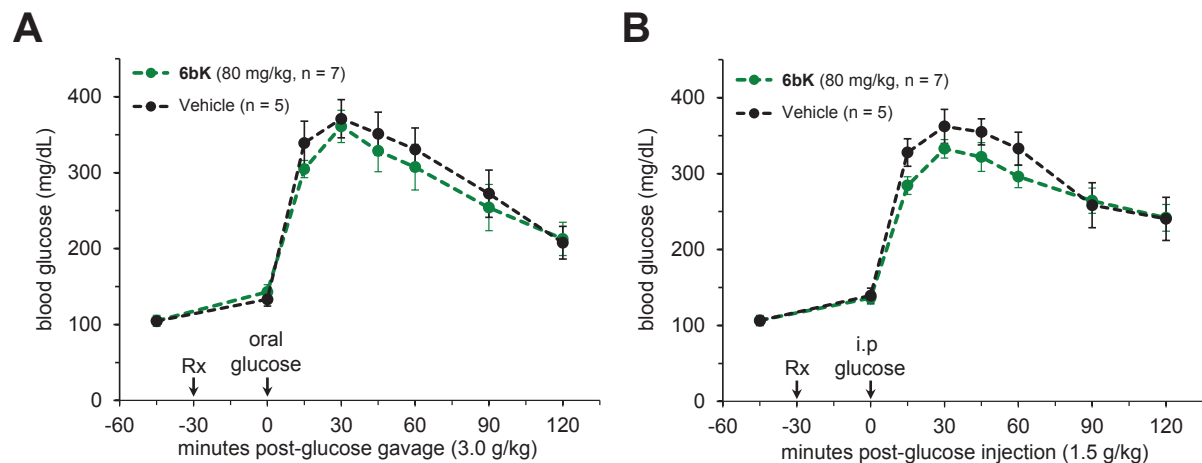


Figure 4.10 | Mice lacking IDE display no effects of 6bK treatment. (A) Mice lacking IDE treated with **6bK** (●, 80 mg/kg) followed by oral glucose produce an identical response compared to vehicle-treated controls (●) of the same genotype (IDE^{-/-}). (B) Similarly, mice lacking IDE treated with **6bK** (●, 80 mg/kg) followed by IPPGTT display an identical response compared to vehicle-treated (●) IDE^{-/-} control mice. All data points and error bars represent mean ± SEM.

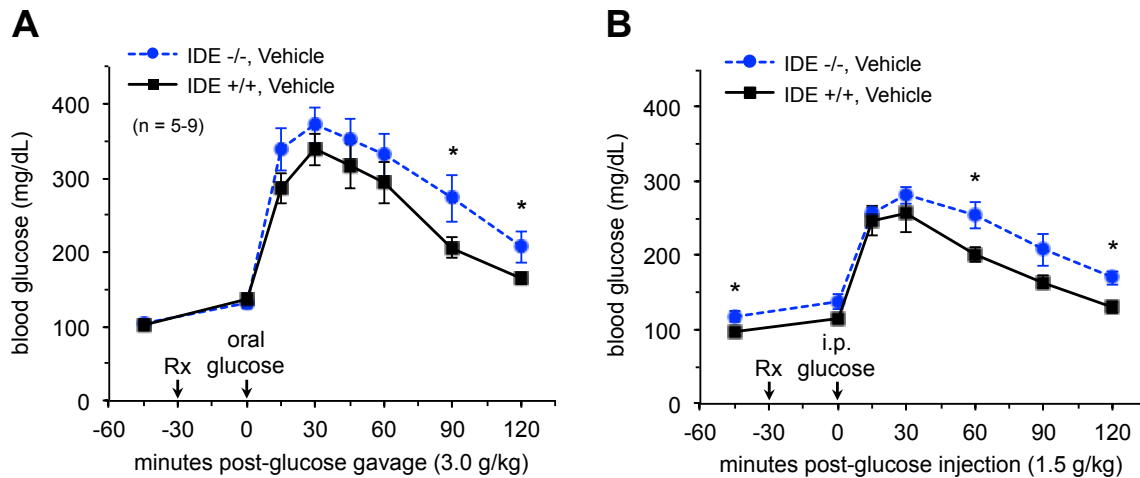


Figure 4.11 | Oral glucose tolerance of mice lacking IDE compared to WT lean mice. Mice lacking IDE (●, IDE^{-/-}) display *impaired* glucose tolerance during OGTT (A) and IPGTT (B) compared to age-matched IDE^{+/+} controls (■), supporting the hypothesis that chronic deletion of IDE leads to pronounced compensatory changes in metabolism that are not predictive of the outcome of IDE inhibition^{6,20}. All data points and error bars represent mean ± SEM.

4.8 – Therapeutic implications of IDE inhibition

This chapter described the application of the first potent, highly selective, and physiologically active small-molecule IDE inhibitor, revealing for the first time that acute IDE inhibition can lead to improved glucose tolerance in lean and obese mice after oral glucose administration, conditions that mimic the intake of a meal (see AUC summary in **Figure 4.12**). Following decades of speculation, these results establish the potential of IDE as a therapeutic target for the treatment of type-2 diabetes^{13,14}.

Our data show that small-molecule IDE inhibitors can improve oral glucose tolerance to an extent comparable to that of the DPP4 inhibitor sitagliptin (**Figure 4.3**)^{8,10}. The potential relevance of these animal studies to human disease is supported by the repeated recognition of IDE as a diabetes susceptibility gene in humans and rodents^{20,45-50}. Moreover, it is established that mice lacking IDE are viable and do not display conspicuous phenotypic or health defects beyond their glucose metabolism^{6,20}. While additional studies are needed to progress these discoveries towards human therapeutics, these attributes of IDE^{-/-} KO mice are encouraging for the potential pharmaceutical inhibition of IDE⁴⁴.

Equally important, our additional *in vivo* and biochemical experiments using **6bK** unveiled that IDE is a regulatory node for several of the key hormones in glucose homeostasis, regulating the stability and signaling of glucagon and amylin, in addition to its assumed role in insulin degradation (**Figure 4.13**)^{6,13,14,19,20}. The identification of two additional pancreatic hormones as endogenous IDE substrates advances our understanding of the role of IDE in regulating physiological glucose homeostasis. Indeed, amylin-mediated effects on gastric emptying and satiety during meals have been recently recognized to have therapeutic relevance in the treatment of diabetes^{8,10}, and our results represent the first demonstration of a small-molecule that can regulate both amylin and insulin signaling. Moreover, the link between IDE and glucagon revealed in this study provides additional evidence of the importance of glucagon regulation in human diabetes⁵¹.

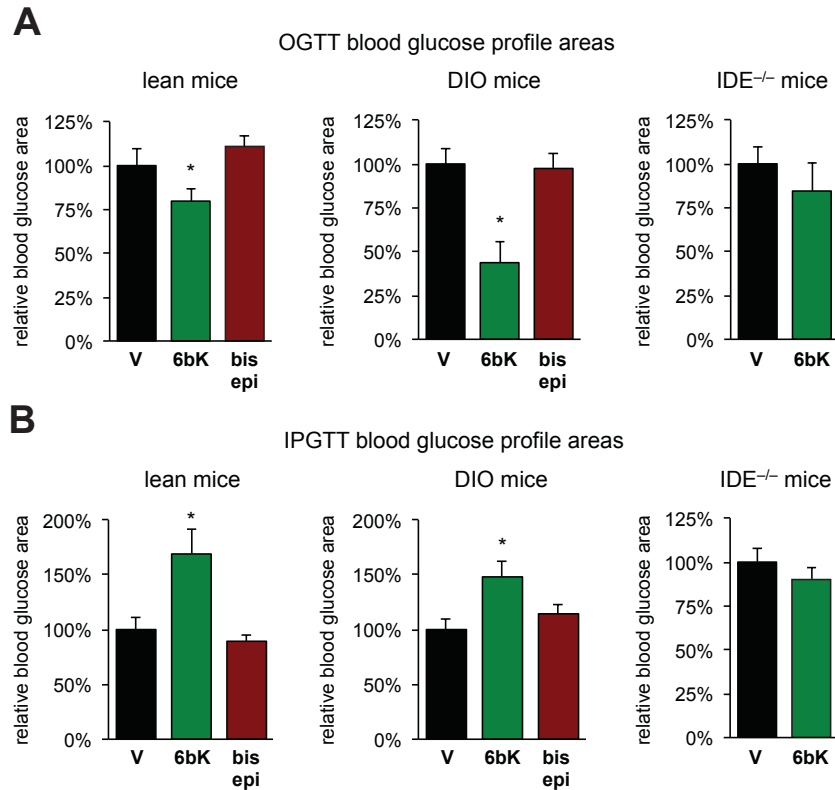


Figure 4.12 | Summary of physiological consequences of acute IDE inhibition by 6bK on glucose tolerance in lean, DIO, and IDE^{-/-} mice. (A) Area under the curve (AUC) calculations, during OGTT, lean and DIO mice treated with **6bK** (■) display improved glucose tolerance (lower blood glucose area), compared to vehicle controls (■) and inactive **bisepi-6bK** (■). (B) In contrast, during IPGTT both lean and DIO mice treated with **6bK** (■) display impaired glucose tolerance (higher blood glucose area) compared to vehicle (■) or **bisepi-6bK** (■) controls. Significance tests were performed using two-tail Student's t-test, and significance levels shown are $p < 0.05$ (*) or $p < 0.01$ (**) versus the vehicle-only control group. See the Methods section for a description of the AUC calculation.

This study also reveals that the therapeutic potential of IDE inhibition using competitive inhibitors poses the pharmacological requirement to circumvent elevation of glucagon levels⁵¹. Based on our findings, the proposed specific strategies

to bring about a therapeutic benefit from IDE inhibition without affecting endogenous glucagon signaling and gluconeogenesis are:

(1) Development of fast- and short-acting IDE inhibitors that can be taken with/prior to food to transiently potentiate endogenous insulin and amylin secreted in response to the meal to help control post-prandial glycemia^{8,15}, but which is cleared or degraded before glucagon secretion resumes. Similar pre-meal therapeutic strategies with short-lived agents have already proven successful with fast-acting insulin analogs, secretagogues¹⁵, and amylin supplementation^{8,9}.

(2) Combination therapy with glucagon-lowering incretin therapies and DPP4 inhibitors⁵². We can speculate that these agents may also provide additive effects when co-administered with an IDE inhibitor; indeed **6bK** treatment resulted in stronger improvements in oral glucose tolerance when co-administered with sitagliptin (**Figure 4.3**)^{8,10}. Alternatively, the combination of an IDE inhibitor with a glucagon receptor antagonist⁵¹, may also prevent elevation of glucagon signaling, as suggested by our experiments with glucagon-receptor knockout mice (**Figure 4.7**).

(3) In addition, our structural findings presented in Chapter 2 raise the possibility of developing IDE inhibitors that selectively obstruct insulin cleavage without affecting IDE-mediated glucagon processing. The results presented in the next chapter of this thesis represent the first series of substrate-discriminating IDE inhibitors, which preferentially block insulin degradation in a way that accommodates for IDE-mediated degradation of glucagon and amylin (Chapter 5).

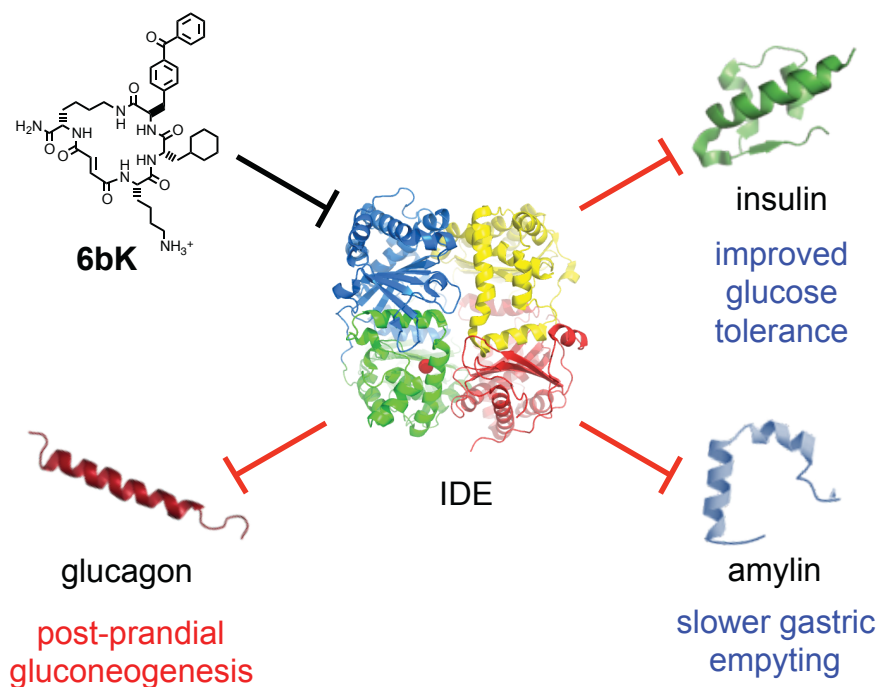


Figure 4.13 | Model for the expanded roles of IDE in glucose homeostasis and gastric emptying based on the results of this study. IDE inhibition increases the abundance and signaling of three key pancreatic peptidic hormones, insulin, amylin, and glucagon, with the corresponding physiological effects shown in blue and red.

More broadly, this work highlights the value of physiologically active small-molecule probes to characterize the functions of genes implicated in human disease as a key step in the drug discovery process that could prove increasingly valuable as human genomic studies become more prevalent^{11,53}. The identification of a highly selective IDE inhibitor using a DNA-encoded library coupled with *in vitro* selection further establishes the value of this approach for the target-based discovery of bioactive small molecules. The unbiased nature of the selection led to the identification of a novel small-molecule binding site in IDE that enables

unprecedented inhibition selectivity for this enzyme. These macrocycles and structural insights therefore may also prove useful in the discovery of novel drug-like small-molecule leads to target IDE. Towards this goal, I developed a high-throughput fluorescence anisotropy assay using a fluorescent **6b** analog that enables screening of large small-molecule collections against this new binding site, providing a path forward for the further discovery and development of novel therapeutic leads against IDE that share the specificity features of **6bK** (Chapter 5).

4.9 – Methods

Dosing and formulation of macrocycle inhibitors for *in vivo* studies. The doses of **6bK** used in this study were chosen based on literature precedent for small molecules and drugs of similar potencies⁵⁴⁻⁶⁰. Procedures using experimental compounds were in accordance with the standing committee on the Use of Animals in Research and Teaching at Harvard University, the guidelines and rules established by the Faculty of Arts and Sciences' Institutional Animal Care and Use Committee (IACUC), and the National Institutes of Health Guidelines for the Humane Treatment of Laboratory Animals.

Purified macrocycle inhibitors were dissolved in DMSO-*d*₆ (~200 to 250 mg/mL stock solutions). A sample aliquot (5 μL) of the macrocycle solution was diluted with 445 μL DMSO-*d*₆, then combined with 50 μL of freshly prepared solution of 20 mM CH₂Cl₂ in DMSO-*d*₆ in for ¹H-NMR acquisition (600 MHz, relaxation time = 2 sec). The inhibitor concentration was calculated using the integral

of the CH₂Cl₂ singlet (δ 5.76 ppm, 2H)⁶¹, which appears in an uncluttered region of these spectra^{62,63}. For injectable formulations (10 mL/kg i.p. injection volume), the macrocycle inhibitor solution in DMSO-*d*₆ (200 – 250 mg/mL, based on free-base molecular weight) was combined with 1:20 w/w Captisol® powder (CyDex)¹². The resulting slurry was supplemented with DMSO-*d*₆ to make up to 5 % of the final formulation volume, mixed thoroughly and dissolved with sterile saline solution (0.9 % NaCl). Vehicle controls were identically formulated with 5 % DMSO-*d*₆ and equal amount of Captisol®. The formulated solutions of inhibitor were clear with no visible particles, and were stored overnight at 4 °C prior to injection.

***In vivo* studies, general procedures.** Wild-type C57BL/6J and diet-induced obese (DIO) C57BL/6J age-matched male adult mice were purchased from Jackson Laboratories. The age range was 13 to 15 weeks for lean mice, and 24 to 26 weeks for DIO mice. All animals were individually housed on a 14-h light, 10-h dark schedule at the Biology Research Infrastructure (BRI), Harvard University. Cage enrichment included cotton bedding and a red plastic hut. Water and food were available *ad libitum*, consisting respectively of normal chow (Prolab® RHM 3000) or high-fat diet (60 kcal % fat, D12492, Research Diets Inc.). Adult IDE knock-out mice (IDE^{-/-}) fully back-crossed to the C67BL/6J line were obtained from Mayo Clinic (Florida), and housed in the Biology Research Infrastructure (BRI), Harvard University, for 8 weeks prior to experiments as described above, and experiments were conducted on age-matched mice cohorts ranging 17 to 21 weeks old. All animal

care and experimental procedures were in accordance with the standing committee on the Use of Animals in Research and Teaching at Harvard University, the guidelines and rules established by the Faculty of Arts and Sciences' Institutional Animal Care and Use Committee (IACUC), and the National Institutes of Health Guidelines for the Humane Treatment of Laboratory Animals. Glucagon-receptor knock-out mice (GCGR^{-/-}) and control WT mice (GCGR^{+/+}) were group-housed with a 14-h light and 10-h dark schedule and treated in accordance with the guidelines and rules approved by the IACUC at Albert Einstein College of Medicine, NY. Power analysis to determine animal cohort numbers was based on preliminary results and literature precedent, usually requiring between 5 and 8 animals per group. Animals were only excluded from the cohorts in cases of chronic weakness, which occurs among GCGR^{-/-} mice, or when we identified occasional DIO mice with an outlier diabetic phenotype (e.g. >200 mg/dL fasting blood glucose). Age- and weight-matched mice were randomized to each treatment group. Double-blinding was not feasible.

Glucose tolerance tests GTT and blood glucose measurements. Prior to a glucose challenge, the animals were fasted for 14 h (8 pm to 10 am, during the dark cycle) while individually housed in a clean cage with inedible wood-chip as a floor substrate, cotton bedding and a red plastic hut. Inhibitor, vehicle or control compounds were administered by a single intraperitoneal (i.p.) injection 30 min prior to the glucose challenge. Dextrose was formulated in sterile saline (3 g in 10 mL total), and the dose was adjusted by fasted body weight. For OGTT, 3.0 g/kg dextrose

was administered by gavage at a dose of 10 mL/kg, and for IPGTT, 1.5 g/kg dextrose injected at a dose of 5 mL/kg. Blood glucose was measured using AccuCheck® meters (Aviva) from blood droplets obtained from a small nick at the tip of the tail, at timepoints -45, 0, 15, 30, 45, 60, 90 and 120 min with reference to the time of glucose injection. The area of the blood glucose response profile curve corresponding to each animal was calculated by the trapezoid method¹, using as reference each individual baseline blood glucose measurement prior to glucose administration ($t = 0$) or the lowest point of the curve. The sum of the trapezoidal areas between the 0, 15, 30, 45, 60, 90 and 120 minute time points corresponding to each animal were summed to obtain the area under the curve (AUC). The relative area values are expressed as a percentage relative to the average AUC of the vehicle cohort, which is defined as 100 % (Fig. 2, Extended Data Figs. 8 and 9). Values are reported as mean \pm S.E.M. Statistics were performed using a two-tail Student's t-test, and significance levels shown in the figures are $*p < 0.05$ versus vehicle control group or $**p < 0.01$ versus vehicle control group unless otherwise stated.

Insulin Tolerance Test (ITT), Glucagon Challenge (GC) and Amylin Challenge (AC). For hormone challenges animals were fasted individually housed as described above. For ITT the fasting period was 6 h (7 am to 1 pm), and for glucagon and amylin challenges the fasting period was 14 h (8 pm – 10 am). Inhibitor or vehicle alone was injected i.p. as previously described, 30 min prior to each hormone challenge. Insulin (Humulin-R®, Eli Lilly) was injected subcutaneously (s.c.) 0.25

U/kg formulated in sterile saline (5 mL/kg). Glucagon (Eli Lilly) was injected s.c. 100 µg/kg formulated in 0.5 % BSA sterile saline (5 mL/kg). Amylin (Bachem) was injected s.c. 250 µg/kg formulated in sterile saline (5 mL/kg). Blood glucose was measured at timepoints -45, 0, 15, 30, 45, 60 and 75 min with reference to the time of hormone injection, by microsampling from a tail nick as described above. Values are reported as mean ± S.E.M. Statistics were performed using a two-tail Student's t-test, and significance levels shown in the figures are * $p < 0.05$ versus vehicle control group or ** $p < 0.01$ versus vehicle control group.

Blood collection and plasma hormone measurements. Blood was collected in EDTA-coated tubes (BD Microtainer®) from trunk bleeding (~500 µL) after CO₂-euthanasia for all hormone assays. The plasma was immediately separated from red blood cells by centrifugation 10 min at 1800 g, aliquoted, frozen over dry ice and stored at -80 °C. Insulin, glucagon, amylin and pro-insulin C-peptide fragment were quantified from 10 µL plasma samples using magnetic-bead Multiplexed Mouse Metabolic Hormone panel (Milliplex, EMD Millipore) according to the manufacturer's instructions, using a Luminex FlexMap 3D instrument. Plasma containing high levels of human insulin (Humulin-R) were quantified using 25 µL samples with Insulin Ultrasensitive ELISA (ALPCO). Values are reported as mean ± S.E.M. Statistics were performed using a two-tail Student's t-test, and significance levels shown in the figures are * $p < 0.05$ versus vehicle control group or ** $p < 0.01$ versus vehicle control group.

Gastric emptying measurements. Mice were fasted 14 h (8 pm to 10 am). Inhibitor or vehicle alone was injected i.p. as previously described, followed 30 min later by an oral glucose bolus (3.0 g/kg, 10 mL/kg) in sterile saline containing 0.1 mg/mL phenol red. At 30 min, the stomach was promptly dissected after CO₂-euthanasia and stored on ice. The stomach contents were extracted into 2.5 mL EtOH (95 %) by homogenization for 1 min using a probe sonicator. Tissue debris were decanted by centrifugation at 4000 g, followed by clearing at 15000 g for 15 min. The supernatant (1 mL) was mixed with 0.5 mL of aqueous NaOH (20 mM), and incubated at -20 °C for 1 h. The solution was centrifuged at 15,000 g for 15 min, and absorbance was determined at 565 nM. The spectrophotometer was blanked with the stomach contents of a mouse treated with colorless glucose solution. The absorbance was adjusted to the amount of glucose solution dosed to each mouse. Values are reported as mean ± S.E.M relative to the original phenol red glucose solution. Statistics were performed using a two-tail Student's t-test, and significance levels shown in the figures are * $p < 0.05$ versus vehicle control group or ** $p < 0.01$ versus vehicle control group.

RT-PCR analysis of liver gluconeogenesis markers phosphoenolpyruvate carboxykinase (PEPCK) and glucose-6-phosphatase (G6Pase). Total RNA was isolated from liver samples (~100 mg) using TRIzol® reagent (Invitrogen, 1 mL/100 mg sample), followed by spin-column purification (RNeasy® kit, Qiagen) and on-column DNase treatment (Qiagen) according to the manufacturer's instructions.

RNA concentrations were determined by UV spectrophotometry (NanoDrop). One microgram of total RNA was used for reverse transcription with oligo(dT) primers (SuperScript® III First-Strand Synthesis SuperMix, Life Technologies) according to the manufacturer's instructions. Quantitative PCR reactions included 1 µL of cDNA diluted 1:100, 0.4 µM primers, 2x SYBR Green PCR Master Mix (Invitrogen) in 25 µL total volume, and were read out by a CFX96™ Real-Time PCR Detection System (BioRad). Transcript levels were determined using two known primer pairs^{30,31} for each gene of interest (Supplementary Table S4), which were normalized against tubulin and beta-actin transcripts ($\Delta\Delta C_T$ method), and expressed relative to the lowest sample. Duplicate control assays without reverse transcriptase treatment were run for each RNA preparation and primer set used. Statistics were performed using a two-tail Student's t-test, and significance levels shown in the figures are $*p < 0.05$ versus vehicle control group or $**p < 0.01$ versus vehicle control group.

Table 4.1 | RT-PCR primers for mouse liver gluconeogenesis markers.

RT-PCR primers ^{30,31}	
PEPCK_1_Fw	GAACTGACAGACTCGCCCTATGT
PEPCK_1_Re	GTTGCAGGCCAGTTGTTG
G6Pase_1_Fw	GTGCAGCTGAACGTCGTCTGT
G6Pase_1_Re	TCCGGAGGCTGGCATTGT
PEPCK_2_Fw	GGTGTTTACTGGGAAGGCATC
PEPCK_2_Re	CAATAATGGGGCACTGGCTG
G6Pase_2_Fw	CATGGGCGCAGCAGGTGTATACT
G6Pase_2_Re	CAAGGTAGATCCGGGACAGACAG
Tubulin_Fw	CCTGCTCATCAGCAAGATCC
Tubulin_Re	TCTCATCCGTGTTCTCAACC
Beta-actin_Fw	CATCCGTAAAGACCTCTATGCCAAC
Beta-actin_Re	ATGGAGCCACCGATCCACA

Western blot for IDE in red blood cells used to corroborate the genotype of IDE^{+/+} and IDE^{-/-} mice. Approximately 15 μ L blood was collected from a tail nick as described in previous procedures into EDTA-coated capillary tubes (Microvette 200 μ L, Sarstedt). A portion of the blood sample (5 μ L) was combined with 5 μ L phosphate-buffered saline (PBS) and 10 μ L loading buffer (LDS NuPage, Life Technologies) containing 0.125 mM dithioerythritol. The sample was heated at 95 $^{\circ}$ C for 10 min, and 2 μ L of the mixture (total 0.5 μ L blood) was loaded into a polyacrylamide gel (4-12% gradient NuPage, Life Technologies). Following electrophoresis and transfer, the PVDF membrane (Immobilon, Millipore) was incubated with blocking buffer (Rockland) at RT for 1 h, and washed with PBS. Primary antibody (1:200 dilution in PBS with 1% BSA, rabbit polyclonal anti-IDE #ab32216, Abcam) was incubated at RT for 1 h, and washed with 0.1% Tween-20 in PBS. Secondary antibody (1:10,000 dilution in PBS, IRDye 680LT goat polyclonal anti-rabbit IgG #827-11081, Licor) was incubated at RT for 1 h, washed with 0.1% Tween-20 in PBS, and imaged on an Odyssey fluorescence scanner (Licor). Western blot of red blood cells was used to confirm the presence of IDE in WT IDE^{+/+} mice as an apparent \sim 100 kD band, and the absence of IDE in IDE^{-/-} KO mice.

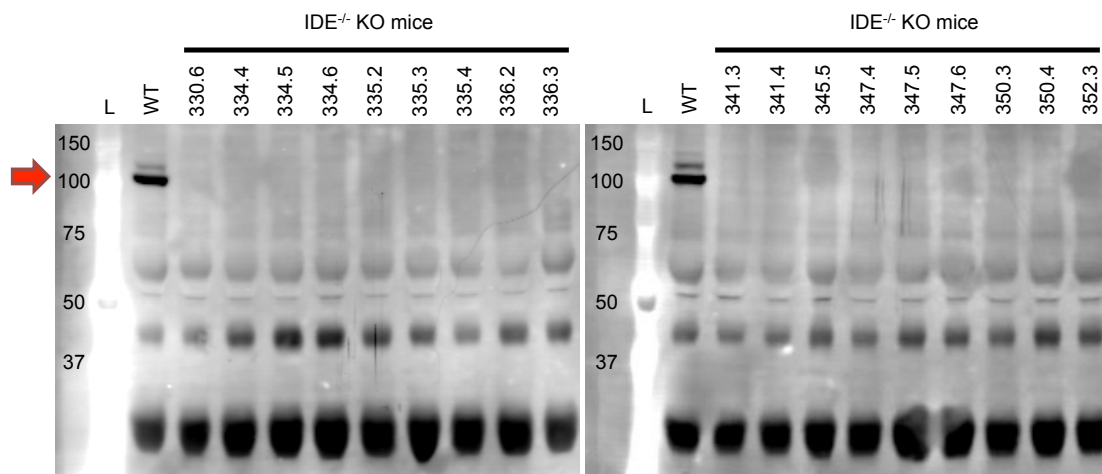


Figure 4.14 | Western blot assay to confirm IDE^{-/-} mice genotypes. Knockout IDE^{-/-} mice and IDE^{+/+} control littermates were obtained from the Leissring group. Western blot for IDE using whole blood lysate (0.5 μ L/well) from IDE^{-/-} mice and a wild-type (WT) control

(**Figure 4.14 cont.**) sample. IDE is observed as a ~100 KDa band (indicated by an arrow). The major non-specific band is consistent with hemoglobin subunits (~16 KDa).

4.10 – References

- 1 Andrikopoulos, S., Blair, A. R., Deluca, N., Fam, B. C. & Proietto, J. Evaluating the glucose tolerance test in mice. *American journal of physiology. Endocrinology and metabolism* **295**, E1323-1332, (2008).
- 2 Ahren, B., Holst, J. J., Martensson, H. & Balkan, B. Improved glucose tolerance and insulin secretion by inhibition of dipeptidyl peptidase IV in mice. *European journal of pharmacology* **404**, 239-245, (2000).
- 3 Winzell, M. S. & Ahren, B. The high-fat diet-fed mouse: a model for studying mechanisms and treatment of impaired glucose tolerance and type 2 diabetes. *Diabetes* **53 Suppl 3**, S215-219, (2004).
- 4 Ahren, B., Winzell, M. S. & Pacini, G. The augmenting effect on insulin secretion by oral versus intravenous glucose is exaggerated by high-fat diet in mice. *The Journal of endocrinology* **197**, 181-187, (2008).
- 5 Surwit, R. S., Kuhn, C. M., Cochrane, C., McCubbin, J. A. & Feinglos, M. N. Diet-induced type II diabetes in C57BL/6J mice. *Diabetes* **37**, 1163-1167, (1988).
- 6 Abdul-Hay, S. O. *et al.* Deletion of insulin-degrading enzyme elicits antipodal, age-dependent effects on glucose and insulin tolerance. *PLoS One* **6**, e20818, (2011).
- 7 Monzillo, L. U. & Hamdy, O. Evaluation of insulin sensitivity in clinical practice and in research settings. *Nutrition reviews* **61**, 397-412, (2003).
- 8 Riddle, M. C. & Drucker, D. J. Emerging therapies mimicking the effects of amylin and glucagon-like peptide 1. *Diabetes Care* **29**, 435-449, (2006).

- 9 Kolterman, O. G., Gottlieb, A., Moyses, C. & Colburn, W. Reduction of postprandial hyperglycemia in subjects with IDDM by intravenous infusion of AC137, a human amylin analogue. *Diabetes Care* **18**, 1179-1182, (1995).
- 10 Drucker, D. J. The biology of incretin hormones. *Cell Metab* **3**, 153-165, (2006).
- 11 Workman, P. & Collins, I. Probing the probes: fitness factors for small molecule tools. *Chem Biol* **17**, 561-577, (2010).
- 12 Stella, V. J. & He, Q. Cyclodextrins. *Toxicologic pathology* **36**, 30-42, (2008).
- 13 Mirsky, I. A. & Broh-Kahn, R. H. The inactivation of insulin by tissue extracts; the distribution and properties of insulin inactivating extracts. *Arch Biochem* **20**, 1-9, (1949).
- 14 Duckworth, W. C., Bennett, R. G. & Hamel, F. G. Insulin degradation: progress and potential. *Endocr Rev* **19**, 608-624, (1998).
- 15 Mooradian, A. D. & Thurman, J. E. Drug therapy of postprandial hyperglycaemia. *Drugs* **57**, 19-29, (1999).
- 16 Hollander, P. *et al.* Effect of pramlintide on weight in overweight and obese insulin-treated type 2 diabetes patients. *Obesity research* **12**, 661-668, (2004).
- 17 Kim, D. *et al.* (2R)-4-oxo-4-[3-(trifluoromethyl)-5,6-dihydro[1,2,4]triazolo[4,3-a]pyrazin-7(8H)-yl]-1-(2,4,5-trifluorophenyl)butan-2-amine: a potent, orally active dipeptidyl peptidase IV inhibitor for the treatment of type 2 diabetes. *J Med Chem* **48**, 141-151, (2005).
- 18 Leissring, M. A. & Selkoe, D. J. Structural biology: enzyme target to latch on to. *Nature* **443**, 761-762, (2006).
- 19 Leissring, M. A. *et al.* Designed inhibitors of insulin-degrading enzyme regulate the catabolism and activity of insulin. *PLoS One* **5**, e10504, (2010).

- 20 Farris, W. *et al.* Insulin-degrading enzyme regulates the levels of insulin, amyloid beta-protein, and the beta-amyloid precursor protein intracellular domain in vivo. *Proc Natl Acad Sci U S A* **100**, 4162-4167, (2003).
- 21 Malito, E., Hulse, R. E. & Tang, W. J. Amyloid beta-degrading cryptidases: insulin degrading enzyme, presequence peptidase, and neprilysin. *Cellular and molecular life sciences : CMLS* **65**, 2574-2585, (2008).
- 22 Shen, Y., Joachimiak, A., Rosner, M. R. & Tang, W. J. Structures of human insulin-degrading enzyme reveal a new substrate recognition mechanism. *Nature* **443**, 870-874, (2006).
- 23 Guo, Q., Manolopoulou, M., Bian, Y., Schilling, A. B. & Tang, W. J. Molecular basis for the recognition and cleavages of IGF-II, TGF-alpha, and amylin by human insulin-degrading enzyme. *J Mol Biol* **395**, 430-443, (2010).
- 24 Duckworth, W. C. & Kitabchi, A. E. Insulin and glucagon degradation by the same enzyme. *Diabetes* **23**, 536-543, (1974).
- 25 Shroyer, L. A. & Varandani, P. T. Purification and characterization of a rat liver cytosol neutral thiol peptidase that degrades glucagon, insulin, and isolated insulin A and B chains. *Archives of biochemistry and biophysics* **236**, 205-219, (1985).
- 26 Bennett, R. G., Duckworth, W. C. & Hamel, F. G. Degradation of amylin by insulin-degrading enzyme. *J Biol Chem* **275**, 36621-36625, (2000).
- 27 Authier, F., Mort, J. S., Bell, A. W., Posner, B. I. & Bergeron, J. J. Proteolysis of glucagon within hepatic endosomes by membrane-associated cathepsins B and D. *J Biol Chem* **270**, 15798-15807, (1995).
- 28 Fontes, G. *et al.* Miniglucagon (MG)-generating endopeptidase, which processes glucagon into MG, is composed of N-arginine dibasic convertase and aminopeptidase B. *Endocrinology* **146**, 702-712, (2005).
- 29 Trebbien, R. *et al.* Neutral endopeptidase 24.11 is important for the degradation of both endogenous and exogenous glucagon in anesthetized pigs.

- American journal of physiology. Endocrinology and metabolism* **287**, E431-438, (2004).
- 30 Kaidanovich-Beilin, O. & Eldar-Finkelman, H. Long-term treatment with novel glycogen synthase kinase-3 inhibitor improves glucose homeostasis in ob/ob mice: molecular characterization in liver and muscle. *J Pharmacol Exp Ther* **316**, 17-24, (2006).
 - 31 Meng, R., Zhu, D., Bi, Y., Yang, D. & Wang, Y. Erythropoietin inhibits gluconeogenesis and inflammation in the liver and improves glucose intolerance in high-fat diet-fed mice. *PLoS One* **8**, e53557, (2013).
 - 32 Young, A. Effects on plasma glucose and lactate. *Adv Pharmacol* **52**, 193-208, (2005).
 - 33 Gelling, R. W. *et al.* Lower blood glucose, hyperglucagonemia, and pancreatic alpha cell hyperplasia in glucagon receptor knockout mice. *Proc Natl Acad Sci U S A* **100**, 1438-1443, (2003).
 - 34 Vuguin, P. M. & Charron, M. J. Novel insight into glucagon receptor action: lessons from knockout and transgenic mouse models. *Diabetes, obesity & metabolism* **13 Suppl 1**, 144-150, (2011).
 - 35 Lee, Y., Wang, M. Y., Du, X. Q., Charron, M. J. & Unger, R. H. Glucagon receptor knockout prevents insulin-deficient type 1 diabetes in mice. *Diabetes* **60**, 391-397, (2011).
 - 36 Ali, S., Lamont, B. J., Charron, M. J. & Drucker, D. J. Dual elimination of the glucagon and GLP-1 receptors in mice reveals plasticity in the incretin axis. *The Journal of clinical investigation* **121**, 1917-1929, (2011).
 - 37 Gedulin, B. R., Jodka, C. M., Herrmann, K. & Young, A. A. Role of endogenous amylin in glucagon secretion and gastric emptying in rats demonstrated with the selective antagonist, AC187. *Regulatory peptides* **137**, 121-127, (2006).

- 38 Watanabe, C. *et al.* Remodeling of hepatic metabolism and hyperaminoacidemia in mice deficient in proglucagon-derived peptides. *Diabetes* **61**, 74-84, (2012).
- 39 Mack, C. M. *et al.* Davalintide (AC2307), a novel amylin-mimetic peptide: enhanced pharmacological properties over native amylin to reduce food intake and body weight. *Int J Obes (Lond)* **34**, 385-395, (2010).
- 40 Young, A. Inhibition of glucagon secretion. *Adv Pharmacol* **52**, 151-171, (2005).
- 41 Crowell, M. D., Mathis, C., Schettler, V. A., Yunus, T. & Lacy, B. E. The effects of tegaserod, a 5-HT receptor agonist, on gastric emptying in a murine model of diabetes mellitus. *Neurogastroenterology and motility : the official journal of the European Gastrointestinal Motility Society* **17**, 738-743, (2005).
- 42 Zhang, C. *et al.* Isolation and characterization of a novel glycogen synthase kinase-3 gene, GmGSK, in *Glycine max* L. that enhances abiotic stress tolerance in *Saccharomyces cerevisiae*. *Biotechnology letters* **32**, 861-866, (2010).
- 43 Kim, Y. G., Lone, A. M., Nolte, W. M. & Saghatelian, A. Peptidomics approach to elucidate the proteolytic regulation of bioactive peptides. *Proc Natl Acad Sci U S A* **109**, 8523-8527, (2012).
- 44 Zambrowicz, B. P. & Sands, A. T. Knockouts model the 100 best-selling drugs--will they model the next 100? *Nat Rev Drug Discov* **2**, 38-51, (2003).
- 45 Karamohamed, S. *et al.* Polymorphisms in the insulin-degrading enzyme gene are associated with type 2 diabetes in men from the NHLBI Framingham Heart Study. *Diabetes* **52**, 1562-1567, (2003).
- 46 Gu, H. F. *et al.* Quantitative trait loci near the insulin-degrading enzyme (IDE) gene contribute to variation in plasma insulin levels. *Diabetes* **53**, 2137-2142, (2004).

- 47 Sladek, R. *et al.* A genome-wide association study identifies novel risk loci for type 2 diabetes. *Nature* **445**, 881-885, (2007).
- 48 Zeggini, E. *et al.* Replication of genome-wide association signals in UK samples reveals risk loci for type 2 diabetes. *Science* **316**, 1336-1341, (2007).
- 49 Bartl, J. *et al.* Disorder-specific effects of polymorphisms at opposing ends of the Insulin Degrading Enzyme gene. *BMC medical genetics* **12**, 151, (2011).
- 50 Mariappan, M. M., Shetty, M., Sataranatarajan, K., Choudhury, G. G. & Kasinath, B. S. Glycogen synthase kinase 3beta is a novel regulator of high glucose- and high insulin-induced extracellular matrix protein synthesis in renal proximal tubular epithelial cells. *J Biol Chem* **283**, 30566-30575, (2008).
- 51 Unger, R. H. & Cherrington, A. D. Glucagonocentric restructuring of diabetes: a pathophysiologic and therapeutic makeover. *The Journal of clinical investigation* **122**, 4-12, (2012).
- 52 Sadry, S. A. & Drucker, D. J. Emerging combinatorial hormone therapies for the treatment of obesity and T2DM. *Nature reviews. Endocrinology* **9**, 425-433, (2013).
- 53 Knight, Z. A. & Shokat, K. M. Chemical genetics: where genetics and pharmacology meet. *Cell* **128**, 425-430, (2007).
- 54 Yang, Q. *et al.* Pharmacological inhibition of BMK1 suppresses tumor growth through promyelocytic leukemia protein. *Cancer cell* **18**, 258-267, (2010).
- 55 Weisberg, E. *et al.* Beneficial effects of combining a type II ATP competitive inhibitor with an allosteric competitive inhibitor of BCR-ABL for the treatment of imatinib-sensitive and imatinib-resistant CML. *Leukemia* **24**, 1375-1378, (2010).
- 56 Wang, L. *et al.* A small molecule modulates Jumonji histone demethylase activity and selectively inhibits cancer growth. *Nature communications* **4**, 2035, (2013).

- 57 Wang, F. *et al.* Identification of a small molecule with activity against drug-resistant and persistent tuberculosis. *Proc Natl Acad Sci U S A* **110**, E2510-2517, (2013).
- 58 Taipale, M. *et al.* Chaperones as thermodynamic sensors of drug-target interactions reveal kinase inhibitor specificities in living cells. *Nat Biotechnol* **31**, 630-637, (2013).
- 59 Matzuk, M. M. *et al.* Small-molecule inhibition of BRDT for male contraception. *Cell* **150**, 673-684, (2012).
- 60 Anastasiou, D. *et al.* Pyruvate kinase M2 activators promote tetramer formation and suppress tumorigenesis. *Nat Chem Biol* **8**, 839-847, (2012).
- 61 Gottlieb, H. E., Kotlyar, V. & Nudelman, A. NMR Chemical Shifts of Common Laboratory Solvents as Trace Impurities. *The Journal of organic chemistry* **62**, 7512-7515, (1997).
- 62 Kleiner, R. E., Dumelin, C. E., Tiu, G. C., Sakurai, K. & Liu, D. R. In vitro selection of a DNA-templated small-molecule library reveals a class of macrocyclic kinase inhibitors. *J Am Chem Soc* **132**, 11779-11791, (2010).
- 63 Georghiou, G., Kleiner, R. E., Pulkoski-Gross, M., Liu, D. R. & Seeliger, M. A. Highly specific, bisubstrate-competitive Src inhibitors from DNA-templated macrocycles. *Nat Chem Biol* **8**, 366-374, (2012).

Chapter 5

Discovery of substrate-selective IDE inhibitors that obstruct insulin degradation but allow IDE-mediated glucagon proteolysis

Patent pending: PCT/US2014/064322 (Nov. 4, 2014)

Patent pending: PCT/US 62/152,723 (Apr. 24, 2015)

Contributions: I designed and performed the experiments described in this chapter. Dr. Amedeo Vetere and Dr. Bridget Wager assisted with the implementation of the high-throughput screen at the Broad Institute. Zachariah H. Foda (Stony Brook University) performed the docking simulations. Help from other colleagues is acknowledged in the text.

5.1 – Introduction: the need for new substrate-selective IDE inhibitors

The first-generation IDE inhibitor **6bK** acts as a competitive inhibitor that obstructs the interactions with the IDE chamber that are essential for binding and unfolding of all known *in vitro* and *in vivo* hormone substrates^{1,2} (>29-51 residues). Likewise **6bK** completely blocks the degradation of the relatively small fluorogenic decapeptide substrate used in the standard IDE assay³. The unbiased competitive mode of inhibition of **6bK** was desirable for the first *in vivo*-active probe tool in order to characterize all the physiological roles of IDE. However, looking towards potential therapeutic applications, a more efficacious class of IDE inhibitors would preferentially block insulin degradation, while permitting glucagon clearance at all times, to further bolster blood glucose control⁴. Indeed, the potentiation of the opposing physiological functions of insulin and glucagon by a traditional substrate-competitive IDE inhibitor is arguably the crucial liability of IDE as a drug target⁵. These observations strongly suggested that we needed to move beyond the **6b** series to discover new IDE inhibitors with a focus on identifying insulin *versus* glucagon substrate discriminating features and drug-like properties.

Other reported inhibitors of IDE, including **Ii1** and **ML345**, also block all substrates from binding the IDE chamber⁶⁻⁸. Because of the known homodimer cooperativity of IDE some researchers have observed modest shifting of the IC₅₀ between some substrates (insulin and A β)^{9,10}. Consistently with the IDE literature¹¹, these effects appear to be biochemical assay artifacts that occur when the binding sites in the IDE homodimer are partially occupied by ligands in the presence of

excess substrate, a condition that is not relevant *in vivo*¹². Modulators of IDE that discriminate among substrates throughout a range of concentrations relevant to target engagement *in vivo* have not been reported. The discovery of substrate-selective IDE inhibitors that abrogate IDE's degradation of insulin but have negligible effect on IDE-mediated degradation of glucagon would represent a major step forward towards IDE-targeted therapeutics.

5.2 – Optimization of an anisotropy assay using a fluorescent probe based on the first-generation DNA-templated macrocyclic inhibitor

Many groups have previously screened for inhibitors of IDE^{6,7,10,13,14}, yet in spite of the advances in high-throughput screening, IDE-specific inhibition among >185 zinc-dependent metalloproteases encoded in the human and mouse genomes¹⁵ represents a major challenge to mainstream drug discovery platforms that rely on activity-based screening of compound collections^{16,17}. Unspecific modes of inhibition, zinc chelation, and covalent adducts to the cysteine residues on the inner chamber of IDE, produce an unacceptable rate of false-positive hits that seldom discriminate specifically among homolog metalloproteases⁷. Indeed, prior to this work the scope of studies towards IDE inhibitors comprised of: 1) designed zinc-chelating hydroxamic acid linear peptide inhibitors^{6,9} that are modestly selective for IDE and have short half-lives *in vivo*⁷; 2) carboxylic acid-based modestly potent inhibitors¹⁰; and 3) a thiol-reactive covalent inhibitor identified from a high-throughput screening effort⁷ (Chapter 1, **Figure 1.11**). The specificity of this adduct

was tentatively determined at low concentrations $<2 \mu\text{M}$, and *in vivo* activity was not reported⁷. The limited results from these previous studies underscore the need for alternative methods to identify IDE inhibitors. The unbiased nature of the *in vitro* selection using the DNA-templated library led to the identification of a novel small-molecule binding site in IDE that enables unprecedented inhibition specificity for this enzyme (Chapter 2). We hypothesized that these structural insights may also prove useful in the discovery of novel drug-like small-molecule leads to target IDE.

To identify new IDE inhibitors that target the distal binding site I developed a fluorescence anisotropy probe-displacement assay¹⁸ based on the structure of the first-generation IDE inhibitor **6b** (**FL-6b**, **Figure 5.1**). Anisotropy is the property of retention of polarization in emitted light when an stationary fluorophore is excited with polarized light¹⁸. However, solutions of fluorescent molecules of low molecular weight ($<1,000$ Da) display anisotropy only while physically bound to a large target (typically $>10,000$ Da) such that the complex tumbles slowly in solution¹⁸. The simple tagging design of **FL-6b** is based on the general feature of the covalent linker of DNA-encoded library hits, and it has been useful to validate putative binders from *in vitro* selection experiments¹⁹. However, the possibility of retailoring a hit from a DNA-templated library selection to perform a high-throughput screen had not been demonstrated. Indeed, in order to scale up a fluorescence anisotropy probe-displacement assay that enables screening of large small-molecule collections the following conditions need to be met¹⁸: *i*) the target needs to be available in high purity and scale usually $>100 \mu\text{g}$ per 384-well plate; *ii*) the fluorescent probe must

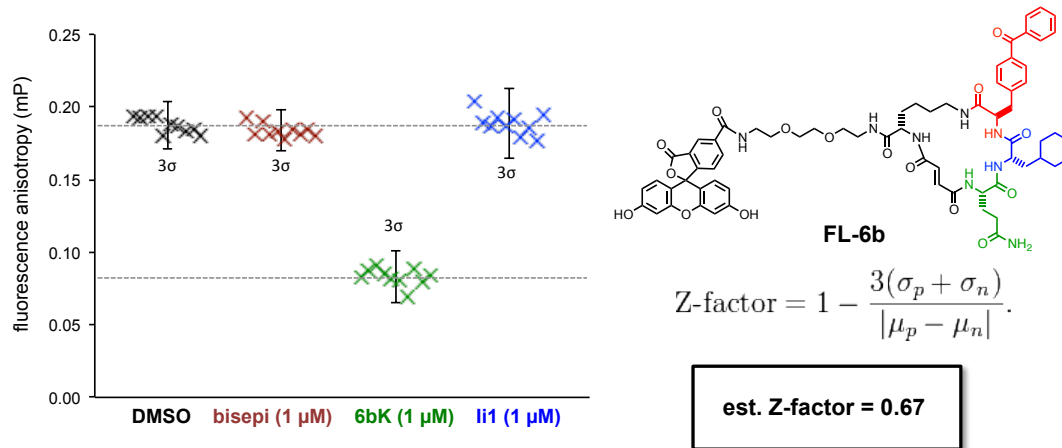


Figure 5.1 | Optimization of an anisotropy-based assay using the fluorescent probe FL-6b, based on the DNA-templated IDE inhibitor 6b. Anisotropy readout from FL-6b (5 nM) by competitive binding to IDE (0.1 μM). Inhibitor 6bK (1 μM) displaces the probe lowering fluorescence anisotropy with excellent signal-to-noise ratio, on the other hand neither the catalytic-site binder li1 (1 μM) nor the low affinity bisepi-6bK (1 μM) produce a significant readout.

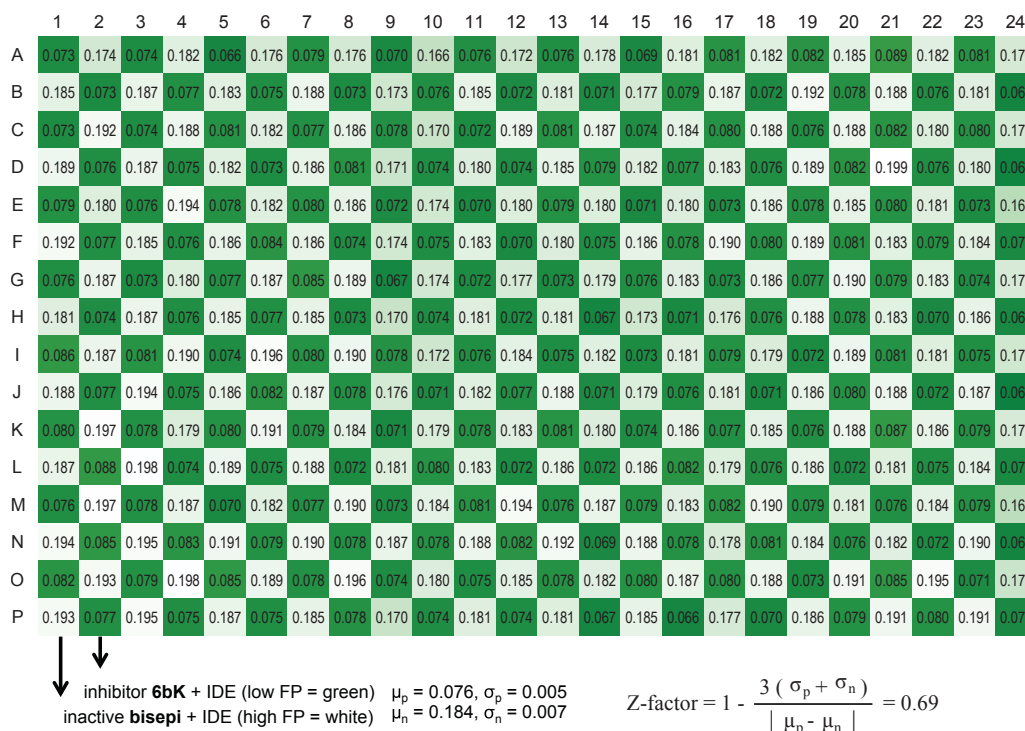


Figure 5.2 | Determination of the assay Z-factor. A 384-well checkerboard (raw data shown in green-white heatmap) was set up using 50 μL total volume (50 mM Tris buffer, pH 7.5, 1.0 M NaCl, 5% DMSO) in the presence of inhibitor 6bK (1 μM) or inactive control bisepi-6bK (1 μM).

have $K_D < 100$ nM and be specific in the presence of high target concentrations $>0.5 - 5$ μ M of target; *iii*) the Z-factor must be > 0.5 and the readout should ideally be stable >15 min to 1 hr; *iv*) a counter-screening method is required to identify inhibitors among the probe-displacing molecules; and *v*) to minimize false-positives the library collection must be non-fluorescent.

In preliminary experiments I showed that **6bK** (1 μ M) leads to a drop in anisotropy by displacement of **FL-6b** from the complex with N-His₆-hIDE₍₄₂₋₁₀₁₉₎ which I expressed and purified from *E. coli* (**Figure 5.1**). The **FL-6b** anisotropy readout was unchanged by treatment with either DMSO alone (5%), with the low affinity ligand **bisepi-6bK**, or with the catalytic domain binder **Ii1**⁶. Finally, the Z-factor > 0.69 was calculated for 384-wells containing either **6bK** (1 μ M) as the positive control, or **bisepi-6bK** (μ M) as the negative control (**Figure 5.2**). To further validate the specificity of **FL-6b** for the IDE distal binding pocket at high protein concentration I titrated the fluorescent probe (5 nM final) using wild-type IDE and the IDE variants Ala479Leu and Gly362Gln. The anisotropy readout of **FL-6b** matched the inhibition potency of **6bK** against each of the three protein variants (**Figure 5.3**). These experiments demonstrated that the fluorescein appendage does not disrupt the selectivity for the distal binding site of IDE, and that the anisotropy probe-displacement Z-factor is suitable for high-throughput screening applications.

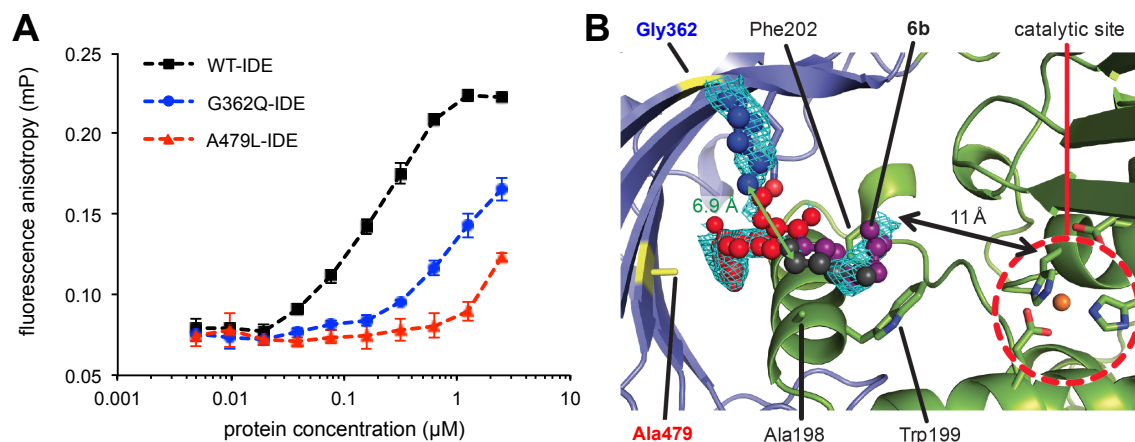


Figure 5.3 | Validation of on-target binding for the probe FL-6b using IDE variants.

The probe (5 nM) was titrated with either wild-type IDE or binding-site mutants A479L and G362Q that hinder binding of the probe to the distal inhibitory site of IDE. The pattern is comparable to **6bK** inhibition potencies for the same IDE variants (see **Figure 2.12**).

5.3 – High-throughput screening of the Broad Institute libraries

In collaboration with Dr. Amedeo Vetere and Dr. Bridget Wagner (Broad Institute) we set up an EnVision spectrophotometer equipped with an automatic plate stacker to read the **FL-6b** anisotropy assay. First, we tested the assay by pin-transfer of a collection of 1000 bioactive small molecules and approved drugs in DMSO (10 mM), called the “pharmakon” plates (**Figure 5.4**). The anisotropy readout was converted to standard Z-scores over the average for the negative control wells (DMSO alone). This preliminary trial produced a Z-factor > 0.6 for the **6bK** positive controls. As expected a number of fluorescent compounds (e.g. doxorubicin and fluorescein) appeared as false positives, and among the non-fluorescent molecules with lowest Z-score we noted the antibiotic bacitracin, which is a weak competitive inhibitor of IDE ($IC_{50} = 10 \mu\text{M}$). These preliminary results were encouraging to scale

up the assay to use a collection of “informer set” plates with 10,000 compounds that are representative of multiple libraries at the Broad Institute (**Figure 5.5**).

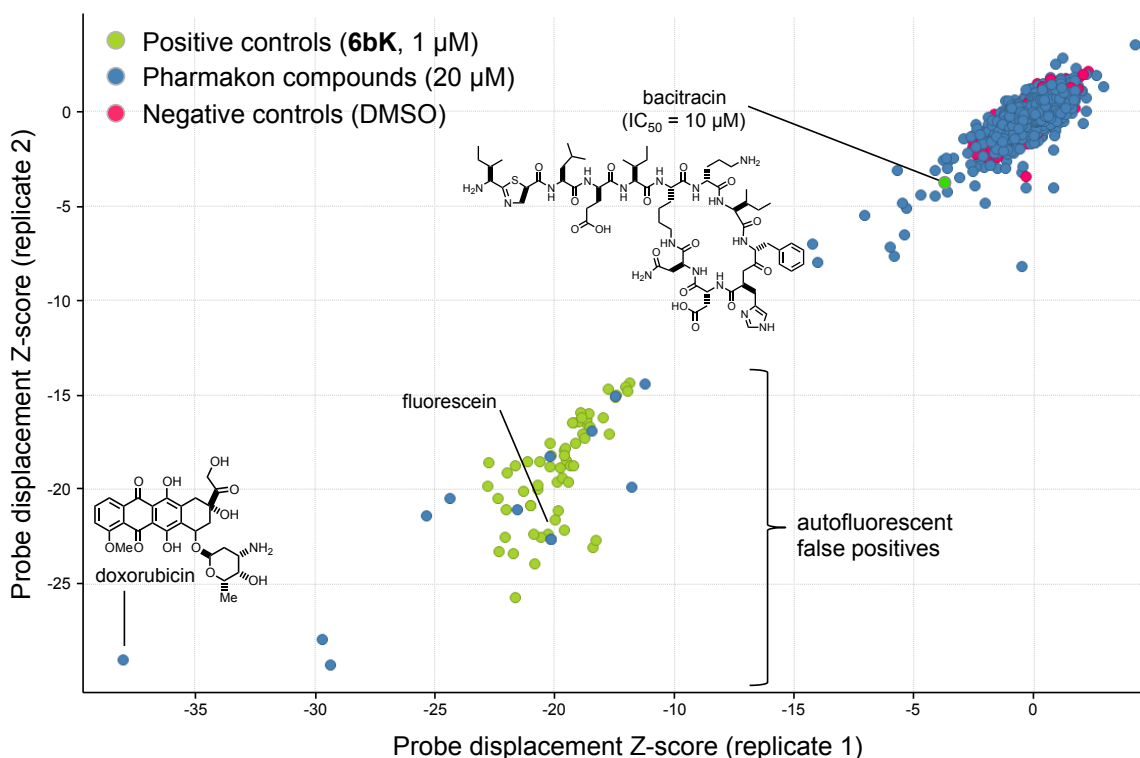


Figure 5.4 | Validation of the anisotropy assay in high-throughput mode using 1,000 drug/bioactive compounds. First trial using pin-transfer of a collection of 1,000 drug/bioactive small molecules in DMSO (10 mM), called “pharmakon” plates. Human N-His₆-IDE₄₂₋₁₀₁₉ (*E. coli* expressed) was mixed with fluorescein-labeled macrocycle **FL-6b** (30 nM) generating a high anisotropy signal in the presence of negative control DMSO (●), or with inactive compounds (●). The inhibitor **6bK** (1 μM), used here as a positive control (●) displaces analog **FL-6b** lowering fluorescence anisotropy with excellent signal-to-noise ratio (Z-factor > 0.6). All the false positive hits display autofluorescence (e.g. fluorescein and doxorubicin), which is not expected for the DOS libraries of the Broad Institute.

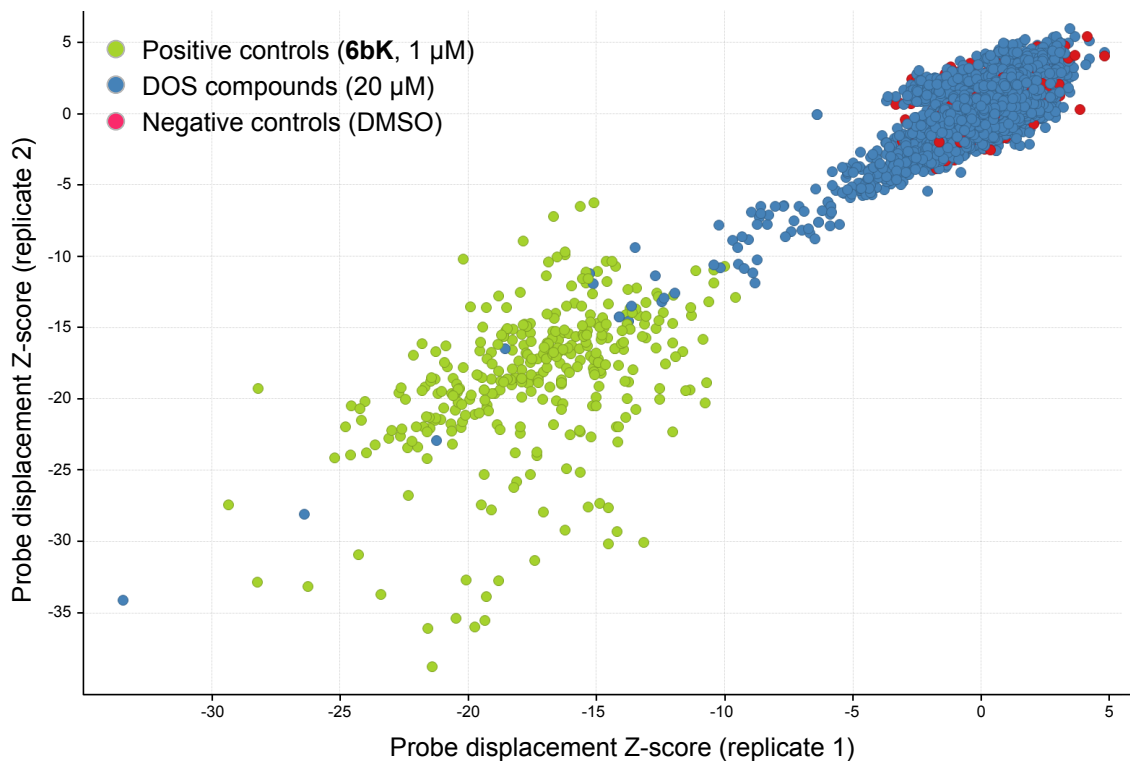


Figure 5.5 | High-throughput anisotropy probe-displacement assay screen using 10,000 compound informer set of the Broad Institute library collections. Unbiased screen with pin-transfer of "DOS informer set" plates comprising 10,000 compounds originating from multiple compound collections. Human N-His₆-IDE₄₂₋₁₀₁₉ (*E. coli* expressed) was mixed with fluorescein-labeled macrocycle **FL-6b** (30 nM) generating a high anisotropy signal in the presence of negative control DMSO (●), or with inactive compounds (●). The inhibitor **6bK** (1 μM), used here as a positive control (●) displaces analog **FL-6b** lowering fluorescence anisotropy with excellent signal-to-noise ratio (Z-factor > 0.5).

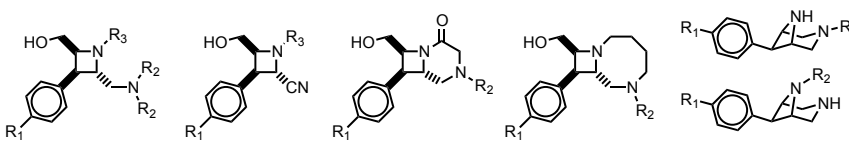
The screen of the "DOS informer set" plates revealed 16 putative IDE binders originating from 3 compound collections (**Figure 5.5**). The set of analogs and stereochemical isomers available at the Broad Institute were purchased to determine the IC₅₀ values using the fluorogenic peptide IDE assay for counter-screening and to reveal the stereochemical structure-activity relationships (SSAR).

First I focused on the biphenyl ether series²⁰ that bears resemblance to the **6b** benzophenone (**Figure 5.6A**). These hits were purchased from the Broad Institute, together with a set 75 structural analogs and stereoisomers, and I used the fluorogenic counter-screening assay to identify several hits of ~1-2 μ M potency. However, the stereochemistry of the macrocyclic portion did not appear to be crucial for inhibition. This SSAR trend suggested the pharmacophore 4-phenoxy-*N*-phenylbenzamide bears most of the ligand efficiency. The hits **BRD-194** and **BRD-815** were further investigated in metalloprotease specificity assays, which revealed these molecules were not sufficiently selective, potentially due to aggregator properties (Section 5.4). Preliminarily, we concluded that this series may prove most useful to extract the pharmacophore 4-phenoxy-*N*-phenylbenzamide, given that this drug-like fragment can be easily derived into a series of analogs in the future. A second group of modestly potent hits belongs to the tricyclic-glycal libraries²¹, however, a search of the Broad databases provided insufficient analogs to study the SSAR (**Figure 5.6B**).

Importantly, more than half of the hits among the “DOS informer set” plates belonged to the azetidine-core library collections²² (**Figure 5.6C**). The compounds that I initially identified were modestly potent inhibitors, however, a chemoinformatic search performed in collaboration with by Mathias Wawer (Broad Institute) using biphenyl-azetidine as the query suggested that the preliminary screen would not capture the full diversity of the azetidine libraries²² (**Table 5.1**). Based on these observations, we performed a second high-throughput anisotropy probe displacement screen against a collection of azetidine core libraries that was biased

with >75% biaryl-substituted molecules (**Figure 5.7**). This effort led to the identification of over 100 putative IDE binding structures with Z-scores < -10 (0.1% hit rate). Next, I selected representative hit structures and determined the IC₅₀ using the fluorogenic decapeptide IDE assay. The resulting collection of 115 azetidine analogs that were purchased to determine the IC₅₀ values and SSAR are shown in **Figure 5.8**. This rich dataset yielded over 50 low- to sub-micromolar IDE inhibitors, which demonstrates the efficiency of the **FL-6b** probe displacement screening method towards the identification of IDE inhibitors and IDE binders with Lipinski-compliant drug-like scaffolds. Inspection of the fluorogenic peptide assay inhibition profiles revealed a class of IDE binders that incompletely block IDE-mediated cleavage (inhibition maximum, I_{MAX} < 100%). This observation provided a strong starting point to identify substrate-selective IDE inhibitors (**Figure 5.9**).

Table 5.1 | Chemoinformatic properties of Broad Institute azetidine libraries²².



DOS Library	Azetidine Amine	Azetidine Monoketo Piperazine	Azetidine Nitrile	Azetidine RCM	Azetidine Bridged Bicyclic	Total all azetidines
# compounds	1666	3048	1472	3228	1278	10692
# biaryl or bicyclic	476	2949	1073	2431	1172	8101
frequency	29%	97%	73%	75%	92%	76%



Figure 5.7 | High-throughput screening of biaryl-substituted azetidine libraries. The top 100 compounds highlighted (●) display low anisotropy signal for **FL-6b** (Z-score < -10).

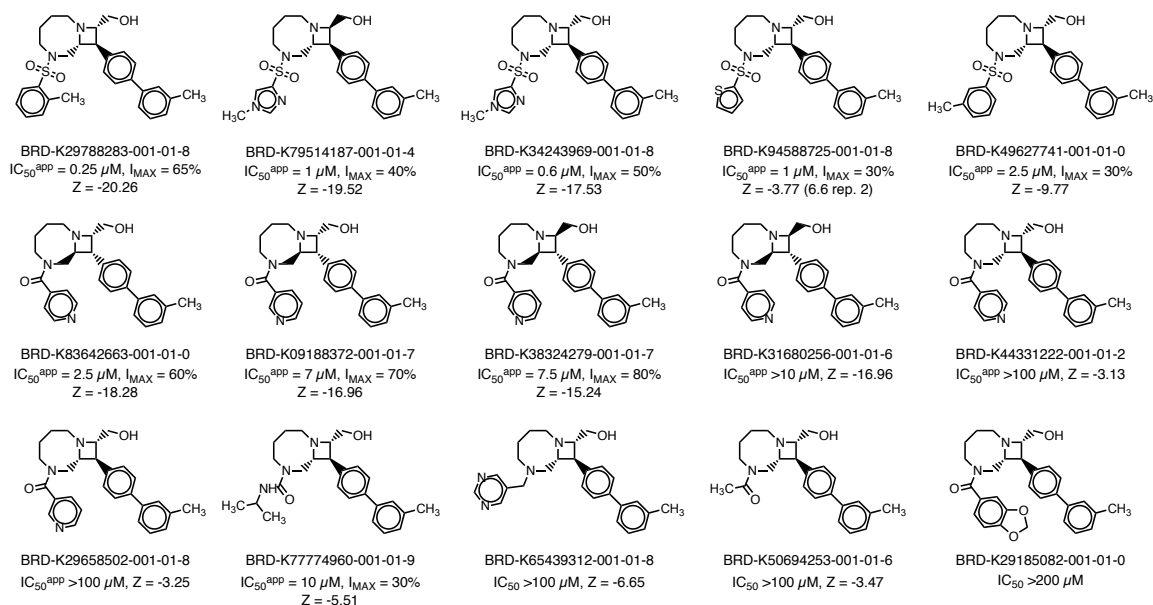


Figure 5.8 (continued in subsequent 3 pages) | Structures of azetidine hits identified as putative distal-site IDE binders and IDE inhibitors. The IC_{50} and I_{MAX} were determined using the fluorogenic peptide IDE proteolysis assay (Mca-RPPGFSAFK(Dnp)-OH).

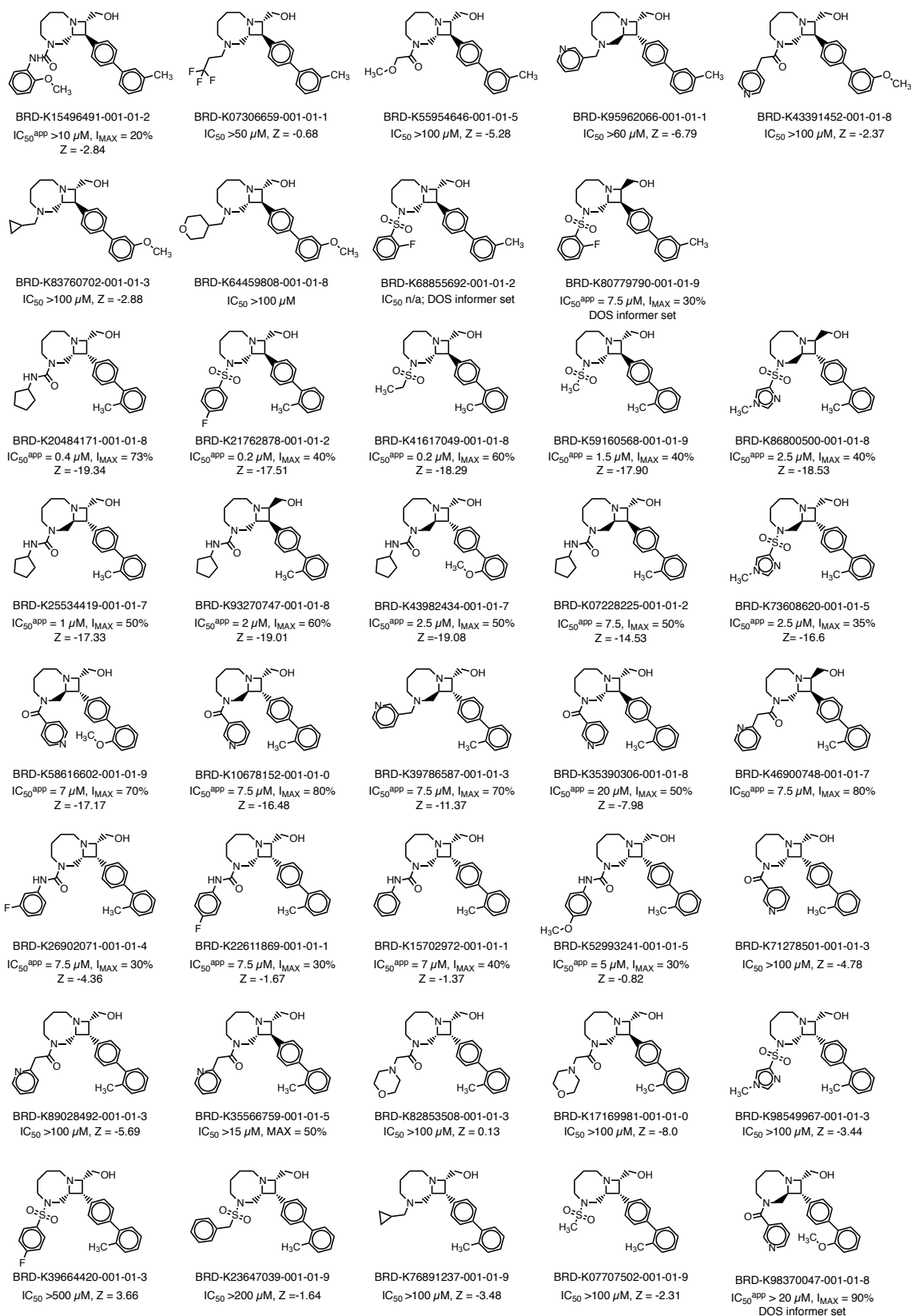


Figure 5.8 (cont.)

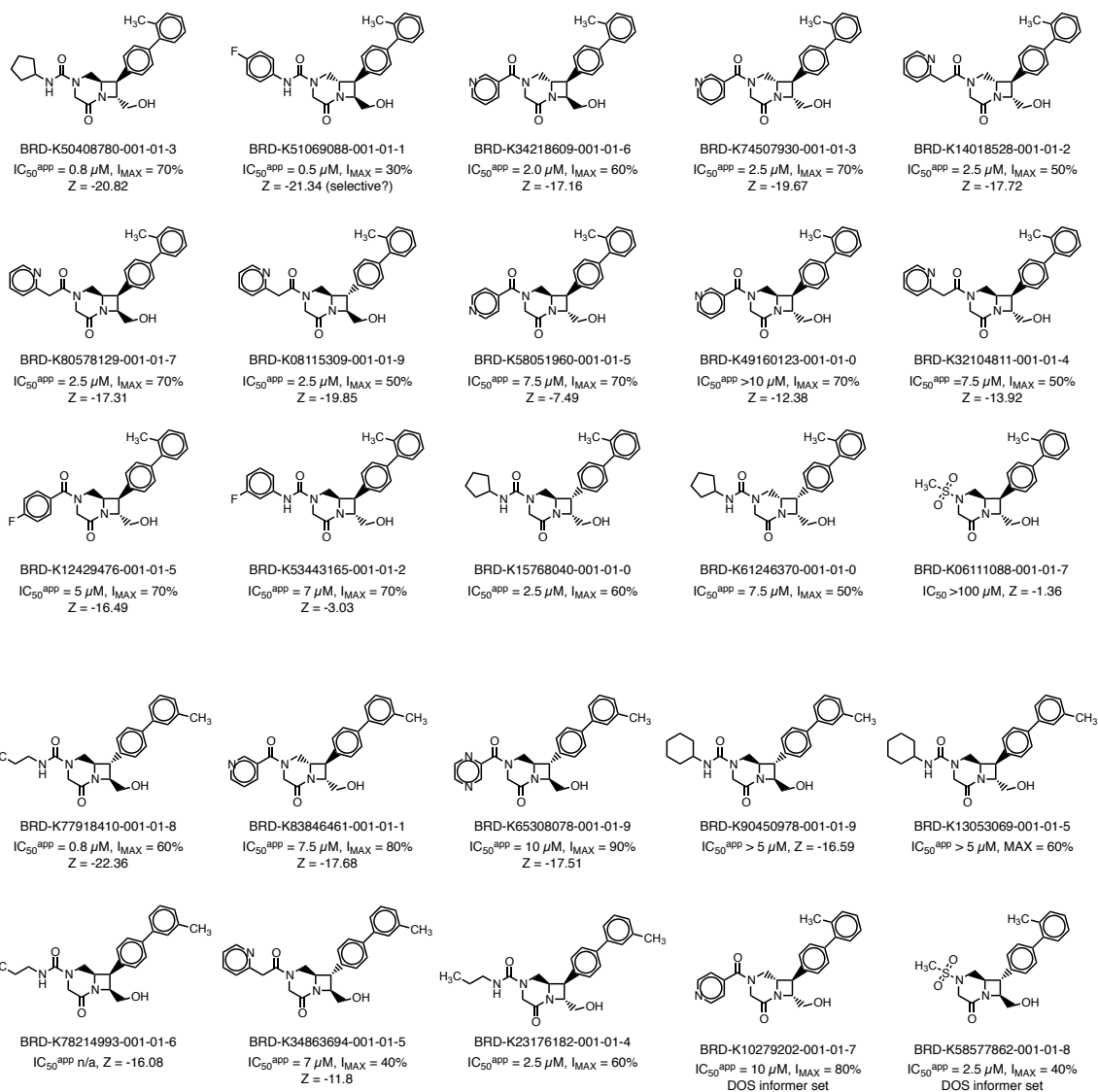


Figure 5.8 (cont.)

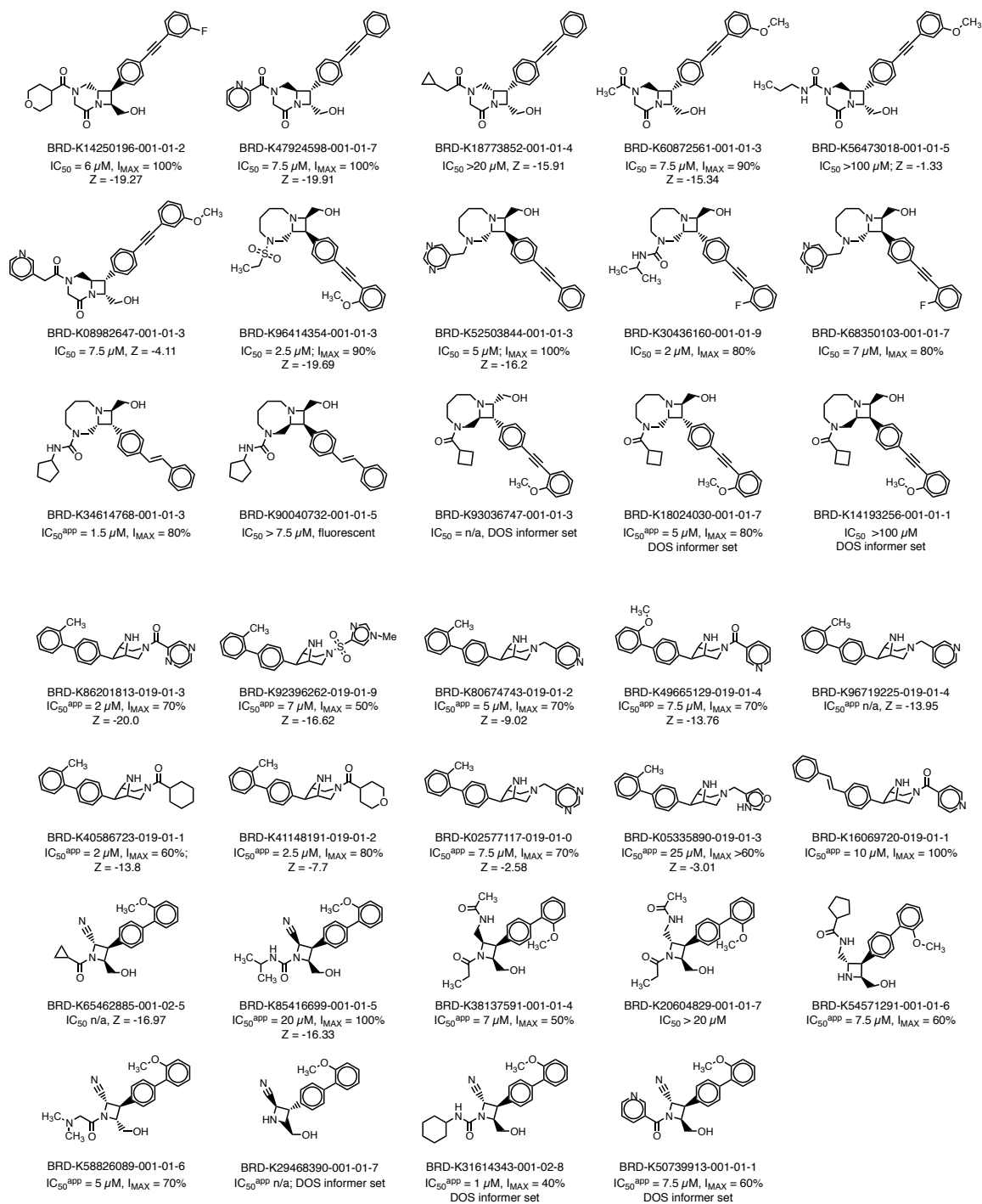


Figure 5.8 (cont.)

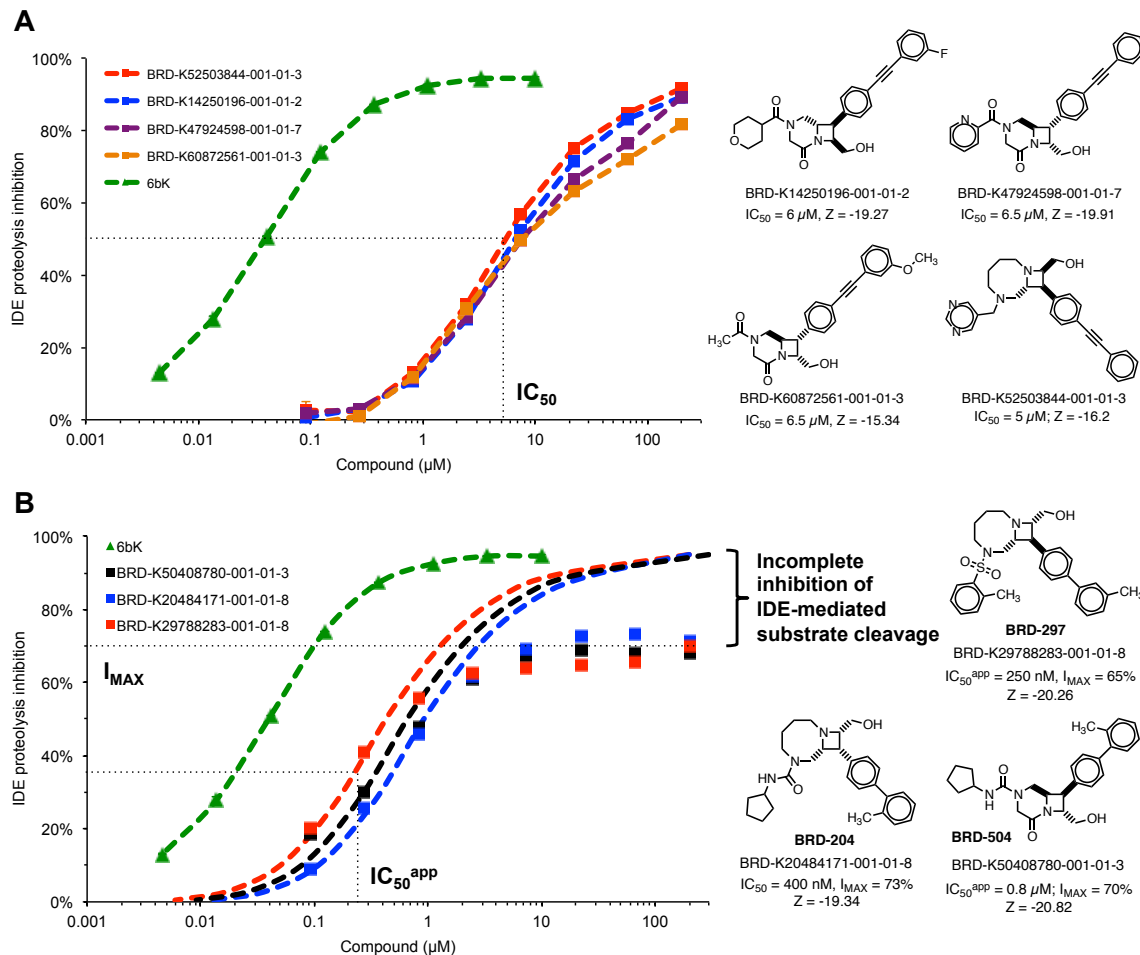


Figure 5.9 | Surrogate proteolysis assay used to identify substrate-selective IDE inhibitors that allow IDE-mediated proteolysis of small peptide substrates. (A) Representative examples of the concentration-dependent profiles of IDE inhibition for “normal” substrate competitive inhibitors, which display complete inhibition of IDE-mediated proteolysis of the fluorogenic Mca-RPPGFSAFK(Dnp)-OH. The inhibition maximum (I_{MAX}) is approximately 100% at high inhibitor concentrations. **(B)** Representative examples of the concentration-dependent IDE inhibition profiles for IDE binders that allow partial IDE-mediated proteolysis of the fluorogenic nonapeptide at all concentrations ($\text{I}_{\text{MAX}} < 100\%$), and that may display proteolytic activity as a ternary IDE-inhibitor-substrate complex.

5.4 – Discovery of substrate-selective inhibitors of IDE-mediated insulin degradation that allow glucagon proteolysis

The literature suggests that substrate-selective inhibition is exceedingly rare for most enzymes classes^{16,17,23}. Nevertheless, we hypothesized that owing to partial occlusion of the distal inhibitory site, a small molecule-IDE ternary complex may achieve substrate discrimination based on the differences in size, structure, and proteolysis kinetics between insulin and glucagon. Towards this goal, I investigated the collection of azetidine hits (**Figure 5.7**), and in particular I focused on a series of compounds with low *Z*-scores for **FL6b**-probe displacement that displayed sub-maximal inhibition of IDE proteolysis of the fluorogenic decapeptide substrate ($I_{MAX} = 70\text{--}80\%$, **Figure 5.8**). This fluorogenic assay reports on the cleavage of Mca-RPPGFSAFK(Dnp)-OH that has weak affinity for IDE ($K_M > 4 \mu\text{M}$) and loosely occupies the catalytic chamber (*e.g.* insulin has 51 residues, and glucagon 29 residues). Therefore, this surrogate assay can be used to reveal IDE binders that partially allow IDE-mediated proteolysis of small substrates, and also provides the IC_{50}^{app} parameter that is linked to the inhibitor affinity for IDE (K_i).

Next, I optimized dual antibody Homogeneous Time-Resolved FRET assays²⁴ against insulin and glucagon to reveal the extent of IDE-mediated cleavage during incubation in the presence of a series of inhibitors. As a control I showed that **6bK** displays concentration-dependent inhibition of IDE degradation of insulin and glucagon with similar EC_{50} (**Figure 5.10**). I selected a series of 16 azetidine compounds ($Z\text{-score} < -15$, $IC_{50}^{app} = 0.25\text{--}2 \mu\text{M}$, $I_{MAX} = 40\text{--}80\%$), which were used

in this assay at 67 μM ($>30 \times \text{IC}_{50}^{\text{app}}$) in order to ensure full occupancy of the IDE binding site, while this is also a conservative concentration that prevents assay artifacts (**Figure 5.11**). This focused screen revealed the desired substrate-selective inhibitory property in a small subset of azetidine IDE inhibitors, in particular **BRD-297** and **BRD-204** ($\text{IC}_{50} = 250 \text{ nM}$ and 400 nM , respectively), which were superior in obstructing IDE-mediated degradation of insulin, but allowed significant glucagon degradation to occur during the IDE incubation (**Figure 5.11**).

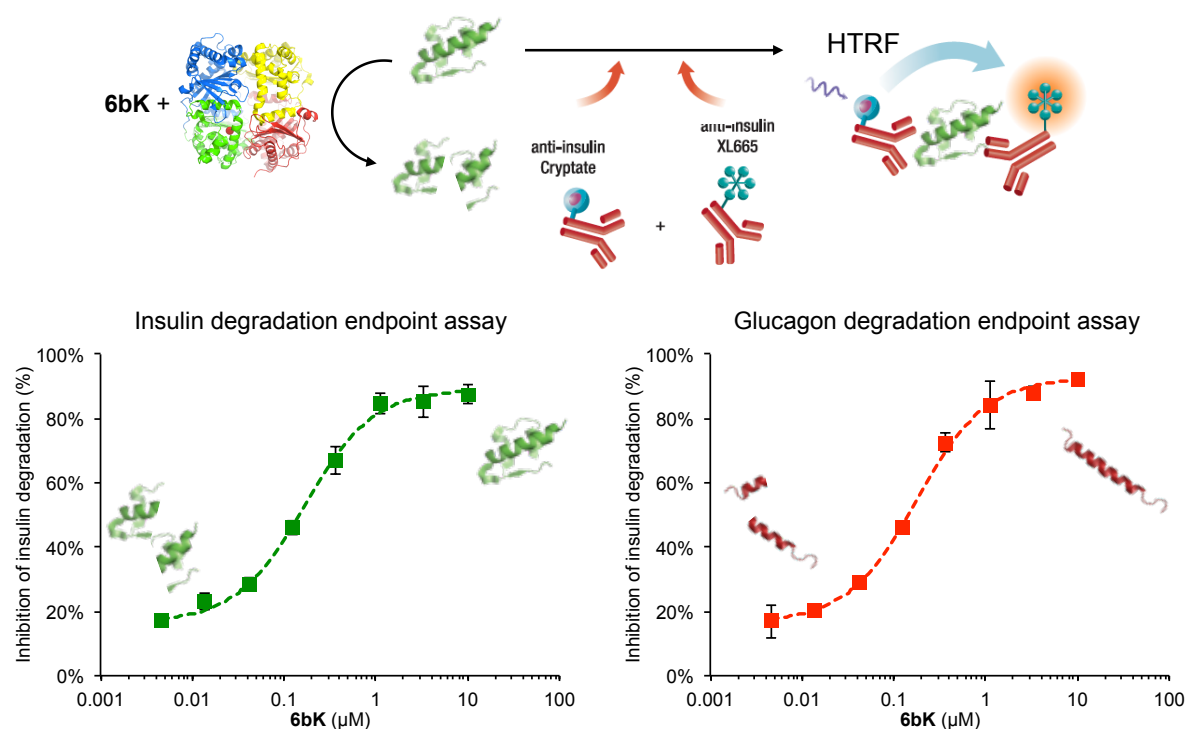


Figure 5.10 | Optimization of homogeneous time-resolved FRET (HTRF) assays to report on IDE-mediated degradation of insulin and glucagon in the presence of inhibitors. The inhibitor **6bK** was used as a positive control to optimize the IDE incubation parameters, in order to generate a sigmoidal profile that reports on **6bK** IDE inhibition in a concentration-dependent manner.

In follow up experiments, I determined the substrate-selective inhibitory properties over a range of concentrations using the HTRF endpoint degradation assays for insulin and glucagon (**Figure 5.12**), using **6bK** as a control. Among the structures tested, only the hits **BRD-297** and **BRD-204** displayed effective discrimination between the two substrates, and also completely abrogated IDE-mediated insulin degradation at high inhibitor concentration (**Figure 5.11**). The SAR trend of this set of molecules indicates that substrate-selectivity is perturbed by minor structural changes, and that in some cases IDE-mediated degradation of insulin is not effectively blocked by specific azetidine hits. The structure and substrate-selective inhibitory properties of the hit **BRD-297** were corroborated by re-synthesis (see Methods, **Figure 5.18**) using an advanced intermediate azetidine core generously provided by the Broad Institute.

These findings suggest that insulin and glucagon are processed by IDE through different binding requirements that can be rationalized and exploited by distal-site small molecule binders, which clash or abrogate interactions between IDE and insulin, but that can accommodate for binding and proteolysis of glucagon within the IDE chamber (**Figure 5.12**).

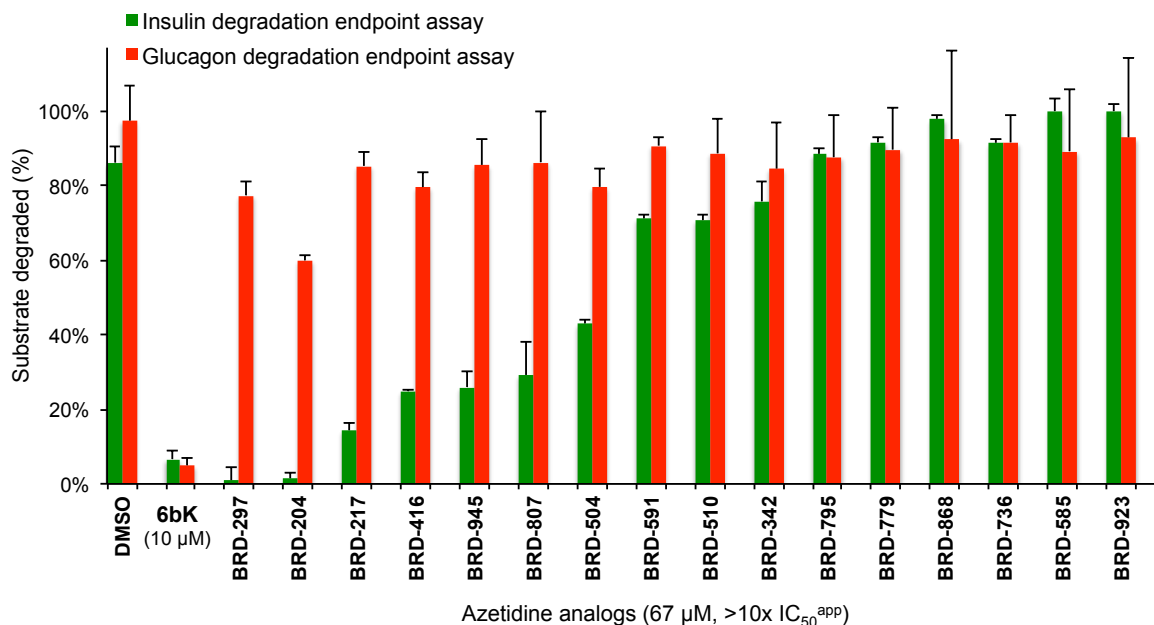


Figure 5.11 | Focused screen for substrate-selective inhibitory properties using the insulin and glucagon degradation endpoint HTRF assays. (A) Selected hits displaying submaximal inhibition in the range of 40–80% for the surrogate fluorogenic peptide cleavage assay were chosen. All compounds (used at final concentration of 67 μM, >10x IC₅₀^{app}) and control incubations were performed in parallel using the same IDE and substrate preparations. Under these conditions, the analogs **BRD-297** and **BRD-204** produce a strong discrepancy in IDE-mediated degradation of glucagon (■) versus insulin (■) compared with IDE treated with DMSO alone, or with positive control **6bK** (10 μM). Other analogs display modest substrate-selective inhibitory properties.

Figure 5.12 (next page) | Concentration dependence profiles for substrate-selective IDE inhibitors. Selected hits that display substrate-selective inhibitory properties were assayed over a range of concentrations using the HTRF endpoint degradation assay for insulin (■) and glucagon (■). Only the hits **BRD-297** and **BRD-204** display strong substrate selectivity, and completely abrogate IDE-mediated insulin degradation.

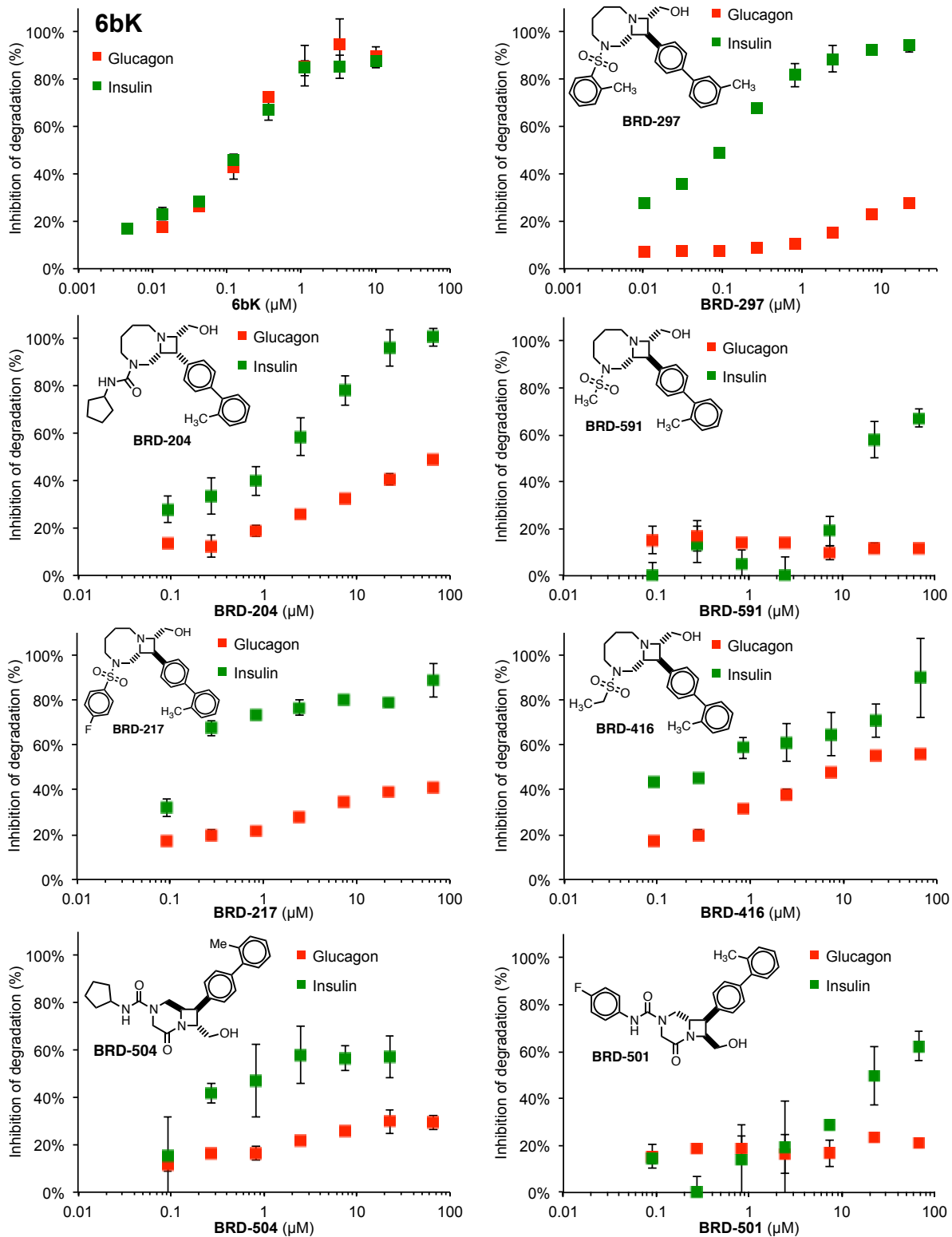


Figure 5.12 Concentration dependence profiles for substrate-selective IDE inhibitors (caption in previous page)

Amyloid-beta and Amylin are also *in vivo* substrates of IDE (see Section 4.6). Amylin is co-secreted with insulin by β -cells to exert glycemic control during meals, by slowing gastric emptying²⁵, promoting satiety^{26,27}, and antagonizing glucagon signaling²⁸. Our findings with **6bK** raised the possibility that IDE inhibition could potentiate the effects of amylin, which may mimic the benefits of supplementation using pramlintide/Symmlin, an injectable analog based on the rodent sequence of amylin^{25,27}. However, there is also significant concern that human amylin may produce amyloid fibrils, which have been suggested to play a role in β -cell dysfunction in the late stage of type-2 diabetes²⁹. Substrate-selective IDE inhibitors could hypothetically be designed to either exclude or accept amylin within the IDE chamber, given that amylin is of intermediate size between insulin and glucagon. Therefore, to determine the possibility of IDE-mediated cleavage in the presence of the new inhibitors we designed a fluorogenic analog of human amylin, Amylin-fp (**Figure 5.13**), by judiciously replacing two residues: Gln10 with the Lys- γ N-anthranilamide fluorophore and Phe23 with the 3-nitrotyrosine quencher, which are 12 residues apart and encompass the IDE cleavage site. This peptide was synthesized and HPLC purified by Dennis Dobrovolsky. Whereas IDE-mediated cleavage of A β 40 and Amylin-fp was blocked by **6bK** with comparable EC₅₀ values to the glucagon and insulin HTRF assays, the inhibitors **BRD-297** and **BRD-204** displayed an intermediate level of IDE cleavage inhibition, but nonetheless permitted significant IDE-mediated processing of the Amylin-fp peptide at the highest concentration tested for each inhibitor (>40-20% the uninhibited rate). These results

suggest that **BRD-297** and **BRD-204** are insulin-selective IDE inhibitors. Therefore, the substrate-selective inhibitors can be conceptualized as re-sculpting a crucial patch of the inner surface of the IDE chamber that brings about discrimination between insulin and the three smaller substrates tested, which may enter the chamber and engage in proteolysis at rates comparable to that of the uninhibited enzyme.

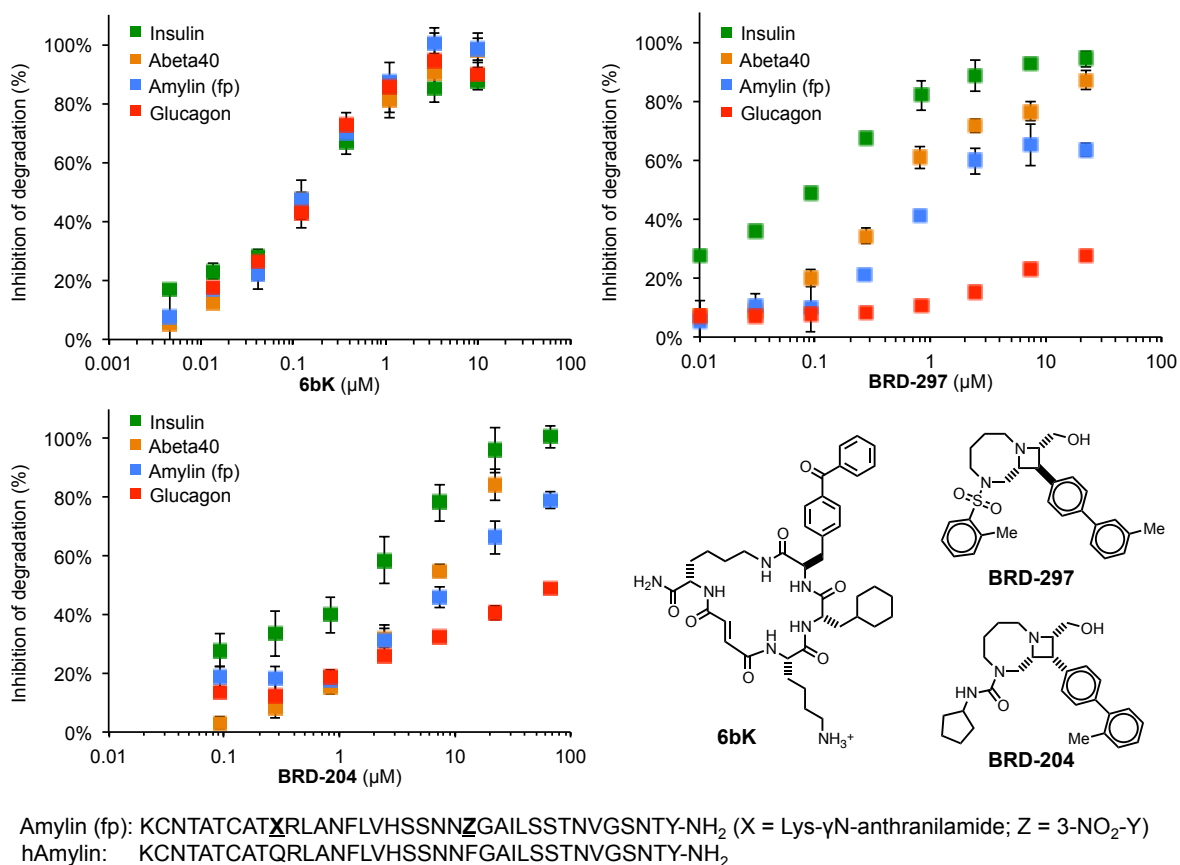


Figure 5.13 | IDE-mediated cleavage of Aβ40 and an amylin fluorogenic analog is partially allowed by insulin-selective IDE inhibitors. The fluorogenic analog of human amylin Amylin-fp was designed by replacing two residues: Gln10 with the Lys-γN-anthranilamide fluorophore and Phe23 with the 3-nitrotyrosine quencher. The IDE cleavage site of human amylin is between Phe15-Leu16¹. Aβ40 was measured by HTRF (CisBio).

5.5 – Metalloprotease specificity of IDE inhibitor hits

A key advantage of the **FL-6b** probe-displacement screening approach is the enrichment for hits that target the distal binding pocket that distinguishes IDE from other metalloproteases (Chapter 2). Similarly to **6bK**, the azetidine inhibitors **BRD-204** and **BRD-297** ($IC_{50} = 250$ nM and 400 nM, respectively) displayed remarkable ≥ 250 to 1,000-fold preference for inhibition of IDE over all other metalloproteases tested: thimet oligopeptidase (THOP), neurolysin (NLN), neprilysin (NEP), matrix metalloprotease 1 (MMP-1), and angiotensin converting-enzyme (ACE) (**Figure 5.14**). The specificity profiles of the structurally related inhibitors **BRD-779** and **BRD-504** displayed comparable >80 and 100-fold preference for IDE inhibition,

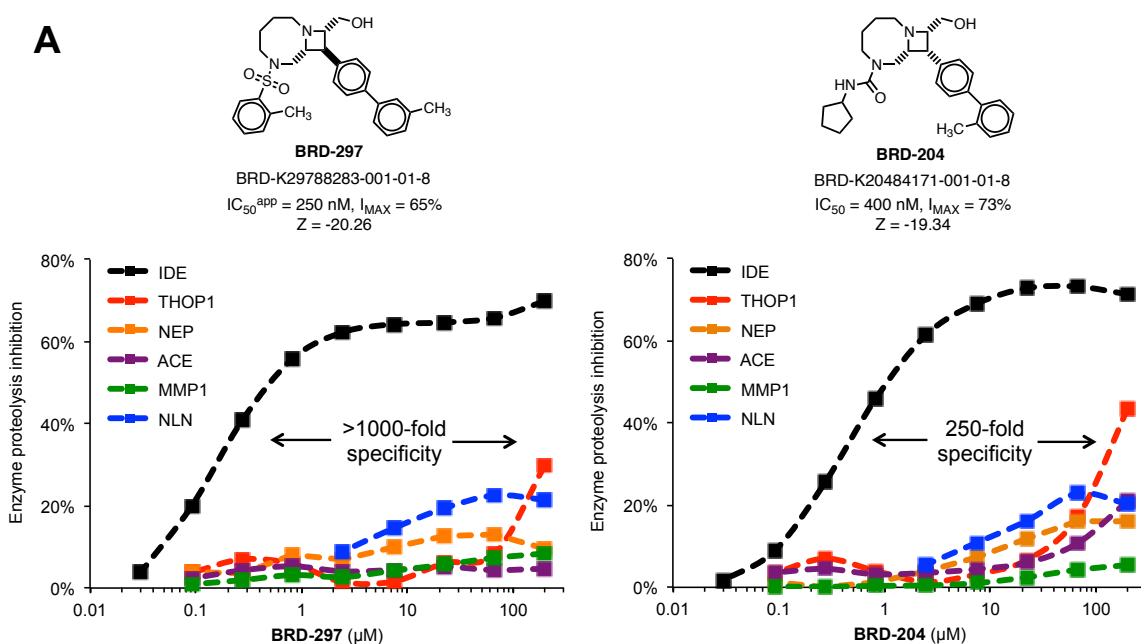


Figure 5.14 | Analysis of metalloprotease specificity for substrate-selective IDE inhibitors (continued on the next page).

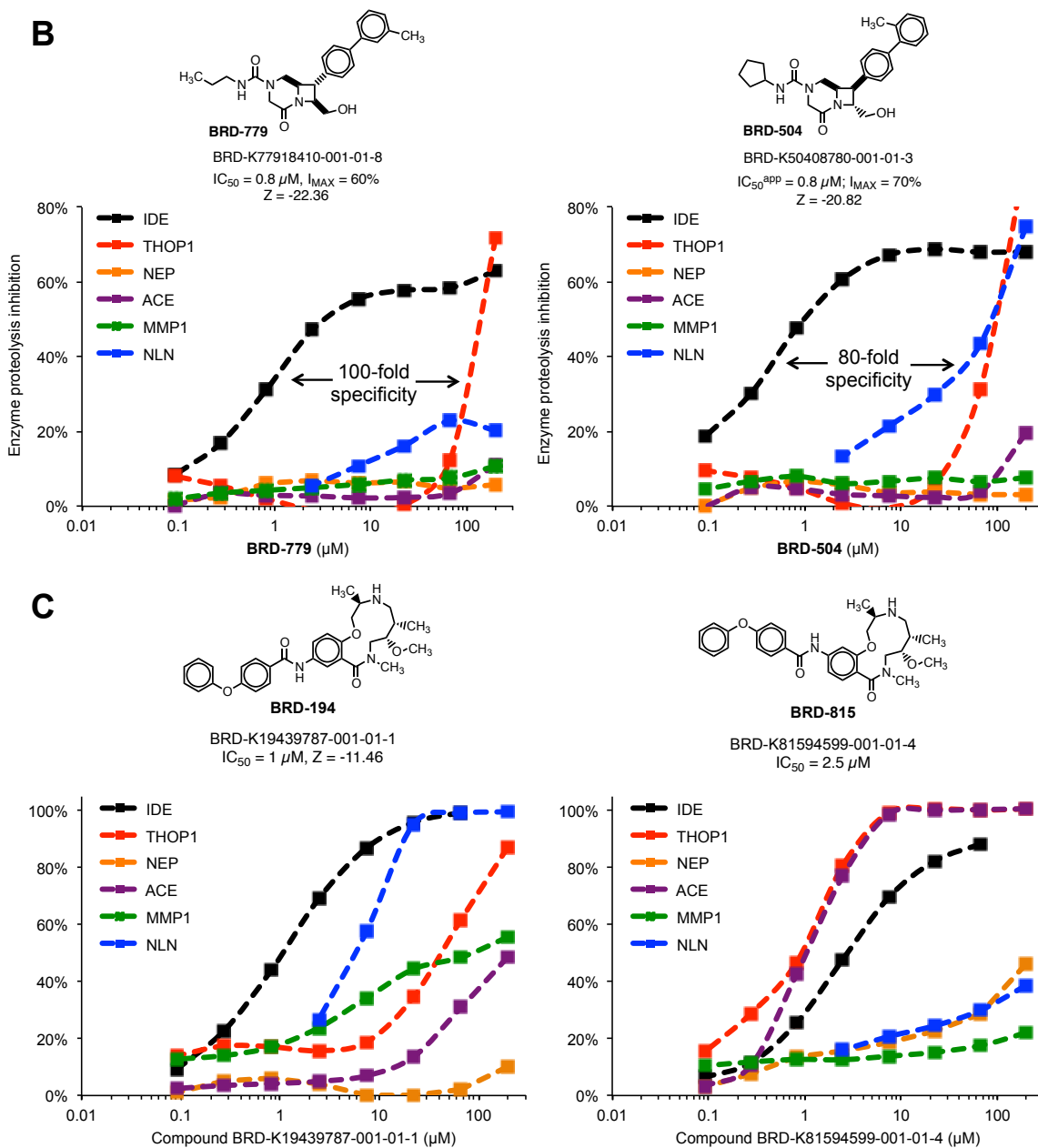


Figure 5.14 (cont.) | Analysis of metalloprotease specificity for substrate-selective IDE inhibitors. The substrate-selective inhibitors **BRD-297** and **BRD-204** achieve remarkable ≥ 250 to 1,000-fold specificity for IDE (■) over all other metalloproteases tested: thimet oligopeptidase (■ THOP), neurolysin (■ NLN), neprilysin (■ NEP), matrix metalloprotease 1 (■ MMP1), and angiotensin converting-enzyme (■ ACE). **(B)** The specificity profiles of the structurally related inhibitors **BRD-779** and **BRD-504** suggest that hits of high selectivity for IDE are enriched by displacement of the anisotropy probe **FL-6b**. **(C)** The hits from the 4-phenoxy-*N*-phenylbenzamide series²⁰ were not as specific for IDE²².

suggesting that high specificity for IDE over other enzymes is a general feature of this series. On the other hand, the biphenyl ether analogs²⁰ **BRD-194** and **BRD-815** identified from the “DOS informer set” plates (**Figure 5.6A**) displayed only modest selectivity for IDE *versus* various enzymes, suggesting that these hits may have non-specific aggregator properties.

5.6 – Binding site mutagenesis and structural basis for substrate-selective IDE inhibition

Next, to demonstrate that the new hits interact with the IDE distal binding site I determined the loss of potency against IDE variants known to disrupt the binding of **6bK**, including Ala479Leu, Gly362Gln and Ile374Gln (**Figure 5.15**). As expected, mutagenesis of the residue Ala479Leu had the strongest impact on hindering the inhibition potency of **BRD-297** and **BRD-204** by at least >150-fold. This mutation similarly blocks **6bK**, **6b** and **FL-6b**, from binding IDE, suggesting that the inhibitors share the same binding site. The nearby mutations Ile362Gln and Gly362Gln, which are residues of the *exo-site* involved in unfolding hormone substrates, also reduce the inhibition potency of **BRD-297** and **BRD-204**.

Together, these biochemical studies provide strong evidence for the proposed distal binding site for **BRD-297** and **BRD-204**. Based on this data Zack Foda and Prof. Markus Seeliger (Stony Brook University) produced a docking model of the ligand **BRD-297** into the **6b** distal binding pocket using the IDE co-crystal structure (PDB: 4LTE, **Figure 5.15B**). The highest scoring pose of the ligand structure is fully

consistent with the IC₅₀ potency of **BRD-297** against the IDE variants Ala479Leu, Gly362Gln, and Ile374Gln (**Figure 5.15A**).

Next, I investigated the impact of the azetidine IDE inhibitors on the rate of glucagon processing compared to IDE alone. I determined the initial rates of glucagon cleavage in the presence of **BRD-297**, **BRD-204**, **BRD-504**, **BRD-799**, and **BRD-591**, again using high inhibitor concentrations (67 μM, >50–200x IC₅₀^{app}) to promote full occupancy of the IDE binding site. The initial concentration of glucagon used in this assay was 1.15 nM (4 ng/mL) and owing to the low affinity of glucagon for IDE (K_M = 3.5 μM)^{30,31} the cleavage of glucagon can only proceed through a ternary complex. The data suggests that the IDE-glucagon-inhibitor ternary complexes of **BRD-297** and **BRD-204** retain significant apparent rates of glucagon degradation compared to IDE alone (**Figure 5.16**). Furthermore, I observed that compounds **BRD-591** and **BRD-799** *accelerate* the rate of IDE-mediated glucagon cleavage, suggesting that substrate-selective IDE inhibitors that make favorable interactions within the IDE-glucagon ternary complex could also be developed.

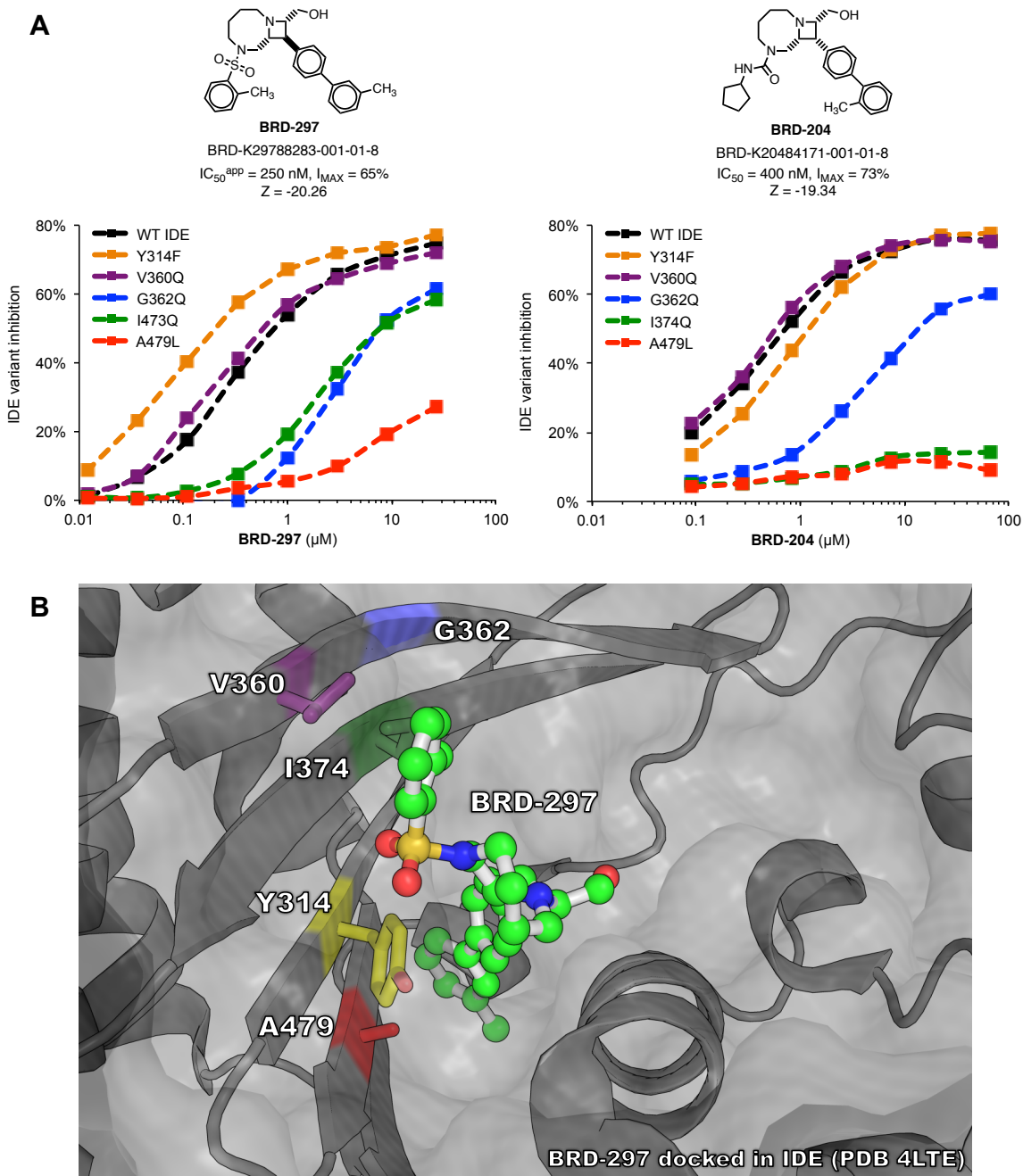


Figure 5.15 | Confirmation of the distal binding site for substrate-selective IDE inhibitors, and a docking model within human IDE. Activity assays for wild-type or mutant human IDE variants in the presence of **BRD-297** and **BRD-204**. (A) Mutagenesis of the residue Ala479Leu (■) hinders the inhibition potency of **BRD-297** and **BRD-204** by at least >150-fold. The nearby mutations Ile362Gln (■) and Gly362Gln (■) also reduce the inhibition potency. (C) These results are consistent with the highest docking score pose for **BRD-297** within human IDE (PDB: 4LTE, ligand **6b** removed).

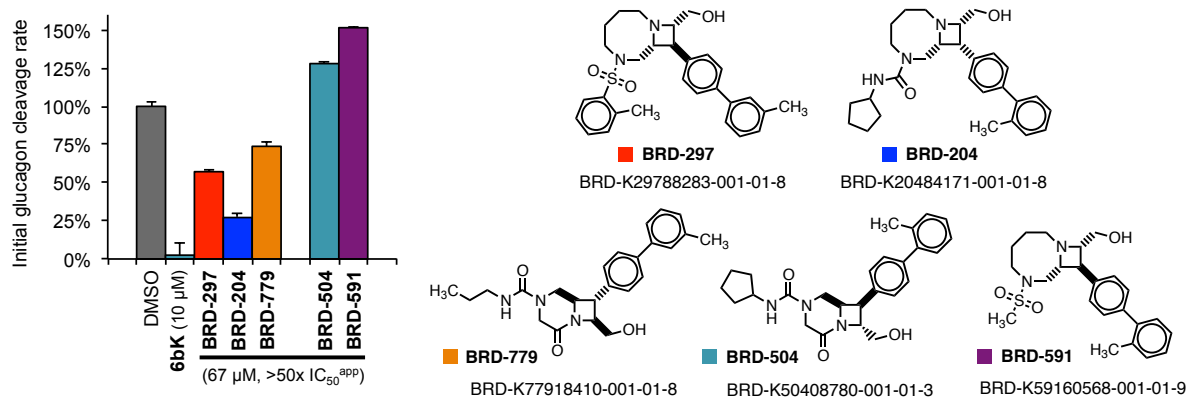


Figure 5.16 | IDE-mediated degradation of glucagon is permitted by the ternary complexes of substrate-selective IDE inhibitors. Selected hits displaying substrate-selective inhibitory properties were chosen. All compounds and control incubations were performed in parallel using the same IDE and preparation of glucagon (4 ng/mL, 1.15 nM final). The enzymatic reaction was incubated in the presence of compounds (67 μM, >50x IC₅₀^{app}), DMSO alone, or **6bK** positive control (10 μM), at 0 °C for 10 min to promote incomplete IDE-mediated degradation of glucagon, which was measured using the HTRF assay. The IDE complexes with hits **BRD-297** and **BRD-204** display significant rates (60 and 30% respectively) of IDE-mediated glucagon proteolysis compared to IDE alone (DMSO control). It is noteworthy that the compounds **BRD-504** and **BRD-591** accelerate IDE-mediated glucagon cleavage, potentially by making favorable interactions that increase the modest affinity of glucagon for IDE ($K_M \sim 3.5 \mu\text{M}$).

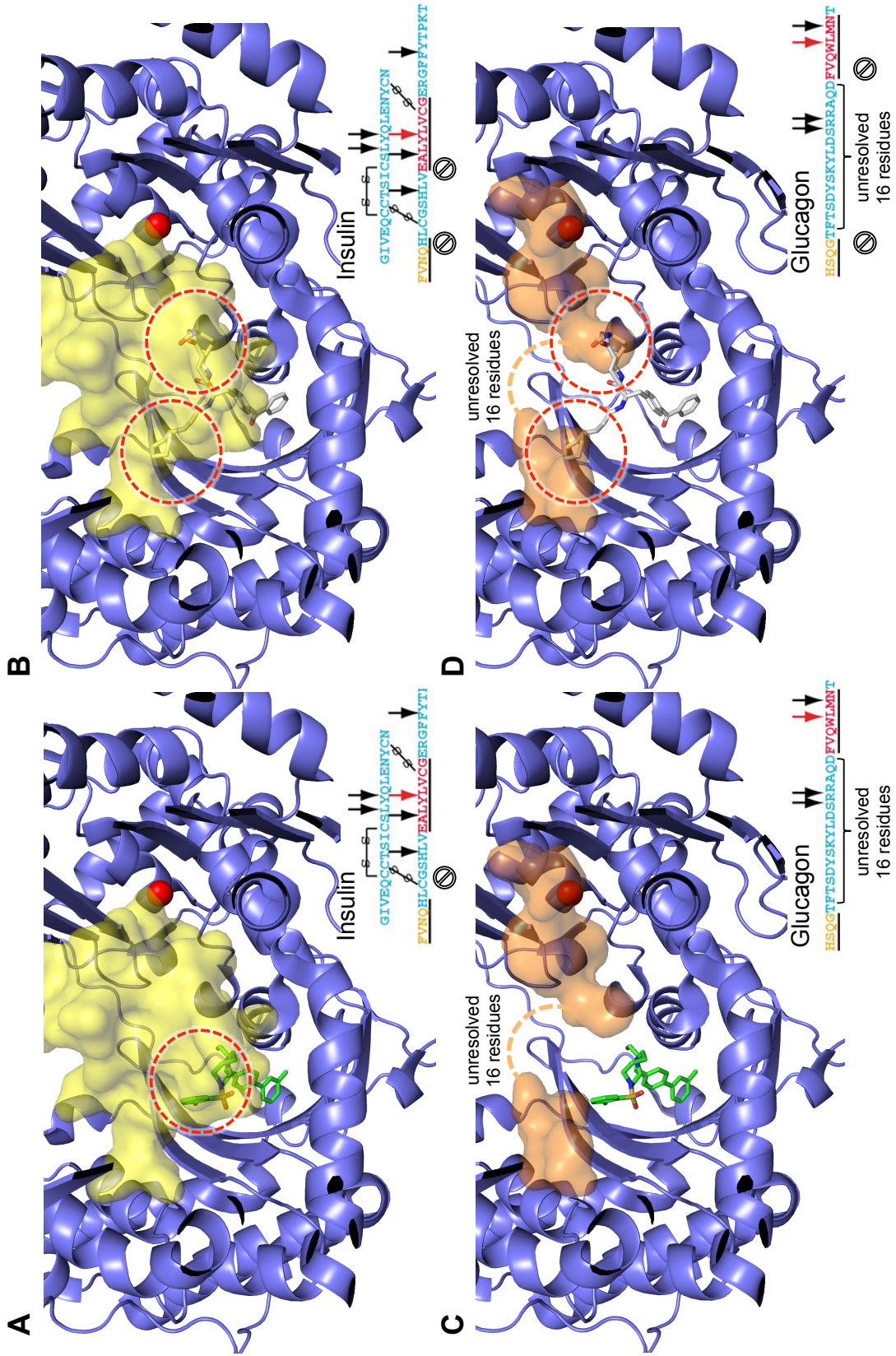


Figure 5.17 | Structural basis for substrate-selective IDE inhibition. Caption in the next page.

Figure 5.17 (cont.) | (A and B) The IDE-insulin X-ray co-crystal structure (PDB: 2WBY) was superimposed with (A) the model of **BRD-297** docked in the IDE structure, and with (B) the IDE-**6b** inhibitor co-crystal structure. Insulin is shown as a yellow surface, and the inhibitors as stick models. These models predict multiple steric clashes (red circles) that abrogate the interactions of insulin when either (A) **BRD-297** or (B) **6b** are bound to IDE. (C and D) Similarly, the IDE-glucagon X-ray co-crystal structure (PDB: 2G49) was superimposed with (A) the model of **BRD-297** docked in the IDE structure and (B) the IDE-**6b** inhibitor co-crystal structure. A 16-residue segment of glucagon (orange surface) is disordered and unresolved in the crystal structure, and only the terminal segments of glucagon are bound to the catalytic site (right) and *exo*-site (left). The superimposed models predict steric clashes (red circles) between **6b** and the IDE-bound segments of glucagon, in contrast **BRD-297** does not abrogate any interactions between IDE and glucagon. The insets in A-D represent the IDE-mediated cleavage sites (major red arrow, minor black arrows), the IDE-bound segments of the substrate are underlined, and the symbols (\odot) highlight the steric clashes with each inhibitor.

To understand the structural basis of **BRD-297** substrate-selective IDE inhibition and how the ternary complex allows glucagon proteolysis we superimposed the co-crystal structures of IDE with glucagon and insulin¹ with our model of **BRD-297** docked in the **6b** binding pocket of IDE (**Figure 5.17A** and **C**). The superimposed models predict that the bulk of the macrocycle structure of **6b** obstructs multiple points of IDE-insulin interactions within the chamber (**Figure 5.17B** see also **Figure 2.13**), and similarly **6b** obstructs the interactions predicted for the electronic density model of glucagon¹ (**Figure 5.17D**). Similar superimposed models produced by Zack predict that **6b** clashes with all substrates that have been co-crystallized within IDE, including amylin³², A β ¹, and ANP³³. Remarkably, this

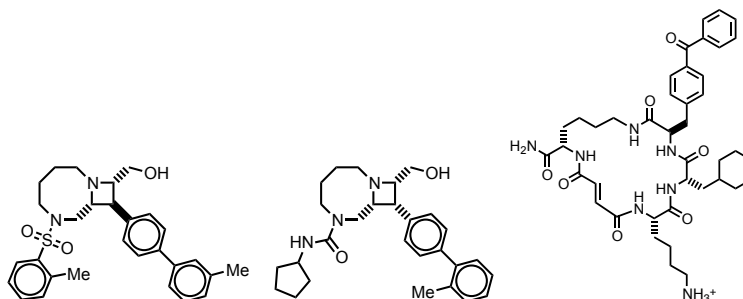
preliminary model of IDE-**BRD-297** does not predict any obstructions with the superimposed IDE-glucagon interactions (**Figure 5.17A**), supporting the biochemical data indicating that **BRD-297** may accommodate for glucagon binding to IDE as a ternary complex that is proteolytically competent for IDE-mediated glucagon cleavage (**Figure 5.16**).

In conclusion, these results offer new insights into the biochemistry of IDE, and provide a first-in-class series of inhibitors capable of substrate discrimination, which clash or abrogate interactions with insulin, but that simultaneously accommodate for binding and proteolysis of glucagon and amylin within the IDE chamber (**Figure 5.13**). The hits **BRD-297** and **BRD-204** are drug lead-compliant (**Table 5.2**)³⁴ and may prove useful to translate these findings *in vivo* based on their sub-micromolar IDE inhibition potencies, excellent metalloprotease specificities, and the promising *in vitro* glucagon cleavage rates of the respective IDE ternary complexes.

More broadly, these findings establish an unprecedented strategy for altering the physiologically active substrates degraded by IDE, rather than merely blocking the enzyme. Altering the IDE ‘degradome’ *in vivo* constitutes a new therapeutic strategy for the treatment of high blood sugar by selectively potentiating insulin over glucagon signaling, and favorably shifting the insulin-glucagon ratio⁴, which has broad implications for glucoregulation in multiple stages of Type-2 Diabetes³⁵. Furthermore, the identification of IDE binders that *accelerate* IDE-mediated glucagon cleavage may provide an opportunity to directly suppress glucagon signaling, while simultaneously potentiating insulin signaling, as a useful adjunct to

conventional antihyperglycemic agents in the management of diabetic hyperglycemia⁴.

Table 5.2 | Calculated drug-like properties³⁶ of substrate-selective hits *versus* **6bK**.



Inhibition properties	BRD-297	BRD-204	6bK
IDE IC ₅₀ ^{app}	250 nM	400 nM	50 nM
I _{MAX} peptide assay	65%	73%	100%
I _{MAX} insulin assay	100%	100%	100%
I _{MAX} glucagon assay	27%	49%	100%
IDE selectivity	>1000x	250x	>1000x
Lipinski properties			
Mw (<500 Da)	490 Da	448 Da	758 Da
cLogP (<5)	4.5	4.5	<1
H-donors (<5)	1	2	8
H-acceptors (<10)	5	5	7
Rotatable bonds (<10)	5	5	10
Polar area (<140 Å ²)	70	60	250

5.7 – Perspective for the future of IDE-based therapeutics

The discovery and development of the first highly-selective and physiologically active IDE inhibitor enabled the detailed study of the physiological

functions of IDE in living animals, illuminating novel IDE substrates *in vivo*, and leading us to delineate new therapeutic strategies for modulating IDE activity to improve post-prandial glucose tolerance. This new understanding of the physiological roles of IDE then led us to develop a more efficacious class of substrate-selective IDE inhibitors that preferentially block insulin degradation, while simultaneously permitting IDE-mediated clearance of glucagon and amylin.

These studies provide the essential foundation towards validating IDE as a drug target. The detailed biochemical characterization of the inhibitory distal site that distinguishes IDE from other enzymes, and the fluorescence anisotropy assay that enables screening of large small-molecule collections against this new binding site offers a path toward the discovery and development of additional therapeutic leads against IDE. Moreover, I demonstrated that by applying this screening strategy it is possible to identify substrate-selective IDE inhibitors that circumvent the intrinsic liability of IDE as a drug target. Indeed, traditional competitive inhibitors would potentiate the opposing physiological functions of glucagon and insulin *in vivo*, restricting the therapeutic benefit of IDE inhibitors to periods of low glucagon secretion, or in co-administration with anti-diabetic agents. For the purpose of this work I have specifically focused on drug target validation for the peripheral pool of IDE and peripheral circulating substrates. IDE in the brain may not prove to be a significant liability (**Figure 5.13**), due to the multiple redundant pathways for degradation of amyloid-beta peptides³⁷, and because impermeability to the blood-

brain barrier is a feature either inherent or designed into most drugs, as exemplified by Neprilysin inhibitors that are used for the treatment of hypertension³⁸.

The IDE inhibitor probes developed herein may become useful tools to discover and validate other physiologically relevant substrates of IDE. For instance, preliminary data obtained during the writing of this thesis suggests that the vasodilator CGRP^{39,40} and the natriuretic hormone ANP^{41,42} are *bona fide* substrates of IDE *in vivo*, making IDE a *vasopeptidase* like ACE and Neprilysin. Mounting evidence suggests that therapies that increase the levels of the hormones released by the heart in response to high blood pressure, called the natriuretic peptides,⁴¹ lead to synergistic improvements in blood pressure control and lower risk of cardiovascular disease when used in combination with classical anti-hypertensive drugs.^{38,43} The ongoing validation experiments will determine if IDE inhibition may produce an anti-hypertensive effect secondary to the anti-diabetic activity, given that the vast majority of patients with diabetes would benefit from preventative and synergistic treatments for blood glucose control and hypertension^{44,45}. In turn, the IDE-mediated degradation of these novel substrates may be characterized in the presence of substrate-selective IDE inhibitors.

Finally, based on the principles established herein, we will be able to develop insulin-selective IDE inhibitors that accelerate IDE-mediated glucagon degradation, simultaneously potentiating insulin signaling, and suppressing glucagon to bolster the management of diabetic hyperglycemia. This is, in my view, the ideal IDE inhibitor.

5.8 – Methods

Fluorescence anisotropy high-throughput screening assay. Human N-His₆-IDE₄₂₋₁₀₁₉ (*E. coli* expressed) was mixed with fluorescein-labeled macrocycle **FL-6b** in 50 mM Tris buffer pH 8.0, with 1 M NaCl, at 25°C. Optimum signal was obtained using a mixture of 30 mM probe **FL-6b** and 0.5 μM IDE. The “DOS informer set” compound plates were pinned onto 384-well plates containing the enzyme-probe mixture (50 μL/well). The azetidine screen was pre-printed on 384-well plates and the enzyme-probe mixture was added (50 μL/well). The final compound concentration was 20 μM, and IDE inhibitor **6bK** was used as a positive control at 1 μM final concentration. After 30 min equilibration, the increase in fluorescence anisotropy was recorded using an EnVision spectrophotometer (excitation 492 nm, emission 523 nm).

HTRF assay for IDE-mediated degradation of insulin. A solution of 0.8 μg/mL IDE (R&D) in pH 7.5 buffer containing 20 mM HEPES, 135 mM NaCl (24 μL) was transferred to a 200 μL tube strip, and combined with 1 μL of each inhibitor (10 mM in DMSO, or as a 3-fold dilution series). A solution of insulin in “Assay Diluent” (25 μL) was added to a final concentration of 20 ng/mL, and incubated at 30 °C for 15 min. This procedure was optimized to result in ~75% degradation of insulin. The reaction was terminated by adding 25 μL of inhibitor **Ii1** (200 nM) and chilled on ice. The remaining insulin was quantified using 10 μL of the quenched enzymatic reaction using the sensitive-range protocol Homogeneous Time-Resolved FRET

Insulin assay (CisBio® 62INSPEB) in 20 μ L total volume according to the manufacturer's instructions (384 well-plate Greiner 784904 non-binding). Fluorescence was measured using a Tecan M1000Pro plate reader (excitation = 320 nm, emission = 665 and 620 nm, lag time = 60 μ s) according the assay manufacturer's recommendations. Blank wells and insulin standard curve were included in the assay.

HTRF assay for IDE-mediated degradation of glucagon. A solution of 0.05 μ g/mL IDE (R&D) in 1x assay "Diluent #5" (24 μ L) was transferred to a 200 μ L tube strip, and combined with 1 μ L of each inhibitor (10 mM in DMSO, or as a 3-fold dilution series). A solution of glucagon in the same buffer (25 μ L) was added to a final concentration of 4 ng/mL, and incubated at RT for 10 min. This procedure was optimized to result in ~75% degradation of glucagon. The reaction was terminated by 1 μ L of inhibitor **Ii1** (5 μ M) and chilled on ice. The remaining glucagon was quantified using 10 μ L of the quenched enzymatic reaction using the sensitive-range protocol Homogeneous Time-Resolved FRET Glucagon assay (CisBio® 62GLCPEF) in 20 μ L total volume according to the manufacturer's instructions (384 well-plate Greiner 784904 non-binding). Fluorescence was measured using a Tecan M1000Pro plate reader (excitation = 340 nm, emission = 665 and 620 nm, lag time = 60 μ s) according the assay manufacturer's recommendations. Blank wells and glucagon standard curve were included in the assay.

HTRF assay for IDE-mediated degradation of A β 40. A solution of 1.76 $\mu\text{g}/\text{mL}$ IDE (R&D) in pH 7.5 buffer containing 20 mM HEPES, 135 mM NaCl (24 μL) was transferred to a 200 μL tube strip, and combined with 1 μL of each inhibitor (10 mM in DMSO, or as a 3-fold dilution series). A solution of insulin in “Assay Diluent” (25 μL) was added to a final concentration of 1.6 ng/mL, and incubated at 30 °C for 15 min. This procedure was optimized to result in ~80% degradation of A β 40. The reaction was terminated by adding 25 μL of inhibitor **Ii1** (200 nM) and chilled on ice. The remaining A β was quantified using 10 μL of the quenched enzymatic reaction using the sensitive-range protocol Homogeneous Time-Resolved FRET A β 40 assay (CisBio® 62B40PEB) in 20 μL total volume according to the manufacturer’s instructions (384 well-plate Greiner 784904 non-binding). Fluorescence was measured using a Tecan M1000Pro plate reader (excitation = 320 nm, emission = 665 and 620 nm, lag time = 60 μs) according the assay manufacturer’s recommendations. Blank wells and insulin standard curve were included in the assay.

Macrocycle docking simulations. Receptor and ligand preparation was performed in the standard method. DOCKing was performed using version 6.6 with default parameters for flexible ligand and grid-based scoring, and the van der Waals exponent was 9. Because of the mutagenesis data strongly pointing to a role of Ala479, we limited docking of the inhibitor to an area within 15 Å of Ala479.

Synthesis of anisotropy probe FL-6b. Approximately 250 mg of O-Bis-(aminoethyl)ethylene glycol trityl resin (NovaPEG Novabiochem®, ~0.8 mmol/g, 0.2 mmol) was swollen with ~10 volumes of anhydrous DMF for 1 h in a peptide synthesis vessel with mixing provided by dry nitrogen bubbling. In a separate flask, *N*^α-allyloxycarbonyl-*N*^ε-2-Fmoc-L-lysine (5 equiv.) and 2-(1*H*-7-azabenzotriazol-1-yl)-1,1,3,3-tetramethyl uronium hexafluorophosphate (HATU, 4.75 equiv.) were dissolved in anhydrous DMF (~10 vol.), then treated with *N,N'*-diisopropylethylamine (DIPEA, 10 equiv.) for 5 min at RT. The solution was combined with the pre-swollen resin and mixed with nitrogen bubbling overnight. The vessel was eluted and the resin was washed three times with *N*-methyl-2-pyrrolidone (NMP, ~10 vol.). Following each coupling step, Fmoc deprotection was effected with 20% piperidine in NMP (~20 vol.) for 20 min, repeated three times, followed by washing three times with NMP (~10 vol.) and twice with anhydrous DMF (~10 vol.). The general procedure for amide coupling of building blocks A (*N*^α-Fmoc-4-benzoyl-D-phenylalanine), B (*N*^α-Fmoc-3-cyclohexyl-L-alanine) and C (*N*^α-Fmoc-*N*^δ-trityl-L-glutamine) was treatment of the resin with solutions of HATU-activated *N*^α-Fmoc amino acids (5 equiv.) for 3-5 hours in anhydrous DMF, mixing with dry nitrogen bubbling. The general procedure for HATU-activation was treating a solution of *N*^α-Fmoc amino acid (5 equiv.) and HATU (4.75 equiv.) in anhydrous DMF (10 vol.) with DIPEA (10 equiv.) for 5 min at RT. Following the final Fmoc deprotection procedure, the α-amine of glutamine was coupled with allyl fumarate monoester (10 equiv.) using activation conditions as previously described with

HATU (9.5 equiv.) and DIPEA (20 equiv.) in anhydrous DMF (~10 vol.) plus the addition of *N*-hydroxysuccinimide (11 equiv). Allyl fumarate coupling was accomplished by overnight mixing with dry nitrogen bubbling, followed by washing five times with NMP (~10 vol.) and three times with CHCl₃ (~10 vol.). Simultaneous allyl ester and *N*-allyloxycarbonyl group cleavage in solid support was effected with three consecutive treatments with a solution of tetrakis(triphenylphosphine)palladium(0) (0.5 equiv.) dissolved in degassed CHCl₃ containing acetic acid and *N*-methyldimorpholine (40:2:1 ratio, ~20 vol.), mixing by nitrogen bubbling for 30 min. The resin was then washed twice subsequently with ~20 vol. of 5 DIPEA in DMF, then twice with a 5% solution of sodium diethyldithiocarbamate trihydrate in DMF (~20 vol.), twice with 5% solution of hydroxybenzotriazole monohydrate in DMF, and finally washed with 50% CH₂Cl₂ in DMF and re-equilibrated with anhydrous DMF (~10 vol.).

Treating the resin with pentafluorophenyl diphenylphosphinate (5 equiv.) and DIPEA (10 equiv.) in anhydrous DMF (~10 vol.) mixing by nitrogen bubbling overnight produced the macrocyclized products. The resin was washed with NMP (~20 vol.) and CH₂Cl₂ (~20 vol.) and dried by vacuum. The macrocyclized product was cleaved from the resin by two 15 min treatments of the macrocycle-bound resin with 95% TFA containing 2.5% water and 2.5% triisopropylsilane (~20 vol.), followed by two TFA washes (~5 vol.). The TFA solution was dried to a residue under rotatory evaporation, and the peptide was precipitated by the addition of dry Et₂O. The ether was decanted and the remaining solid was dried and dissolved in a

minimum volume of 3:1 DMF-water prior to purification by HPLC. Purification was performed on a C18 21.2x250 mm column (5 μm particle, 100 \AA pore size, Kromasil®), using a gradient of 30 to 80% MeCN/water over 30 min, and solvents containing 0.1% TFA. Purity was determined by HPLC (Zorbax SB-C18 2.1x150 mm column, 5 μm particle) with UV detection at 230 nm, using a gradient of 30 to 80% MeCN/water over 30 min, and solvents containing 0.1% TFA. The formula of final product was confirmed by accurate mass measurements using an Agilent 1100 LC-MSD SL instrument.

Fractions containing the desired PEGylated macrocyclic peptide were combined and freeze-dried to produce a white powder (11.2 mg, 5.6% based on resin loading). The PEGylated macrocyclic peptide (TFA salt, 1.5 mg) was dissolved in dry DMF and treated with DIPEA (10 μL) and 5-carboxyfluorescein *N*-succinimidyl ester (1.12 mg, 1.5 equiv.) for 2 hours. The mixture was acidified with TFA (10 μL) and purified by HPLC. Fractions containing the desired fluorescein-labeled macrocyclic peptide **FL-6b** were combined and freeze-dried to produce a white powder (1.26 mg, 67.5%), which was dissolved in DMSO- d_6 (3.35 mM).

^1H NMR (600 MHz, DMSO- d_6) δ 10.15 (s, 3H), 8.91 (s, 1H), 8.77 (s, 1H), 8.53 – 8.40 (m, 3H), 8.24 (s, 1H), 8.11 – 8.05 (m, $J = 9.9$ Hz, 1H), 8.03 – 7.95 (m, 1H), 7.78 – 7.73 (m, 1H), 7.73 – 7.62 (m, $J = 26.5, 16.3$ Hz, 5H), 7.61 – 7.50 (m, 5H), 7.37 (d, $J = 8.0$ Hz, 1H), 7.31 (s, 1H), 7.28 (d, $J = 7.4$ Hz, 2H), 7.20 (s, 2H), 7.14 (d, $J = 7.6$ Hz, 2H), 6.88 – 6.79 (m, $J = 25.2$ Hz, 2H), 6.72 – 6.62 (m, 6H), 6.62 – 6.50 (m, 6H),

5.37 – 5.28 (m, 4H), 4.57 (mz, 1H), 4.23 – 4.13 (m, 2H), 4.06 – 3.97 (m, 1H), 2.04 – 1.94 (m, $J = 7.4$ Hz, 9H), 1.92 – 1.85 (m, 1H), 1.65 – 1.41 (m, 12H).

High resolution mass, calculated for $C_{67}H_{74}N_8O_{16}$ $[M+H]^+ = 1247.5296$, found 1247.542, $\Delta = 9.93$ ppm.

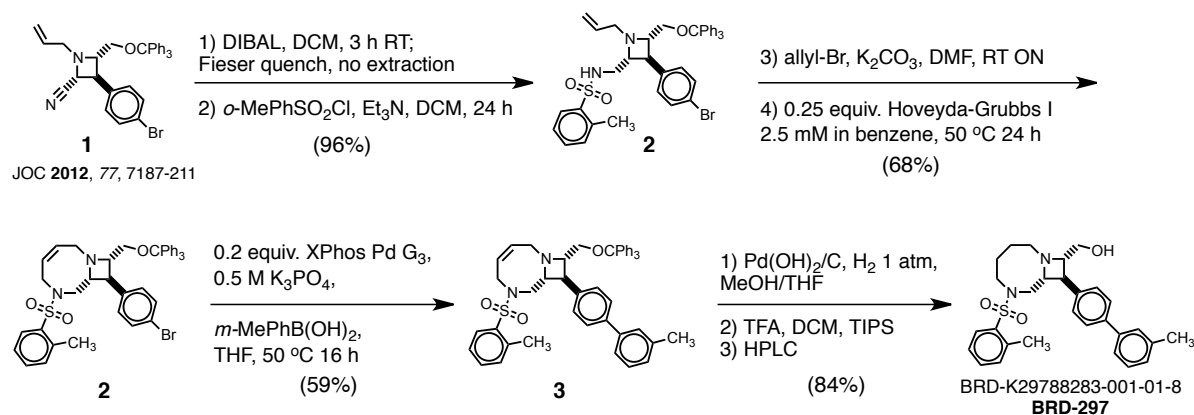
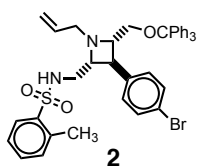
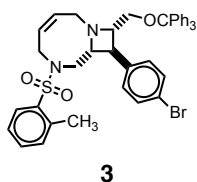


Figure 5.18 | Synthesis of BRD-297. Intermediate **1** was provided by the Broad Institute.



***N*-(((2*R*,3*S*,4*S*)-1-allyl-3-(4-bromophenyl)-4-((trityloxy)methyl)azetidin-2-yl)methyl)-2-methylbenzenesulfonamide (**2**).** A solution of (2*R*,3*S*,4*S*)-1-allyl-3-(4-bromophenyl)-4-((trityloxy)methyl)azetidine -2-carbonitrile (2 g, 3.64 mmol) in 200 mL of CH₂Cl₂ was cooled to 0 °C. To this solution DIABAL (1 M in CH₂Cl₂) was added dropwise (18.2 mL, 5 equiv., 18.2 mmol), and stirred at 0 °C to RT for 3 h. The solution was again cooled to 0 °C, and added MeOH dropwise (100 μL) until no

gas evolved, and worked up using the Fieser method: first 0.73 mL water was added slowly, and stirred vigorously for 5 min 0 °C. Then 0.73 mL 15% NaOH was added and stirred 5 min; followed by addition of 1.8 mL water and stirred vigorously 30 min 0 °C to RT. Approximately 1.5 g MgSO₄ was added and stirred vigorously for 15 min. The solids were filtered, and washed with 50 mL EtOAc five times, and the filtrates were combined, dried over 3 g MgSO₄ and refiltered. The solution was evaporated to a residue under vacuum, and dissolved in 100 mL CH₂Cl₂. This solution was treated with 2,6-lutidine (5.1 mL, 43.7 mmol), followed by *o*-toluenesulfonyl chloride (5.3 mL, 36.4 mmol), and stirred overnight at RT. The solution was treated with ethylenediamine (2.67 mL, 40 mmol) for 10 min, washed with saturated NaHCO₃, dried over NaSO₄, and evaporated to a residue under vacuum. Purification by column chromatography (5 → 40% EtOAc/hexanes) and evaporation of the collected fractions gave 2.487 g of the title compound **2** (96.5%, 3.51 mmol), a white solid. High resolution mass, calculated for C₄₃H₄₃BrN₂O₃S [M+H]⁺ = 707.1938, found 707.196, Δ = -1.47 ppm.

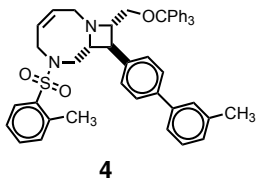


(8*R*,9*S*,10*S*,*Z*)-9-(4-bromophenyl)-10-(phenoxyethyl)-6-(*o*-tolylsulfonyl)-1,6-diazabicyclo[6.2.0]dec-3-ene (3). A solution of sulfonamide intermediate **2** (1.175 g, 1.66 mmol) in 150 mL of DMF was treated with K₂CO₃ (2 g, 13.3 mmol, 8 equiv.)

followed by allyl bromide (570 μ L, 6.64 mmol, 4 equiv.) and stirred overnight at RT. The solution was evaporated to a residue under vacuum, and dissolved in 100 mL EtOAc. The solids were filtered, and washed with 50 mL EtOAc five times, and the filtrates were combined and evaporated to a residue under vacuum. Purification by column chromatography (5 \rightarrow 40% EtOAc/hexanes) and evaporation of the collected fractions gave 1.07 g of the *N*-allylated product (86%, 1.43 mmol), a white solid. High resolution mass, calculated for $C_{43}H_{43}BrN_2O_3S$ $[M+H]^+$ = 719.1938, found 719.196, Δ = 3.06 ppm. The bis-allyl intermediate (420 mg, 0.564 mmol) was dissolved in benzene (250 mL, 2.25 mM) and purged vigorously with argon gas for 30 min. The solution was added Grubbs-Hoveyda catalyst (110 mg, 0.135 mmol, 0.25 equiv.) and heated to 90 $^{\circ}$ C overnight (16 h). The solution was evaporated to a residue under vacuum, followed by purification by column chromatography (5 \rightarrow 40% EtOAc/hexanes) and evaporation of the collected fractions gave 322.5 mg of cyclized title compound **3** (79.5%, 0.448 mmol), a white solid.

1H NMR (600 MHz, DMSO- d_6) δ 8.32 (s, J = 20.1 Hz, 1H), 7.72 (d, J = 7.8 Hz, 1H), 7.54 (t, J = 7.4 Hz, 1H), 7.50 (s, J = 8.3 Hz, 1H), 7.49 (s, 1H), 7.43 (d, J = 7.5 Hz, 1H), 7.40 – 7.34 (m, J = 7.5 Hz, 6H), 7.32 (s, 1H), 7.32 – 7.29 (m, J = 18.5 Hz, 3H), 7.29 (s, 1H), 7.26 (s, 1H), 7.25 (t, J = 7.1 Hz, 2H), 7.20 (s, J = 8.4 Hz, 1H), 7.19 (s, J = 10.8 Hz, 1H), 5.69 – 5.60 (m, 2H), 4.28 – 4.23 (m, J = 3.0 Hz, 1H), 3.86 (dd, J = 14.3, 6.8 Hz, 1H), 3.76 (d, J = 17.9 Hz, 1H), 3.51 (dd, J = 13.2, 1.8 Hz, 1H), 3.46 (d, J = 17.7 Hz, 1H), 3.29 – 3.25 (m, 2H), 3.23 – 3.15 (m, 2H), 3.05 (dd, J = 13.4, 10.3 Hz, 1H), 3.01 – 2.97 (m, 2H), 2.50 (s, J = 1.1 Hz, 3H).

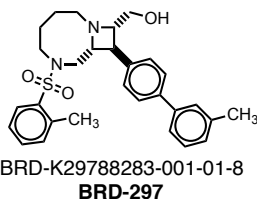
High resolution mass, calculated for $C_{43}H_{43}BrN_2O_3S$ $[M+H]^+ = 719.1938$, found 719.196, $\Delta = 3.06$ ppm.



(8*R*,9*S*,10*S*,*Z*)-9-(3'-methyl-[1,1'-biphenyl]-4-yl)-6-(*o*-tolylsulfonyl)-10-((trityloxy)methyl)-1,6-diazabicyclo[6.2.0]dec-3-ene (3). A solution of bromoaryl intermediate **3** (100 mg, 0.139 mmol) was dissolved in THF (30 mL), added 10 mL of K_3PO_4 solution (0.5 M, >20 equiv.), followed by *m*-tolylboronic acid (37.7 mg, 0.278 mmol, 2 equiv.), and the heterogeneous mixture was purged vigorously with argon gas for 30 min. The solution was added X-Phos-Pd G3 catalyst (25 mg, 0.028 mmol, 0.2 equiv.), and stirred overnight (16 h) at 50 °C. The solution was added EtOAc (50 mL), followed by 2 g $MgSO_4$, and the organic layer was decanted over a filter with a pad of Celite®. The aqueous slurry was washed 3 times with 50 mL EtOAc, and these fractions were used to wash the Celite®. The combined organic fraction was dried over $MgSO_4$ and evaporated to a residue under vacuum, followed by purification by column chromatography (5 → 40% EtOAc/hexanes) and evaporation of the collected fractions gave 60 mg of title compound **4** (59%, 0.082 mmol), a white solid.

1H NMR (600 MHz, $DMSO-d_6$) δ 7.74 (d, $J = 7.8$ Hz, 1H), 7.58 (d, $J = 8.0$ Hz, 2H), 7.54 (t, $J = 7.5$ Hz, 1H), 7.46 – 7.43 (m, 2H), 7.43 – 7.36 (m, 9H), 7.35 – 7.28 (m,

9H), 7.27 – 7.23 (m, $J = 7.1$ Hz, 3H), 7.16 (d, $J = 7.2$ Hz, 1H), 5.70 – 5.63 (m, 2H), 4.33 – 4.25 (m, 1H), 3.93 – 3.85 (m, 1H), 3.81 (d, $J = 18.0$ Hz, 1H), 3.52 (dd, $J = 24.0, 14.6$ Hz, 2H), 3.30 – 3.25 (m, 2H), 3.21 (dd, $J = 9.5, 6.9$ Hz, 1H), 3.09 (dd, $J = 13.4, 10.4$ Hz, 1H), 3.06 – 2.99 (m, 2H), 2.52 (s, $J = 2.7$ Hz, 3H), 2.36 (s, 2H). High resolution mass, calculated for $C_{48}H_{46}N_2O_3S$ $[M+H]^+ = 731.3302$, found 731.330, $\Delta = -0.27$ ppm.



((8*R*,9*S*,10*S*)-9-(3'-methyl-[1,1'-biphenyl]-4-yl)-6-(*o*-tolylsulfonyl)-1,6-diazabicyclo[6.2.0]decan-10-yl)methanol (BRD-297, BRD-K29788283). A solution of intermediate **3** (60 mg, 0.082 mmol) was dissolved in THF (10 mL), added 1 mL MeOH, 10 drops of AcOH, and 20 mg 20% Pd(OH)₂/C, and stirred vigorously overnight (16 h) under an atmosphere of H₂ gas from a balloon. The solution was evaporated to a residue under vacuum, and treated with 10 mL of TFA solution containing 2.5% water and 2.5% triisopropyl silane (v/v). After 10 min the solution was evaporated to a residue under vacuum, and the mixture was purified by HPLC (10 → 70% MeCN/water containing 0.1% TFA). Fractions containing **BRD-297** were combined and freeze-dried to produce a white powder (33.8 mg, 0.0689 mmol, 84% yield).

^1H NMR (600 MHz, $\text{DMSO-}d_6$) δ 9.21 (s, 1H), 7.13 (m, 2H), 7.10 (d, $J = 7.8$ Hz, 1H), 7.00 (t, $J = 7.4$ Hz, 1H), 6.97 – 6.92 (m, 3H), 6.90 (d, $J = 7.1$ Hz, 2H), 6.85 (t, $J = 7.6$ Hz, 1H), 6.79 (t, $J = 7.6$ Hz, 1H), 6.63 (d, $J = 7.4$ Hz, 1H), 5.03 (s, 1H), 4.14 (s, 1H), 3.81 (s, 1H), 3.38 – 3.22 (m, $J = 17.3$ Hz, 3H), 3.20 – 3.09 (m, 3H), 3.07 – 2.95 (m, $J = 27.6$ Hz, 1H), 2.62 (d, $J = 18.7$ Hz, 1H), 1.95 (s, 3H), 1.82 (s, 3H), 1.50 – 1.27 (m, $J = 43.9, 24.5, 8.9$ Hz, 3H), 1.26 – 1.18 (m, 1H).

High resolution mass, calculated for $\text{C}_{29}\text{H}_{34}\text{N}_2\text{O}_3\text{S}$ $[\text{M}+\text{H}]^+ = 491.2363$, found 491.237, $\Delta = 1.42$ ppm.

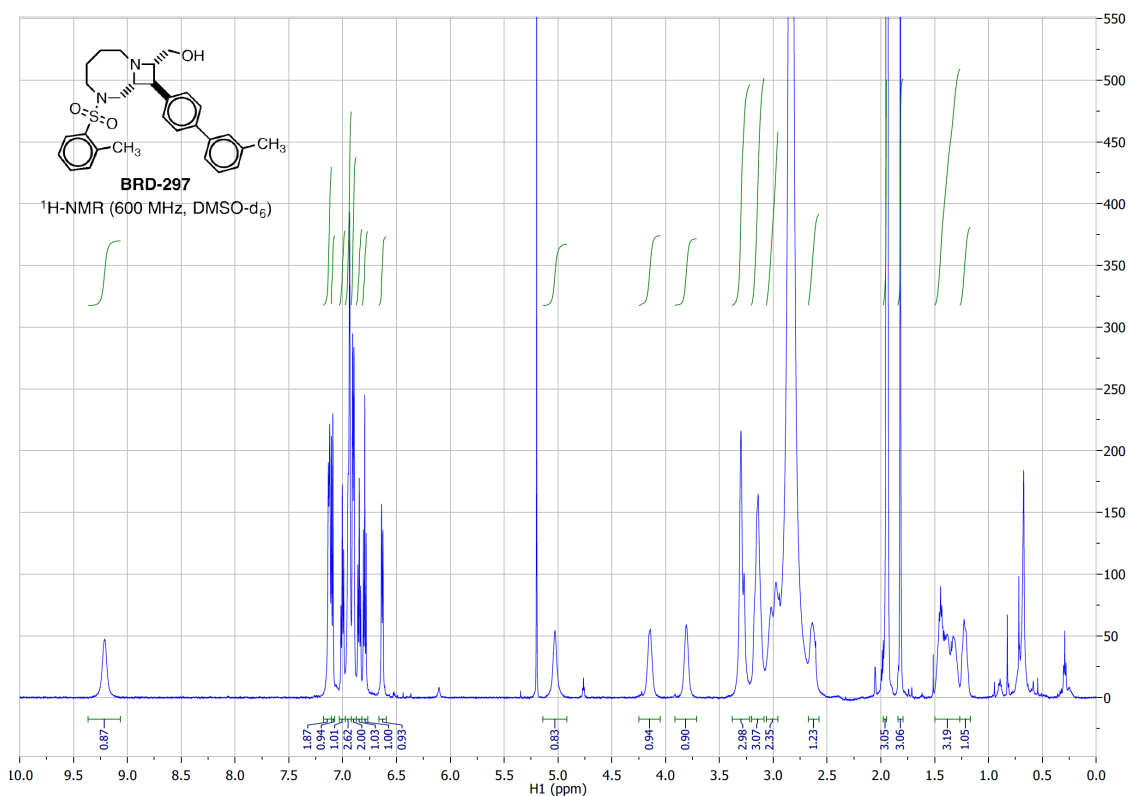


Figure 5.19 | Spectra for $^1\text{H-NMR}$ of **BRD-297**.

References

- 1 Shen, Y., Joachimiak, A., Rosner, M. R. & Tang, W. J. Structures of human insulin-degrading enzyme reveal a new substrate recognition mechanism. *Nature* **443**, 870-874, (2006).
- 2 Manolopoulou, M., Guo, Q., Malito, E., Schilling, A. B. & Tang, W. J. Molecular basis of catalytic chamber-assisted unfolding and cleavage of human insulin by human insulin-degrading enzyme. *J Biol Chem* **284**, 14177-14188, (2009).
- 3 Malito, E. *et al.* Molecular bases for the recognition of short peptide substrates and cysteine-directed modifications of human insulin-degrading enzyme. *Biochemistry* **47**, 12822-12834, (2008).
- 4 Unger, R. H. & Cherrington, A. D. Glucagonocentric restructuring of diabetes: a pathophysiologic and therapeutic makeover. *The Journal of clinical investigation* **122**, 4-12, (2012).
- 5 Ledford, H. Blocking insulin breakdown shows promise against diabetes. *Nature News* (2014). <<http://www.nature.com/news/blocking-insulin-breakdown-shows-promise-against-diabetes-1.15273%3E>>.
- 6 Leissring, M. A. *et al.* Designed inhibitors of insulin-degrading enzyme regulate the catabolism and activity of insulin. *PLoS One* **5**, e10504, (2010).
- 7 Bannister, T. D. *et al.* ML345, A Small-Molecule Inhibitor of the Insulin-Degrading Enzyme (IDE). *Probe Reports from the NIH Molecular Libraries Program* (2010). <<http://www.ncbi.nlm.nih.gov/pubmed/23833801%3E>>.
- 8 Charton, J. *et al.* Imidazole-derived 2-[N-carbamoylmethyl-alkylamino]acetic acids, substrate-dependent modulators of insulin-degrading enzyme in amyloid-beta hydrolysis. *European journal of medicinal chemistry* **79**, 184-193, (2014).

- 9 Abdul-Hay, S. O. *et al.* Optimization of peptide hydroxamate inhibitors of insulin-degrading enzyme reveals marked substrate-selectivity. *J Med Chem* **56**, 2246-2255, (2013).
- 10 Charton, J. *et al.* Structure-activity relationships of imidazole-derived 2-[N-carbamoylmethyl-alkylamino]acetic acids, dual binders of human insulin-degrading enzyme. *European journal of medicinal chemistry* **90**, 547-567, (2015).
- 11 Song, E. S., Rodgers, D. W. & Hersh, L. B. Mixed dimers of insulin-degrading enzyme reveal a cis activation mechanism. *J Biol Chem* **286**, 13852-13858, (2011).
- 12 Sies, H. From enzymology in vitro to physiological chemistry in vivo. *Trends in Biochemical Sciences* **5**, 182-185, (1980).
- 13 Cabrol, C. *et al.* Small-molecule activators of insulin-degrading enzyme discovered through high-throughput compound screening. *PLoS One* **4**, e5274, (2009).
- 14 High-Throughput Screening - Age-Related Disorders - Malcolm A. Leissring. (2009). <<http://www.mayo.edu/research/labs/age-related-disorders/high-throughput-screening%3E>>.
- 15 Puente, X. S., Sanchez, L. M., Overall, C. M. & Lopez-Otin, C. Human and mouse proteases: a comparative genomic approach. *Nature reviews. Genetics* **4**, 544-558, (2003).
- 16 Drag, M. & Salvesen, G. S. Emerging principles in protease-based drug discovery. *Nat Rev Drug Discov* **9**, 690-701, (2010).
- 17 Turk, B. Targeting proteases: successes, failures and future prospects. *Nat Rev Drug Discov* **5**, 785-799, (2006).
- 18 Owicki, J. C. Fluorescence polarization and anisotropy in high throughput screening: perspectives and primer. *Journal of biomolecular screening* **5**, 297-306, (2000).

- 19 Kleiner, R. E., Dumelin, C. E. & Liu, D. R. Small-molecule discovery from DNA-encoded chemical libraries. *Chem Soc Rev* **40**, 5707-5717, (2011).
- 20 Fitzgerald, M. E. *et al.* Build/couple/pair strategy for the synthesis of stereochemically diverse macrolactams via head-to-tail cyclization. *ACS combinatorial science* **14**, 89-96, (2012).
- 21 Gerard, B. *et al.* Synthesis of stereochemically and skeletally diverse fused ring systems from functionalized C-glycosides. *The Journal of organic chemistry* **78**, 5160-5171, (2013).
- 22 Lowe, J. T. *et al.* Synthesis and profiling of a diverse collection of azetidine-based scaffolds for the development of CNS-focused lead-like libraries. *The Journal of organic chemistry* **77**, 7187-7211, (2012).
- 23 Hermanson, D. J. *et al.* Substrate-selective COX-2 inhibition decreases anxiety via endocannabinoid activation. *Nature neuroscience* **16**, 1291-1298, (2013).
- 24 Degorce, F. *et al.* HTRF: A technology tailored for drug discovery - a review of theoretical aspects and recent applications. *Current chemical genomics* **3**, 22-32, (2009).
- 25 Kolterman, O. G., Gottlieb, A., Moyses, C. & Colburn, W. Reduction of postprandial hyperglycemia in subjects with IDDM by intravenous infusion of AC137, a human amylin analogue. *Diabetes Care* **18**, 1179-1182, (1995).
- 26 Gedulin, B. R., Jodka, C. M., Herrmann, K. & Young, A. A. Role of endogenous amylin in glucagon secretion and gastric emptying in rats demonstrated with the selective antagonist, AC187. *Regulatory peptides* **137**, 121-127, (2006).
- 27 Mack, C. M. *et al.* Davalintide (AC2307), a novel amylin-mimetic peptide: enhanced pharmacological properties over native amylin to reduce food intake and body weight. *Int J Obes (Lond)* **34**, 385-395, (2010).

- 28 Young, A. Inhibition of glucagon secretion. *Adv Pharmacol* **52**, 151-171, (2005).
- 29 Westermark, P., Andersson, A. & Westermark, G. T. Islet amyloid polypeptide, islet amyloid, and diabetes mellitus. *Physiological reviews* **91**, 795-826, (2011).
- 30 Shroyer, L. A. & Varandani, P. T. Purification and characterization of a rat liver cytosol neutral thiol peptidase that degrades glucagon, insulin, and isolated insulin A and B chains. *Archives of biochemistry and biophysics* **236**, 205-219, (1985).
- 31 Duckworth, W. C. & Kitabchi, A. E. Insulin and glucagon degradation by the same enzyme. *Diabetes* **23**, 536-543, (1974).
- 32 Guo, Q., Manolopoulou, M., Bian, Y., Schilling, A. B. & Tang, W. J. Molecular basis for the recognition and cleavages of IGF-II, TGF-alpha, and amylin by human insulin-degrading enzyme. *J Mol Biol* **395**, 430-443, (2010).
- 33 Ralat, L. A. *et al.* Insulin-degrading enzyme modulates the natriuretic peptide-mediated signaling response. *J Biol Chem* **286**, 4670-4679, (2011).
- 34 Lipinski, C. A., Lombardo, F., Dominy, B. W. & Feeney, P. J. Experimental and computational approaches to estimate solubility and permeability in drug discovery and development settings. *Advanced drug delivery reviews* **46**, 3-26, (2001).
- 35 Mooradian, A. D. & Thurman, J. E. Drug therapy of postprandial hyperglycaemia. *Drugs* **57**, 19-29, (1999).
- 36 Properties calculated with the online tool Chemicalize.org (ChemAxon). <http://www.chemicalize.org/%3E>.
- 37 Malito, E., Hulse, R. E. & Tang, W. J. Amyloid beta-degrading cryptidases: insulin degrading enzyme, presequence peptidase, and neprilysin. *Cellular and molecular life sciences : CMLS* **65**, 2574-2585, (2008).

- 38 Mangiafico, S., Costello-Boerrigter, L. C., Andersen, I. A., Cataliotti, A. & Burnett, J. C., Jr. Neutral endopeptidase inhibition and the natriuretic peptide system: an evolving strategy in cardiovascular therapeutics. *European heart journal* **34**, 886-893c, (2013).
- 39 Russell, F. A., King, R., Smillie, S. J., Kodji, X. & Brain, S. D. Calcitonin gene-related peptide: physiology and pathophysiology. *Physiological reviews* **94**, 1099-1142, (2014).
- 40 Kim, Y. G., Lone, A. M., Nolte, W. M. & Saghatelian, A. Peptidomics approach to elucidate the proteolytic regulation of bioactive peptides. *Proc Natl Acad Sci U S A* **109**, 8523-8527, (2012).
- 41 Potter, L. R. Natriuretic peptide metabolism, clearance and degradation. *The FEBS journal* **278**, 1808-1817, (2011).
- 42 Muller, D., Baumeister, H., Buck, F. & Richter, D. Atrial natriuretic peptide (ANP) is a high-affinity substrate for rat insulin-degrading enzyme. *European journal of biochemistry / FEBS* **202**, 285-292, (1991).
- 43 Corti, R., Burnett, J. C., Jr., Rouleau, J. L., Ruschitzka, F. & Luscher, T. F. Vasopeptidase inhibitors: a new therapeutic concept in cardiovascular disease? *Circulation* **104**, 1856-1862, (2001).
- 44 Parati, G., Bilo, G. & Ochoa, J. E. Benefits of tight blood pressure control in diabetic patients with hypertension: importance of early and sustained implementation of effective treatment strategies. *Diabetes Care* **34 Suppl 2**, S297-303, (2011).
- 45 *Centers for Disease Control and Prevention. National Diabetes Statistics Report: Estimates of Diabetes and Its Burden in the United States, 2014. Atlanta, GA: US Department of Health and Human Services; 2014.*

Appendix

Perl scripts used for deconvolution of *in vitro* selections

Contributions: The following Perl scripts were coded by Dr. Ralph Kleiner, and they were used in Chapter 2 with minor modifications.

```
#!/usr/bin/perl
use warnings;
open (FILE01, "/Users/FILE.fastq");
open (SEQ1, ">/Users/FILE.fastq.txt");
$i = 0;

while ($line1 = <FILE01>) {
    if ($line1 =~ /^@/) {
        $line2 = <FILE01>;
        chomp($line2);
        if (primer($line2) == 1) {
            $i = $i + 1;
            $revcom = reverse $line2;
            $revcom =~ tr/ACGT/TGCA/;
            print SEQ1 ">$i\n";
            print SEQ1 "$revcom\n";
        }
    }
}

sub rev_com {
    my ($DNA) = @_;
    my ($revcom);
    $revcom = reverse $DNA;
    $revcom =~ tr/ACGT/TGCA/;
    return $revcom;
}

sub primer{
    my ($line) = @_;
    my (@chars1, @chars2);
    my ($compvall);
    @chars1 = split(//, $line);
    # @chars2 = split(//, "GAGTGGGATG"); # search for index with offset 0 for selections 1 and
    7
    # @chars2 = split(//, "TGAGTGGGAT"); # search for index with offset 1 for selections 2 and
    8
    # @chars2 = split(//, "CTGAGTGGGA"); # search for index with offset 2 for selections 3 and
    9
    # @chars2 = split(//, "ACTGAGTGGG"); # search for index with offset 3 for selections 4 and
    10
    # @chars2 = split(//, "CACTGAGTGG"); # search for index with offset 4 for selections 5 and
    11
    # @chars2 = split(//, "TCACTGAGTG"); # search for index with offset 5 for selections 6 and
    12
    $compvall = (($chars1[0] eq $chars2[0]) + ($chars1[1] eq $chars2[1]) + ($chars1[2] eq
    $chars2[2]) + ($chars1[3] eq $chars2[3]) + ($chars1[4] eq $chars2[4]) + ($chars1[5] eq
    $chars2[5]) + ($chars1[6] eq $chars2[6]) + ($chars1[7] eq $chars2[7]) + ($chars1[8] eq
    $chars2[8]) + ($chars1[9] eq $chars2[9]));
    if ($compvall >= 7) {
        return 1;}
    else {
        return 0;}
}

print "Sequence trimming completed.\a\n";
```

```
#!/usr/bin/perl
use warnings;
open (FILE1, "/Users/FILE.fastq.txt");
open (SEQ, ">/Users/FILE.txt");

    my $offset = 5; my $dots = "....." ; # for selections 1 and 7
# my $offset = 4; my $dots = "...." ; # for selections 2 and 8
# my $offset = 3; my $dots = "... " ; # for selections 3 and 9
# my $offset = 2; my $dots = ".. " ; # for selections 4 and 10
# my $offset = 1; my $dots = ". " ; # for selections 5 and 11
# my $offset = 0; my $dots = " " ; # for selections 6 and 12

my @codon1 = ("TTCCTC", "AGCTCA", "ATCGGA", "TGTGCA", "AGACTC", "CTTCAG", "AGTCGA", "ATGACG",
"ACTAGC", "CAACCT", "TCGGTA", "GCTTAC"); #, "CATCTC", "GAATTC"); # Codon AKA 16 is "CATCTC"
#          1          2          3          4          5          6          7          8
9          10         11         12         13         14
my @codon2 = ("GCTGAA", "AACGGT", "GTCGAT", "GATTGC", "GGACTT", "ACGGAT", "AGGACT", "TCGAGT",
"GCAAGA", "CTTGTG", "GGCTAA", "CTGGAA"); #, "CATCTC", "GAATTC"); # EcoRI is "GAATTC" and 16 is
"CATCTC"

my @codon3 = ("GGCTTT", "AGGCTT", "GCCAAA", "AGGAAC", "CGTATG", "CATGAG", "GCAGTA", "GCGTAT",
"GAGACA", "CTGTAG", "GGAATC", "TAGCTG"); #, "GCTCTT", "GAATTC"); # Codon AKA 16 is "GCTCTT"

my @scaffold = ("AAC", "CTA", "AGA", "TAC", "CAA", "TGA", "ACA", "GAA");

sub codon_match {
    my ($codon, $line, $pos, $mis) = @_;
    my ($n, @chars1, @chars2);
    my ($id) = 0;
    for ($n=0; $n<14; $n++) {
        @chars1 = split(/,/, $codon->[$n]);
        @chars2 = split(/,/, $line);
        if (($chars1[0] eq $chars2[$pos-1]) + ($chars1[1] eq $chars2[$pos]) + ($chars1[2] eq
$chars2[$pos+1]) + ($chars1[3] eq $chars2[$pos+2]) + ($chars1[4] eq $chars2[$pos+3]) +
($chars1[5] eq $chars2[$pos+4])) >= (6-$mis)){
            $id = $n+1;
            last;
        }
    }
    return $id;
}

sub scaffold_match_perfect_for {
    my ($scaffold, $line) = @_;
    my ($n);
    my ($id) = 0;
    for ($n=0; $n<8; $n++) {
        if ($line =~
/^.....$dots$
scaffold->[$n]/){
            $id = $n+1;
            last;
        }
    }
}
```

```
        return $sid;
    }

    sub scaffold_match_perfect_rev {
        my ($scaffold, $line) = @_;
        my ($n);
        my ($sid) = 0;
        for ($n=0; $n<8; $n++) {
            if ($line =~
/^.....$dots$
scaffold->[$n]/){
                $sid = $n+1;
                last;
            }
        }
        return $sid;
    }

    sub rev_com {
        my ($DNA) = @_;
        my ($revcom);
        $revcom = reverse $DNA;
        $revcom =~ tr/ACGT/TGCA/;
        return $revcom;
    }

    sub codon {
        my ($codon, $line, $pos) = @_;
        if (codon_match($codon, $line, $pos, 1) >=1) {
            return codon_match($codon, $line, $pos, 1);}
        elsif ((codon_match($codon, $line, $pos, 1) == 0) && (codon_match($codon, $line, $pos,
2) >=1)) {
            return codon_match($codon, $line, $pos, 2);}
        else { return 0; }
    }

    $i = 0;

    while ($line1 = <FILE1>) {
        $line3 = <FILE1>;
        chomp($line3);
        $i = $i + 1;
        # $s = barcode_match(\@barcodeS, $line3, 1, 2);
        $a1 = codon_match(\@codon1, $line3, 53 + $offset, 1);
        $b1 = codon_match(\@codon2, $line3, 64 + $offset, 1);
        $c1 = codon_match(\@codon3, $line3, 75 + $offset, 1);
        $d1 = scaffold_match_perfect_for(\@scaffold, $line3);
        print SEQ ">$i\n";
        #print SEQ "S$s A$c1 B$b1 C$a1 D$d1\n"; #with internal barcode
        print SEQ "S1 A$c1 B$b1 C$a1 D$d1\n"; #without internal barcode
    }

    sub primer{
        my ($line) = @_;
        my (@chars1, @chars2, @chars3);
```

```
my ($compval1, $compval2);
@chars1 = split(/, $line);
# @chars2 = split(/, "CCATTACTCGCCCTGTACAC"); #this is the new primer
@chars2 = split(/, "GCAGTACCAACCCTGTACAC"); #this is the original primer
@chars3 = split(/, "CTGACTACAGAGTGGGATG");
$compval1 = (($chars1[5] eq $chars2[0]) + ($chars1[6] eq $chars2[1]) + ($chars1[7] eq
$chars2[2]) + ($chars1[8] eq $chars2[3]) + ($chars1[9] eq $chars2[4]) + ($chars1[10] eq
$chars2[5]) + ($chars1[11] eq $chars2[6]) + ($chars1[12] eq $chars2[7]) + ($chars1[13] eq
$chars2[8]) + ($chars1[14] eq $chars2[9]) + ($chars1[15] eq $chars2[10]) + ($chars1[16] eq
$chars2[11]) + ($chars1[17] eq $chars2[12]) + ($chars1[18] eq $chars2[13]) + ($chars1[19] eq
$chars2[14]) + ($chars1[20] eq $chars2[15]) + ($chars1[21] eq $chars2[16]) + ($chars1[22] eq
$chars2[17]) + ($chars1[23] eq $chars2[18]) + ($chars1[24] eq $chars2[19]));
$compval2 = (($chars1[5] eq $chars3[0]) + ($chars1[6] eq $chars3[1]) + ($chars1[7] eq
$chars3[2]) + ($chars1[8] eq $chars3[3]) + ($chars1[9] eq $chars3[4]) + ($chars1[10] eq
$chars3[5]) + ($chars1[11] eq $chars3[6]) + ($chars1[12] eq $chars3[7]) + ($chars1[13] eq
$chars3[8]) + ($chars1[14] eq $chars3[9]) + ($chars1[15] eq $chars3[10]) + ($chars1[16] eq
$chars3[11]) + ($chars1[17] eq $chars3[12]) + ($chars1[18] eq $chars3[13]) + ($chars1[19] eq
$chars3[14]) + ($chars1[20] eq $chars3[15]) + ($chars1[21] eq $chars3[16]) + ($chars1[22] eq
$chars3[17]) + ($chars1[23] eq $chars3[18]) + ($chars1[24] eq $chars3[19]));
    if ($compval1 >= 15) {
        return 1;}
    elsif ($compval2 >= 15) {
        return -1;}
    else {
        return 0;}
}

print "Codon assignment complete.\a\n";
```



```
#!/usr/bin/perl
use warnings;
open (SEQCODONS, "/Users/FILE.txt");
open (MORECODONS, "/Users/Codonlist.txt");

@filename = qw(Final/Sample_4-2_JMJD2A.R1.fastq_freq.txt
Other/Bc2.txt Other/Bc3.txt Other/Bc4.txt Other/Bc5.txt Other/Bc6.txt Other/Bc7.txt
Other/Bc8.txt Other/Bc9.txt Other/Bc10.txt Other/Bc11.txt Other/Bc12.txt Other/Bc13.txt
Other/Bc14.txt Other/Bc15.txt Other/Bc16.txt Other/Bc17.txt Other/Bc0.txt);

@arraylist = (@array1, @array2, @array3, @array4, @array5, @array6, @array7, @array8, @array9,
@array10, @array11, @array12, @array13, @array14, @array15, @array16, @array17, @array18);

@arrayname = qw(Bc1 Bc2 Bc3 Bc4 Bc5 Bc6 Bc7 Bc8 Bc9 Bc10 Bc11 Bc12 Bc13 Bc14 Bc15 Bc16 Bc17
Bc0);

for (my ($i) = 0; $i<18; $i++) {
    open ($arrayname[$i], ">$filename[$i]") or die "$! error trying to overwrite";
}

while ($line3 = <MORECODONS>) {
    $line4 = <MORECODONS>;
    chomp($line4);
    ($A2, $B2, $C2, $D2) = split(/\t/, $line4);
    $D3 = substr $D2, 0, 2;
    $code2 = join("\t", $A2, $B2, $C2, $D3);
    if ($A2 =~ "A") {
        push(@array1, $code2);}
    }

while ($line1 = <SEQCODONS>) {
    $line2 = <SEQCODONS>;
    chomp($line2);
    ($s, $A, $B, $C, $D) = split(/\t/, $line2);
    $code = join("\t", $A, $B, $C, $D);
    if ($s =~ "S1") {
        push(@array1, $code);}
    else {
        push(@array1, $code);}
    }

@arraylist = (\@array1, \@array2, \@array3, \@array4, \@array5, \@array6, \@array7, \@array8,
\@array9, \@array10, \@array11, \@array12, \@array13, \@array14, \@array15, \@array16,
\@array17, \@array18);

sub count {
    my ($array_ref, $fh) = @_;
    my ($n);
    my %per;
    my %count;
    my @array = @$array_ref;
    map { $count{$_}++ } @array;
    $n = scalar(@array);
    foreach $_ (keys(%count)){
        $per{$_} = ($count{$_})/$n;
    }
}
```

```
    map { print {$fh} "$_ = $count{$_} $per{$_}\n"} sort {$count{$b} <=> $count{$a}}
keys(%count);
print {$fh} "total reads    =    $n";
}

for (my($j) = 0; $j<18; $j++) {
    count($arraylist[$j], $arrayname[$j]);
}

print "Codon counting completed.\a\n";
```

1
A1 B1 C1 D1
2
A1 B1 C2 D1
3
A1 B1 C3 D1
4
A1 B1 C4 D1
5
A1 B1 C5 D1
6
A1 B1 C6 D1
7
A1 B1 C7 D1
8
A1 B1 C8 D1
9
A1 B1 C9 D1
10
A1 B1 C10 D1
11
A1 B1 C11 D1
12
A1 B1 C12 D1
13
A1 B2 C1 D1
14
A1 B2 C2 D1
15
A1 B2 C3 D1
16
A1 B2 C4 D1
17
A1 B2 C5 D1
18
A1 B2 C6 D1
19
A1 B2 C7 D1
20
A1 B2 C8 D1
21
A1 B2 C9 D1
22
A1 B2 C10 D1
23
A1 B2 C11 D1
24
A1 B2 C12 D1
25
A1 B3 C1 D1
26
A1 B3 C2 D1
...
13823
A12 B12 C11 D8
13824
A12 B12 C12 D8